The Pennsylvania State University

The Graduate School

Intercollege Program of Materials Science and Engineering

CERAMIC COATINGS FOR NUCLEAR FUEL CLADDING

TO ENHANCE ACCIDENT TOLERANCE

A Dissertation in

Materials Science and Engineering

by

Ece Alat

Submitted in Partial Fulfillment
of the Requirements
for the Degree of

Doctor of Philosophy

May 2018

The dissertation of Ece Alat was reviewed and approved* by the following:

Arthur T. Motta
Professor of Mechanical and Nuclear Engineering and Materials Science and Engineering
Chair of the Nuclear Engineering Program
Dissertation Co-Advisor
Co-Chair of Committee

Douglas E. Wolfe
Professor of Materials Science and Engineering
Department Head of the Advanced Coatings at the Applied Research Laboratory
Dissertation Co-Advisor
Co-Chair of Committee

Joan M. Redwing
Professor of Materials Science and Engineering, Chemical Engineering and Electrical Engineering
Associate Director of the Materials Research Institute

Allison Beese
Assistant Professor of Materials Science and Engineering

Hojong Kim
Assistant Professor of Materials Science and Engineering
Norris B. McFarlane Faculty Professor

Suzanne Mohney
Professor of Materials Science and Electrical Engineering
Chair of the Intercollege Graduate Degree Program in Materials Science and Engineering

*Signatures are on file in the Graduate School

ABSTRACT

This research is focused on developing nuclear fuel claddings with ceramic coatings that can perform well during normal operation and can withstand transient conditions such as loss of coolant accident for longer durations than current cladding material and then provide longer coping times. This was done by creating TiAlN coatings using physical vapor deposition and optimizing the deposition parameters and multilayer architecture to achieve the best performance.

Zirconium-based alloys are currently widely used as cladding materials due to their low neutron absorption cross-section, good mechanical properties and high melting point. However, waterside corrosion of these alloys cause zirconium oxide formation and hydrogen generation which leads to hydrogen pick up and hydride embrittlement. Moreover, hydrogen generation in case of accelerated corrosion at higher temperatures due to loss of active cooling can lead to hydrogen explosions such as observed in the Fukushima-Daiichi accident when hydrogen explosions in the reactor building worsened the accident conditions. This accident motivated research into Accident Tolerant Fuels (ATF), which are fuels that are more forgiving in case of a loss-of-coolant-accident (LOCA). This research is an innovative approach since it considers application of TiN and TiAlN ceramic coatings on ZIRLO® substrate by cathodic arc physical vapor deposition (CA-PVD), which improve corrosion resistance without a major change in core design and contribute to the design safety.

Cathodic arc physical vapor deposition was used since it provides flexibility in coating properties by adjustment of deposition parameters. A systematic study was performed to identify the optimum deposition parameters to achieve enhanced adhesion of nitride-based coatings on ZIRLO® substrates and best corrosion performance. The developed coatings are subjected to scratch tests and long-term corrosion tests. First, the single-layer TiAlN and single-layer TiN coating deposition on ZIRLO® sheets were characterized in detail with regards to their as-

deposited coating properties (topography, uniformity, crystal structure, residual stresses), failure modes during scratch testing and oxide formation after corrosion testing. Second, a multilayer coating design architecture is investigated to achieve enhanced corrosion resistance. Then the 8-layer TiN/TiAlN coatings deposited on ZIRLO® tubes were exposed to long-term corrosion testing. Throughout the study, the following parameters were optimized to provide best corrosion resistance: (i) substrate surface roughness, (ii) substrate surface preparation method, (iii) titanium bond coating layer thickness, (iv) total coating thickness, (v) cathode composition, (vi) substrate bias, (vii) nitrogen partial pressure and (viii) multilayer design architecture.

Mechanical performance evaluation involved scratch testing and post-scratched sample failure mode characterization. The corrosion tests were performed at Westinghouse in autoclave in static pure water at 360ºC and 18.7 MPa up to 128 days in order to evaluate the normal operating condition performance of the coatings. Furthermore, supercritical water testing was performed in University of Michigan autoclave at in deaerated water at 542ºC and 24.5 MPa for 48 hours. Additionally, differential scanning calorimetry and thermogravimetric analysis were performed to test oxidation onset point in air atmosphere. Furthermore, high temperature air oxidation testing was performed in furnace in air atmosphere up to 800ºC. Weight gain analysis and characterizations (optical microscopy, X-ray diffraction, scanning electron microscopy, energy-dispersive spectroscopy, Raman spectroscopy) were performed to examine as-deposited coating properties and to evaluate coating performance after corrosion and mechanical testing.

The results determined that 8-layer TiN/TiAlN coatings deposited with optimized parameters achieved good adhesion and substantially enhanced corrosion performance, which makes this approach promising for development of accident tolerant nuclear fuel cladding.

TABLE OF CONTENTS

LIST OF FIGURES

LIST OF TABLES

ACKNOWLEDGEMENTS

First and foremost, I would like to thank my co-advisors Dr. Arthur T. Motta and Dr. Douglas E. Wolfe for providing me with the invaluable opportunity and privilege of working in their group. I was fortunate to receive their guidance and mentorship during my Ph.D. work at Penn State, which has formed me into the scientist and person I am today. It has been an honor to work with them. I would like to acknowledge our collaborators at Westinghouse Electric Co.: Dr. Robert Comstock and Dr. Joanna Partezana. I would also like to thank Dr. Shikha Ebrahim and Dr. Fan-Bill Cheung for our collaborative study.

I would like to thank my committee members, Dr. Joan Redwing, Dr. Allison Beese and Dr. Hojong Kim for their time, consideration, helpful guidance, and insightful comments during this process. I owe thanks to Dr. Kenan Unlu who initiated my Ph.D. journey at Penn State by his valuable guidance and sincere support. I would like to thank all the members of the Materials for Nuclear Power and the Advanced Coatings groups for providing a great atmosphere to work. I would like to acknowledge the staff members in the ARL Advanced Coatings Department and the MRI Materials Characterization Lab for helping me throughout the course of this work.

I am extremely thankful to my parents, Hikmet and Ali Alat, my aunt Beyhan Erpek, my brother Enis Alat, and my cousin Sena Edizler. Without their continuous support, I would not be where I am today. I would like to express my sincere thanks to Ismail Alperen Ayhan for his invaluable support and making State College my home. I would like to acknowledge Dr. Jeremy Schreiber for his support and for hosting movie nights. I wish to address special thanks to all my friends for their support and priceless memories.

Chapter 1

Introduction

1.1. Nuclear Reactors and Cladding

The world needs an increasing supply of cleanly-generated electricity. Nuclear power can contribute to this need since it is a highly efficient, low-cost clean energy source [1]. However, the current state of nuclear power plants still needs to be further improved for operational reliability under normal and transient conditions. The most common reactors are boiling water reactor (BWR) and the pressurized water reactor (PWR). Among these, the pressurized water reactor (PWR), which is a type of light water reactor (LWR), is the most widely used in the world [2–4]. The main difference of the PWR type nuclear power plant from the BWR is that PWRs are composed of two separate water loops: primary and secondary, whereas the BWR has a single cycle. Having two separate loops provides the advantage of restricting the irradiated water in the nuclear reactor building, at the cost of some thermal efficiency.

Figure 1-1 shows a schematic representation of a PWR nuclear power plant. The PWR nuclear power plant is composed of five main parts: reactor pressure vessel, steam generator, steam turbine, generator and condenser. Energy is created within the reactor core at the nuclear reactor with the splitting of uranium atoms in the nuclear fuel rod (nuclear fission), resulting in heat generation. The generated heat is transferred to the coolant water which flows by the nuclear fuel rods. The coolant water is kept under pressure in the reactor core by the pressurizer to allow it to be at high temperature (and then increase efficiency) without boiling. The heated water is transferred from the reactor core to the steam generator, where it transfers heat to the water in the secondary loop to produce steam. Then, the water in the primary loop, returns to the reactor building to be reused. Meanwhile, the steam in the secondary loop is used to turn the turbines in

the generator and create electricity. Finally, the steam is condensed back to water in the condenser and returns to the steam generator to be reused again in the secondary loop. [3,5]
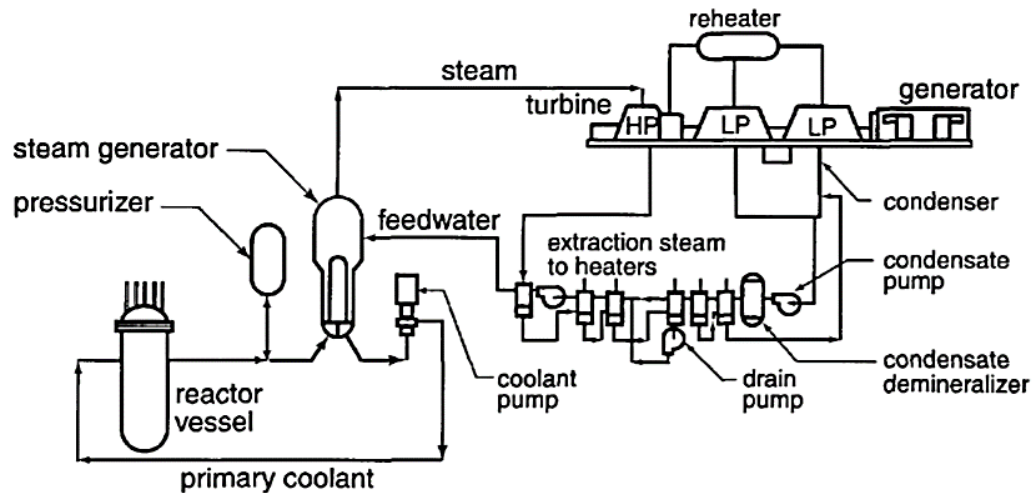
Figure 1-1. Schematic representations of the five major parts in a pressurized water reactor (PWR) power plant [4].

Figure 1-2 shows a schematic representation of a nuclear fuel assembly [4]. A nuclear fuel assembly is composed of about 200 tubes kept in place by with spacer grids. These tubes include both guide tubes and fuel rods containing enriched uranium dioxide (or a mixture of uranium and plutonium oxide in the case of MOX fuel) in the form of ceramic fuel pellets stacked in the cladding tube [4]. The cladding separates the fuel pellets from the surrounding coolant water, thus functioning as a barrier to avoid fission product release while permitting neutron flux and heat transfer to the coolant water [6]. During normal operation conditions, the fuel cladding is exposed to the coolant water (Chemistry; O_2:<0.05 ppb, H_2: 2-5 ppm, pH: 6.9, 7.4, B: 0-2200 ppm, Li: 0.5-5 ppm) at 280-330°C and 15.5 MPa, and a neutron flux on the order of 6-9 x 10^{13} n $cm^{-2}s^{-1}$ (E>1 MeV) [4,5]. Therefore, the cladding materials must have a combination of material properties including low neutron absorption cross-section, high thermal conductivity, high chemical stability, good mechanical properties, and a high melting point to maintain performance during operation [7].
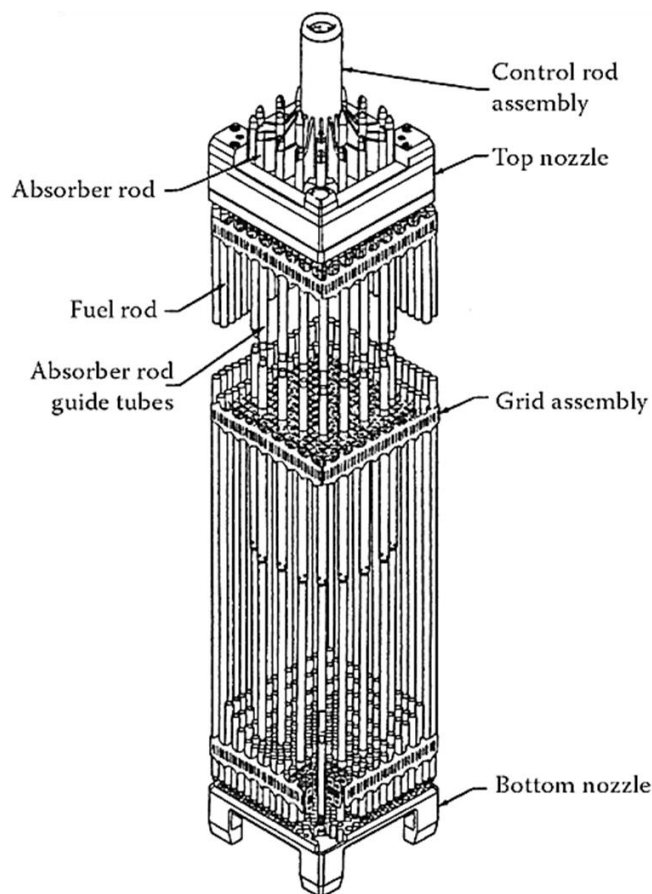
Figure 1-2. Schematic representation of a nuclear fuel assembly. [4]

Zirconium-based alloys have been widely used as LWR cladding tubing materials because of their low neutron absorption coefficient, high strength and good corrosion resistance in water near 300°C [7,8,5]. Zr-based alloys have been continuously optimized to improve their corrosion resistance and strength with the aim of achieving improved safety margins and higher burnup. Throughout the years, the positive effects of Sn, Fe and Cr alloying elements on corrosion resistance, yield strength and creep resistance have been observed, and eventually, Zircaloy-4 (Zr-4, Zr-1.5 wt.% Sn- 0.2 wt.% Fe- 0.1 wt.% Cr [9]) became the standard cladding material for PWRs since 1970s [7]. Recent trends have transitioned to zirconium-niobium alloys since Nb provides better corrosion resistance [10]. This has led to the development of new Zr-based alloys including M5 (Zr-1 wt.% Nb- 0.05 wt.% Fe - 0.015 wt.% Cr- 0.01 wt.% Sn [9]) and

ZIRLO® [1] (Zr-1 wt.% Nb- 1 wt.% Sn- 0.1 wt.% Fe [9]), which exhibited better corrosion performance, creep resistance and in-reactor performance compared to Zircaloy-4, and has now replaced it in reactor cores [7,11–13].

Although Zr-based alloys have advanced properties, waterside degradation of nuclear fuel cladding limits its life.

1.2. Accident Tolerant Fuels (ATFs)

The cladding performance is highly challenged in the case of design-basis (DB) or beyond design basis (BDB) accident conditions. The stages of one of the principal DB accidents, the loss-of-coolant-accident (LOCA), are schematically shown in Figure 1-3. During a LOCA core cooling capability is lost, and decay heat boils off the remaining coolant water. The temperature increases as a result and at ~800°C, alpha to beta phase transformation takes place. As the temperature increases, corrosion reactions and the corresponding heat and hydrogen generation are significantly accelerated [6]. Meanwhile, oxygen diffusion due to enhanced high temperature corrosion on clad surface makes alpha phase more brittle. The pressure outside the cladding tube drops because of coolant water loss and inside the cladding, the pressure rises with increased temperature. This results in ballooning and burst of the cladding. The cladding temperature may increase above 1200ºC leading to a significant acceleration of the corrosion reaction and corresponding hydrogen generation. If the emergency core cooling system (ECCS) is operational, then the fuel is quenched with the injected coolant into the core. However, if the ECCS is not operational, then the degradation can lead to fuel rod melting [14]. An example of this occurred during the US Three Mile Island (TMI) accident in 1979, which occurred due to a

---

[1] ZIRLO® is a registered trademark of the Westinghouse Electric Company LLC, its Affiliates and/or Subsidiaries in the United States of America and may be registered in other countries throughout the world. All rights reserved. Unauthorized use is strictly prohibited. Other names may be trademarks of their respective owners.

malfunctioning of the coolant system, leading to fuel damage, partial melting of core internals and radioactive material release [15]. A more recent example occurred in the Fukushima-Daiichi accident, which started as a station blackout (SBO) accident but progressed to a beyond design basis accident. The Fukushima-Daiichi accident occurred in 2011 in Japan due to an earthquake and tsunami, in which a loss of offsite power created a station blackout condition in which there was little cooling for the reactors. In this case, as the temperature increased, high temperature steam oxidation (exothermic) of the Zr-based alloy cladding led to large amounts of heat production [16]. In particular, the generation of large amounts of hydrogen resulted in elevated hydrogen concentrations in the reactor buildings which led to hydrogen explosions that severely worsened the accident development [12,15,17]. This accident motivated research into Accident Tolerant Fuels (ATF). These are defined as fuels that provide additional coping time in the case of a loss of active cooling in the reactor core making external intervention possible before severe fuel damage can occur [12,11].
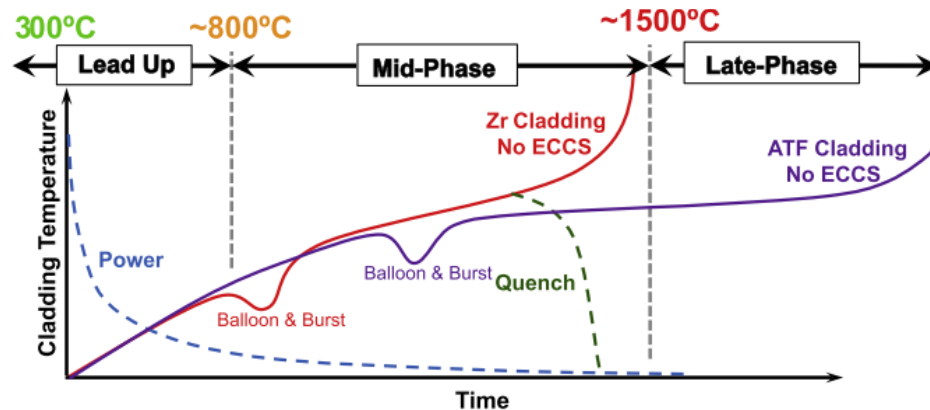
Figure 1-3. General overview of coolant–limited accident progression inside an LWR core comparing Zr-based alloy cladding behavior with accident tolerant fuel (ATF) cladding expectation in the case of no emergency core cooling system (ECCS) [14]

Different accident tolerant fuel concepts have been investigated by various groups. These studies were based on preliminary fuel cladding performance technology criteria that were identified through the scope of light water reactor sustainability program: critical performance, desired performance and licensing criteria [11]. These criteria are summarized in the Advanced

LWR Nuclear Fuel Cladding System Development Trade-off Study document and some of them can be listed as a maximum operating temperature >650°C, melting temperature >2000°C, higher strength (UTS>437 MPa), and a coping time > 10 h [11].

The ATF cladding concepts can be grouped into three categories: (i) full replacement, (ii) hybrid and (iii) protective coating applications. Candidate ATF technologies thus include coated Zr-based alloys (coating) [11], SiC ceramic matrix composite/ Zr-based alloy hybrids (hybrid) [11], SiC/SiC (full replacement) [11,18–32], advanced Zr-based alloys (fully replacement) [11], FeCrAl coated Mo-alloys (full replacement) [12,33,34], FeCrAl (full replacement) [35], Ti_3SiC_2 (full replacement) [34], Ti_2AlC (full replacement) [34] and engineered stainless steel alloys (full replacement) [12,11,34,16,36]. Full replacement approaches require end cap seal technology development in the case of SiC, fuel modification due to neutronic penalty in the case of FeCrAl and major engineering design changes to the reactor cores, which are not preferred due to limited experience and vast amount of effort required for licensing. Hybrid cladding designs require bonding technique development between the SiC ceramic matrix composite (CMC) and Zr-based alloy tubing. The third concept involves applying a protective coating layer application to the outer skin of the Zr-based alloy cladding tube. The challenges regarding a protective coating application involve the requirement for low neutronic penalty, ease of fabrication, mechanical properties, adhesion of the coating to the cladding and coating process scalability to production size compounds. Although these are challenges, a protective coating application is one of the most promising approaches that would improve the corrosion characteristics of the currently used Zr-based claddings without requiring a major change in cladding material. Coating designs that have been studied for Zr-based alloy substrates involve metallic, nonmetallic, oxide, carbide, nitride and multilayer coating designs [7,11,37–69]. These designs are summarized in Table 1-1. In this study, we focused on TiN and (Ti,Al)N coatings since they have been proven to enhance component mechanical performance and chemical stability, especially in the tooling industry for years.

Table 1-1. Summary of coating designs for Zr-based alloys compiled from [7,11,37].

Reference	Coating material	Deposition method	Thickness	Corrosion test	Remarks
Sridharan et al., 2007 [38]	N, C, O	Ion implantation	~0.12 μm	Autoclave 300, 500°C 25 MPa – 168 h	Comparable oxide layer thickness after corrosion.
Peng et al., 2006 [39]	Al	Ion implantation	~0.30 μm	Air 500°C 2 h	Reduced mass gain with increasing implantation fluence, maximum reaching 30% of the untreated sample
Abdelrazek et al., 1997 [40]	Pyrolytic carbon	Thermal cracking	-	-	Technological parameters for the preparation investigated, low coating rate
Skarohlid et al., 2014; Ashcheulov et al., 2015 [41]	Pyrolytic carbon	CVD	~0.30 μm	Steam 950-1100°C 30 min	Slightly improved steam oxidation resistance; stability after short time ion irradiation (10 dpa, 5 h, 3 MeV Fe^{2+})
Kim et al., 2014 [42]	Si	PS and LBS	70-120 μm	Steam 1200°C 2000 s	Improved oxidation resistance
Baczynski et al., 2014 [43]	Ti	Magnetron sputtering	0.0215, 0.043 μm	Steam 700°C	Improved oxidation resistance
Hwasung et al., 2016 [44]	$ZrSi_2$	Sputtering	~0.85 μm	Air 700°C 5 h	33% reduction in weight gain
Hauffe, 1976 [45]	Sn	Evaporation	0.02-0.23 μm	Air, 500°C, 80 days Steam, 403°C, 80 days Autoclave, 349°C, 17.6 MPa, 63 days	Slightly improved resistance under both autoclave and oxidation test with coating thickness up to 0.1 μm
Sridharan et al., 2007 [38]	Y	Sputtering and heavy ion bombardment	~0.1 μm	Autoclave 400°C 25 MPa, 168 h	Improved corrosion resistance

Reference	Material	Method	Thickness	Conditions	Results
Brachet et al., 2015; Idarraga-Trujllo et al., 2013	Cr	PVD	5-30 μm	Autoclave 360°C, 415°C 10 MPa, 200 days Steam, 1300°C	Excellent corrosion resistance (tens of times lower) and reduced hydrogen pickup under normal conditions
Ivanova et al., 2013 [46]	Cr	Cathodic arc evaporation	4 μm	Autoclave, 360°C, 18 MPa, 1000 h Steam, 1100°C, 4 h	Significant improved high-temperature steam oxidation resistance up to 1200°C
Kim et al., 2013 [47]	Cr	PS and LBS	80 μm	Steam, 1200°C, 2000 s	
Park et al., 2015 [48]	Cr	Arc ion plating	~10 μm	Steam, 1200°C, 2000 s	Negligible reduction of residual strength and ductility before the completely consumption of the metallic Cr layer
Kim et al., 2015 [49]	Cr	3D laser coating	80-200 μm	Steam, 1200°C, 2000 s	Good oxidation resistance without severe damage. Oxide layer was composed of equiaxed grains with pores at the grain boundaries.
Kim et al., 2016 [50]; Park et al., 2016 [51]	Cr	3D laser coating/cold spraying	80-200 μm	Steam, 1200°C, 3000 s	Improved ballooning and rupture resistance
Carr et al., 2016 [52]	Al-Zr	Magnetron sputtering and thermal annealing	~1 μm	Steam, 800-1000°C, 2 h	AlZr intermetallic formation; improved oxidation resistance at 800°C, no protective effect at 1000°C
Luscher et al., 2013 [53]	Ni-Zr	Electroplating and thermal treatments	2.5-10 μm	Steam, 290-370°C, 64 days	Thick coating cracked after annealing, NiZr intermetallic formation; too low oxidation temperatures
Terrani et al., 2013 [54]	FeCrAl alloy and 310 steel	HIP of Zr powder inside cans	~2 mm	Steam, 1300°C	Brittle intermetallic formed; improved oxidation resistance but too thick coatings; eutectic in binary Fe-Zr at ~900°C
Zhong et al., 2016 [55]	FeCrAl alloy	PVD	-0.3-1.1 μm	Steam, 700-100°C, 10 h Autoclave, 288°C, 9.5 MPa, 20 days	NiFe2O4 spinel formation under normal BWR condition, two times higher mass gain; significantly reduced oxidation resistance with high Al content during steam exposure

Reference	Material	Method	Thickness	Test conditions	Observations
Baney & Tulenko, 2003 [56]	Al$_2$O$_3$	Magnetron sputtering or electron beam evaporation and oxidation	~1 μm	Autoclave, 350°C, 20 MPa, 24 h	Unstable, soluble, and transform to AlOOH during normal conditions
Hul et al., 2011	ZrO$_2$	Plasma electrolytic oxidation	30 μm	Autoclave, 500°C, 25 MPa, 500 h	Better corrosion resistance in static autoclave, similar weight changes in a flowing system
Baney & Tulenko, 2003 [56]; Al-Olayyan et al., 2005 [57]	SiC	Pulsed plasma enhanced CVD	~1 μm	Autoclave, 350°C, 20 MPa Steam, 1200°C	Unstable, soluble during autoclave test; little improvement during steam oxidation
Pantano et al., 2014	Ti$_2$AlC	Cold spray or HVOF	40 μm	Steam, 1200°C	Composition change during HVOF; loose structure with pores and impurities; poor performance and fast oxidized
Maier et al., 2015 [58]	Ti$_2$AlC	Cold spray	~90 μm	Air, 700°C, 60 min Steam, 1005°C, 20 min	High hardness and wear resistance, relatively dense structure, significantly improved oxidation resistance
Tang et al., 2016 [37]	Ti$_2$AlC	Magnetron sputtering and thermal annealing (800°C)	~5 μm	Steam, 800-1200°C, 4 h	Dense and phase-pure coatings, protective alumina scale formed at 800°C, little improvement as temperature exceeded 1000°C, thick coating needed
Yeom et al., 2016 [59]	Ti$_2$AlC	Magnetron sputtering and thermal annealing (900°C)	1-5 μm	Autoclave, 400°C, 10.3 MPa, 72 h	Formation of microcracks after laser treatment; protective effect shown during autoclave test
Roberts, 2016 [60]	Cr$_2$AlC	Magnetron sputtering and thermal annealing	~1 μm	Autoclave, 360°C, 18.6 MPa, 10 days	Partial spallation observed after autoclave test, improved corrosion resistance for coated area

Reference	Coating	Deposition method	Thickness	Test conditions	Remarks
Sung et al., 2001 [61]	TiN	PVD	4 μm	-	Improved friction and wear damage resistance
Khatkhatay et al., 2014 [62]	TiN and TiAlN	Pulsed laser deposition	~2 μm	Autoclave, 500°C, 25 MPa, 48 h	Significant improved corrosion resistance, better performance of TiN coatings
Kim et al., 2013 [63]	CrN				
Daub et al., 2015 [64]	CrN, CrAlN, and TiAlN	PVD	2-4.5 μm	Autoclave, 350°C, 16.5 MPa, 30 days Steam, 1000-1100°C, 15 min	Excellent corrosion resistance and reduced steam oxidation of CrN coatings, unstable of CrAlN and TiAlN coatings during autoclave tests; reduced hydrogen ingress
Jin et al., 2016 [65]	Cr_3C_2+NiCr	HVOF	250 μm	Autoclave, 400°C, 10.3 MPa, 3 days Steam/air, 700-1000°C, 60 min	Loose structure of the coatings, higher mass gain during autoclave test, reduced steam oxidation rate
Park et al., 2016 [51]	Mo/FeCrAl	Cold spraying	15+200 μm	Steam, 1200°C, 3000 s	Negligible interdiffusion between the coating and the substrate and oxidation after test; 1.17 mm interdiffusion layer generated for coatings without barrier
Park, 2004 [66]	Al/amorphous alumina	Electron beam evaporation and sputtering	~1 μm	Autoclave, 343°C, 20.1 MPa, 200 days	Unstable, dissolve of the coatings during autoclave test
Kuprin et al., 2014, 2015 [67,68]	CrZr/Cr/CrN	Vacuum cathodic arc evaporation	~7 μm	Air, 600-1100°C, 60 min	Several times decreased oxidation rate
Wiklund et al., 1996 [69]	Alternating TiN/Ti	Reactive evaporation	1-4 μm	Autoclave, 360°C, 22 MPa, 200 days	Greatly improved corrosion and hydriding properties of Zircaloy; large number of sublayers preferred for optimal performance
Ivanova et al., 2013 [46]	Alternating Cr/CrAl	Vacuum cathodic arc evaporation	~4 μm	Autoclave, 360°C, 18 MPa, 1000 h Steam, 1100°C, 4 h	Around 10 times decreased corrosion rate and several times decreased oxidation rate

1.3. Motivation/Objective

Thus, a promising approach for developing ATF is the application of a protective coating to a Zr-based alloy cladding tube. However, most proposed coating designs in discussed literature have only been tested in laboratory scale and many of the coating deposition processes cannot be scaled to production size efficiently. Furthermore, coating studies in literature were mostly performed on Zircaloy-4 substrates with limited studies discussing adhesion of coatings to ZIRLO® substrates. Thus, the objective of this study is to develop coatings that adhere well to ZIRLO® to enhance corrosion resistance both during normal operation conditions and in the case of a loss of coolant accident.

1.4. Proposed Work

It is hypothesized that adherent TiN and (Ti,Al)N coatings can be deposited on ZIRLO® substrates by using cathodic arc physical vapor deposition (CA-PVD) to enhance corrosion resistance both during normal operation and accident conditions. It is anticipated that:

(a) The deposited CA-PVD coatings will have compressive residual stresses that will help resist crack propagation.

(b) The coating will adhere well to the ZIRLO® substrate and isolate it from the surrounding coolant water. These coatings will increase the corrosion performance of ZIRLO® samples by forming a passivating oxide layer on the surface of the (Ti,Al)N and TiN coatings which will act as a barrier for further oxidation.

(c) This protective layer will limit further oxidation, hydrogen generation and oxygen/hydrogen penetration in the case of a high temperature excursion.

(d) For the multilayer design architecture, increased corrosion tolerance is expected. For example, if degradation occurs to the top layer, successive layers may act as a new barrier and maintain the corrosion performance of the coating.

1.5. Background

1.5.1. TiN and (Ti,Al)N Coatings Deposition

Transition metal nitrides provide enhanced hardness, wear resistance and chemical inertness due to a mixed bonding structure involving ionic, covalent and metallic bonds [70]. TiN and (Ti,Al)N coatings have been widely used for years on high-speed tool steels, cemented carbides, and cermet substrates for various cutting and finishing operations in the tooling industry [70–77].

Table 1-2. Typical parameters and quantity of target ions of different PVD processes [78].

Parameters	Processes			
	Magnetron sputtering	Anodic arc ion plating	Electron beam ion plating	Cathodic arc ion plating
Evaporation tool	Sputter effect	Electron beam	Electron beam	Thermal arc
Phase transformation	Solid-vapor	Solid-vapor	Liquid-vapor	Solid-vapor
Geometry of target/cathode	Flexible	Limited	Limited	Flexible
Quantity of ionized target atoms (%)	1-5	5-40	<1	50-100
Additional ionization	Aimed	Unusual	Aimed	Not necessary
Inert gases necessary	Yes	No	Variable	No
Reactive deposition possible	Yes	Yes	Yes	Yes

Several physical vapor deposition (PVD) methods can be used to deposit these coatings. Table 1-2 shows typical parameters of magnetron sputtering, anodic arc ion plating, electron beam ion plating, and cathodic arc ion plating. Among these, magnetron sputtering, and cathodic arc PVD (CA-PVD) are most commonly used [70]. Compared to other methods, the CA-PVD method of coating deposition provides additional advantages such as higher ionization and flexibility in cathode geometry, which generally results in increased coating adhesion and manufacturing scalability [70,78]. In this study, the cathodic arc physical vapor deposition method will be used to deposit the coatings. Details of the CA-PVD process are provided in the following sections.

To achieve corrosion-resistant coatings, the deposited coatings should be dense and free of porosity and defects [79]. CA-PVD is a line-of-sight deposition process and has several advantages over other PVD processes such as the energetic particle bombardment on the substrate surface leading to good adhesion, dense coating formation, coating microstructure improvement, grain size reduction, microhardness enhancement due to high preferred orientation and the development of compressive stresses that help terminate crack propagation, tailorability of the interfacial products (especially in multilayer coatings), and scalability to production size and quantities [70,79–82]. However, there are also some disadvantages of the CA-PVD process, which should be considered. The first disadvantage is the potential deleterious effect of high compressive stresses on coating adhesion. Although high compressive stresses can improve the coating mechanical properties, residual stresses can also affect adhesion adversely depending on the type (compressive or tensile) or how large its magnitude is [79,83]. Extensive residual stresses are caused by thermal expansion coefficient differences between the coating and the substrate during temperature changes, and by intrinsic stresses caused by ion bombardment, composition fluctuations during the deposition process caused for example by variation in the ion-to-vapor arrival ratio. Depending on the deposition conditions residual stresses can reach the GPa level [79]. The second disadvantage of CA-PVD is the possibility of macroparticle formation.

Macroparticles can disrupt the continuity of the deposited coating and lead to coating degradation. However, they can be minimized by using macroparticle filters or steered CA-PVD [80]. These filters include magnetic filters, straight filters, duct filters, S-filter, out-of-plane double-and bent filter. [80].

Different coating process parameters such as substrate temperature, bias voltage, arc current and nitrogen pressure allow the coating properties to be tailored for application-specific use in extreme environments [82,84,85]. The substrate bias affects film microstructure, coating composition (Al content in (Ti,Al)N coating), impinging ion energy on the growing film (i.e., residual stress, density) which can lead to a denser coating, resputtering of depositing species, and surface texture [70,72,85,86]. Another effect of bias voltage is related to the reaction kinetics; a high bias voltage results in increased substrate surface temperature, thus increasing the kinetic energy of incident ions which facilitates the chemical reaction (Ti + $\frac{1}{2}N_2$ $\rightarrow$ TiN) by overcoming the activation barrier at much lower temperatures as compared to standard equilibrium conditions [25]. Additionally, the nitrogen content (i.e., partial pressure) affects coating composition, crystallography, hardness, toughness, wear/abrasion performance and degree of adhesion [72,87]. Thus, deposition parameters should be optimized depending on the application requirements.

1.5.2. Thermal Properties of TiN and (Ti,Al)N Coatings

Thermal properties of ATF coating designs are important since they are expected to maintain their properties at high temperature, as explained in Section 1-2. Figure 1-4 shows the equilibrium binary phase diagram of titanium and nitrogen. Pure titanium crystallizes as alpha (α) phase having a hexagonal crystal structure (a=0.2973 nm, c=0.47888 nm) up to 880°C [88,89]. TiN exhibits a face centered cubic NaCl crystal structure and a lattice parameter of 0.423 nm [70,90], as shown in Figure 1-5a. When Al is incorporated into the structure, titanium atoms are substituted by aluminum atoms and the lattice parameter decreases to almost 0.417 nm since Al

atoms are smaller than the Ti atoms [70,91,92]. After a certain concentration of Al, the crystal structure transforms into hexagonal, as shown in Figure 1-5b. Figure 1-6 shows the metastable TiN-AlN phase diagram for 50 at.%N [93,94]. During the deposition of $(Ti_{1-x}Al_x)N$ coatings, for a substrate temperature of 325°C, a cubic structure forms below 64 at.%Al (corresponding to 32 at.%Al on the diagram), a hexagonal structure forms above 68 at.%Al (corresponding to 34 at.%Al on the diagram) and a two-phase region exists in between the specified compositions. However, it should be noted that, differing from Figure 1-4, Zhou et al. [95] observed the coexistence of cubic NaCl and hexagonal wurtzite structure (AlN) in the range of 0.6<x<0.7 for $(Ti_{1-x}Al_x)N$ coatings deposited with a substrate temperature of 450°C.
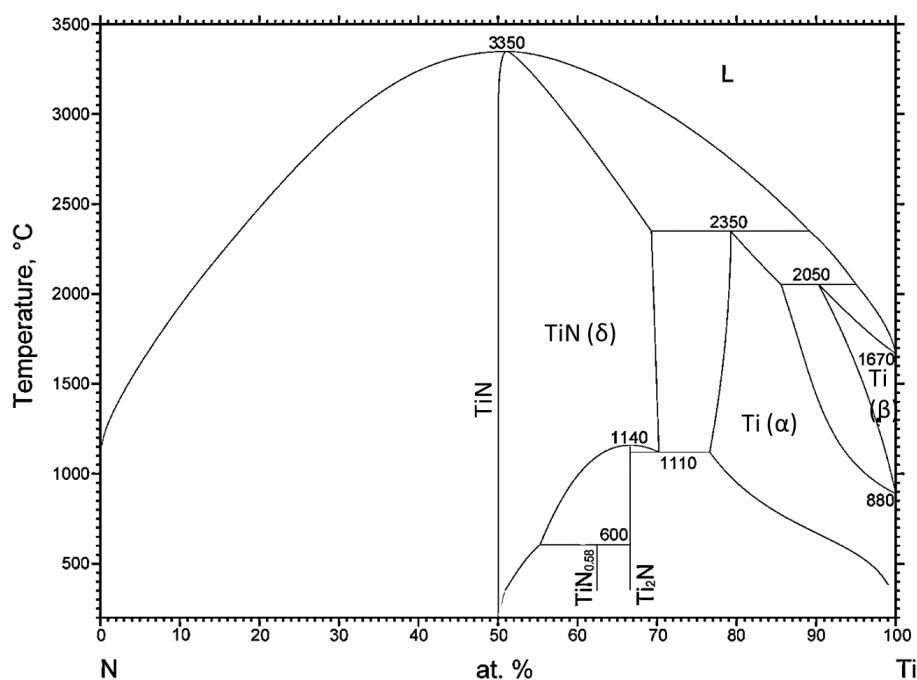
© ASM International 2006.   Diagram No. 907045

Figure 1-4. Ti-N equilibrium phase diagram adapted from the experimental investigation of Vahlas et al. [89].
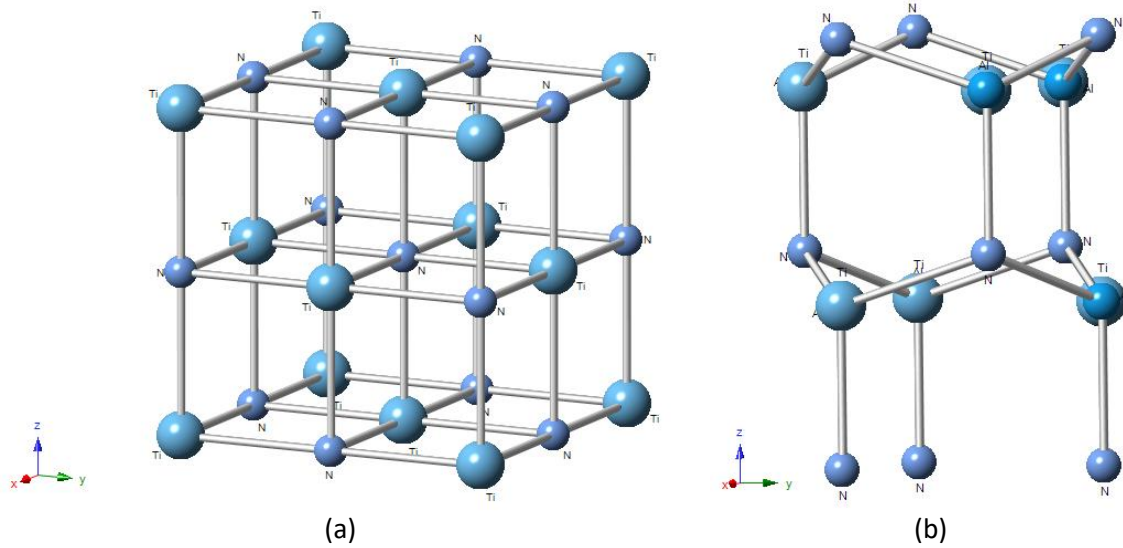
Figure 1-5. Crystal structures of (a) TiN (Crystal system: cubic; space group: Fm$\bar{3}$m) and (b) Ti$_{0.32}$Al$_{0.68}$N (Crystal system: hexagonal; space group: P6$_3$/mmc). (Images were drawn using Crystal Maker software based on the TiN data of Inamura et al. [96] and the Ti$_{1-x}$Al$_x$N of Tuilier et al. [97])
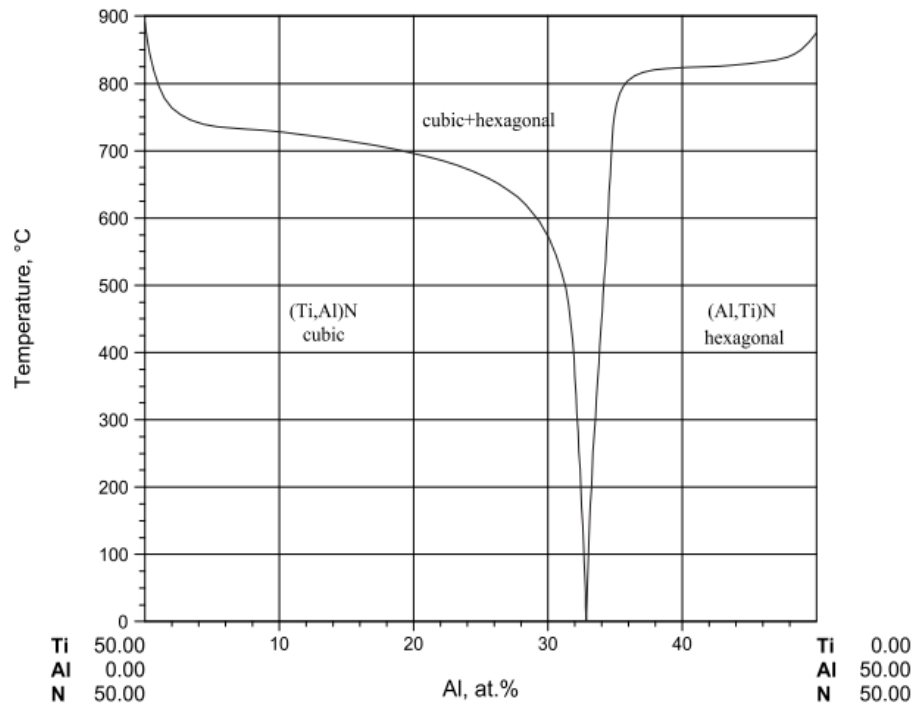
Figure 1-6. Metastable TiN-AlN phase diagram (vapor deposition phase diagram [98]) prepared according to experimental work of Cremer et al. [93,94].

Wang et al.[99] showed that coating adhesion to the substrate depends on the microhardness and the thermal expansion coefficient compatibility between the coating and the

substrate. A large mismatch between the microhardness and/or thermal expansion coefficients between the coating and the substrate results in poor adhesion [70]. In (Ti,Al)N and TiN coatings deposited by cathodic arc deposition, the coefficient of thermal expansion (CTE) of (Ti,Al)N (coating composition was not provided in the reference) was determined to be 7.5 x 10^{-6} K^{-1} while that of TiN is 9.4 x 10^{-6} K^{-1} [99]. At room temperature, ZIRLO® has a hexagonal crystal structure (α phase), but it undergoes phase transformations as $T_{\alpha \leftrightarrow \alpha+\beta}$=741°C and $T_{\alpha+\beta \leftrightarrow \beta}$=973°C, where β phase has a body-centered cubic crystal structure [100]. Previous studies have shown that the thermal expansion behavior of ZIRLO® and Zircaloy-4 is similar for the temperature range of 290-400ºC [101]. The CTE of Zircaloy-4 is ~6.3 x 10^{-6} K^{-1} (in tube axial direction) at 360ºC [102]. Therefore, application of a titanium bond coating would be expected to improve coating adhesion since its CTE of 8.5 x 10^{-6} K^{-1} (at room temperature) [103], lies in between that of the substrate and the coating.

Samani et al. [104] performed thermal conductivity measurement on CA-PVD single-layer TiN, single-layer (Ti,Al)N and multilayer TiN/(Ti,Al)N structures. It was shown that single layer TiN has a thermal conductivity of ~11 W/M-k. Incorporation of aluminum into the structure decreases the thermal conductivity such that single layer (Ti,Al)N has a thermal conductivity value ~4.8 W/mK. Furthermore, it was also shown that as the number of bilayers in the multilayer structure increases, thermal conductivity decreases.

1.5.3. Mechanical Properties of TiN and (Ti,Al)N Coatings

Mechanical properties that are important for coatings developed for nuclear fuel claddings involve fracture, fretting-corrosion, wear and spallation resistance considering the conditions experienced at both normal and accident conditions that were explained in section 1-2 [37]. Kimura et al. [105] demonstrated that arc ion plated TiN coatings had a microhardness of ~2000 HV, however (Ti,Al)N hardness values varied depending on the coating composition.

Figure 1-7 shows the change in the hardness value of $Ti_{1-x}Al_xN$ coatings with respect to the change in coating composition. Figure 1-8 shows the fracture toughness variations with respect to the change in coating composition. Both hardness and fracture toughness increase with increase in Al content in the $Ti_{1-x}Al_xN$ coating until x=0.6 [95,105,106]. Above this value they started to decrease which was attributed to the hexagonal crystal structure formation. So, there is an optimum Al concentration in terms of the mechanical performance, which should be considered during coating deposition.
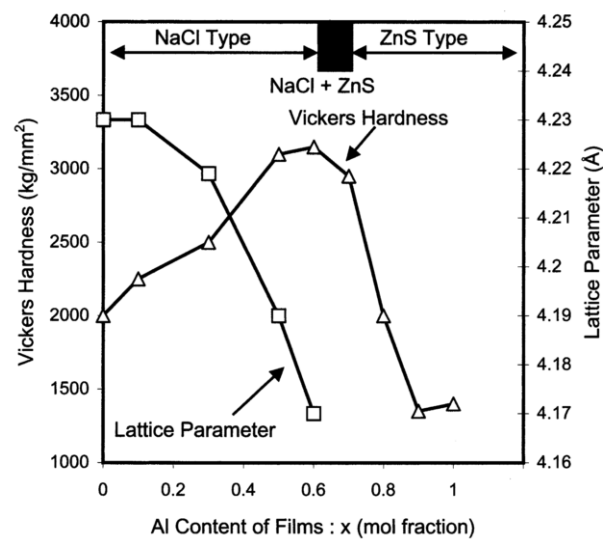
Figure 1-7. Average hardness numbers as a function of aluminum content in (Ti,Al)N coatings [105].
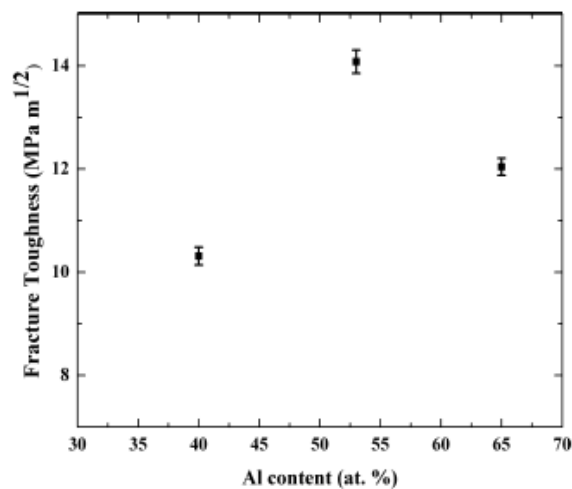
Figure 1-8. Fracture toughness with respect to the aluminum content in the (Ti,Al)N coatings [107].

Considering the possible hardness difference between the substrate and the coating, a solution was searched to enhance adhesion. In the literature, Ti arc etching or Ti bombardment for several minutes prior to the coating deposition were shown to improve coating adhesion [75]. Specifically, the use of titanium as a bond coating and its effect on coating performance were studied for TiN coatings on various stainless steel substrates [108–111] and it was demonstrated that adhesion improved in TiN coatings deposited by plasma assisted chemical vapor deposition (PACVD) and PVD as Ti interlayer thickness increased. Furthermore, Pishow et al. mentioned the titanium interlayer thickness optimization requirement to achieve better adhesion between the oxidized stainless steel substrate and PVD TiN coating [109]. Additionally, it should be noted that in the case of titanium-based hard coatings, the hardness is affected by microstructure and the amount of residual stress within the coating.

For multilayer coating design, structures which increase the total number of layers result in a larger number of interfaces which enhance hardness and strength. This was observed in (Ti,Al)N multilayer super lattice coatings having a lattice periodicity of 5-10 nm bilayer thickness [70].

1.5.4. TiN and (Ti,Al)N Coatings Corrosion Performance

There are many corrosion studies performed on TiN and (Ti,Al)N. Corrosion studies performed on PVD TiN and (Ti,Al)N coatings have been performed in air, water and oxygen environments at high temperature [62,92,95,112–123]. These are summarized in Table 1-3. Further information and details of the listed corrosion studies are provided in the following paragraphs in the current section.

Table 1-3. Studies on corrosion performance of PVD TiN and TiAlN coatings.

Author (year)	Substrate material	Coating material	Fabricating methodology	Thickness (μm)	Corrosion testing conditions	Remarks
Wittmer et al. (1981) [113]	Si/SiO$_2$	TiN with Ti bond coating (0.015 μm)	rf triode sputtering	0.23-0.32	Dry O$_2$ 500-600°C	- Rutile TiO$_2$ forms. - Thermally activated oxidation. - Activation energy 2.05 ± 0.04 eV. - Oxidation follows parabolic law. - Oxygen diffusion through the oxide is the rate limiting step.
Műnz (1986) [91]	Stainless steel & high-speed steel	Ti$_{27.5}$Al$_{28.9}$N$_{43.6}$	sputter ion plating	3-5	Air up to 1000°C	- Increasing aluminum content increased oxidation initiation temperature compared to TiN. - TiN oxidation initiation was 550°C. - TiAlN oxidation initiated at 700-750°C. - Formation of amorphous Al$_2$O$_3$ prevents further oxidation at 700°C tested up to 400 h. - At 800°C, oxidation behavior changed after ~6 h indicating not enough stability of the amorphous Al$_2$O$_3$.
McIntyre et al. (1990) [118]	Stainless steel	Ti$_{0.5}$Al$_{0.5}$N	dc magnetron sputter (negative substrate bias of 0 or 150 V)	2-5	Pure O$_2$ from 6 h at 750 to 7 min at 900°C	- Initially parabolic oxidation. - TiO$_2$ formation at the end of initial parabolic regime. - Two partially crystalline oxide sublayers (upper Al-rich and lower Ti-rich) with no measurable nitrogen concentrations. - Aluminum diffused outward, while oxygen diffused inward. - Above 850°C, oxygen transport became the rate limiting step. - Activation energy was not constant and increased with temperature.
Tompkins (1991) [114]	Silicon wafer	TiN	reactive sputter deposition	0.35	Air and dry 5% O$_2$ 350-450°C	- TiO$_2$ forms. - Oxidation initiation time observed. - Quadratic growth kinetics after the initiation time. - Air oxidation rate is higher than dry O$_2$ oxidation rate.

Table 1-3. (continued)

Reference	Substrate	Coating	Deposition method	Thickness (μm)	Environment	Observations
Vaz et al. (1997) [127]	High-speed steel	(Ti,Al)N	combined DC and RF magnetron sputtering	2.9-5.6	Air 500-900°C 1-168 h	- Three TiAlN compositions were investigated: $Ti_{0.62}Al_{0.38}N$, $Ti_{0.35}Al_{0.65}N$, and $Ti_{0.19}Al_{0.81}N$. - Oxidation resistance: $Ti_{0.35}Al_{0.65}N > Ti_{0.62}Al_{0.38}N > Ti_{0.19}Al_{0.81}N$. - At 500°C, mixed titanium and aluminum oxide layer with 10 at.% nitrogen formed on $Ti_{0.35}Al_{0.65}N$. - At 600°C, mixed titanium and aluminum oxide layer without nitrogen, and at 750-900°C, two-layer oxide structure observed on $Ti_{0.35}Al_{0.65}N$ and $Ti_{0.62}Al_{0.38}N$. - Oxidation initiation time observed. - Parabolic oxidation growth rate.
Zhou et al. (1999) [92]	Stainless steel, quartz glass and glass ceramic	(Ti,Al)N	Combined RF-plasma assisted planar magnetron sputtering	0.4-1	Air up to 1200°C	- Hexagonal structure was observed at 60 mol% Al. - Oxidation resistance increases with increasing aluminum content up to x=0.7 in $(Ti_{1-x}Al_x)N$, which corresponded to two-phase region. - Oxidation initiation was delayed up to 950°C in air with Al content increase.
Vennemann et al. (2003) [133]	High speed steel	$Ti_{0.25}Al_{0.26}N_{0.46}$	Reactive DC magnetron sputtering	2.7	O_2 1000°C 100 MPa	- TiO_2 formed as top oxide layer followed by Al_2O_3 layer below.
Korablov et al. (2003) [124]	Stainless steel	TiN	PVD	3	Water 20-800°C 100 MPa	- At 200°C, unstable brookite-TiO_2 formed and transformed to amorphous anatase-TiO_2 after 25 h. - At 400°C, crystalline anatase-TiO_2 formed - At 500°C, Ti_2O_3 formation and blue coloring on surface occurred. - At 600-800°C, rutile-TiO_2 and Ti_2O_3 were observed together
Korablov et al. (2005) [134]	Stainless steel	$Ti_{0.35}Al_{0.65}N$	PVD	3	Water 20-950°C 100 MPa	- Measurable weight gain started at 700°C in TiN, and at 750°C in TiAlN. - At 200°C, γ-AlOOH was determined. - At 300°C, $Al(OH)_3$ and γ-AlOOH were observed - At 400°C, anatase-TiO_2 and k'-Al_2O_3 were determined. - At 500 and 600°C, anatase, rutile and Ti_2O_3 were observed.

Table 1-3. (continued)

Reference	Substrate	Coating	Method	No.	Conditions	Observations
Hsieh et al. (2006) [119]	High speed steel	TiN, $Ti_{0.4}Al_{0.6}N$, $Ti_{0.6}Al_{0.4}N$	DC magnetron sputtering	3	Air 500-800°C	- Maximum surface morphology maintenance temperature for TiN was 600°C, for $Ti_{0.6}Al_{0.4}N$ was 700°C, and for $Ti_{0.4}Al_{0.6}N$ was 800°C.
Chim et al. (2009) [112]	Stainless steel	TiN, $Ti_{0.5}Al_{0.5}N$	Lateral rotating cathodic arc	3	Air 500-1000°C 1 h	- TiN: oxidation started at 500°C, full oxidation at 700°C, complete delamination at 800°C. - TiAlN: oxidation starter at 600°C, full oxidation and partial delamination occurred at 1000°C. - TiN oxide phase is TiO_2. - TiAlN oxide phases are TiO_2, Al_2O_3 and AlTiO.
Yang et al. (2009) [115]	Silicon	$Ti_{0.5}Al_{0.5}N$	Lateral rotating cathodic arc	N/A	Air 900°C 2 h	- Complete oxidation of the coating occurred - Outward diffusion of Al and Ti, and inward diffusion of O occurred. - Oxide phases are tetragonal TiO_2 (outermost layer and inner), and Al_2O_3 (intermediate layer).
Qiang et al. (2010) [128]	Ti-based alloy, Silicon	$Ti_{0.5}Al_{0.5}N$	Cathodic arc ion plating	N/A	Air 650°C/100 h 700°C/100 h 800°C/10 h 800°C/30 h	- Parabolic oxidation. - α-Al_2O_3 on the surface followed by TiO_2 at 800°C. - Nitrogen escaped from the coating during oxidation.
Zhu et al. (2012) [135]	WC-Co cemented carbide	$Ti_{0.5}Al_{0.5}N$	Cathodic arc evaporation	5	Air 850-1000°C 15-120 min	- Residual compressive stresses in the coating. - Slight weight gain after oxidation test. - Oxides are Al_2O_3 and TiO_2.
Khatkhatay et al. (2014) [62]	Zircaloy-4	TiN, $Ti_{0.35}Al_{0.65}N$	Pulsed laser deposition	1	Deaerated water 500°C 25 MPa 48 h	- TiO_2-anatase and TiO_2-rutile phases were observed as the oxide phases. - Coatings limited the substrate oxidation. - In the case of TiAlN coating, nonuniform substrate oxidation was observed.

TiN oxidation has been determined to initiate at 500-550ºC in air [92,95,120]. Oxidation growth kinetics have been described in different studies as parabolic [112], quadratic [114], and pseudolinear [121,124] for coatings deposited with different deposition techniques. Anatase and rutile phases were observed as the oxide phase depending on temperature. TiN oxidation was described to be nonprotective in air due to the delamination of the oxide layer. This oxide spallation was attributed to the molar volume difference between TiN and TiO_2, which are 11.4 cm^3 and 18.8 cm^3 per mole, respectively [113,124,125]. Furthermore, it was mentioned that nitrogen released from the TiN during the oxidation process was entrapped in the coating layer causing pore formation and eventual degradation of the corrosion performance of the TiN coatings [119]. This contradicts with the suggestion of Piippo et al. [126] who performed corrosion studies on CVD TiN coatings in electrolyte environment and stated that enhanced TiN corrosion resistance in aqueous environments can be attributed to the formation of a thin oxide film and elemental nitrogen at the interface of TiO_2-TiN.

Initially, Rudenja et al. [127] determined the Pourbaix diagram of TiN-H_2O and Ti-H_2O systems at room temperature shown in Figure 1-9. TiN has a large thermodynamically stable region. As a result of the reaction 2, $Ti(OH)_3$ formation, and then at a zero potential and a pH value of 7, it is expected to observe TiO_2, as a result of the reaction 3 [127]. Recently, Cook et al. [128] determined the Pourbaix diagrams of aluminum and titanium for high-subcritical and low-supercritical water conditions for dissolved species concentrations of 10^{-6} mol/kg and 10^{-8} mol/kg at 25 MPa pressure and 350°C and 400°C, respectively.
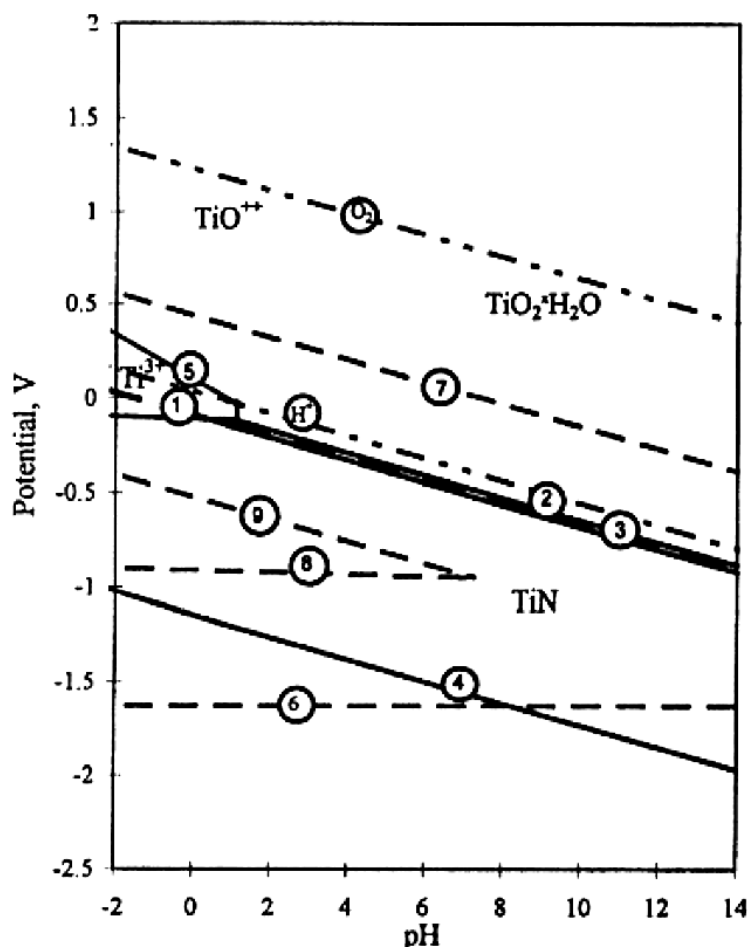
Figure 1-9. E-pH diagram for TiN-H$_2$O and Ti-H$_2$O (dashed lines) systems at 25°C [127].

The Pourbaix diagrams for aluminum and titanium are shown in Figure 1-10 and Figure 1-11, respectively. Although these diagrams are prepared for 25 MPa, they can provide some insight on the possible behavior at typical PWR normal operation condition (15 MPa). The electrochemical potential is -820 mV$_{SHE}$ and pH ~7 for PWR core environment [5,129]. Accordingly, titanium was shown to form stable oxides and to provide passivity for hydrothermal corrosion at normal operation conditions and both TiO$_2$ and Al$_2$O$_3$ showed good stability above the critical point [128].

(a)　350°C, 25 MPa and 10^{-6} mol/kg

(b) 350°C, 25 MPa and 10^{-8} mol/kg

(c)　400°C, 25 MPa and 10^{-6} mol/kg

(d)　400°C, 25 MPa and 10^{-8} mol/kg
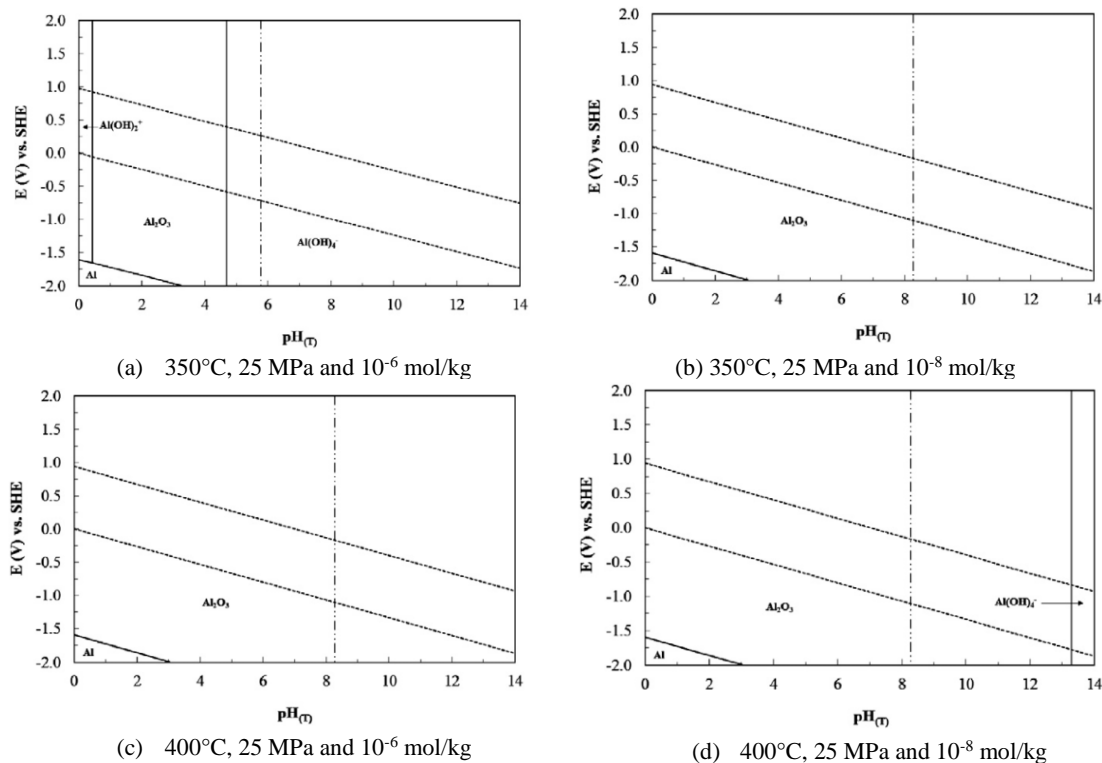
Figure 1-10. Aluminum Pourbaix diagrams. Vertical dashed lines correspond to the neutral water pH at the given temperature [128].

(a)　350°C, 25 MPa and 10^{-6} mol/kg

(b) 350°C, 25 MPa and 10^{-8} mol/kg

(c)　400°C, 25 MPa and 10^{-6} mol/kg

(d)　400°C, 25 MPa and 10^{-8} mol/kg
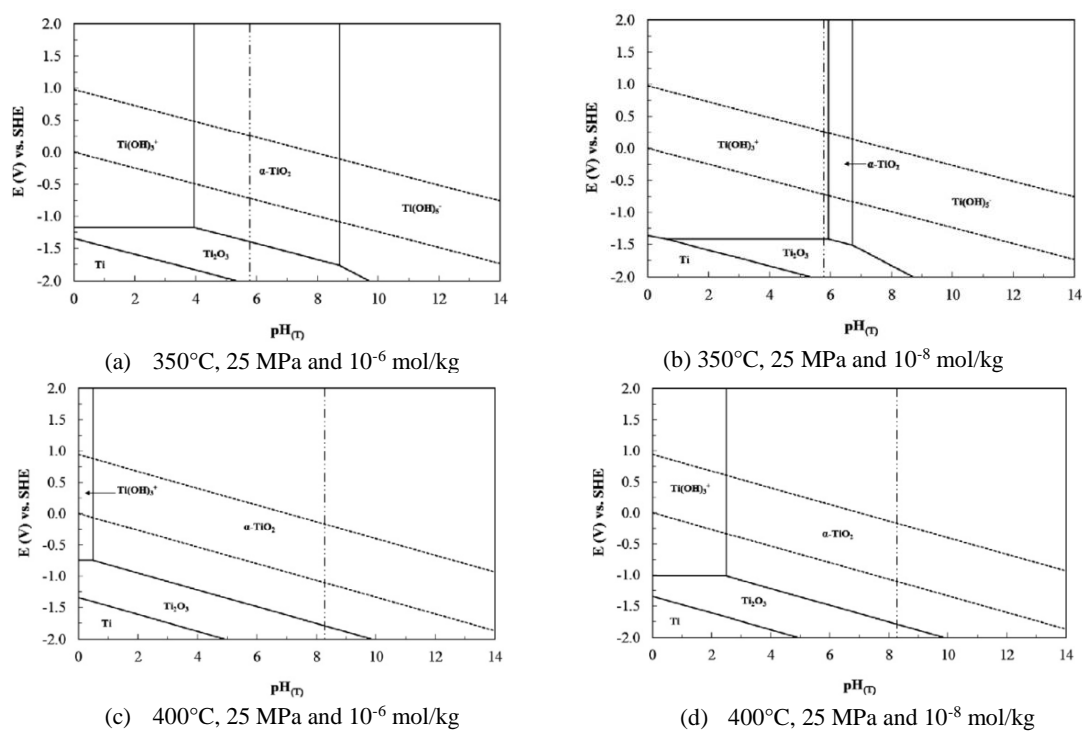
Figure 1-11. Titanium Pourbaix diagrams. Vertical dashed lines correspond to the neutral water pH at the given temperature [128].

Korablov et al. [117] performed TiN oxidation tests in high temperature and high pressure water environment. Although not much detail was provided about the coating deposition method, it was said to be a PVD method. As titanium oxidizes, titanium dioxide forms. Naturally occurring polymorphs of TiO_2 are brookite, anatase and rutile [130]. In water environment, TiN oxidation started with the formation of non-stable brookite (TiO_2, orthorhombic) at 200°C. As the duration increased, the brookite was observed to transform into an amorphous anatase (TiO_2) phase. As temperature increased to 400°C, crystalline anatase (TiO_2, tetragonal) phase formation was observed. Finally, above 500°C, Ti_2O_3 and rutile (TiO_2, tetragonal) phases were observed to be the oxide phases. Additionally, Khatkhatay et al. [62] performed supercritical water tests on PVD TiN coatings deposited on Zircaloy-4 substrate. This study demonstrated that TiN coatings can be used to protect Zircaloy-4 claddings against corrosion in supercritical water environment. As the oxide phase, anatase and rutile were observed to be forming on the surface.

Oxygen diffusion in rutile occurs by a vacancy mechanism. A summary of the oxygen diffusivity studies in rutile available in the literature is presented in Figure 1-12. Slower diffusivity than dry oxygen environment was observed in the case of hydrothermal environment. [131]
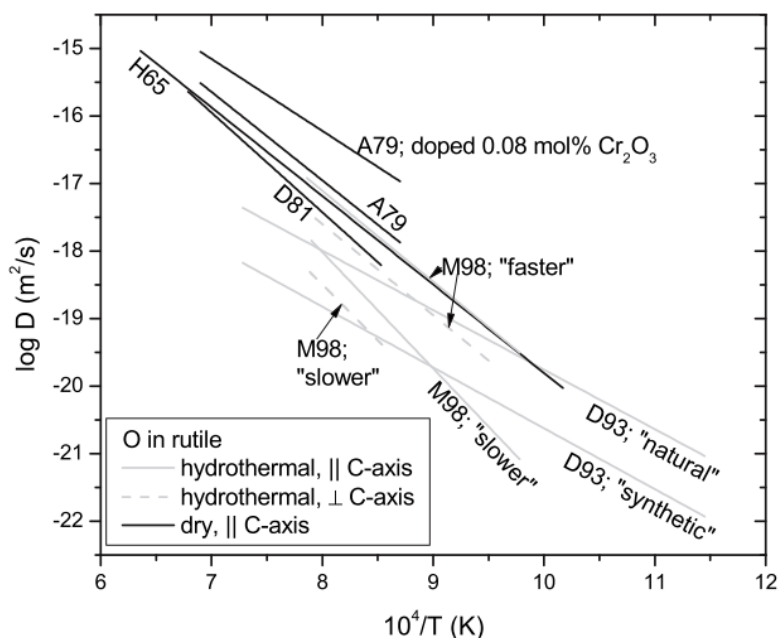
Figure 1-12. Summary of experimental results on the temperature dependence of oxygen diffusion in rutile, under dry conditions in air, and under hydrothermal conditions. Abbreviations: A79 – Arita et al. (1979); H65 – Haul and Dümbgen (1965); D81 – Derry et al. (1981); D93 – Dennis and Freer (1993); M98 – Moore et al. (1998) [131].

In the case of (Ti,Al)N coatings, two oxidizing species are available which are titanium and aluminum. According to Ellingham's diagram, aluminum oxidation is expected to be observed first since it has a more negative Gibbs free energy than that of titanium. Zhou et al. investigated oxidation initiation of TiN and (Ti,Al)N coatings and determined that the oxidation initiation in (Ti,Al)N can be shifted higher to 950°C in air by increasing the aluminum content to the point where cubic and hexagonal phases coexist as shown in Figure 1-13 [92,95]. Vaz et al. [115] performed oxidation studies at high temperature air environment in order to determine the oxidation behavior as a function of Al content in the (Ti,Al)N coatings. Figure 1-14 shows the weight gain as a function of temperature for (Ti,Al)N in which the oxide growth rate was determined to be parabolic [113,115,122]. As presented in Figure 1-15, the oxidation behavior of (Ti,Al)N proceeded through the formation of two oxide sublayers, one of them Ti rich and the other one being Al rich. It was also demonstrated that different oxide layers formed based on the temperature depending on the coating composition. Specifically, it was determined that increased

aluminum content enhances the corrosion resistance up to 65 at.% through alumina layer formation. This oxidation enhancement was determined to be caused by the formation of a dense amorphous Al_2O_3 layer which decreases diffusion out of or into the film [70,115]. However, starting with the transition from the NaCl to the wurtzite hexagonal structure, the corrosion performance was reduced, becoming similar to the oxidation behavior of pure AlN without Al_2O_3 layer observation as outermost layer. Although, an Al-rich layer was observed to be the outermost layer in the studies of Vaz et al. [115] and McIntyre et al. [113], there are also studies in which a Ti-rich layer was observed to be the outermost layer [121,122]. Observation of titanium dioxide ahead of aluminum oxide was attributed to cracks from the oxide formation which occurred due to the thermal expansion coefficient difference between TiO_2 and Al_2O_3, and opened the way for titanium diffusion to surface [121].
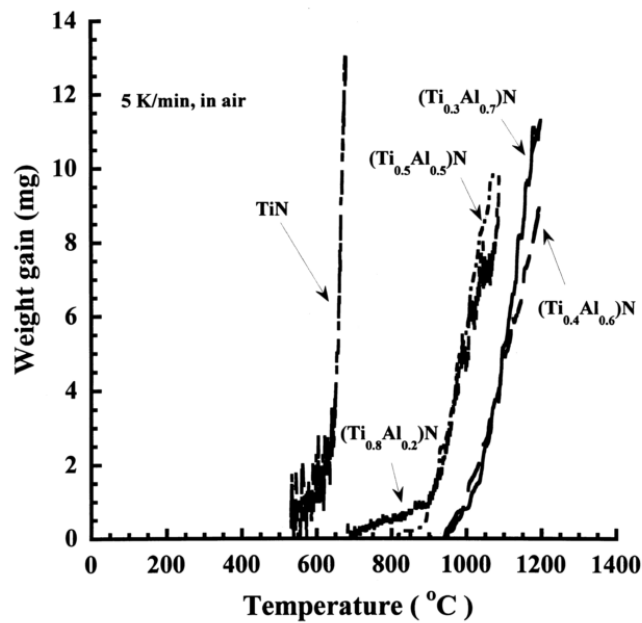
Figure 1-13. Oxidation curves as a function of the Al concentration [95].
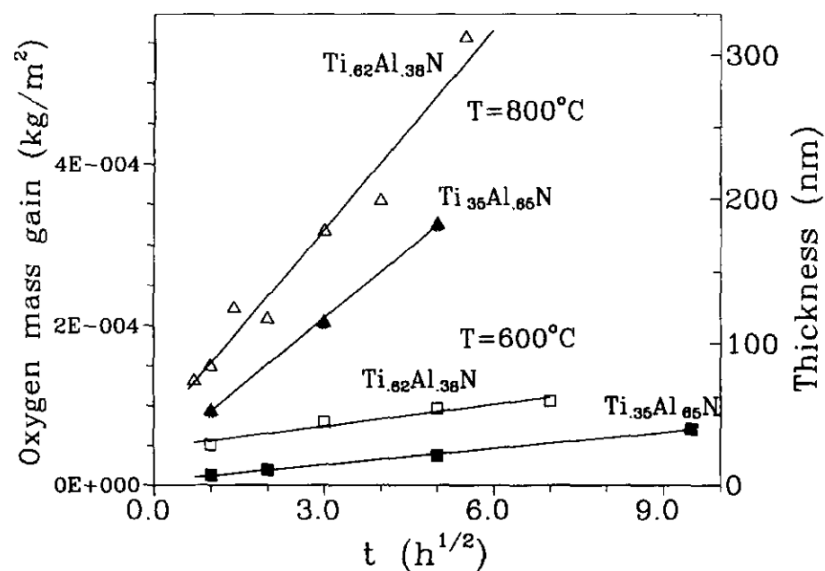
Figure 1-14. Weight gain and corresponding oxide thickness determined by Rutherford backscattering spectroscopy as a function of square root of annealing time [115].
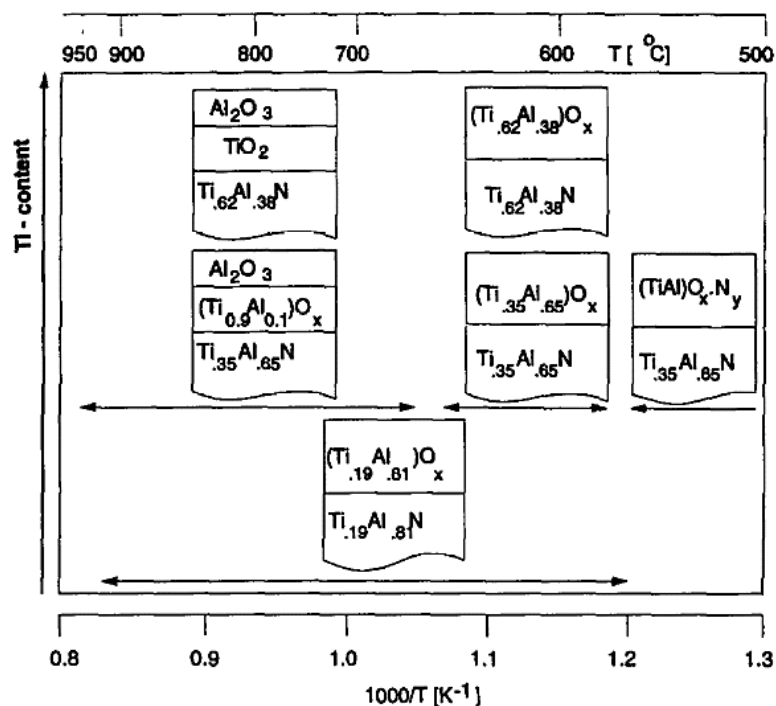
Figure 1-15. Schematic representation of air oxidation behavior of (Ti,Al)N coatings with various compositions [115].

Beck et al. [132] showed that in the case of pure aluminum oxidation in dry oxygen at 450-575°C, an amorphous Al_2O_3 and crystalline γ-Al_2O_3 two phase mixture was formed, in which the rate limiting step of amorphous Al_2O_3 growth is Al diffusion towards oxide-gas interface and of crystalline γ-Al_2O_3 growth is O diffusion towards oxide-metal interface through the amorphous film. Eklund et al. [133] demonstrated that crystallization of γ-Al_2O_3 takes place at ~900°C. Additionally, θ-Al_2O_3 phase was observed at 1000-1100 °C in amorphous or low γ-Al_2O_3 films. At ~1100°C, γ-Al_2O_3 to α-Al_2O_3 transformation was observed. Figure 1-16 shows the compiled oxygen diffusion coefficient data obtained in three different Al_2O_3 phases α, γ and amorphous [134]. Amorphous Al_2O_3 showed a higher oxygen diffusion coefficient compared to the crystalline γ-Al_2O_3. The activation energies of amorphous and γ-Al_2O_3 were lower than those in α-Al_2O_3. This was attributed to the defective spinel phase of the amorphous and γ -Al_2O_3. [134]
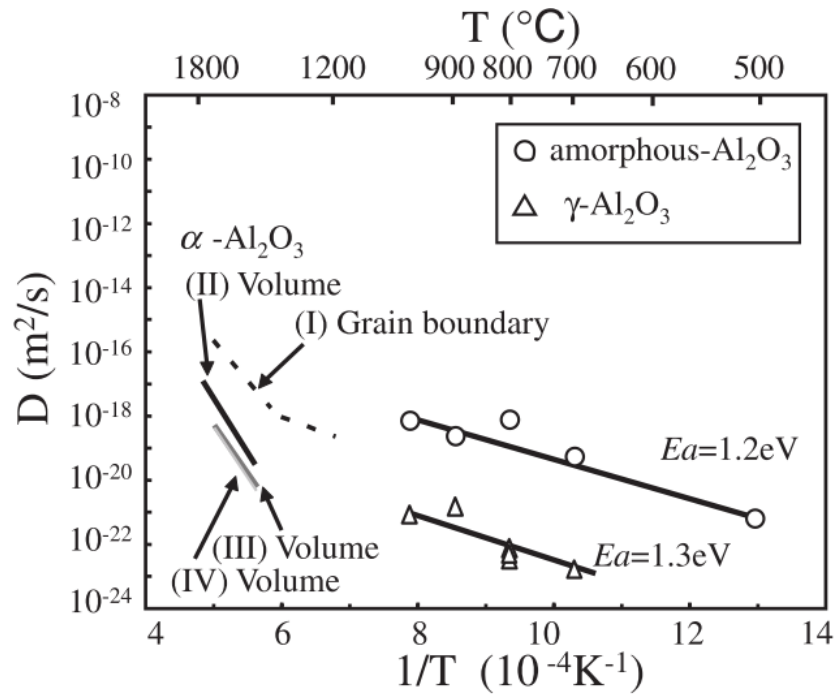
Figure 1-16. ^{18}O diffusion results for both amorphous and γ-Al_2O_3 films obtained in [134]. Volume and grain boundary diffusion data taken from the literature on α-Al_2O_3 single crystals and bulk are also plotted. α-Al_2O_3 polycrystals: (I) Oishi and Kingery. α-Al_2O_3 single crystal: (II) Oishi and Kingery; (III) Prot and Monty; (IV) Gall, Lesage and Bernardini. [134]

Doping or alloying additions have been utilized to improve the coating performance. For example, Zr and V increase the wear resistance, Cr and Y enhance the oxidation resistance, B increase abrasive wear behavior, and Si enhances hardness and chemical inertness [70].

As a part of the corrosion performance evaluation of these coatings for applicability in nuclear cladding applications, Kashkarov et al. performed a hydrogenation study on TiN coatings deposited on Zr-1Nb samples by using the vacuum arc deposition method. The study demonstrated that even with thicknesses as low as 400 nm these coatings are effective hydrogen diffusion barriers [135].

1.5.5. TiN and (Ti,Al)N Coatings Neutronic Performance

Neutron absorption in coatings results in a loss of reactivity relative to uncoated cladding which reduces fuel efficiency. The calculated penalty on burnup and cycle length increases linearly with coating thickness. Considering that these coatings are developed for the nuclear fuel cladding applications, one must consider the neutron penalty. Younker and Fratoni [136] performed a neutronic analysis by using the Monte Carlo Serpent code to evaluate the neutronic penalty of such coatings. They considered pressurized water reactor parameters and based on Zircaloy-4 cladding, they determined a reference cycle length of 443 effective full power days (EFPD). Then they investigated the cycle length penalty caused by different coating materials with various coating thicknesses deposited on Zircaloy-4. For the (Ti,Al)N coatings, they determined cycle length penalty values as -3.4, -16.9 and -35.3 EFPD for coating thicknesses of 10, 50 and 100 μm, respectively. As a reference, the cycle length penalty values caused by a Zircaloy-4 layer of 10, 50 and 100 μm thickness were also investigated and determined to be -1.2, -3.9 and -8.8 EFPD. They also demonstrated that the penalty in the case of (Ti,Al)N coating with 10 μm thickness can be compensated with a fuel enrichment of increment less than 0.05 at.%.

Thus, they concluded that neutronic penalty can be limited when ceramic coatings have a thickness less than 30 μm.

1.6. Summary

The aim of this research study is to develop corrosion resistant ceramic coatings which adhere well to ZIRLO® substrates and that can withstand nuclear reactor environment both under normal operation conditions and in the case of a loss-of-coolant accident. Up to this point, an introduction and background on the proposed coating material and coating deposition method have been provided with the intention of demonstrating the rationale of this research study. The following chapters present the approach conducted in this research to test the hypothesis and evaluate the results.

Chapter 2 describes the experimental and theoretical approaches. The experimental part includes information about the sample preparation methods, coating deposition technique and parameters, corrosion tests, mechanical tests, and analytical material characterization methods used to examine the as-deposited and tested samples. Chapter 3 presents the results obtained through the corrosion tests and characterizations. The relevant discussion of the presented results and neutronic analysis is provided in Chapter 4. Finally, Chapter 5 summarizes the conclusions obtained from this research and presents suggestions for future study.

Chapter 2

Experimental Methods

The experimental procedure of this research study was constructed with the objective of developing corrosion resistant coatings that can withstand nuclear reactor environment both during normal operation and accident conditions, mainly the loss-of-coolant-accident. As described in the introduction chapter, TiN and TiAlN coatings were investigated as a barrier against the corrosive environment of the nuclear reactor. ZIRLO®, which is a zirconium-based alloy developed by Westinghouse Co., was selected as the substrate material since it is one of the most widely used nuclear fuel cladding materials. TiN, TiAlN, and multilayer TiN/TiAlN coatings were deposited on ZIRLO® substrates using the cathodic arc physical vapor deposition (CA-PVD) technique. Details of the deposition process are described in following sections. Among a variety of coating deposition methods, CA-PVD was selected because of its distinct advantages, which are discussed in more detail in section 2.3. The research was conducted in a systematic manner in which select deposition parameters were varied to optimize coating properties and will be referred henceforth as generations (GENs).

Figure 2-1 shows the simplified route of the parameter optimization approach conducted in each GEN. First, substrate surface preparation was performed by surface grinding, which was followed by characterization using optical profilometry to determine the substrate surface roughness value. Upon confirmation of the required substrate surface roughness value, coatings were deposited by CA-PVD, which is a flexible deposition method, known for producing high coating adhesion. Variations in the deposition parameters provided adjustment of the coating composition, crystal structure and microstructure, and thus coating properties. After the coating deposition stage, analytic materials characterization was performed using X-ray diffraction (XRD), scanning electron microscopy (SEM) and energy dispersive spectroscopy (EDS) to

characterize the coating phase and microstructure, and the details of these characterizations are provided in section 2.6. To evaluate the corrosion resistance, samples were tested in various corrosive environments such as in an autoclave having static pure water at 360°C and 18.7 MPa for up to 128 days, in an autoclave at 542°C and 25 MPa, and in air up to 1000°C in a furnace, followed again by characterization using XRD, SEM and EDS to evaluate the coating oxidation behavior and overall corrosion performance. Based on the corrosion performance, coating deposition processing parameters and/or substrate surface roughness were modified until optimum coating properties for enhanced corrosion resistance was achieved. A more detailed discussion of each of the generations and the coating corrosion performance improvement will be explained in more detail in the following sections.
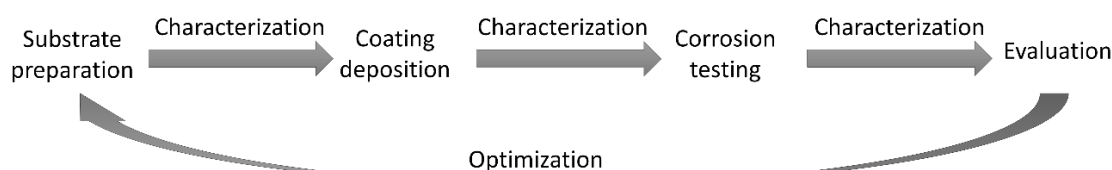
Figure 2-1. The schematic representation of the parameter optimization approach performed in each generation.

2.1. Substrate material properties

ZIRLO® is a registered trademark of Westinghouse Co. and during this research the substrate material was provided in sheet and tubular geometries by Westinghouse Co. Initial coating studies were performed on flat substrates (sheet) as a simpler geometry than tubing free from complex stress states made it easier to deposit uniform coatings and to evaluate coating adhesion performance compared to the curved surface of a tubular geometry. Figure 2-2a shows a schematic of a flat sample (sheet). The thickness of the flat ZIRLO® sheets was 0.05 cm. These sheets were cut to dimensions of 5 cm x 2.5 cm x 0.05 cm using a shear. Figure 2-2b shows the

dimensions of a tubular sample. The outer diameter of the tubular sample was ~1 cm and the inner diameter was ~0.85 cm, resulting in a wall thickness of 0.075 cm. The tubes were cut to a length of ~4 cm using a slow-speed diamond saw. After cutting, the cut edges of both flat and tubular samples were prepared with 240 grit dry SiC papers to achieve the desired surface roughness value of 0.1, 0.25. 0.5, or 0.875 µm Ra.
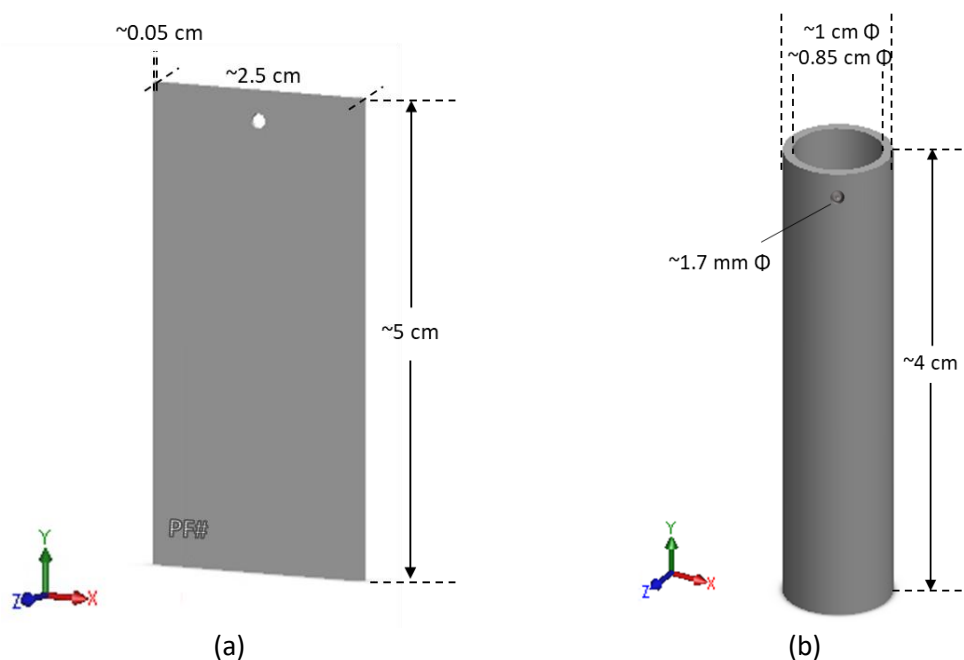
Figure 2-2. Schematic representation of the (a) flat and (b) tubular ZIRLO® samples showing dimensions.

2.2. Substrate surface preparation

The surface of the metal substrate contained hydrocarbons and other residues which needed to be removed before coating deposition to achieve good coating adhesion. Thus, the ZIRLO® substrate surface was prepared using SiC hand grinding, SiC lathe grinding, green scotch brite grinding or alumina grit blasting depending on the GEN. The rirst method considered for the surface preparation was SiC hand grinding. SiC hand grinding was used as the surface preparation method for the first eight GENs until the last GEN (GEN-9) of coatings. During

GEN-9, other methods (SiC lathe, green scotch brite and alumina grit blast preparation methods) were used to investigate the effect of substrate surface preparation method on the coating adhesion and corrosion performance by comparing the results obtained from samples prepared by the different methods.

For flat samples, the sample was laid flat and half of its surface was ground while holding along one long edge. Then, the sample was rotated 180° to grind the remaining section. The same procedure was applied to the other face of the flat sample. For SiC hand grinding, samples were laid on 800 grit pad, and both of its surfaces were dry ground lengthwise with SiC papers of 240, 600 and 800 grits as described previously. In the case of the green scotch brite method, the flat samples were laid on a spec wipe. Then, the grinding process was performed lengthwise using Norton St. Gobain brand green scotch brite composed of 240 grit Al_2O_3. After achieving the desired substrate surface roughness, a hole with a diameter of 1.65-1.75 mm was drilled centered on the short side and ~3.2 mm away from the top short edge, followed by scribing the sample ID on the surface close to the bottom left of the sample at a distance ~6.5 mm away from the bottom edge, as shown in Figure 2-2a.

For tubular samples, a ~1.7 mm diameter hole was drilled and the sample ID scribing was performed before the substrate surface preparation rather than afterwards, due to their complex geometry. In the case of the lathe preparation method, samples were mounted in the lathe, which was set to 270 rpm. Grit paper strips having 240, 600 and 800 grit were wrapped around the spinning tube and the paper was moved slowly back and forth on the tubular sample surface over its full length. The last method considered was alumina grit blasting, which was performed using 400 grit Al_2O_3.

Finally, samples were ultrasonically cleaned with acetone for 10 minutes, rinsed with deionized water, ultrasonic cleaned for 10 minutes in methanol, rinsed with deionized water and blown dry with nitrogen gas.

The surface roughness of the samples was tightly controlled to achieve the desired value. Roughness measurements were performed using a noncontact optical profilometer prior to positioning substrates in the deposition chamber subsequently.

2.3. Cathodic arc physical vapor deposition method

As mentioned before cathodic arc vapor physical vapor deposition (CA-PVD) is a line-of-sight coating process. The CA-PVD process involves condensation of the depositing species from a plasma phase.

Figure 2-3 shows a schematic representation of the cathodic arc physical vapor deposition (CA-PVD) equipment and process used in this study. The CA-PVD equipment model number was 2020, produced by the Surface Engineering Group, Incorporated (S.E.G.) in Mendota Heights, MN. The dimensions of this vacuum chamber of the CA-PVD equipment were 50.8 cm x 50.8 cm x 50.8 cm. The equipment was fitted with a vacuum pump and a gas inlet into the chamber, which was used to inject argon gas and nitrogen gas (99.999 % purity). The deposition system could use three sources simultaneously which could be used to double or triple the coating deposition rate if needed. In this study, two solid water-cooled cathodes were used during each deposition trial. The diameter of the cylindrical cathodes was 6.3 cm and their thickness was 3.2 cm. One of the cathodes was a dished elemental high purity (99.999%) titanium cathode and the other one was a TiAl cathode. Two different compositions for the TiAl cathode were used, depending on the desired objectives, either 33 at.% Ti – 67 at.% Al (46.6 wt.% Ti – 53.4 wt.% Al) or 20 at.% Ti – 80 at.% Al (30.7 wt.% Ti – 69.3 wt.% Al).
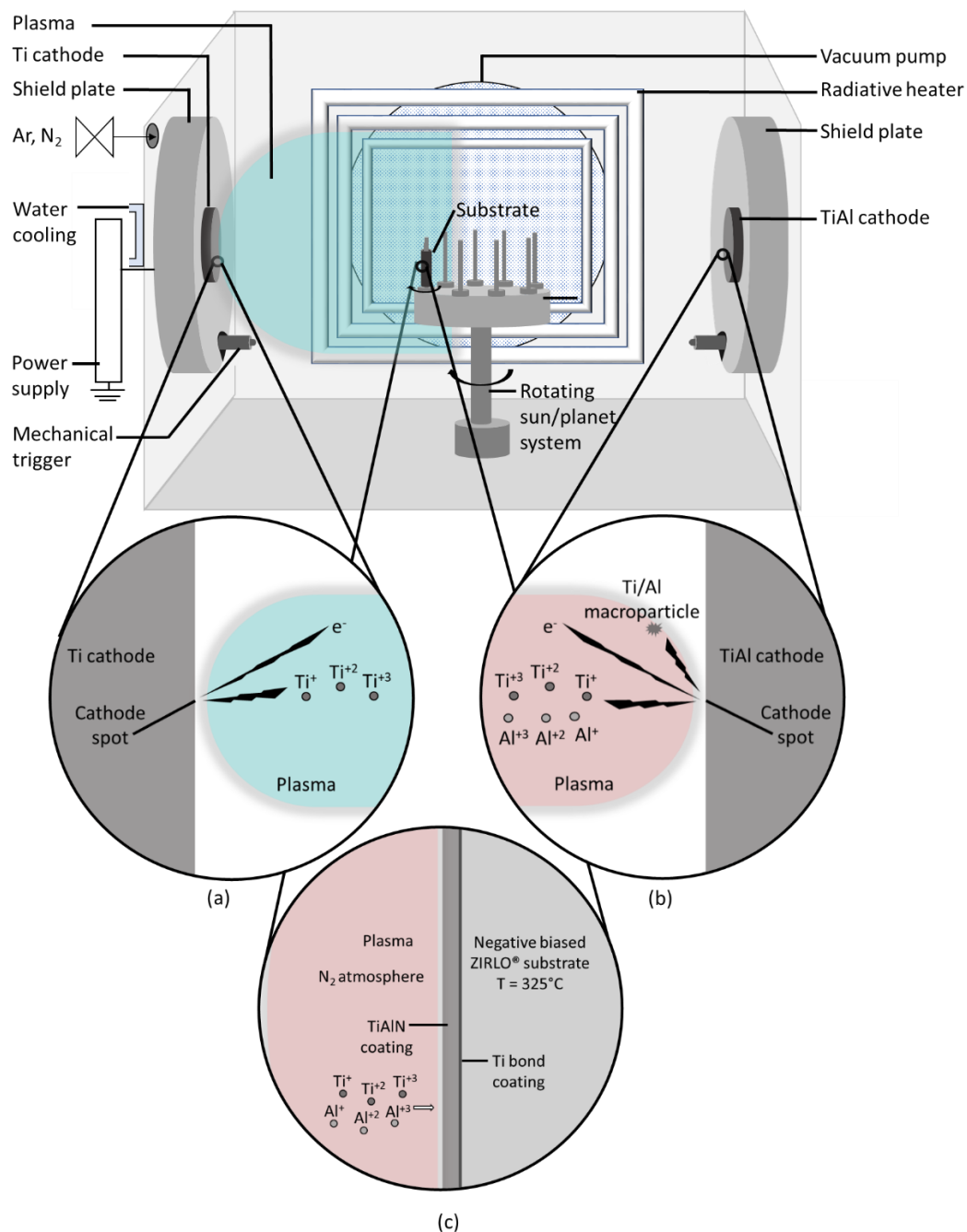
Figure 2-3. Schematic representation of the cathodic arc physical vapor deposition (CA-PVD) equipment and process.

The titanium and the desired TiAl cathodes were placed at 180° from each other within the deposition chamber. A Miller XMT 304 CC/CV DC welder power supply was used as the power source for the arc. The substrates were mounted on the rotating sun/planet system in the

center of the chamber ~23 cm away from the cathodes. The rotating sun/planet system accommodates up to eight samples. The mounted samples rotated individually to achieve uniform coating on the substrate surface. The sun/planet system rotated clockwise at 6.75 rpm with individual sample holders rotating clockwise at 2.4 rpm.

The tubular samples were mounted by fastening them at the two ends, which helped to keep them in position, whereas flat samples were mounted by using a clamp (Figure 2-4). In the case of flat sample mounting, shadow bars were also used (Figure 2-4a). These shadow bars were placed in parallel to the long edge of flat samples to avoid increased coating buildup along these sample edges during coating deposition. The chamber was heated using a radiative heater located on the back side of the chamber and the substrate temperature was measured radiantly by a thermocouple having a tip located parallel to the center of the cathodes in the center of the planetary rotation in the z-direction located 5 cm away from the center of each sample in the x-y direction. The described thermocouple location corresponded to the bottom edge of the samples in the case of 2.5 cm riser usage. During deposition, all faces and edges of flat samples were coated with the exception of the clamped region, whereas in the case of tubular samples, the entire outer surface was coated. The radiant heater temperature was set to 325ºC.

(a)   (b)
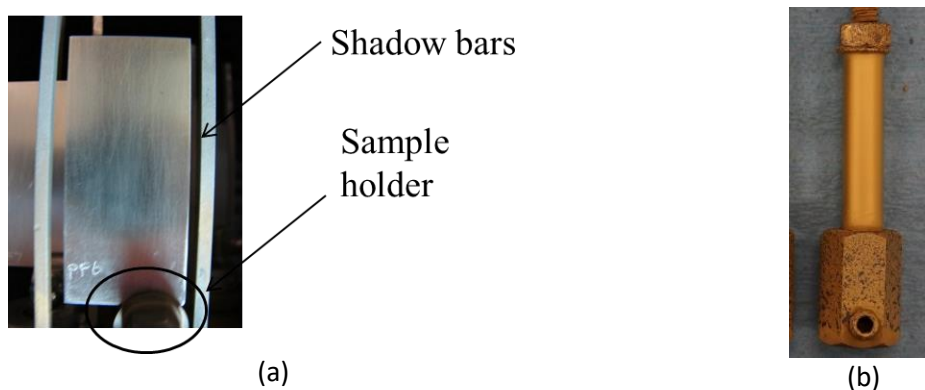
Figure 2-4. Digital images showing the mounting method of (a) flat sample and (b) tubular sample during the deposition process.

The CA-PVD coating process was performed in three stages: (1) vacuum, (2) ion etching and (3) coating:

(1)   In the vacuum stage, the chamber was evacuated to a high vacuum level < 2.7 x 10^{-3} Pa (2 x 10^{-5} Torr) using the vacuum pump.

(2)   The aim of ion etching is to remove oxides and clean the substrate surface that might have oxidized or contaminated while waiting in air before being placed into the deposition chamber. The ion etching stage was performed for 5 minutes. During this step, argon gas was introduced into the chamber and a pressure of 0.7 Pa (5 x 10^{-3} Torr) was established. The substrate was negatively biased to -1000 V using a 10 kW Advanced Energy MDX II DC power supply. Because of the high negative bias voltage of -1000 V on the substrate surface, titanium ions were accelerated towards the substrate such that they bombard the substrate surface, thus removing the native oxide from the substrate surface through sputtering. This effectively clean the substrate surface before coating deposition. The substrates were also heated by the ion bombardment.

 (3)   Sample coating included two processes: arc vaporization and coating deposition. Coating deposition involved first the deposition of the titanium bond coating (Ti-BC) layer and then the deposition of the coating layer consisting of TiAlN layer or TiN layer or both TiAlN and TiN in the case of multilayer coatings.

In the arc vaporization process, the anode acts as a passive electron collector and the cathode provides the depositing species [80,137]. The arc vaporization process is initiated when the mechanical trigger creates an arc by making a temporary short circuit between the cathode and the anode [137]. The current density in the arc is extremely high (can be as high as 10^9 A/cm^2 [138]) and the arc voltage is low (typically 20 V [80]) [79,137]. This results in a high power density (10^9 W/cm^2 [80]) and in the formation of "cathode spot" on the cathode material [79,137]. At the cathode spot, melting, evaporation, and molten or solid particle ejection take place which results in arc erosion of the cathode surface [137]. The arc spot can be confined to the cathode surface by using either a passive border or magnetic fields [139] achieved by placing magnets behind the cathode targets. In this study, we utilized random arc on the cathode surface. Electron
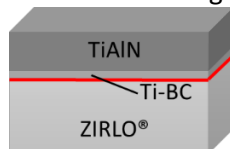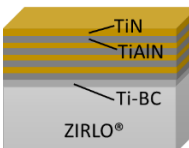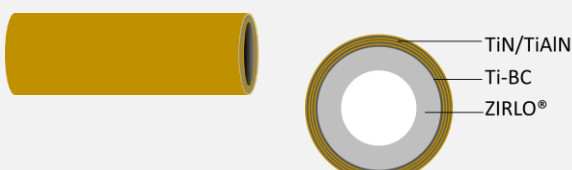
bombardment at the anode and ion bombardment at the cathode leads to heating up of the electrodes [137]. Typical cathode temperatures are 50-200°C [139]. Cathode temperature is controlled through water cooling.

The left magnified image in Figure 2-3a shows a schematic of the arc vaporization process in the case of the dished high purity (99.999%) elemental titanium cathode. A high percentage of the vaporized species was ionized in the arc [137]. The arc vaporization of the titanium cathode resulted in vaporization and ionization of titanium ions forming a blue colored plasma as illustrated in Figure 2-3a. Ions are often multiply charged, that is, charge states of +1, +2 and +3 for titanium ions [139,140]. These ions were used to fabricate the Ti-BC layer and the TiN coating layer. The magnified image on the right of Figure 2-3b schematically shows the arc vaporization process in the case of a TiAl cathode. To obtain the titanium and aluminum ions for the TiAlN coating layer, a TiAl cathode with the select composition (either 33 at.% Ti − 67 at.% Al or 20 at.% Ti − 80 at.% Al) was vaporized. Multiply charged titanium and aluminum ions of +1, +2 and +3 can be observed forming a plasma [139,140] as illustrated in pink. Since electrons move faster than the ions, the space charge in the plasma becomes positive, resulting in the acceleration of positive ions away from the plasma to the negatively biased substrate resulting in high energies of 50-150 eV (much higher than thermal energies) [137].

First, the Ti-BC layer was deposited in an inert argon atmosphere at 1.6 Pa (1.2 x 10^{-2} Torr). The substrate bias was -150 V. Negative biasing was applied to achieve electron repulsion and particle flux enhancement towards the substrate surface through ion acceleration due to the difference between the potential of the substrate and the plasma [80]. In fact, a positive space charge layer is formed on the negative biased substrate surface, called the sheath [80]. The energetic condensation of the cathode species having a substantial kinetic and potential energy from the plasma onto the substrate is accompanied by high-energy ion bombardment [137]. There is not much study on the potential energy release of these ions but the studies showed that ions will stop on the surface by losing their kinetic energy at a rate of 100 eV/nm, which can also be

accompanied with short collision cascades [80]. Titanium ions bombard the substrate surface and

penetrate below the substrate surface resulting in ion implantation and in good coating adhesion.

Table 2-1. Schematic representation of various deposition parameter(s) and different design architectures for various generations. The investigated parameters are highlighted with red color on the figures.

Generation	Investigated parameter
GEN-1	Titanium bond coating (Ti-BC) thickness
GEN-2	TiAlN coating thickness Substrate surface roughness
GEN-3	TiN coating TiAlN deposition parameter effect
GEN-4	Multilayer design architecture
GEN-5	Scratched sample
GEN-6	Supercritical water test
GEN-7	Multilayer coated tube

GEN-8	Substrate surface preparation	Sectioning effect
GEN-9	Deposition parameter effect	Furnace test
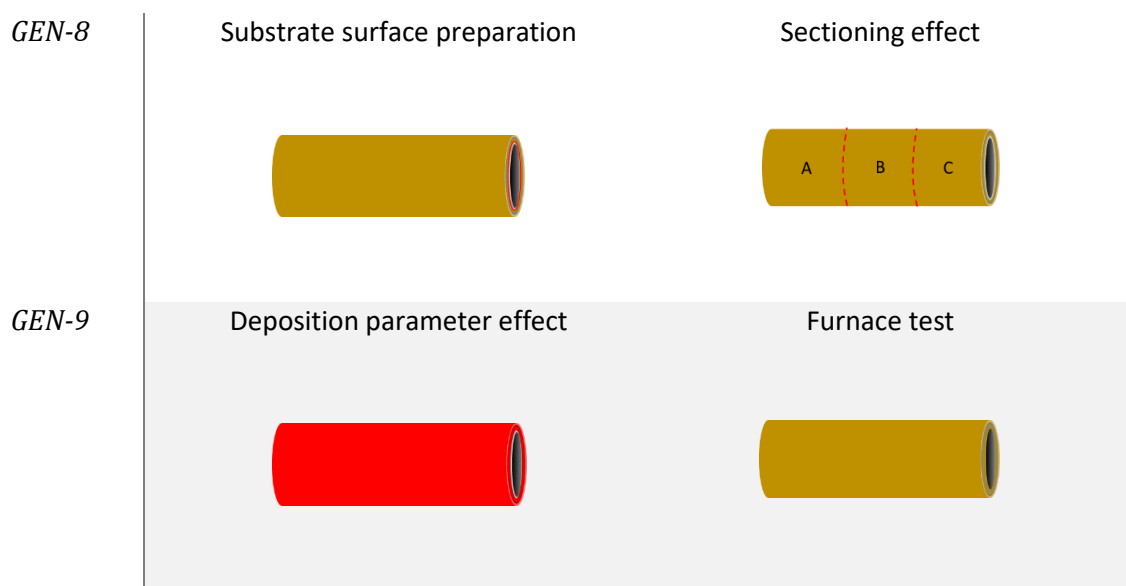
After the bond coating is deposited, the coating layer of TiAlN layer or TiN layer (or both TiAlN and TiN in the case of multilayer coatings) was deposited. The bottom magnified image in Figure 2-3c shows the TiAlN coating layer deposition. The TiAlN coating layer deposition was a reactive deposition performed in a nitrogen atmosphere at a nitrogen partial pressure value ranging between 1.6-1.9 Pa ((1.2-1.4) x 10^{-2} Torr) and using a substrate bias value between (-50) – (-150) V. The nitrogen partial pressure and the substrate bias values were determined depending on the desired coating properties of the relevant generation. Negative substrate bias attracted the positively charged titanium and aluminum ions towards the substrate surface which energetically condensed on the surface as they react with the surrounding nitrogen gas atmosphere. Finally, the TiN coating layer was deposited through the reaction of the titanium ions arriving on -150 V biased substrate surface with the nitrogen atoms in the reactive atmosphere at a 1.6 Pa (1.2 x 10^{-2} Torr) nitrogen partial pressure.

In this study, filtered CA-PVD (to avoid macroparticles) was not used since it decreases the deposition rate causing low coating deposition rates. Instead, the production of macroparticles was minimized through deposition parameter optimization.

As described at the beginning of this chapter, the deposition parameters were systematically varied and grouped according to generations. Table 2-1 summarizes and schematically shows the deposition parameters investigated and optimized in each successive generation with respect to their impact on corrosion resistance of each of the multilayer design architecture. In the first generation (GEN-1), the thickness of the bond coating was investigated by depositing titanium bond coating (BC) thicknesses values of 0.2, 0.4, 0.6 and 0.8 µm, which were achieved by deposition time adjustment. In the second generation (GEN-2), both the ZIRLO® coupon substrate surface roughness (0.1, 0.25. 0.5, and 0.875 µm Ra) and the TiAlN thickness (4, 8, and 12 µm) were investigated. In the third generation (GEN-3), both monolithic TiN and monolithic TiAlN coatings deposited with varying substrate bias (50, 100, and 150 V) and nitrogen partial pressure (1.6 and 1.9 Pa) were investigated. The fourth generation (GEN-4) investigated the TiN/TiAlN multilayer coating design architecture: multilayer designs of 2-, 4-, 8-, and 16-layers of TiN/TiAlN coatings were examined. The self-healing nature of the coatings were investigated in the fifth generation (GEN-5). For the first five generations, the autoclave tests were performed at Westinghouse at 360°C, but the coatings deposited in the sixth generation which were composed of multilayer TiN/TiAlN were tested in an autoclave at the University of Michigan at 542°C. The details of the autoclave tests are described in the following sections. Starting from generation 7 (GEN-7), coatings were deposited on tubular geometries. From GEN-7 through GEN-9, substrate geometry, substrate surface preparation, deposition parameter (cathode composition, substrate bias, and arc current) and sectioning effects were investigated. Finally, a high temperature (800-1200°C) furnace test was performed to evaluate the corrosion performance of the final optimized coating design architectures.

2.4. Mechanical testing

Scratch testing was performed to determine the failure modes and the adhesion strength of the coatings according to ASTM C1624: Standard test method for adhesion strength and mechanical failure modes of ceramic coatings by quantitative single point scratch testing [141]. The test was performed using the Romulus IV Universal Materials Tester (Spokane, WA, USA) on coated flat and tubular samples. Figure 2-5a shows a schematic representation of the progressive scratch test method. A Rockwell C, 200 μm radius diamond stylus was used to develop a ~1 cm scratch on the coating with a tangential force. Progressive loading with normal force was applied from 0 to 50 N with a 50 N/min rate corresponding to 0.83 N/s. Figure 2-5b schematically shows the initiation of chevron crack cluster formation (lN). The coating damage was examined using optical microscopy (OM), scanning electron microscopy (SEM) and energy dispersive spectroscopy (EDS) to identify failure modes and the initiation point of each failure mode on the scratch. Then, the critical scratch load for each failure mode was determined by comparing the relevant OM and SEM images with the corresponding load-distance diagrams.

(a)   (b)
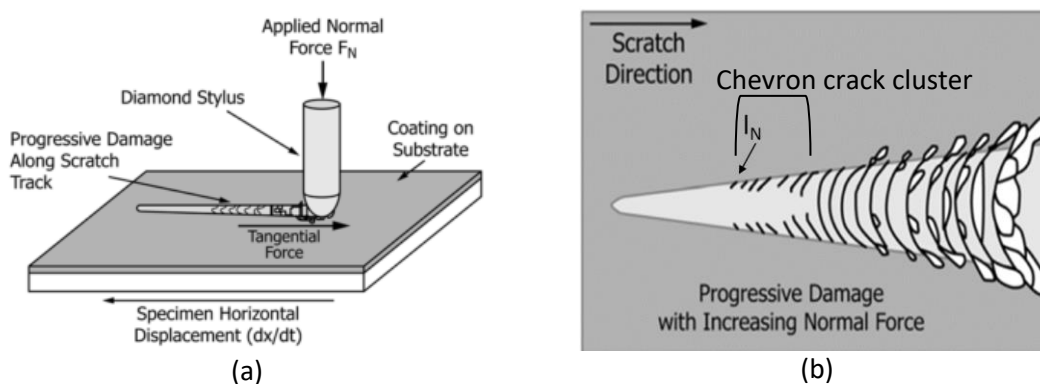
Figure 2-5. Schematic representation of (a) progressive scratch test method and (b) progressive damage. [141]

2.5. Corrosion testing

2.5.1. Autoclave testing

Two methods of autoclave corrosion testing were performed. Figure 2-6a shows a picture of the Westinghouse autoclave where corrosion tests were performed in static pure water at 360°C and 18.7 MPa for up to 128 days to assess the coating performance during normal operation conditions. This autoclave corrosion testing was performed according to ASTM G2: Standard Test Method for Corrosion Testing of Products of Zirconium, Hafnium, and Their Alloys in Water at 680°F (360°C) or in Steam at 750°F (400°C) [142]. This standard describes a test method used to evaluate the corrosion performance of zirconium-based alloys and specifically it has been used to determine the corrosion performance of nuclear fuel claddings. The autoclave material was 316 stainless steel. An uncoated ZIRLO® sample was also included in each autoclave test to serve as a reference to assess the performance of various coating design architectures. Static pure water is defined to be Grade A in the relevant standard having a pH value ranging between 5-8 [142]. In a pressured water reactor, the reactor environment has a pH value of 6.9-7.4 [5], the nuclear reactor temperature range is 280-330°C and the pressure is 15.5 MPa [4,5]. Figure 2-6b shows the Westinghouse autoclave tree in which the samples were mounted within the autoclave system.

(b) (c)
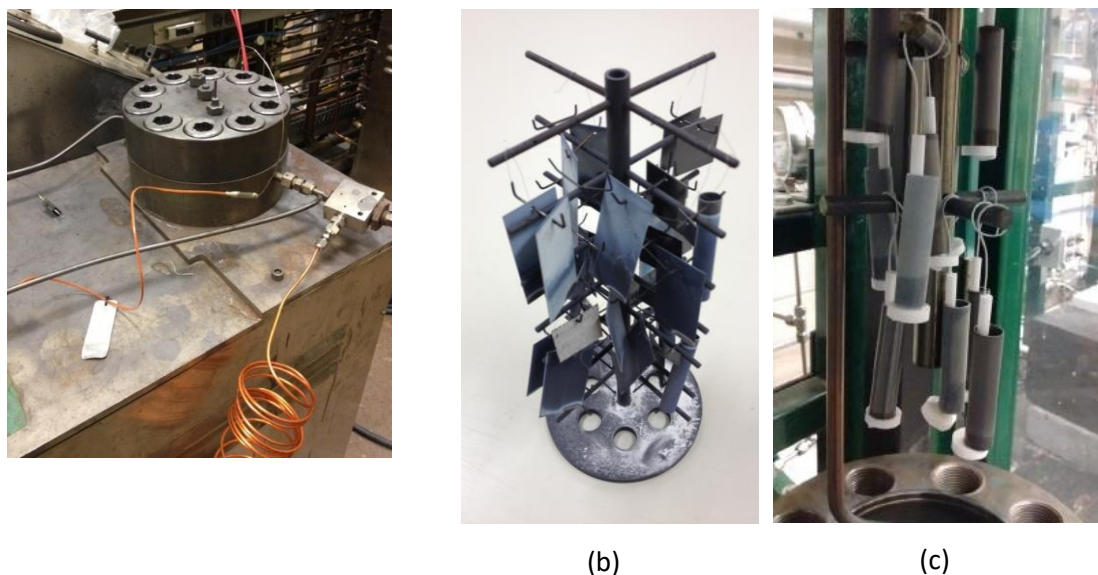
Figure 2-6. The Westinghouse (a) autoclave apparatus and (b) autoclave tree which were used to perform the static pure water tests at 360°C and 18.7 MPa. (c) The University of Michigan autoclave apparatus which was used to perform supercritical water (SCW) test in water at 542°C and 24.5 MPa.

The second type of autoclave testing was performed at the University of Michigan in a deaerated supercritical water recirculation loop held at 542°C and 24.5 MPa for 48 hours to assess the coating performance at higher temperature. The dissolved oxygen content of the supercritical water was less than 10 ppb. Figure 2-6c shows the University of Michigan autoclave tree.

During these autoclave tests, weight gain analysis was performed according to the ASTM G2 standard. The weight gain measurement is a widely used technique to assess the oxide formation during exposure. It is a valid measure of corrosion as long as there is no oxide dissolution or spalling. The measurement is performed by weighing the sample at the start of the test and at its end. By calculating the sample surface area exposed to the corrosive environment, it is possible to determine the weight gain per unit area. To determine the weight gain amount, the initial and final weight values are subtracted from each other and then divided by the surface area that was calculated.

2.5.2. Furnace testing

Furnace testing in air was performed at the Applied Research Laboratory at Penn State University. The aim of this test was to determine the corrosion behavior of the deposited coatings in high temperature air environment. Air oxidation performance of coated samples was investigated at a temperature range of 500-800°C.

2.5.3. Differential scanning calorimetry (DSC) and thermogravimetric analysis (TGA)

Differential scanning calorimetry (DSC) and thermogravimetric analysis (TGA) were performed to determine the phase transformation temperature, oxidation initiation temperature and weight gain due to oxidation as the samples were tested in air. Coated and uncoated flat ZIRLO® samples were cut to 4.8 mm x 5.6 mm dimension to fit into alumina crucibles. The cutting process was followed by grinding the edges with 320 grit silicon carbide paper. Then, samples were ultrasonically cleaned in acetone for 10 minutes and methanol for 10 minutes. DSC and TGA analyses were performed using a SDT Q600 Thermal Analysis instrument (New Castle, DE) by heating from room temperature to 1200°C at a rate of 5°C/min in air with a flow rate of 100 mL/min, and holding at 1200°C for one hour. The collected DSC and TGA data were analyzed using the TA Universal Analysis software. The temperature for the initiation of oxidation was determined from the intersection of the reaction peak starting point tangent line with the extended DSC curve as described in ASTM E2009 with the diagram in Figure 2-7 [143]. The data was also confirmed with conducting manual calculations using the Origin software.
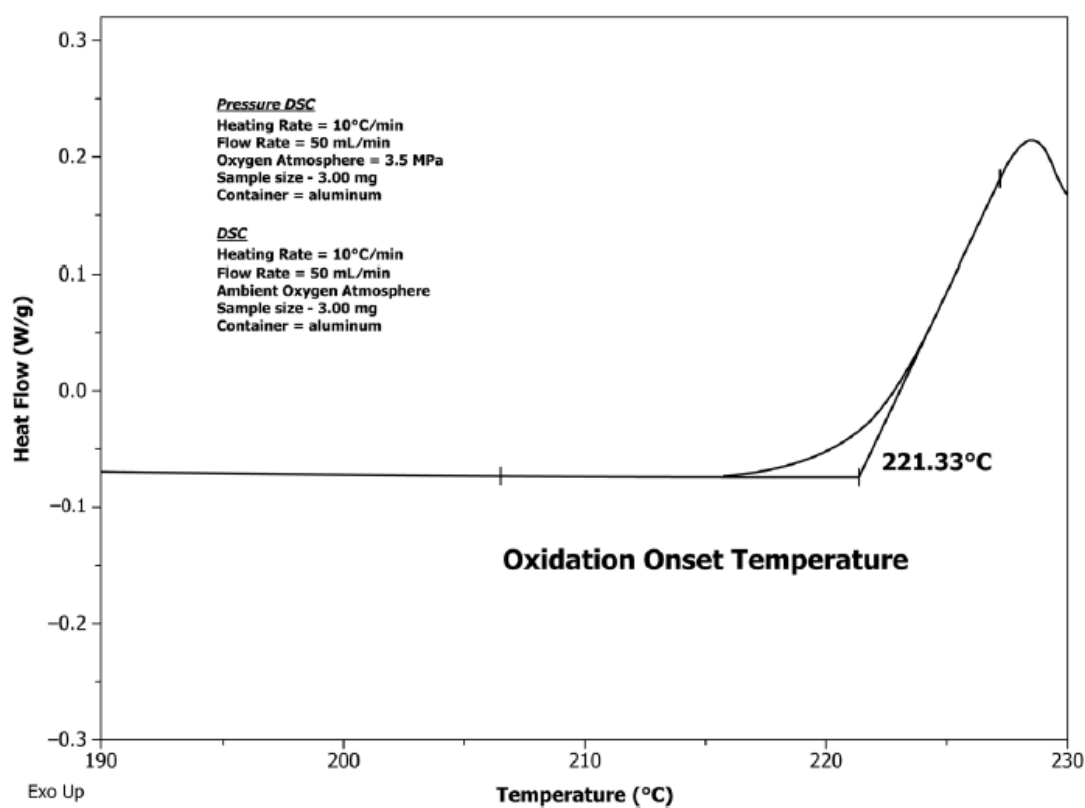
Figure 2-7. DSC oxidation onset temperature (OOT), extrapolated onset temperature. [143].

2.6. Material characterization

2.6.1. Cross-sectional sample preparation

Cross-sectional samples were prepared by cutting the samples either in the vertical or horizontal direction depending on the required analysis. For example, Figure 2-8a and b show digital images of the untested GEN-9 flat and tubular samples cut into ~7 mm long sections.

Figure 2-9a shows a digital image of the Allied Techcut 4™ instrument used to cut the samples with a diamond metal bonded, high concentration, 12.7 cm (5") Φ blade x 0.038 cm (0.015") thick wafering blade at speeds ranging from 100-130 rpm. Allied cutting fluid (60-20110) was used as the coolant during cutting operation. Epoxy mounts were prepared with Allied resin (145-10010) and Allied hardener (145-10015), mixing with a 10:3 weight ratio and curing at room temperature.
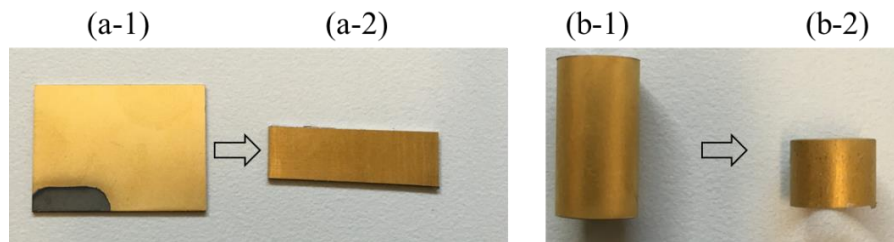
Figure 2-8. Digital images of characterized virgin samples; show as-received (a-1) flat and (b-1) tubular samples with (a-2) and (b-2) showing cut sections for cross-section analyses.

Figure 2-9b shows a digital image of the Allied automatic polisher. This polisher was used to grind and polish the samples. During these processes three samples were placed in the instrument, but individual pressure at 1-3 lb was applied on each sample. The grinding process was performed with water and using SiC papers having 240, 600, 800, 1200 grit for 4-8 minutes as needed depending on the quality of surface finish after each step in the specified sequence. Then, additional polishing was performed with 3 μm and 1 μm diamond slurry; followed by 0.04 μm colloidal silica to achieve a mirror finish. After each polishing and grinding step, the sample surface was rinsed with dionized water to remove deforming loosely adhered particles. Prior to SEM analysis, the epoxy mounted cross-section sample surface was sputter coated with iridium to avoid charging during SEM examination.

(a)   (b)

Figure 2-9. (a) Allied Techcut 4™ instrument and (b) Allied automatic polisher.

2.6.2. Scanning electron microscopy (SEM)

Figure 2-10 shows the FEI Quanta 200 Environmental scanning electron microscopy (SEM) instrument, located in the Pennsylvania State University Materials Characterization Laboratory, which was used to perform high resolution imaging of the samples. SEM analysis was performed both in the secondary electron mode and the backscattered electron mode. Both surface and cross-section analysis of the as-deposited and tested samples were conducted. Secondary electron imaging was performed on the sample surface to observe surface defects and surface topography, while backscatter electron mode was mainly used to examine the cross-section of the samples to distinguish the different individual layers, determine the deposited coating thickness, analyze the interface between the substrate and the coating, observe coating spallation/delamination and image coating and substrate oxidation. The data was collected at 80 Pa with 20 kV high voltage and a spot size of 4. The collected images were analyzed using ImageJ software.

Figure 2-10. The FEI Quanta 200 Environmental scanning electron microscope (SEM) instrument located within the Materials Characterization Laboratory at the Pennsylvania State University.

2.6.3. Energy dispersive spectroscopy (EDS)

Energy dispersive spectroscopy was performed to identify and quantify the chemical composition of the samples in the as-deposited coating as well as the degree of oxygen penetration after corrosion testing. Both surface and cross-sectional analyses were performed. FEI Quanta 200 Environmental scanning electron microscopy (SEM) instrument with the incorporation of EDS detector. Characteristic X-rays were collected and analyzed using the AZtec software. The data was collected at 80 Pa pressure and 20 kV high voltage, substrate height adjusted to 12.5 mm, and spot size ~6.8 to achieve a dead time of ~40%. The EDS analyses was performed in three modes composed of point analysis, elemental line scan, and elemental mapping. Figure 2-11 presents EDS analysis performed on the cross-section of 33 days autoclave tested PF324: (TiN/TiAlN 8-layer) / Ti / ZIRLO® (0.25 μm R_a), as an example. Figure 2-11a shows the SEM image; Figure 2-11b shows a point analysis spectrum obtained from the top TiN layer; Figure 2-11c shows the cross-section line scan performed from the coating surface towards the ZIRLO® substrate; Figure 2-11d shows the EDS-elemental mapping analysis

performed on the cross-section of the sample. Detailed results for these examinations are presented in the next chapter.

(a)

(b)

(c)

(d)
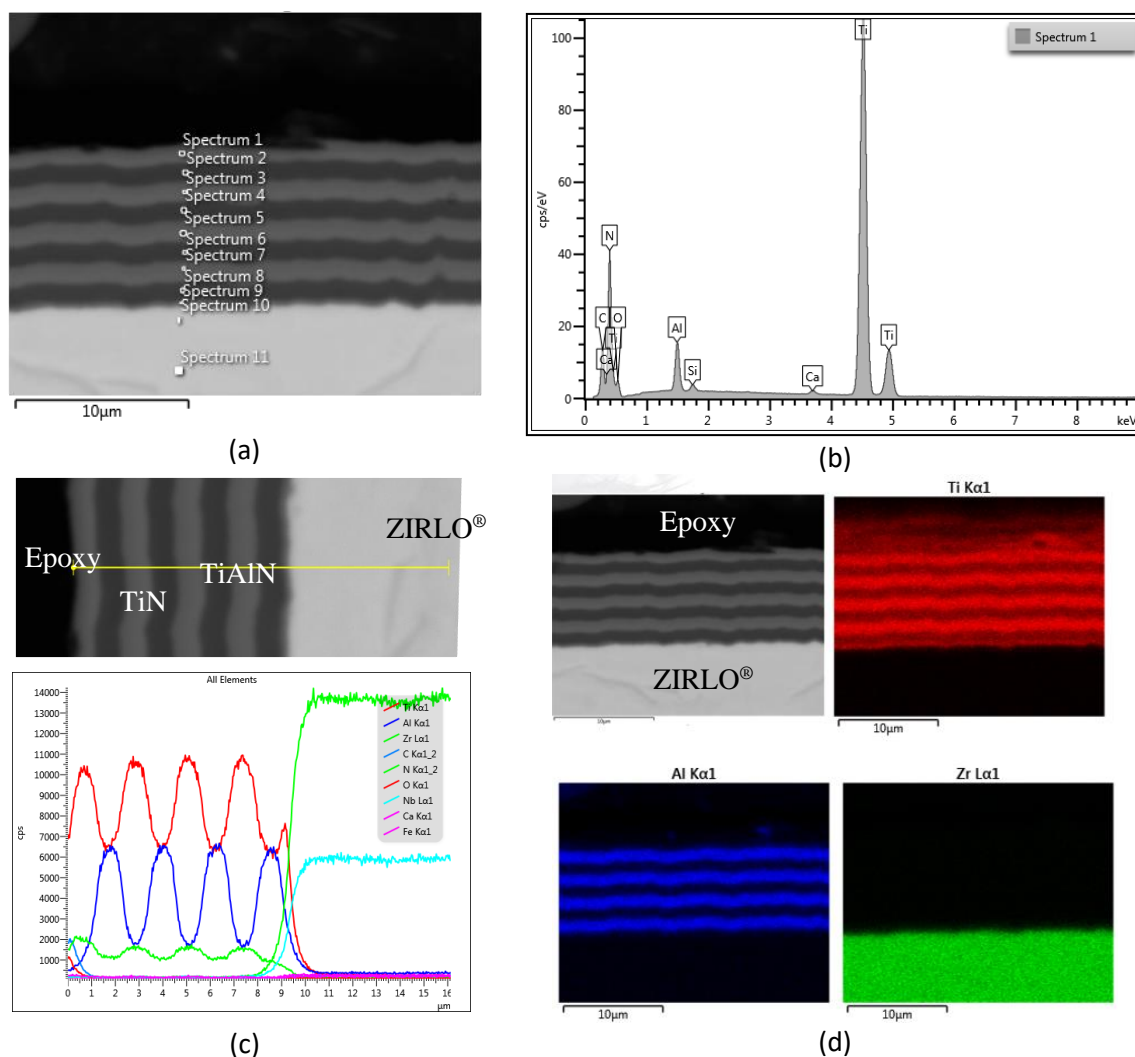
Figure 2-11. EDS analysis results performed on the sample PF324: (TiN/TiAlN 8-layer) / Ti / ZIRLO® (0.25 μm R_a) showing (a) cross-section image, (b) point analysis, (c) elemental line scan and (d) elemental mapping.

2.6.4. X-ray diffraction (XRD)

XRD analysis was used to determine the phases and crystal structures of the substrate, coating and oxides formed after corrosion testing. Figure 2-12 shows an image of the PANalytical XPert Pro Multi-Purpose Diffractometer (MPD) instrument located in the Pennsylvania State

University Materials Characterization Laboratory. X-ray diffraction (XRD) patterns were obtained with the MPD instrument. The instrument has a 240 mm radius and the 2θ scan was performed using Cu Kα radiation (Kα$_1$=1.54056 Å, Kα$_2$=1.54443Å) with fixed divergence slit (0.25°), receiving slit (0.25°), and a step size of 0.026°. XRD analysis was performed on the surface of the flat and tubular samples. Two different XRD scans were acquired, which included normal Bragg-Brentano (XRD-BB) and Grazing Incidence (GIXRD). XRD-BB scans were performed to determine coating crystallography and phases from the surface through the substrate which also provided information about coating and substrate preferred orientation. The aim of the grazing incidence measurements was to distinguish the coating phases from the substrate phases and was performed with varying incidence angles ranging from 0.5°-15° that were adjusted depending on the desired depth of analysis. The penetration depth of the incident X-ray through the coating thickness depending on the incident angle value was determined by using the HighScore software. The corresponding penetration depth ranges for specified incident angle range used were calculated to be 0.2-8 μm for TiN layer and 0.3-9 μm for TiAlN layer based on the density assumptions of ρ_{TiN}=5.5 g/cm^3 and ρ_{TiAlN}=5.5 g/cm^3, respectively.

Figure 2-12. The PANalytical XPert Pro Multi-Purpose Diffractometer (MPD) instrument located in the Materials Characterization Laboratory at the Pennsylvania State University.

2.6.4. Raman spectroscopy

Raman spectroscopy was performed to identify chemistry of the coatings. Horiba LabRam – Vlabinir spectrometer was used located at the Pennsylvania State University Materials Characterization Laboratory. The excitation wavelength used was 532 nm (110 mW laser) (notch filter ± 10 cm^{-1}). Grating was set to 300 gm/mm which provides a spectral resolution of ~4 cm^{-1} at 532 nm). Power of 4-5 mW was incident on the samples through a standard x50 microscope objective. Spectral range was 50-1500 cm^{-1} and the acquisition time was 30 sec. Instrument was used in duo scan, line scan and depth scan modes. The Raman spectra analysis were performed sing the LabSpec6- HORIBA scientific software.

2.7. Neutronic model and methodology

To evaluate the neutronic performance of TiAlN coatings, the Monte Carlo code Serpent [144] was used to calculate the k$_{eff}$ in the presence of coatings. The calculation assumed a single assembly model based on a typical PWR 17x17 assembly [145]. Such an assembly contains 264 fuel rods, 24 guide tubes, and 1 instrumentation tube. Reflective boundary conditions on four sides were used to generate an infinite array of assemblies with finite length. The assembly extremities contain axial reflectors composed of a water and steel mixture (50%-50% volume mix, 100 cm length). Table 2-2 shows the core parameters used in the calculations. The cycle length and attainable burnup were projected from the depletion of a single assembly averaging reactivity under the assumption of constant power throughout the lifetime of the assembly [146]. To correct for the infinite lattice, radial leakage was assumed to be 3%. Neutronic results for TiAlN, TiN and 8-layer TiAlN/TiN used ENDF/B-VII cross-sections. However, since ENDF/B-VII does not contain Yb cross-section data, JEFF 3.1.1 cross-section data was used for all doping results. Cross-sections (ENDF/B-VII) were applied at the following temperatures: 1057 K for

fuel, 637 K for clad, 600 K for coolant, and thermal scattering cross-sections were applied to water. Depletion calculations employed Chebyshev Rational Approximation Method (CRAM) and a high-resolution flux spectrum based on the unified energy-grid structure to calculate one-group cross-sections.

As a reference, undoped monolithic and multilayer coatings were analyzed using the model described above, and coatings were applied to the cladding exterior. The reference UO_2 was assumed 4.5 at.% enriched and Zircaloy-4 (0.1% Cr, 0.21% Fe, 1.45% Sn, and 98.24% Zr; 6.56 g/cm^3) was chosen as the reference cladding material. The reference cycle length was found to be 446.5 EFPD (effective full power days) with ENDF/B-VII cross-section data. The reference cycle length was recalculated to be 445.5 EFPD with JEFF 3.1.1 cross-section data. The results of this calculation are shown in Chapter 4.

Table 2-2. Pressurized water reactor (PWR) reference design properties [145].

Property	Value
Total power, MW	3400
Assemblies	157
Core average coolant temperature, °C	303
Pressure, bar	155
Core average coolant density, °C	0.719
Active length, cm	426.720
Pellet diameter, cm	0.820
Clad thickness, cm	0.057
Fuel rod outer diameter, cm	0.950
Pitch-to-diameter ratio	1.326

2.8. Summary

This chapter provided information on the experimental methods used in this research study to create corrosion resistant coatings that can withstand nuclear reactor environment both during normal operation and accident conditions. First, substrate ZIRLO® material was examined

and its surface was prepared for proper coating deposition with good adhesion. Then, coatings were deposited using the cathodic arc physical vapor deposition process. The theory and considered parameters to deposit coatings with desired properties were described in the relevant sections of this chapter. Coating properties were optimized through coating generations and the optimized property information were also introduced in this chapter. Then, testing and characterization methods performed throughout the study to evaluate the coating performance were described. Finally, the procedure for neutronic analysis was discussed.

Chapter 3

Coating Optimization Results

This study has been conducted with the aim of developing coatings to enhance the corrosion resistance of nuclear fuel claddings both during normal operation conditions and in the case of a loss of coolant accident. As described in more detail in the introduction chapter, ceramic materials have high melting point, high chemical stability and good wear resistance. They have been used as coating materials, especially in the tooling industry, for years. Among the different types of ceramic coatings, physical vapor deposited TiN and TiAlN coatings have been proved to be more effective in enhancing the corrosion resistance of the substrate material because of the formation of passivating TiO_2 and Al_2O_3 layers upon interaction with the oxidizing environment. Thus, the application of TiN and TiAlN coatings against oxidation shows potential; however, there has been limited study in the literature on their corrosion performance in high temperature water and steam environments.

Nuclear fuel claddings are generally made of zirconium-based alloy mainly because of their low neutron absorption cross-section, yet their corrosion performance could be improved by depositing a protective coating. Several types of coatings have been considered. Khatkhatay et al. [62] considered depositing single layer TiN and single layer $Ti_{0.35}Al_{0.65}N$ by pulsed laser deposition on Zircaloy-4 tubes and corrosion tested them in deaerated water at 500°C and 25 MPa. They observed that coated tubes stayed intact while uncoated tubes experienced severe oxidation and they emphasized that optimization of $Ti_{0.35}Al_{0.65}N$ coating might make it outperform TiN coating. The pulsed laser deposition method provides flexibility and growth control but is not suitable for large-scale film growth. Although, Khatkhatay et al.'s study provides some insight about the performance of TiN and TiAlN coatings in a nuclear reactor environment, there has been no study on the TiN and TiAlN coating performance at normal

operation conditions of a pressurized water reactor (PWR) in literature. As a result, in this study, we decided to apply TiN and TiAlN coatings on ZIRLO® substrate and investigate their corrosion performance both at normal operation conditions and at higher temperatures. To deposit TiN and TiAlN on ZIRLO® substrate, we decided to use cathodic arc physical vapor deposition (CA-PVD) method. CA-PVD is a method that can be used to deposit various types of coatings, and in addition to its various advantages that were mentioned several times in previous chapters, they are also scalable to the production size.

This research project has been conducted in a systematic manner to achieve coating adhesion and corrosion performance enhancement through deposition generations. We sequentially optimized one deposition parameter per generation to be able to individually determine the effect of each parameter on the coating adhesion and corrosion performance.

3.1. As-received ZIRLO® Substrate Properties

In this study, ZIRLO® has been used as the substrate material, since it has been proved to be a convenient nuclear fuel cladding material with good mechanical properties and high oxidation resistance. ZIRLO® materials were obtained from Westinghouse Co. in sheet and tubular geometries. Digital images of as-received sheet (L5 cm x W2.5 cm x T0.05 cm) and tube (L4cm x $\varnothing_{outer}$1 cm and $\varnothing_{inner}$0.85 cm) samples are shown in Figure 3-1a and b, respectively. In Figure 3-1a, a lined pattern on the sample surface parallel to the width of the sheet ZIRLO® can be observed. These lines are created because of the fabrication process [147] used to produce these ZIRLO® sheets. Further characterization was performed using X-ray diffraction (XRD) to determine phases and texture, and energy dispersive spectroscopy (EDS) in the SEM to determine the chemical composition of the as-received ZIRLO® samples since these properties can affect the deposited coating properties and adhesion between the coating and the ZIRLO® substrate.
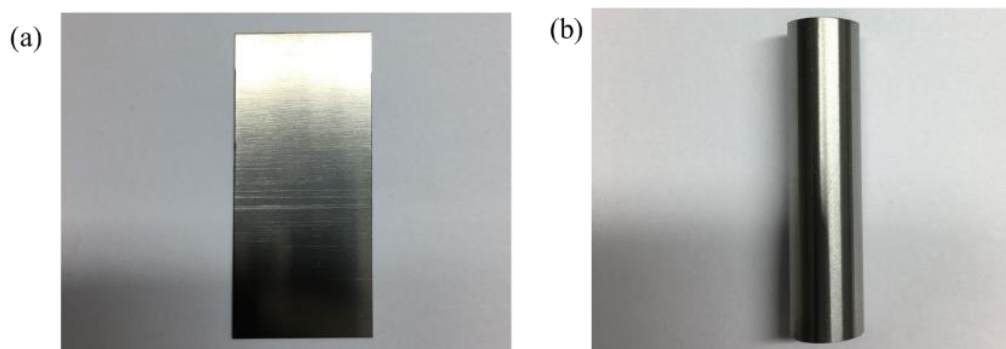
Figure 3-1. Digital image of as-received (a) ZIRLO® sheet (L5 cm x W2.5 cm x T0.05 cm), (b) ZIRLO® tube (L4cm x Ø$_{outer}$1 cm and Ø$_{inner}$0.85 cm).

The EDS measurement was conducted at point analysis mode on four different locations on the sample surface and averaged. The results are presented in Table 3-1. The measured niobium and iron values were determined to be higher than the ZIRLO® chemical composition given in literature as 1 wt.% Nb, 1 wt.% Sn, 0.1 wt.% Fe and balance Zr [147]. The variation in the measured composition values from the literature might origin from the surface roughness of the sample, overlapping of Zr L$_α$ (2.042 keV [148]), Zr L$_β$ (2.124 keV [148]) and Nb L$_α$ (2.166 keV [148]), and not using standards specific for our samples in addition to the poor energy resolution, low peak-to-background ratio and input signal limitation disadvantages of the EDS analysis [149]. Data also showed an oxygen composition of 2.96 ± 0.18 wt.%. The measured oxygen content might not be representative of the overall of substrate content since it might be due to oxidation on the surface due to the reaction of zirconium with air or the cleaning process with methanol and isopropanol. Throughout the study, ZIRLO® composition was also measured from cross-section samples and oxygen content was determined to be similar confirming the values measured from the surface. However, the oxygen content observed in the case of cross-section samples can also be attributed to the cross-section sample procedure during which samples come in contact with several alcohols having oxygen and carbon in them (carbon was also detected in the case of cross-section samples which was attributed to the smearing from the

epoxy mounting.) or oxidation that might have occurred during iridium coating that was applied to avoid charging during electron microscopy.

Table 3-1. As-received ZIRLO® composition measured from sample surface based on energy dispersive spectroscopy (EDS) point analysis data.

	Zr	Nb	Sn	Fe	O
at.%	82.14 ± 0.63	2.17 ± 0.10	0.68 ± 0.09	0.16 ± 0.05	14.86 ± 0.81
wt.%	93.40 ± 0.02	2.51 ± 0.11	1.01 ± 0.13	0.11 ± 0.04	2.96 ± 0.18
Ref wt.% [147]	balance	1	1	0.1	

Figure 3-2 shows XRD-Bragg Brentano (Cu Kα radiation) patterns taken from ZIRLO® sheet and tubes. The XRD scanning was performed along the longitudinal axes of the ZIRLO® sheet and tubes. Both ZIRLO® sheet and ZIRLO® tube patterns were compatible with the α-Zr phase having hexagonal close packed crystal structure and a pattern with the ICDD PDF# 00-005-0665. The powder diffraction lines corresponding to their standards are shown above for comparison. This phase identification indicated the polycrystalline hexagonal crystal structure of the ZIRLO®. The samples were clearly textured, as the peak intensities do not match the powder pattern. In particular, a higher intensity of the (002) plane was observed compared to the standard pattern. This is caused by the preferred crystallite orientation generated during sample production (rolling [147] and pilgering). Overall, peak intensities in the case of ZIRLO® sheet XRD pattern were higher and more symmetric compared to the peaks observed in the ZIRLO® tube XRD pattern. A non-symmetric peak shifting observed in the case of tubular ZIRLO® XRD pattern occurred towards lower angles due to a geometrical effect. Thus, a high percentage of the planes parallel to the surface have the basal plane orientation, as expected.
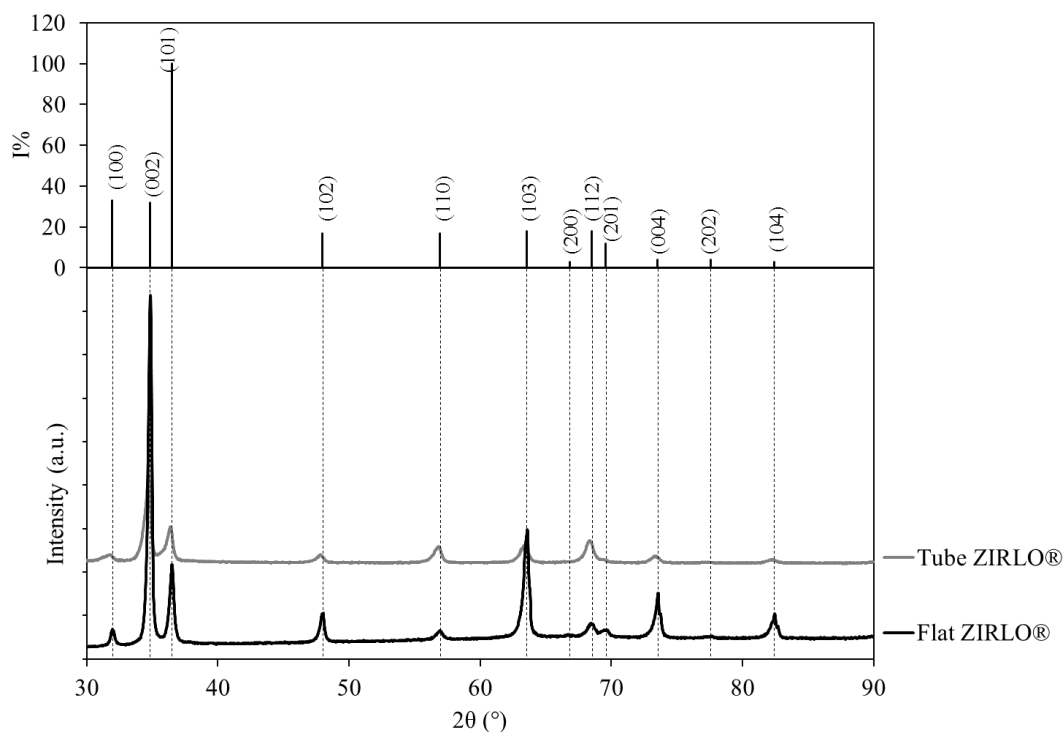
Figure 3-2. XRD-Bragg Brentano patterns of uncoated flat and tube ZIRLO® samples along axial direction with Cu K_α (K_α=1.54 Å) radiation. The powder diffraction pattern lines corresponding to the ICDD PDF# 00-005-0665 standard are shown above for comparison.

3.2. Monolithic TiAlN and monolithic TiN coating deposition on ZIRLO® sheets

Initial coating development studies were performed by depositing single-layer TiAlN and single-layer TiN coatings on flat samples to maximize research efficiency considering the ease of production and to understand the effect of each layer on corrosion performance.

3.2.1. Scratch testing and post-scratch observations

Scratch testing was performed according to the ASTM C1624: Standard test method for adhesion strength and mechanical failure modes of ceramic coatings by quantitative single point scratch testing. Measurement parameter information were provided in Section 2.4. ZIRLO® sheet surfaces were ground by hand using SiC to a substrate surface roughness value of 0.25 μm R_a.

TiAlN coating was deposited in nitrogen atmosphere with a 1.6 Pa partial pressure and using 60 A arc current. Parameters investigated through scratch testing involved deposition time (TiAlN coating thickness), substrate bias and cathode composition. Deposition parameter summary of samples tested for scratch testing is presented in Table 3-2.

Table 3-2. Cathodic arc physical vapor deposition (CA-PVD) parameter summary of TiAlN coatings prepared for scratch testing. Varied parameter for each sample is indicated with bold font.

Deposition time (BC/TC)* (min)	Negative substrate bias (BC/TC) (V)	Cathode composition (at.% Ti/Al)
8/150	150/50	33/67
8/300	150/50	33/67
8/450	150/50	**33/67**
8/450	150/50	**20/80**
8/450	150/**0**	20/80
8/450	150/**25**	20/80
8/450	150/**50**	20/80
8/450	150/**100**	20/80

*BC=bond coat, TC=Top coat

3.2.1.2. Deposition time variation

The coating deposition time affects coating thickness. The resulting coating thickness depends not only on deposition time but also on other properties which affect coating density such as substrate bias and arc current. Deposition time variation effect was investigated by depositing single layer TiAlN coatings for three different time durations of 150 min, 300 min and 450 min. Figure 3-3 shows the cross-section scanning electron microscopy (SEM) backscattered electron (BSE) images of equivalent TiAlN coatings deposited for 150 min, 300 min and 450 min. The cross-section SEM-BSE images of samples having TiAlN coatings deposited for different durations are presented in Figure 3-3. These images show the uniform and dense TiAlN coatings were deposited. The coating surface texture mimicked the substrate surface texture, helping to keep the coating thickness fixed throughout the sample surface.
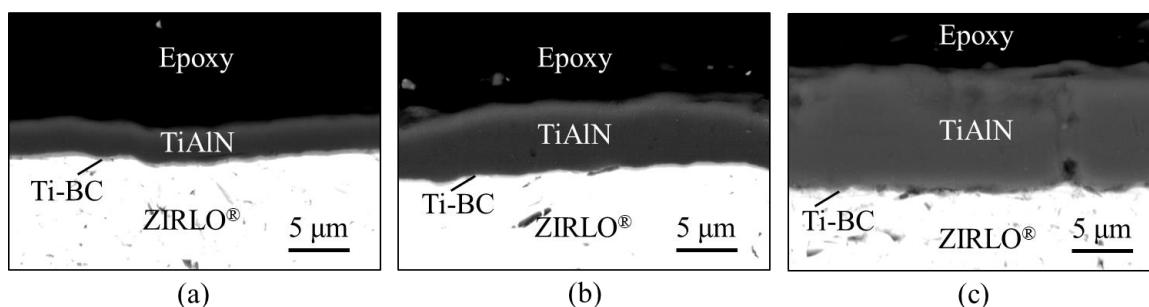
Figure 3-3. Cross-section scanning electron microscopy (SEM) backscattered electron (BSE) images of TiAlN coatings deposited for 150 min, 300 min and 450 min.

Figure 3-4 shows the relationship between TiAlN layer deposition time and TiAlN coating thickness obtained. Coating thickness measurements were made from the cross-section SEM-BSE images of the samples (three examples were provided in Figure 3-3) using ImageJ software. On average, 13 measurements per sample were made on SEM-BSE images taken from at least three different locations of the cross-sectioned sample. Figure 3-4 shows the average of these coating thickness measurements of each sample. Accordingly, the coating deposition durations of 150 min, 300 min and 450 min led to coating thicknesses of 2.6±0.3 μm, 4.1±1.0 μm and 9.6±0.5 μm, respectively. A linear relationship was established between the deposition time and the coating thickness. Thus, the deposition rate was 0.0231 μm/min.
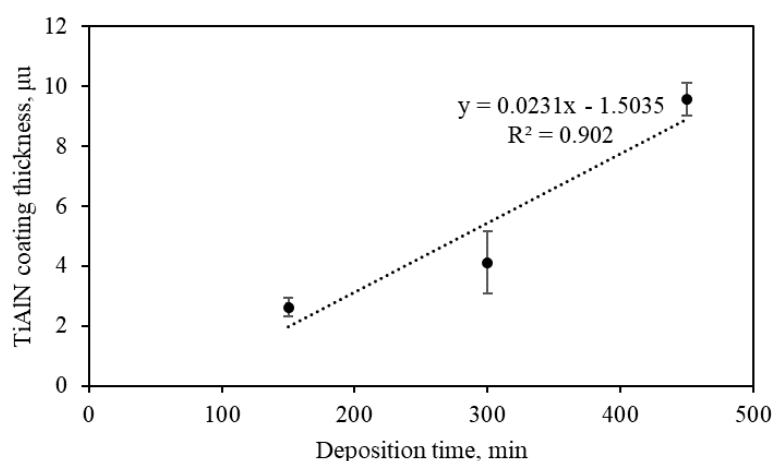
Figure 3-4. Graph showing the change in TiAlN coating thickness with respect to the deposition time.

Then, scratch testing was performed to evaluate coating adhesion according to the procedure that was described in Section 2.4. The loading rate, during scratch testing of different samples, was primarily kept fixed and specifically, the loading rate during scratch testing of TiAlN coatings deposited for 150 min, 300 min and 450 min were 47.4 N/min, 49.3 N/min and 50.4 N/min, respectively. Figure 3-5 shows the coating failure mode with respect to the load applied. TiAlN coating deposited for 150 min experienced gross spallation at 17.84 N (Figure 3-5a). The gross spallation was also observed in 300 min deposited TiAlN coating at the end of the scratch testing corresponding to a loading of 49.3 N (Figure 3-5b). TiAlN coating deposited for 450 min did not show gross spallation during the scratch testing up to a value of 50.4 N. Additionally, differing from the coatings deposited for shorter times, TiAlN coating deposited for 450 min showed recovery spallation which initiated at 21.5 N loading (Figure 3-5c). An inverse relationship between the coating deposition time and critical load to cause gross spallation was expected based on previous results in literature [141]. However, in this study an increase in coating deposition time (coating thickness) led to an increase in the critical load to cause gross spallation.

TiAlN coatings (in this section) were deposited using 33 at.% Ti – 67 at. % Al cathode with a substrate bias of -50 V and an arc current of 60 A at 325°C chamber temperature in 1.6 Pa N_2 atmosphere. In summary:

- TiAlN coating deposition rate for set parameters was determined to be 0.0231 μm/min.
- Deposition time resulted in increased coating thickness, almost linearly.
- Increased coating thickness led to an increase in the critical load value to cause gross spallation of the TiAlN coating.
- Coating thickness affected the coating failure mode during scratch testing.
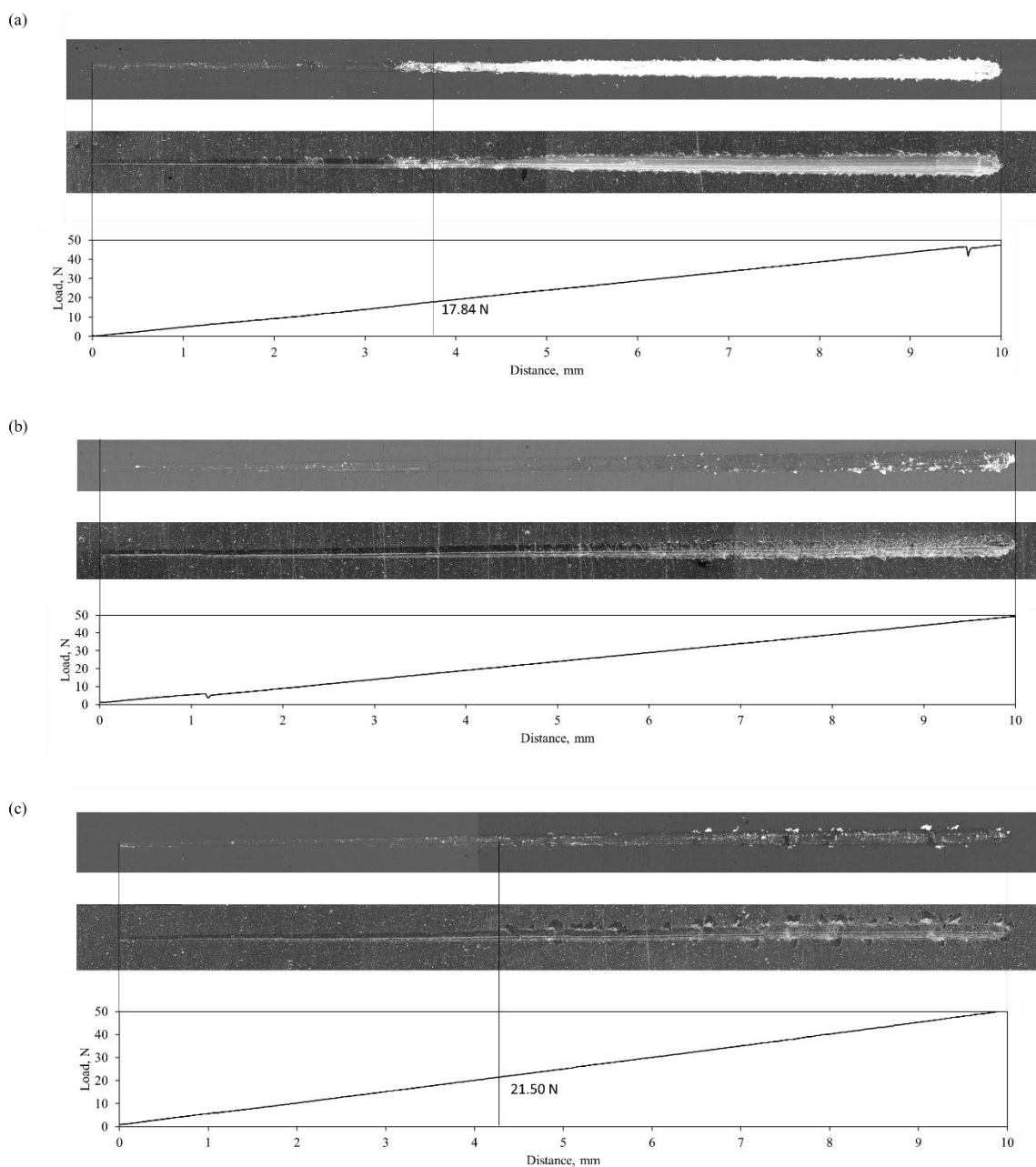
Figure 3-5. Scanning electron microscopy-backscattered electron (top) and secondary electron (bottom) images of scratches obtained after scratch testing of TiAlN coating deposited for (a) 150 min, (b) 300 min and (c) 450 min. Loading rate during scratch testing of TiAlN coatings deposited for 150 min, 300 min and 450 min were 47.4 N/min, 49.3 N/min and 50.4 N/min, respectively.

3.2.1.3. Cathode composition variation

The effect of cathode composition was investigated by depositing single-layer TiAlN coatings with two different cathode compositions of 33 at.% Ti – 67 at.% Al and 20 at.% Ti – 80 at.% Al. Figure 3-6 shows the surface scanning electron microscopy (SEM) secondary electron (SE) images and cross-section SEM backscattered electron (BSE) images of coatings deposited by using cathodes having 20 at.% Ti – 80 at. Al and 33 at.% Ti – 67 at.% Al. Both coating surfaces had a vertical wavelike texture mirroring the substrate surface texture obtained from SiC grinding. Both surfaces had sphere-like macroparticles at sizes that can reach up to 10 μm. Macroparticle formation is a common defect of arc coatings and they is attributed to (i) low melting point aluminum droplet formation in the case of TiAlN deposition [70,150] and (ii) excess incompletely ionized atoms because of too fast evaporation rate that may coalesce to macroparticles during flight [72]. A higher volume fraction of macroparticles was observed in the case of the coating deposited with 80 at.%Al cathode. The cross-section SEM-BSE image of coating deposited with the cathode having 80 at.% Al showed a pore-free, uniform thickness TiAlN coating. There were only a few crack-like features along the coating. Macroparticles were also observed in the cross-section SEM images, a less dense growth occurs underneath the macroparticle, while almost unperturbed coating deposition rate is observed on top of the macroparticles. The reason of this is high ion bombardment on the top compared to the negligible ion bombardment occurring under the macroparticle as they shadow underneath and decrease the ion and coating deposition flux in their vicinity leading to a low-density zone or a gap between the defected region and the unperturbedly growing region, which results in an almost parabolic boundary between the perturbed and unperturbed region [151,152] and also makes macroparticles less adhered to the surface [150]. For small macroparticles (Ø < ~5 μm), deposition rate on top of the macroparticle did not vary significantly from that of the unperturbed regions, but for larger macroparticles, a slight decrease in deposition rate was observed on top of the macroparticle

which decreases even more towards the edges of the perturbed nodular macroparticle. For large macroparticles, having lower deposition rate on top of the nodular structure can be attributed to the lack of contact with the substrate because of porous boundary in between the nodule and the substrate, and eventually not being able to maintain the negative substrate bias effect. Deposition rate decrease towards the sides of the nodular macroparticle can be attributed to not being able to receive ions orthogonally. The existence of nodular macroparticle on surface and coating deposition on top of it with at almost the same rate with the unperturbed regions leads to increased surface roughness which is not desired for applications involving, decorative coatings, optical and electrical fields. In the case of coating deposited with the cathode having 67 at.%Al, a few pore-like features and deformation regions were observed. Some of the deformations might have occurred during cross-section sample preparation. Additionally, coating thicknesses were measured to investigate any variations due to the change in aluminum content. The coating thicknesses were measured using ImageJ from cross-section SEM-BSE images taken from five different locations on both sides of the coating (3-measurement locations from one side, 2-measurement locations from the other side) and three measurements at each location, which lead to 15 measurements. The average TiAlN coating thickness was determined to be 10.6 ± 0.8 µm and 9.6 ± 0.5 µm for coatings deposited with a cathode of 20 at.% Ti – 80 at.% Al and 33 at.% Ti – 67 at.% Al, respectively. Thus, increased aluminum content resulted in a slight increase in the coating thickness.

80 at.% Al 67 at.% Al

Surface
SEM-SE

Cross-section
SEM-BSE
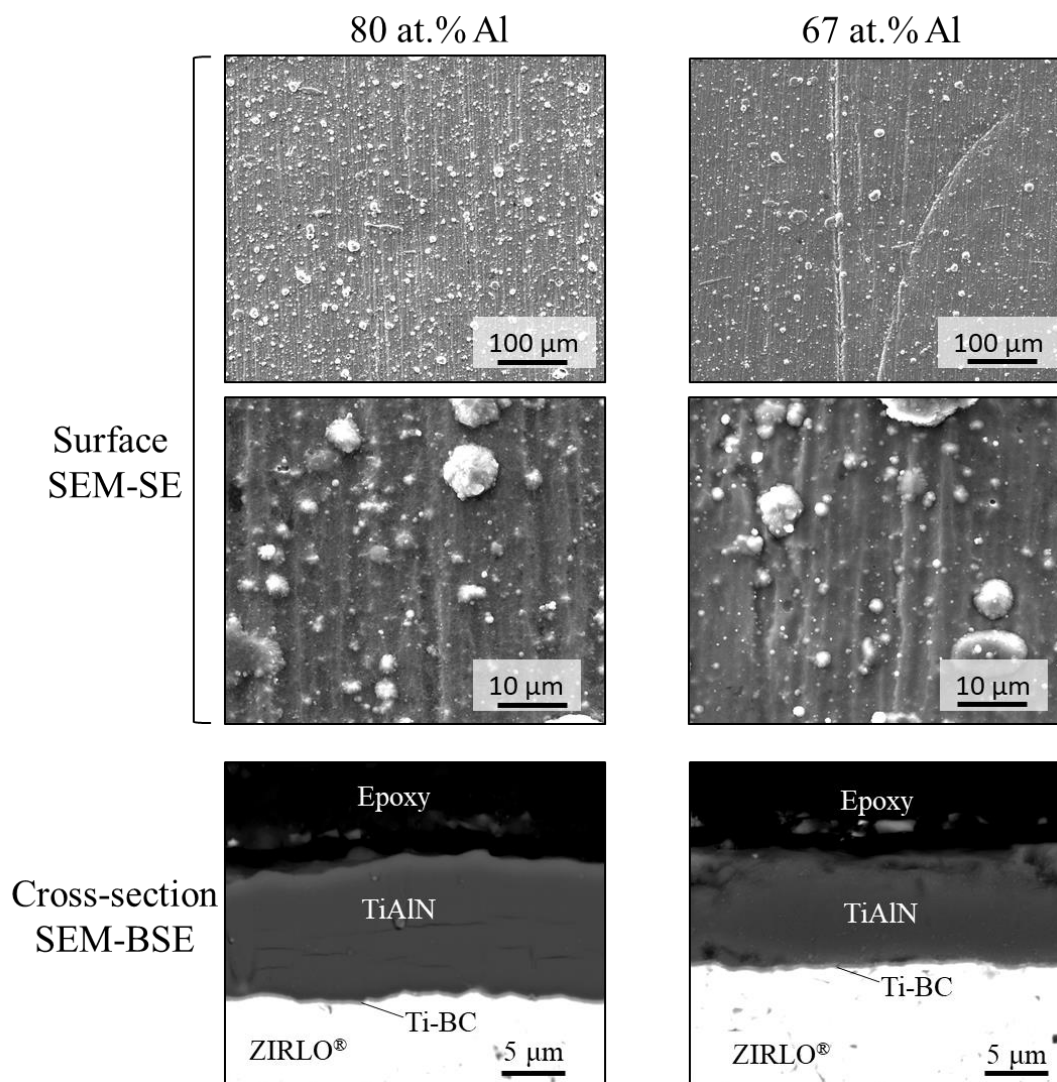
Figure 3-6. The surface scanning electron microscopy (SEM) secondary electron (SE) images and cross-section SEM backscattered electron (BSE) images of coatings deposited by using cathodes having 20 at.% Ti – 80 at. Al and 33 at.% Ti – 67 at.% Al.

Table 3-3 presents the TiAlN coating chemical composition determined by using the energy dispersive spectroscopy (EDS) equipment mounted to the scanning electron microscopy instrument as described in Section 2.6.3. The coating chemical compositions were measured from five different locations on both sides of the coating (3-measurement location from one side, 2-measurement location from the other side). The chemical composition measurement was performed from the middle of the coating thickness. The data presented in Table 3-3 represents

the average of 5 measurements for each sample. The aluminum to titanium ratio was determined

to be 3.76 and 1.97 for coatings deposited with 20 at. % Ti - 80 at.% Al and 33 at. % Ti - 67 at.%

Al, respectively. Thus, the coating composition mimicked the cathode composition.

Table 3-3. Composition of TiAlN coatings deposited by using cathodes having 20 at.% Ti – 80 at. Al and 33 at.% Ti – 67 at.% Al. Coating compositions were determined using energy dispersive spectroscopy (EDS) point analysis

Cathode composition	Ti, at.%	Al, at.%	N, at.%	Ti, wt.%	Al, wt.%	N, wt.%
20 at.% Ti – 80 at.% Al	8.76 ± 0.20	32.98 ± 0.34	58.26 ± 0.50	19.73 ± 0.36	41.85 ± 0.29	38.39 ± 0.50
33 at.% Ti – 67 at.% Al	13.10 ± 0.47	25.83 ± 0.60	59.68 ± 2.34	28.71 ± 0.77	31.90 ± 0.54	38.26 ± 1.51

Figure 3-7 shows the Raman spectra of the single layer TiAlN coatings deposited with

cathodes having a composition of 33 at.% Ti – 67 at.% Al and 20 at.% Ti – 80 at.% Al. TiAlN

coating deposited with 33 at.% Ti – 67 at.% Al cathode showed two broad bands having peaks at

257 and 673 cm^{-1}. TiAlN coating deposited with 20 at.% Ti – 80 at.% Al. TiAlN showed four

peaks at 190, 485, 625 and 774 cm^{-1}. Both spectra exhibited peaks that could be indexed as the

TiAlN phase. The total spectral density between the two broad bands was increased in the case of

20 at.% Ti – 80 at.% Al cathode deposited TiAlN coating compared to the 33 at.% Ti – 67 at.%

Al cathode deposited TiAlN coating.
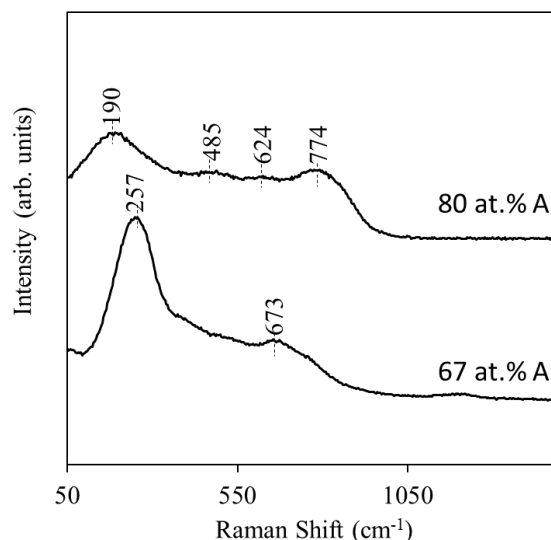
Figure 3-7. Overlaid Raman spectra of coatings deposited with cathodes having a composition of 33 at.% Ti – 67 at.% Al and 20 at.% Ti – 80 at.% Al.

Figure 3-8 shows the overlaid X-ray diffraction - grazing incidence (GIXRD) measurement patterns of coatings deposited with cathodes having a composition of either 33 at.% Ti – 67 at.% Al or 20 at.% Ti – 80 at.% Al . GIXRD was performed using a Cu-Kα (1.54048 Å) radiation and with a grazing incidence angle of 1°. Peak identification was performed using JADE software. For a cathode composition of 67 at.% Al, the coating phase is determined to be $Ti_{0.5}Al_{0.5}N$ (ICDD PDF# 04-005-5251), which has a cubic crystal structure. For a cathode composition of 80 at.% Al, peak patterns were fitting with the $Ti_{0.32}Al_{0.68}N$ phase (ICDD-PDF# 04-017-4686) and AlN (ICDD PDF# 04-004-4544), which have hexagonal crystal structure. The difference between the two patterns can easily be observed from the (200) peak of $Ti_{0.5}Al_{0.5}N$ phase at 43.14°, which is not observed in the case of $Ti_{0.32}Al_{0.68}N$ phase pattern. Broad peaks appeared suggesting an amorphous or nanocrystalline composite coating structure. This broadening was more pronounced for coatings deposited with 80 at.% Al indicating increased nanocrystalline composite structure.

Scratch testing was performed on samples having TiAlN coating deposited with either 33 at.% Ti – 67 at.% Al or 20 at.% Ti – 80 at.% Al cathode. The post-scratch testing SEM images

and load-distance diagram for TiAlN coating deposited with 33 at.% Ti – 67 at.% Al cathode was provided in Figure 3-5c. The loading rate was 50.4 N/min, there was no gross spallation, but there was recovery spallation. In the case of TiAlN coating deposited with 20 at.% Ti – 80 at.% Al cathode, scratch testing was performed with a loading rate of 50.19 N/min as shown in Figure 3-9. Recovery spallation was observed but at a lower load value of 15.2 N compared to the TiAlN coating deposited with 33 at.% Ti – 67 at.% Al cathode. Additionally, gross spallation occurred at 41.7 N.

In conclusion, the cathode composition has a strong influence on the coating composition. TiAlN coatings with higher aluminum content and hexagonal crystal structure required lower critical load to cause recovery spallation and gross spallation indicating lower adhesion. So, it is recommended to keep aluminum content limited in the TiAlN coating.

Figure 3-8. GIXRD measurement patterns of coatings deposited with cathodes having a composition of 33 at.% Ti – 67 at.% Al and 20 at.% Ti – 80 at.% Al. GIXRD was performed using a Cu-Kα (1.54048 Å) radiation and with a grazing incidence angle of 1°.
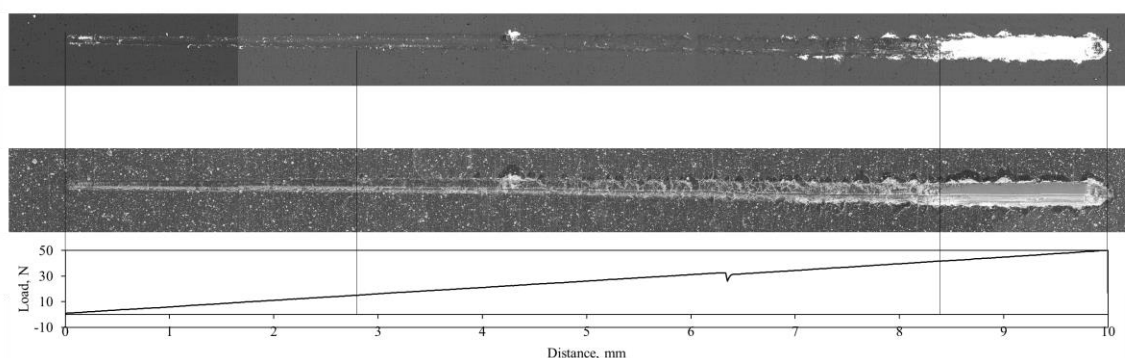
Figure 3-9. Scanning electron microscopy-backscattered electron (top) and secondary electron (bottom) images of scratches obtained after scratch testing of TiAlN coating deposited with 20 at.% Ti – 80 at.% Al cathode.

3.2.1.4. Substrate bias variation

The substrate bias effect was investigated by depositing single layer TiAlN coatings with four different substrate bias values of 0 V, 25 V, 50 V and 100 V as it was shown in Table 3-2. Figure 3-10 shows digital images of as-deposited coatings. The images presented in the Figure 3-10 were taken after cutting samples. All coatings had a dark gray color, but they had a different shine. Coating deposited with no substrate bias, was adherent and had a darker gray color with a matte finish. Coatings deposited with 25 V and 50 V substrate bias were also adherent and glossy, in contrast to the appearance of the coating deposited with no substrate bias. Coatings deposited with 100 V substrate bias had a less shiny surface finish and coating was flaking off, which can be observed clearly at the right edge of the sample image (arrow)presented in Figure 3-10.
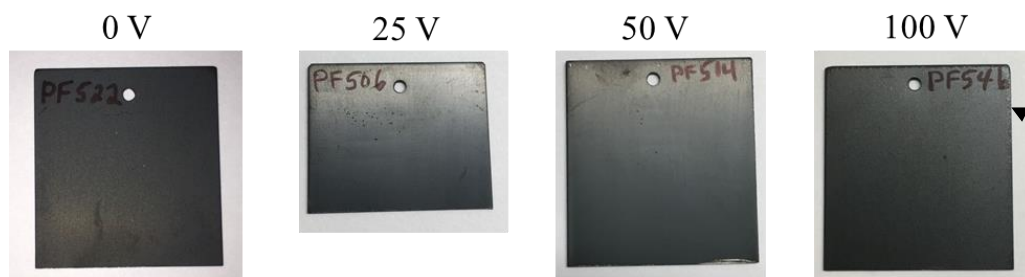
Figure 3-10. Digital images of TiAlN coated ZIRLO® sheets. Deposition process was performed with four different substrate biases: 0 V, 25 V, 50 V and 100 V.

Figure 3-11 shows scanning electron microscopy images of coating surfaces taken in two different modes: backscattered electron (BSE) and secondary electron (SE). The surface of the coating deposited with 0 V substrate bias was full of spherical macroparticles in various sizes. This spherelike deposition on the surface indicates a passive deposition with a 90° angle strike on the flat sample surface without the effect of a force that can cause deviation in the geometry. This nonsmooth surface covered with spherelike macroparticles could be the reason of the matte finish observed in the digital image of the coating shown in Figure 3-10. The surface characteristics of the coating deposited with 25 V and 50 V were similar to each other with a surface topography that mirrored the substrate surface topography obtained after SiC surface grinding. Coatings deposited with 25 V and 50 V substrate bias also had spherelike macroparticles on the surface but to a much less extent than for the coating deposited with 0 V. The number and size of the macroparticles on the surface of these two types of coatings were similar to each other; however, macroparticles in the case of coatings deposited with 50 V substrate bias were less spherelike than the coatings deposited with 25 V substrate bias, which can be due to the increased attraction forces caused by ion bombardment with higher kinetic energy. The surface of the coating deposited with a substrate bias of 100 V was completely different than the other three samples as can be observed in Figure 3-11. The coating surface exhibited a spattered appearance, which can be attributed to the excessive energy of the ion bombardment due to too high substrate bias.

Almost no macroparticles similar to those previously observed macroparticles on the coatings deposited with 0 V, 25 V and 0 V were seen, but a few very small (~1 μm) spherelike macroparticles on the surface were observed with the appearance of a back spatter.
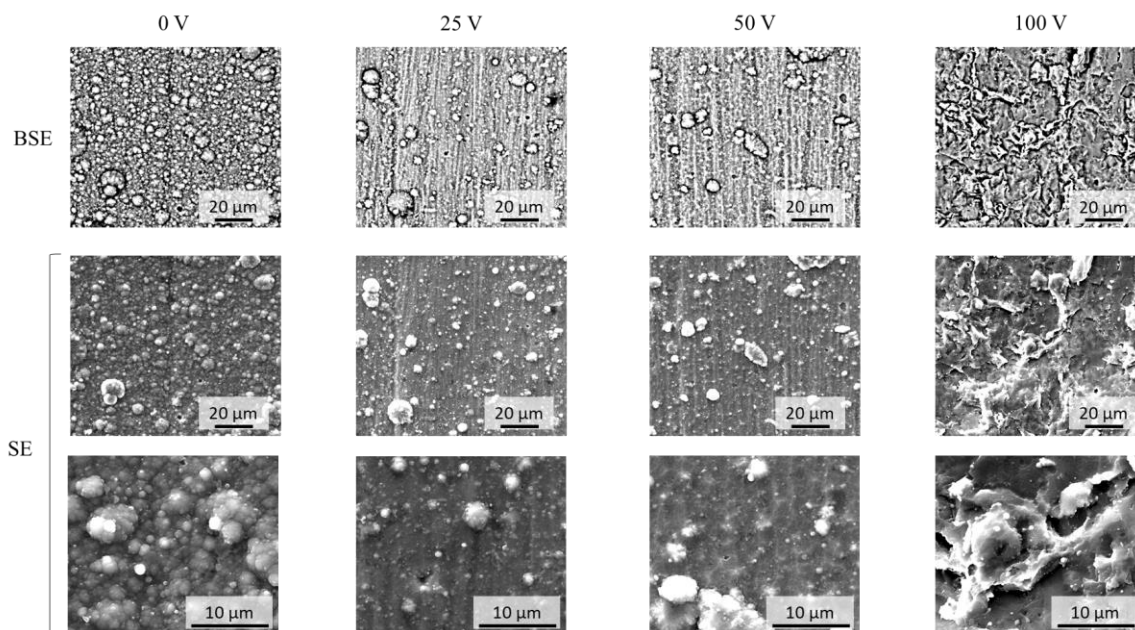
Figure 3-11. Scanning electron microscopy images of coating surfaces taken using two different imaging modes: backscattered electron (BSE) and secondary electron (SE). Deposition process was performed with four different substrate biases: 0 V, 25 V, 50 V and 100 V.

Figure 3-12 shows cross-sectional SEM-BSE images of TiAlN coatings deposited with four different substrate bias values of 0 V, 25 V, 50 V and 100 V. The coating deposited with 0 V substrate bias exhibited a ~15 μm thickness and was adherent to the substrate but had a porous structure. The coating deposited with 25 V substrate bias had ~10 μm thickness and showed much less porosity compared to the coating deposited with 0 V substrate bias. Some crack-like features of 5-10 μm in length were observed within the coating indicating possible delamination at these regions. The coating deposited with 50 V substrate bias had a coating thickness in between that of coatings deposited with 0 V and 25 V substrate bias. Crack-like features were also observed in the 50 V deposited coatings with similar characteristics to the ones observed in coatings deposited with 25 V substrate bias, but no porosity was observed in this case. The coating deposited with

100 V substrate bias was very delicate most likely due to high intrinsic residual stresses. It exhibited longer cracks in the coating and delamination at regions closer to surface and decohesion of the coating. Because of excessive deformation on the coating surface, it is difficult to determine the exact thickness of the coating, but it was estimated to be ~5 μm. High resolution imaging results shows that to obtain successful coatings, the 50 V substrate bias is an optimum substrate bias value, providing smoother surface with minimum macroparticles, dense structure with minimum porosity and good adhesion with minimum delamination. Thus, this substrate bias was chosen.
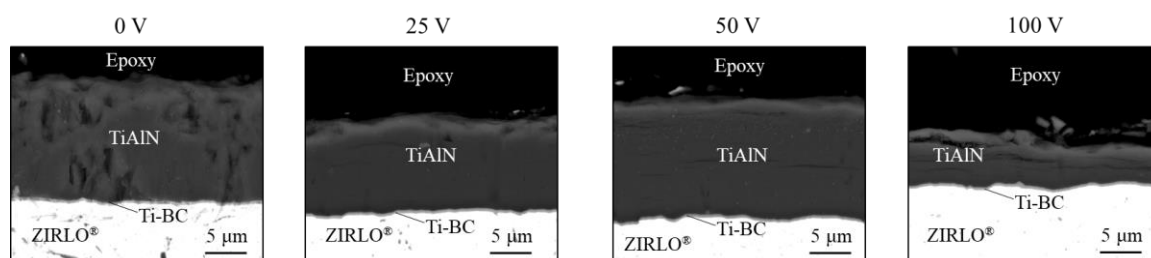
Figure 3-12. The cross-section SEM-BSE images of the TiAlN coatings deposited with four different substrate bias values of 0 V, 25 V, 50 V and 100 V.

Figure 3-13 shows the coating thicknesses measured using ImageJ. The average coating thickness values were determined from 15 measurements. The average TiAlN coating thicknesses were determined to be 14.7 ± 0.5 μm, 11.2 ± 0.6 μm, 13.1 ± 1.5 μm and 3.9 ± 1.2 μm, respectively for the 0 V, 25 V, 50 V and 100 V conditions. The large error bar for the coating deposited with 100 V substrate bias originated from coating deformation during sample preparation. An approximate linear relationship is observed between the substrate bias and coating thickness, according to which as substrate bias increased, coating thickness decreased.
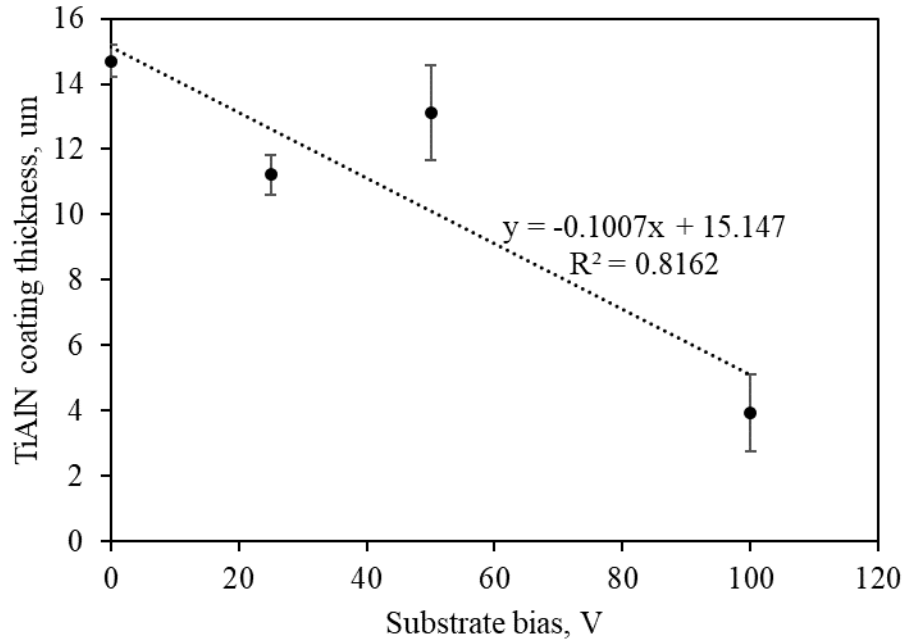
Figure 3-13. TiAlN coating thickness variation with the substrate bias value used during the deposition process.

Figure 3-14 shows the average coating chemical composition determined by energy dispersive spectroscopy (EDS). The sample chemical composition was measured from five different locations from the middle of the coating thickness. The data presented in the Figure 3-14 represents the average of 5 measurements. The composition variation with substrate bias was very slight (Nitrogen content decrease with increasing substrate bias, but within the standard deviation). Titanium, aluminum and nitrogen compositions are 8.5±0.38 at.%, 32.7±0.38 at.% and 56.9±2.1 at.% on average. Thus, aluminum composition is ~4 times greater than the titanium composition, which is reasonable considering the cathode composition used during the coating deposition process, which was 20 at. % Ti - 80 at.% Al.
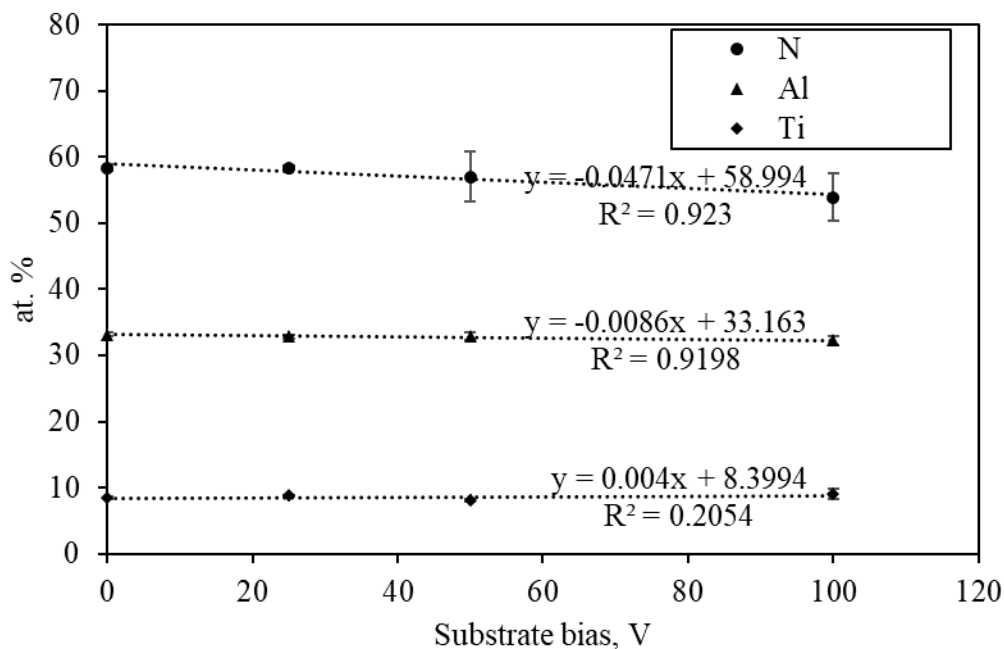
Figure 3-14. The TiAlN coating chemical composition variation based on the substrate bias used during the deposition process.

Figure 3-15 shows the overlaid GIXRD measurement patterns of coatings deposited with 0 V, 25 V, 50 V and 100 V. GIXRD was performed using Cu-Kα radiation with a grazing incidence angle of 1°. Peak identification was performed using JADE software. Most of the peak patterns were fitted with the $Ti_{0.32}Al_{0.68}N$ phase diffraction pattern data shown in yellow (in the caption) having the ICDD-PDF# 04-017-4686, which is a hexagonal crystal structure. There was peak shifting. Some peaks shifted to higher angles indicating compressive stresses as expected. There are also some peaks shifting towards lower angles which is attributed to the compressive strains in normal direction but elongation parallel to the coating surface due to the Poisson's ratio [153]. The diffraction peaks were relatively broad indicating nanocomposite coating structure. With increased substrate bias, the peaks became broader, indicating decreased sample crystallinity. Other peaks were identified as $Ti_{0.5}Al_{0.5}N$ (ICDD PDF# 04-005-5251) and AlN (ICDD PDF# 04-004-4544). $Ti_{0.5}Al_{0.5}N$ has a cubic crystal structure and AlN has a hexagonal

crystal structure. X-ray diffraction examination of the coating shows evidence of both the cubic and hexagonal phases.
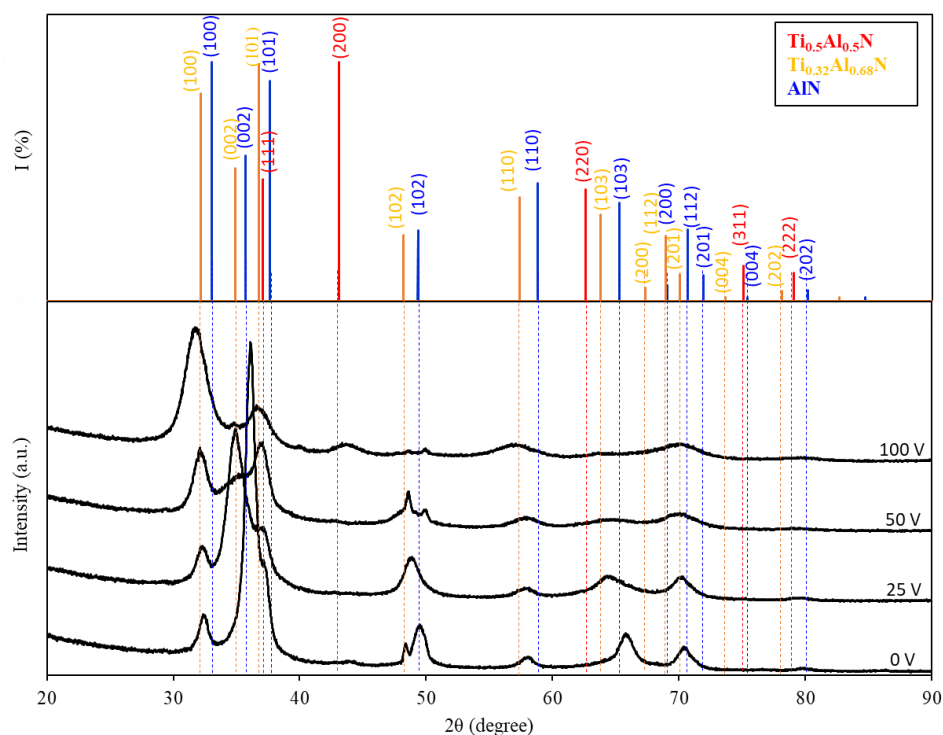
Figure 3-15. GIXRD measurement patterns of coatings deposited with 0 V, 25 V, 50 V and 100 V. GIXRD was performed using a Cu-Kα (1.54048 Å) radiation and with a grazing incidence angle of 1°.

The coating adhesion performance of coatings deposited with different substrate biases of 0 V, 25 V, 50 V and 100 V was evaluated by comparing the critical load to start gross spallation in each of the coatings. Figure 3-16 shows the SEM backscatter electron images of the failure progress during the scratch testing. For TiAlN coating deposited with 0 V substrate bias, scratch test progressed through parallel crack formation, angular crack formation and finally recovery spallation towards the end of the scratch testing without gross spallation even at the maximum loading of 48.5 N. For TiAlN coating deposited with 25 V substrate bias, three main deformation mechanisms were observed through the scratch. Lateral cracks started to form at 3 μm scratch length and 13.1 N load. Second deformation mode was the buckling spallation that started to occur at 5.9 μm scratch length and 26.9 N load. Simultaneously, recovery spallation was initiated

at the two edges of the scratch. Finally, gross spallation of the coating, i.e. critical load to start

spallation, occurred at 8.4 µm scratch length and 38.7 N load.
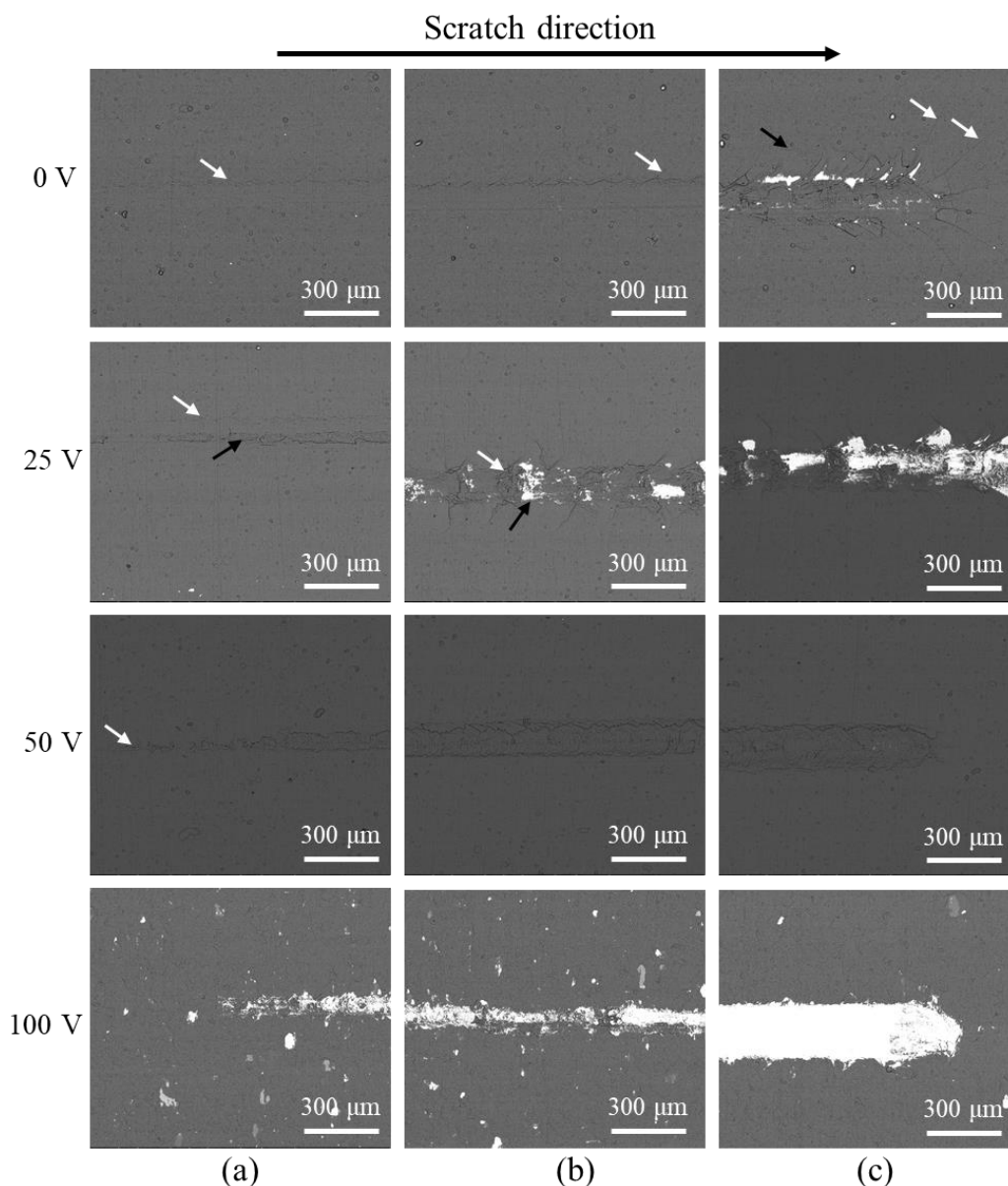
Figure 3-16. SEM backscatter electron images of the failure progress during the scratch testing performed on sample having a TiAlN coating deposited with 0 V, 25 V, 50 V and 100 V negative substrate bias, 60 A source current, cathode with 20 at.% Ti – 80 at.% Al. For 0 V: (a) parallel cracks (white arrow), (b) angular cracks (white arrow), (c) recovery spallation (black arrow) and angular cracks (white arrows). For 25 V: (a) parallel cracks (white arrow) and spallation (black arrow), (b) buckling spallation (white arrow), recovery spallation and chipping (black arrow), (c) transverse cracks, crushed fragments and gross spallation. For 50 V: (a) minor spallation (white arrow), (b) buckling cracking, (c) no gross spallation. For 100 V: (a) chipping, (b) transverse cracks, (c) gross spallation.

In the case of TiAlN coating deposited 50 V, coating spallation was not observed even at maximum load of 47.9 N. For the coating deposited with 100 V substrate bias, critical load to cause spallation was determined to be 2.9 N.

3.2.2. Corrosion testing and post-corrosion testing observations

3.2.2.1. Differential scanning calorimetry (DSC) and thermogravimetric analysis (TGA)

Differential scanning calorimetry (DSC) and thermogravimetric analysis (TGA) were performed to determine the oxidation initiation temperature of ZIRLO®, TiN and TiAlN in air atmosphere. Measurement and analysis were conducted as described in Section 2.5.3. Tested samples were uncoated flat ZIRLO®, TiN coated ZIRLO® involving a titanium bond coating and TiAlN coated ZIRLO® involving a titanium bond coating. The cathode composition used to deposit the TiAlN layer was 33 at.% Ti - 67 at.% Al. Samples with a 0.5 cm diameter were cut from uncoated ZIRLO®, TiN coated ZIRLO® (TIN/Ti/ZIRLO®) and TiAlN coated ZIRLO® (TiAlN/Ti/ZIRLO®) to fit into the crucible of the DSC/TGA measurement instrument. Figure 3-17a shows the digital images of the TiN and TiAlN coated ZIRLO samples before and after differential scanning calorimetry and thermogravimetric analysis. The TiN coated sample had a gold color whereas the TiAlN sample had a gray color prior to DSC (Figure 3-17a). After testing, both samples were excessively oxidized, turning almost completely into white powder. The temperature for the initiation of oxidation was determined from the intersection of the reaction peak starting point tangent line with the extended DSC curve as described in ASTM E2009.

Figure 3-17b shows the results of differential scanning calorimetry (DSC) experiments performed on uncoated ZIRLO®, TiN/Ti/ZIRLO® and TiAlN/Ti/ZIRLO® samples. DSC analysis was conducted with manually drawn tangent lines and as shown in Figure 3-17b, the oxidation

onset temperatures were determined to be ~999°C, ~1050°C and ~1133°C for ZIRLO®, TiN and TiAlN, respectively. In the case of TiN and TiAlN coated sample DSC curves, two different slopes were observed. The oxidation onset temperatures determined from the location of the minimum slope on the curve were 1007°C and 1000°C for TiN coated and TiAlN coated samples, respectively. The reason of these values is the existence of ZIRLO® as the substrate material, which started to oxidize before coating oxidation. This is because the substrate was in contact with the air in the chamber since the coating was removed from the edges during the cutting process, which was performed to prepare the samples for the DSC an TGA analysis.

Figure 3-17c shows the results of thermogravimetric analysis (TGA) performed on uncoated ZIRLO®, TiN/Ti/ZIRLO® and TiAlN/Ti/ZIRLO® samples. All three samples had a weight gain of ~34% which was attributed to the ZIRLO® oxidation. The weight change % decrease that occurred towards the end of the TGA analysis in the case of ZIRLO® sample (starred in Figure 3-17c) occurred because ZIRLO® sample was completely covering the crucible bottom surface and touching the inner wall of the crucible, and it crumbled with a burst due to increased thermal expansion stresses at higher temperatures in the crucible. The burst caused some sample to fall from the crucible which is observed as the weight loss. According to the oxidation onset point analysis, the oxidation onset temperatures were determined to be ~995°C, ~1043°C and ~1108°C for ZIRLO®, TiN and TiAlN, respectively. Oxidation onset temperatures determined from TGA data are slightly different from the temperatures determined from the DSC data. Considering that the DSC and TGA data were collected simultaneously from the same samples, the slight difference between the oxidation onset temperatures was attributed to the preciseness of the manually drawn tangent lines and ignored. Overall, DSC and TGA data supported each other in terms of reaching to the conclusion of TiN and TiAlN coatings are helpful in postponing oxidation initiation temperature in air atmosphere.

(a)

	TiN/Ti/ZIRLO®	TiAlN/Ti/ZIRLO®
Before		
After		

(b)
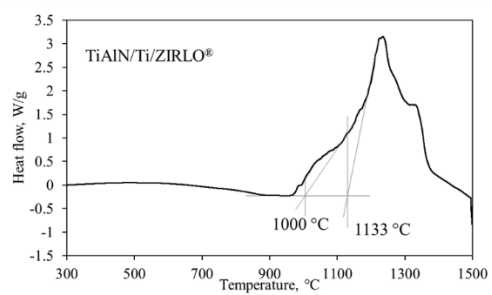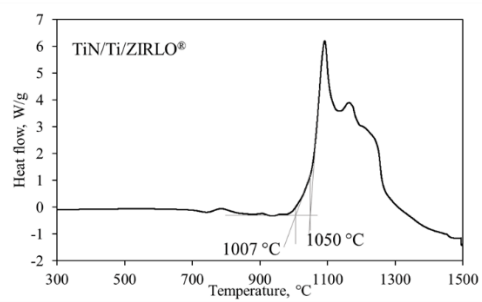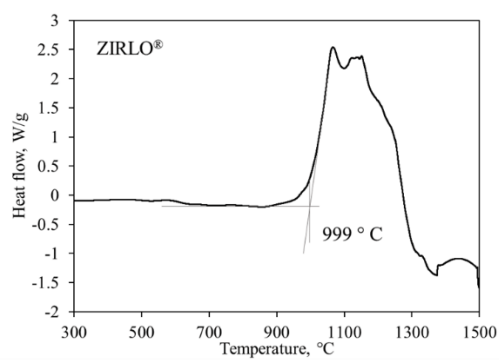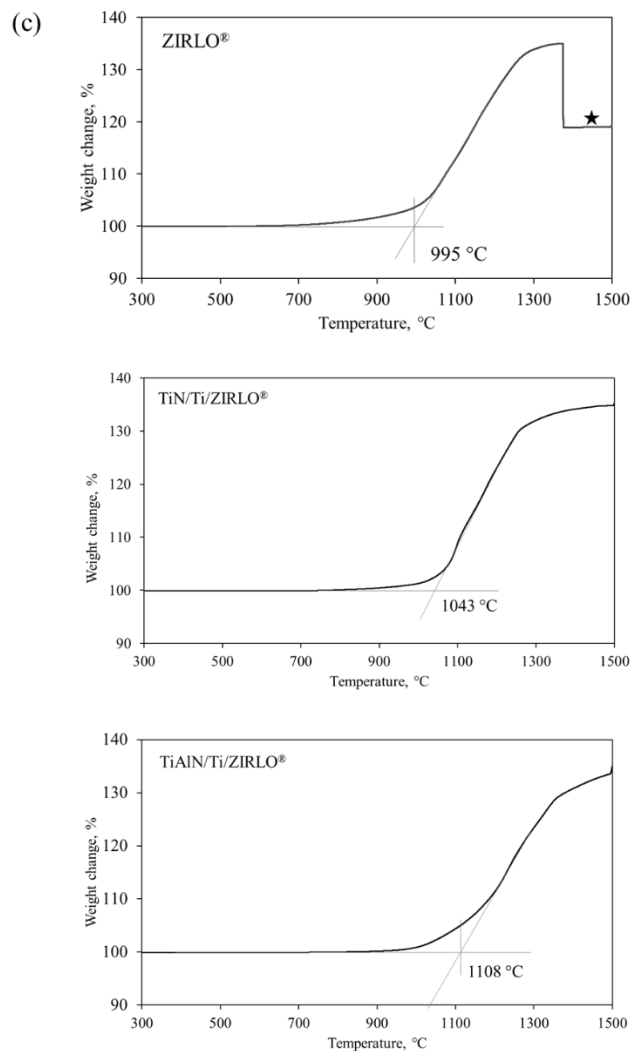
Figure 3-17. (a) Digital images of the TiN and TiAlN coated ZIRLO samples before and after the simultaneous differential scanning calorimetry and thermogravimetric analysis (SDT) performed up to 1500°C. (b) Differential scanning calorimetry and (c) thermogravimetric analysis (TGA) ZIRLO®, TiN coated ZIRLO® and TiAlN coated ZIRLO®.

3.2.2.2. Autoclave testing in static pure water at 360°C and 18.7 MPa for 3 days

Autoclave testing of single-layer TiAlN and single-layer TiN coated ZIRLO® sheets was performed at Westinghouse in static pure water at 360°C and 18.7 MPa pressure up to 3 days according to the ASTM G2 standard as described in Section 2.5.1. Single-layer TiAlN and single-layer TiN coatings deposited on ZIRLO® sheets for autoclave testing were prepared to investigate

the effects of (i) titanium bond coating (Ti-BC) thickness, (ii) substrate surface roughness, (iii) coating thickness, (iv) substrate bias and (v) nitrogen partial pressure on the corrosion performance of the coated material. Table 3-4 shows the summary of the parameters investigated. Substrate surface preparation was performed by SiC hand grinding as described in Section 2.2. Substrate surface roughness values presented in Table 3-4 were determined using profilometry after substrate surface preparation prior to the coating deposition. The Ti-BC was deposited in an argon atmosphere using a pure titanium cathode with 150 V substrate bias and 65 A arc current. After Ti-BC deposition, either single-layer TiAlN or single-layer TiN coating was deposited. TiAlN layer deposition was performed in nitrogen atmosphere using the 33 at.%Ti – 67 at.% Al cathode with 60 A arc current. TiN layer deposition was performed in nitrogen atmosphere using the pure titanium cathode with 150 V substrate bias and 65 A arc current. The possibility of varying coating thickness by controlling the deposition time was demonstrated in Section 3.2.1.2. Accordingly, Ti-BC and TiAlN coating thickness were varied through deposition time adjustment. The as-deposited coating thickness values presented in Table 3-4 were determined by scanning electron microscopy imaging of the coated sample cross-sections. Cross-section samples were prepared according to the procedure described in Section 2.6.1 and examined as described in Section 2.6.2.

The corrosion behavior was investigated and determined through visual examination, weight gain analysis, high resolution imaging, phase identification and compositional inspection. The weights of the coated samples before the corrosion test and after the corrosion test were measured, and the difference between these two values indicate the change that is caused by the corrosion test. If the oxide layer forming on the surface after the corrosion test stays on the surface of the sample after the corrosion process, a weight gain is expected. If the oxide formed after the corrosion test does not stay on the surface (i.e., if spallation occurs), then a lower weight, in other words negative weight gain, can be observed. Weight gain analysis is not enough to evaluate the corrosion behavior on its own, but it provides an estimate of the corrosion

performance of the coating. In this section, weight gain data is presented in groups depending on

the investigated parameter.

Table 3-4. Cathodic Arc Physical Vapor Deposition Parameters for TiAlN and TiN coating
fabrication

Coating	Ra (µm)	Coating Thickness (µm)	Deposition time (BC/TC) (min)	Substrate Bias (BC/TC)	N_2 partial pressure (Pa)	Varying Parameter
TiAlN	0.100	~4	8/112.5	150/50	1.6	TiAlN = 4 µm Ra = 0.1 µm
TiAlN	0.250	~4	8/112.5	150/50	1.6	TiAlN = 4 µm Ra = 0.25 µm
TiAlN	0.500	~4	8/112.5	150/50	1.6	TiAlN = 4 µm Ra = 0.5 µm
TiAlN	0.875	~4	8/112.5	150/50	1.6	TiAlN = 4 µm Ra = 0.875 µm
TiAlN	0.100	~8	8/225	150/50	1.6	TiAlN = 8 µm Ra = 0.1 µm
TiAlN	0.250	~8	8/225	150/50	1.6	TiAlN = 8 µm Ra = 0.25 µm
TiAlN	0.500	~8	8/225	150/50	1.6	TiAlN = 8 µm Ra = 0.5 µm
TiAlN	0.875	~8	8/225	150/50	1.6	TiAlN = 8 µm Ra = 0.875 µm
TiAlN	0.100	~12	8/450	150/50	1.6	TiAlN = 12 µm Ra = 0.1 µm
TiAlN	0.250	~12	10/450 8/225	150/50	1.6	TiAlN = 12 µm Ra = 0.25 µm
TiAlN	0.500	~12	8/450	150/50	1.6	TiAlN = 12 µm Ra = 0.5 µm
TiAlN	0.875	~12	8/450	150/50	1.6	TiAlN = 12 µm Ra = 0.875 µm
TiAlN	0.250	~13	6/450	150/50	1.6	Ti BC-0.2 µm
TiAlN	0.250	~14	8/450	150/50	1.6	Ti BC-0.4 µm
TiAlN	0.250	~12	10/450	150/50	1.6	Ti BC-0.6 µm
TiAlN	0.250	~14	15/450	150/50	1.6	Ti BC-0.8 µm
TiAlN	0.250	~12	8/450	150/50	1.9	slightly increased N_2 pressure
TiAlN	0.250	~12	8/450	150/100	1.9	increased substrate bias to 100 V and N_2 pressure
TiN	0.250	~12	8/370	150/150	1.6	Composition (TiN)

*BC=bond coat, TC=Top coat

Before coating deposition, the substrate surface must be prepared by grinding the surface

to remove native oxides that might degrade coating adhesion and to achieve adequate surface

roughness that is rough enough to provide more surface area to achieve more bonding and mechanical interlocking between the substrate and the coating, while remaining smooth enough to avoid unfilled valleys at the substrate and coating interface [154]. The effect of substrate surface roughness on the TiAlN coating durability was investigated through examination of four different substrate surface roughness values (0.100, 0.250, 0.500 and 0.875 μm R_a). The substrate surface roughness is represented with R_a because considered values are the arithmetic average values of peaks and valleys. Figure 3-18 shows cross-sectional scanning electron microscopy (SEM) backscattered electron (BSE) images of samples having substrate surface roughness of 0.25 μm R_a and 0.875 μm R_a. In the case of 0.875 μm R_a, unfilled valleys were observed, indicating too high of a substrate surface roughness. Thus, there is an optimum substrate surface roughness value that can provide good adhesion between the substrate and coating and this was investigated through corrosion testing.
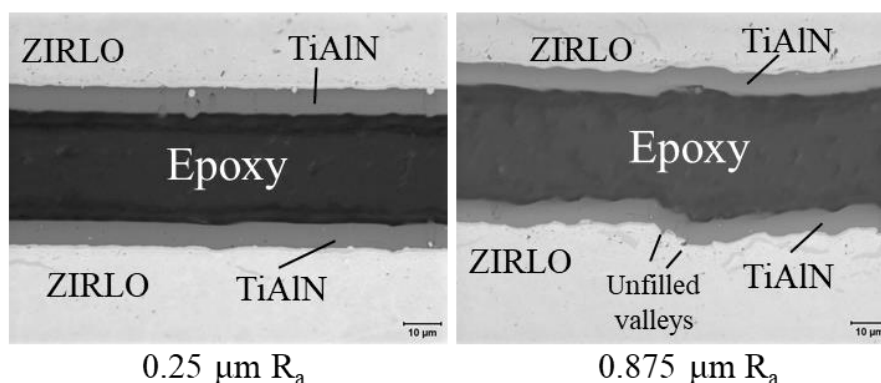
Figure 3-18. Cross-sectional SEM-Back scattered electron images of as-deposited samples having monolithic TiAlN coating with a substrate surface roughness values of 0.25 μm R_a and 0.875 μm R_a.

Figure 3-19 shows digital images of 4 μm thick TiAlN coated ZIRLO® sheets having surfaces prepared to different substrate surface roughness values before and after corrosion testing. These digital images were selected as an example to present visually observable changes that occur during the corrosion test. The as-deposited samples showed coatings with a shiny silver surface. After the corrosion test, the coating colors changed to a mixture of matte gray and

white regions. This color change is likely related to the oxidation of the coated surface. As expected, uncoated regions (where the substrate was held during deposition) showed a different corrosion appearance compared to the rest of the coated surface.
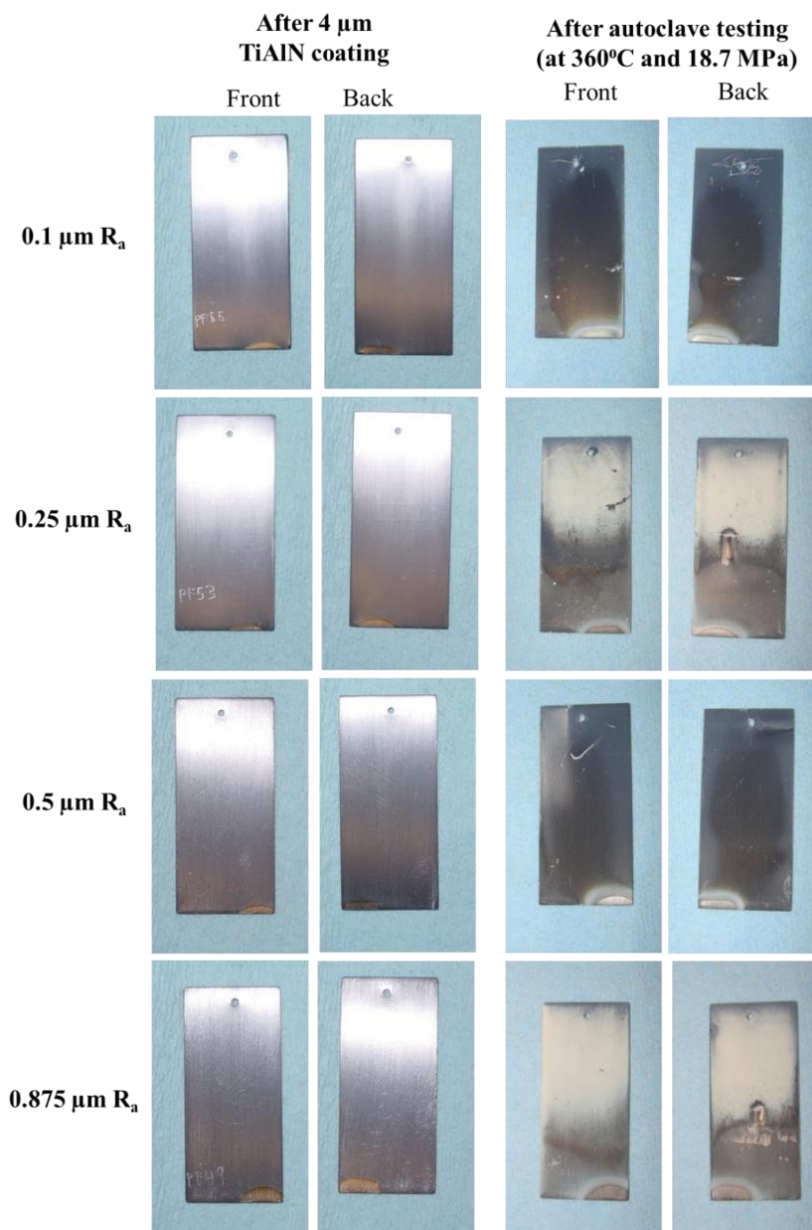
Figure 3-19. Digital images of as-deposited and autoclave tested 4 μm TiAlN/Ti/ZIRLO® sheets having substrate surface roughness values of 0.1, 0.25, 0.5 and 0.875 μm R_a, as indicated.

TiAlN coating thickness optimization is also important since cathodic arc physical vapor deposition process introduces intrinsic compressive stresses which can often exceed the

interfacial adhesion strength of the coating leading to a lower critical load for spallation. The TiAlN coating thicknesses that were considered involved 4, 8 and 12 μm, which were achieved through deposition durations of 112.5, 225 and 450 min, respectively. Figure 3-20 shows the weight gain data obtained with respect to four different ZIRLO® substrate surface roughness values of 0.1, 0.25, 0.5 and 0.875 μm R_a, and three different TiAlN coating thickness values of 4, 8 and 12 μm. In this case, one sample corresponding to each property value was tested. Among tested samples, a combination of substrate surface roughness of 0.25 μm R_a and a coating thickness of 12 μm provided the minimum positive weight gain without spallation as confirmed through visual observation. As a result, this combination was chosen as the optimum design for enhanced coating adhesion.
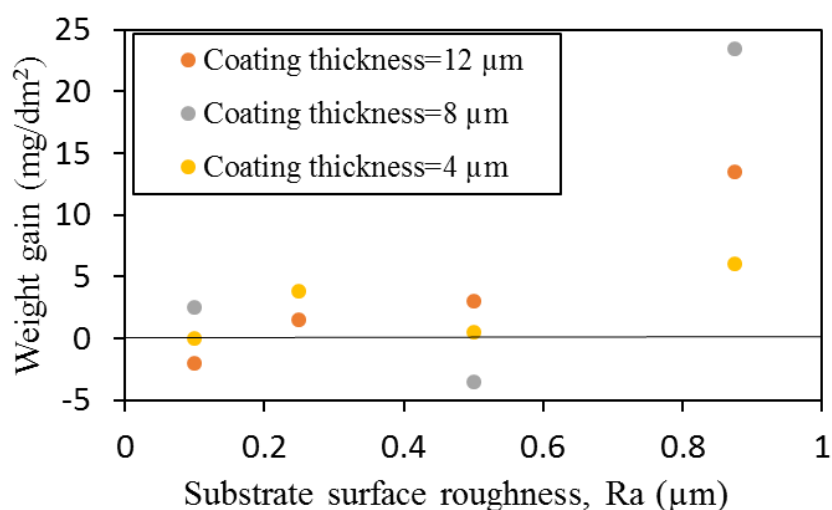
Figure 3-20. Sample weight gain data after autoclave test exposure at 360ºC and 18.7 MPa for 3 days with respect to ZIRLO® substrate surface roughness and TiAlN coating thickness values. The combination of a 0.25 μm R_a substrate surface roughness and a 12 μm top coat layer thickness provided the optimum coating characteristics to obtain best adhesion among investigated samples.

Figure 3-21 shows the weight gain observed after autoclave testing of ~13 μm TiAlN coated ZIRLO® sheets having titanium bond coating at four different thicknesses of 0.2, 0.4, 0.6 and 0.8 μm between the ZIRLO® substrate and the single-layer TiAlN coating. The titanium bond coating has a fundamental role in enhancing the coating adhesion by dissolving the native oxides

remaining on the substrate surface prior to the coating deposition and by balancing intrinsic stresses between the coating and the substrate that originate from the production process or extrinsic stresses originating from temperature variations. To determine the optimum titanium bond coating thickness, four different Ti-BC thickness values of 0.2, 0.4, 0.6 and 0.8 μm were investigated. One sample each was tested for 0.2, 0.4 and 0.8 μm Ti-BC thickness whereas four samples were tested for 0.6 μm Ti-BC. The coating deposition rate was kept between 0.03-0.05 μm/min such that deposition times of 6, 8, 10 and 15 min yielded Ti-BC thickness values of 0.2, 0.4, 0.6 and 0.8 μm, respectively. The TiAlN deposition parameters were kept fixed leading to a TiAlN of ~13 μm thickness to be able to investigate the Ti-BC thickness effect individually. Although almost all of the coatings were deposited with the indicated parameters, during the 0.8 μm Ti-BC layer deposition, a substrate bias drop to 0 V was experienced, which might have degraded the coating density. Two uncoated ZIRLO® sheets were included in the test as a reference for the evaluation of the TiAlN coated ZIRLO® corrosion performance. As shown in Figure 3-21, after 3-day autoclave testing, the uncoated ZIRLO® sheet showed an average weight gain of 14.4 mg/dm^2. The coated samples with 0.2 and 0.4 μm Ti-BC showed negative weight gain, which means that they lost weight during the test indicating coating spallation. The weight loss of the 0.4 μm Ti-BC sample was slightly higher than that of the 0.2 μm Ti-BC sample, indicating either more coating spallation in the case of 0.4 μm Ti-BC sample or excessive coating spallation in the case of 0.2 μm Ti-BC sample assisted with ZIRLO® oxidation which led to a slight increase in weight gain. Sample having a 0.8 μm Ti-BC showed positive weight gain, which can either mean coating oxidation without any coating spallation or coating oxidation with some spallation. This can only be resolved through visual examination. The average weight gain of the samples having 0.6 μm titanium bond coating thickness was ~3 mg/dm^2, was similar to that of samples having a titanium bond coating thickness of 0.8 μm. During visual examination, minor spallation was observed in the case of 0.8 μm Ti-BC, which can possibly be attributed to the substrate bias drop which occurred during deposition. The 0.6 μm Ti-BC samples did not show

any spallation on their surface and had an average weight gain equal to ~20% of the uncoated

ZIRLO®, which suggests significant corrosion protection. Thus, 0.6 µm Ti-BC was chosen as the

optimum Ti-BC thickness value to achieve adhesion between the ZIRLO® substrate and the

TiAlN coating.
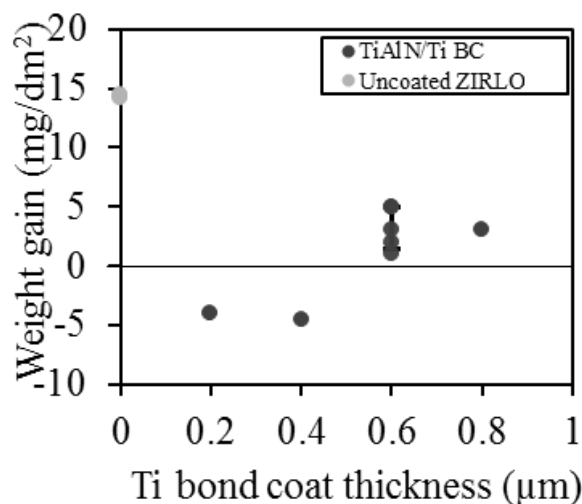
Figure 3-21. Sample weight gain data after autoclave test exposure at 360ºC and 18.7 MPa for 3 days with respect to Ti bond coat thickness with TiAlN (~13 µm thickness) top coating.

In addition to the titanium bond coating thickness, substrate surface roughness and TiAlN

coating thickness effects, substrate bias and nitrogen partial pressure effects on the coating

adhesion and coating corrosion performance were also investigated. In this case, two different

substrate bias values (50 and 100 V) and two different nitrogen partial pressure (1.6 and 1.9 Pa)

were used to investigate the effect of bias and nitrogen partial pressure on coating adhesion and

corrosion performance. Additionally, TiN coating corrosion performance was also investigated.

The effect of variation of select coating deposition parameters on weight gain is shown in Table

3-5, and the resultant weight gain data is presented in Figure 3-22. As mentioned in the previous

paragraph, uncoated ZIRLO® exhibited a weight gain of 14.4 mg/dm^2 after 3 days of autoclave

testing. The increase in nitrogen partial pressure to 1.9 Pa resulted in a higher average weight gain

value of 17 mg/dm^2, which is much larger than that measured on the sample having the same

coating thickness and surface roughness but deposited with 1.6 Pa N_2 pressure. The data presented in Table 3-5 also showed that increased substrate bias slightly improved corrosion resistance of the layers, resulting in a lower weight gain of 10.1 mg/dm^2. As shown in Figure 3-22, TiN showed the lowest average weight gain of 1.2 mg/dm^2 among the samples studied after the autoclave test, with no delamination. This result corresponding to a significant improvement in the corrosion resistance of the coated material relative to the uncoated substrate. In summary, an increase in nitrogen partial pressure showed a slight reduction in corrosion performance for the deposition conditions studied. An increase in substrate bias slightly improves corrosion resistance, but the magnitude of the change is less than that effected by a change in nitrogen partial pressure for the deposition conditions studied.

Table 3-5. Weight gain data after autoclave testing at 360 °C and 18.7 MPa for 3 days samples having TiAlN coatings deposited with various substrate biases and nitrogen gas partial pressures that were.

Coating	Substrate Bias (BC/TC)	N$_2$ partial pressure (Pa)	Weight gain (mg/dm^2)
TiAlN	150/50	1.6	1.5
TiAlN	150/50	1.9	17
TiAlN	150/100	1.9	10.1
No coating	N/A	N/A	14.4
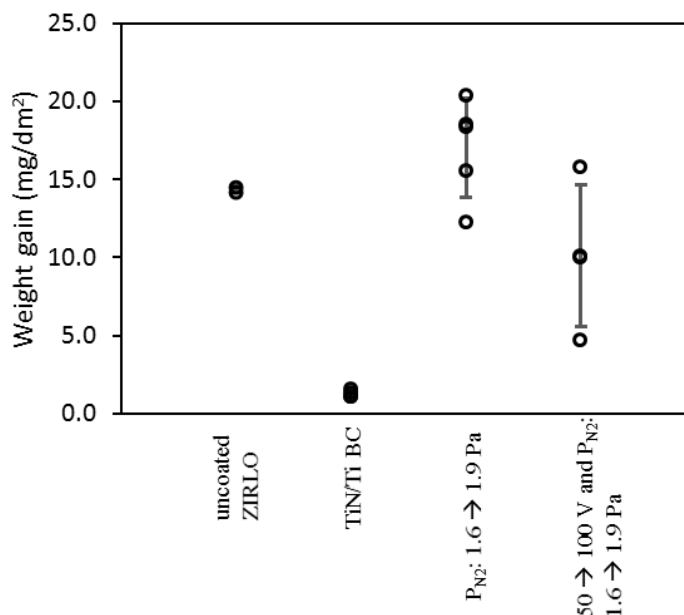
Figure 3-22. Weight gain data of samples that were autoclave tested at 360 °C and 18.7 MPa for 3 days having TiAlN and TiN coatings deposited with various substrate biases (50 V and 100 V) and nitrogen gas partial pressures (1.6 and 1.9 Pa).

Phase identification of the uncoated ZIRLO®, TiAlN coated and corrosion layers formed on corrosion tested samples were performed using X-ray diffraction (XRD) Bragg Brentano (BB) measurement using Cu K$_\alpha$ radiation. Figure 3-23 shows the overlaid XRD-BB patterns of uncoated flat ZIRLO® (Figure 3-23a), TiAlN coated ZIRLO® sheet (Figure 3-23b) and 3 days autoclave tested TiAlN coated ZIRLO® sheet (Figure 3-23c). The uncoated ZIRLO® XRD-BB scan was performed on as-received ZIRLO® sheet. The obtained XRD-BB patterns were identified using JADE software and the database. The peaks from the substrate material were identified as consistent with the hexagonal α-Zr phase (ICDD PDF# 00-005-0665). The higher intensity at (0002) plane compared to the reference pattern (ICDD PDF# 00-005-0665) means texturing during fabrication leading to higher percentage of basal poles aligned with the sample normal. The coating was identified to be $Ti_{0.5}Al_{0.5}N$ (ICDD PDF# 04-005-5251) having a cubic rocksalt structure with a lattice parameter of 0.42 nm. In the case of the 3-day autoclave tested

sample XRD-BB pattern, in addition to the α-Zr and $Ti_{0.5}Al_{0.5}N$ phases, anatase (TiO_2, ICDD PDF# 04-002-8296) and boehmite (AlO(OH), ICDD PDF# 00-021-1307) peaks were observed. The latter were attributed to the exposure to corrosive environment during autoclave testing.
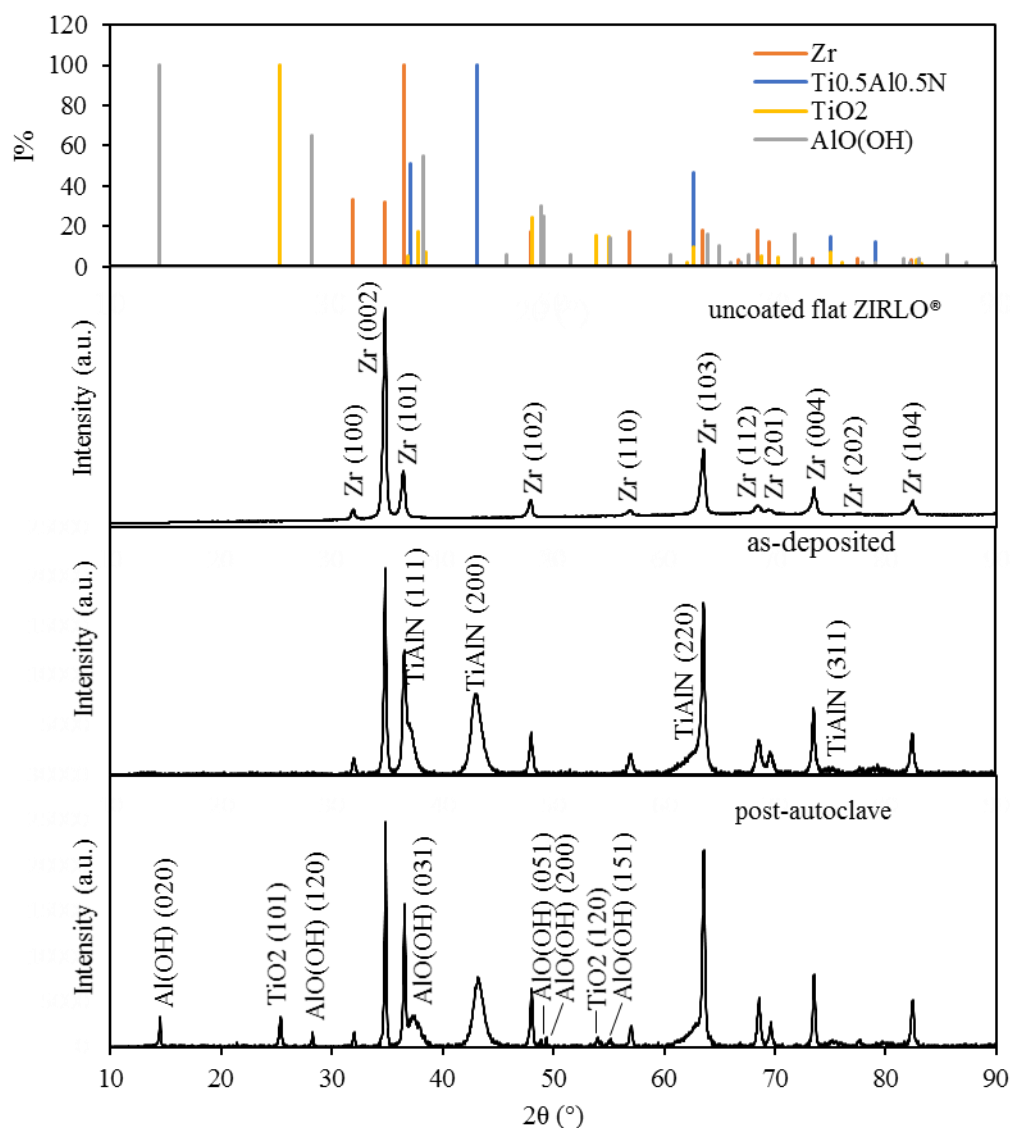
Figure 3-23. XRD Bragg Brentano (Cu $K_α$ radiation) patterns of uncoated ZIRLO®, as-deposited TiAlN coated ZIRLO®, and post autoclave testing of TiAlN coated ZIRLO® at 360ºC for 3 days.

In the as-coated XRD pattern, a slight shift to higher angles in the TiAlN peak was observed, possibly indicating compressive strains in the coating as has been previously observed for TiAlN coatings deposited by CA-PVD process [34]. Part of the stresses in the sample are

intrinsic residual stresses associated with the CA-PVD process, which are due to the higher energy of the ionic species bombarding the substrate during deposition. There are also stress contributions due to compositional variations and differences in thermal expansion. Thus, extrinsic residual stress (190 MPa) occurred upon cooling to room temperature from the deposition temperature (325ºC) and thermal expansion mismatch between the TiAlN and ZIRLO® as calculated for υ=0.23 [155] and E=406.5 [156]; which is tensile since TiAlN has a higher CTE than ZIRLO®. Additionally, there was a slight shift of the Zr peaks towards lower 2θ values, again possibly indicating tensile strains which is attributed to the balancing of the coating compressive strains. After the autoclave test, it was determined that TiAlN, anatase and most of the boehmite phase peaks shifted towards lower 2θ values as compared to the literature (unstressed) values, indicating tensile strains in the newly formed phases, possibly caused by strain relaxation because of aluminum depletion during autoclave testing and the extrinsic residual stress occurred upon cooling from the autoclave test temperature to room temperature which is determined to be 210 MPa (Calculations are provided in Appendix A). It is also possible that the peak shift is caused by variations in composition in the phases studied.

Figure 3-24 shows surface and cross-sectional SEM images performed on two different regions of a TiAlN coated ZIRLO® sample having a titanium bond coating thickness of 0.6 μm. Coating spallation was observed in some locations as shown in the SEM image of Figure 3-24a. Figure 3-24b shows a cross-section SEM-BSE image performed on a region corresponding to the spallation region. Poor substrate surface preparation quality was observed. Figure 3-24c shows the SEM-BSE image of a region where the TiAlN coating was remained adhered to the surface. Figure 3-24d shows the cross-section SEM-BSE image corresponding to this region. In contrast to Figure 3-24b, adequate substrate surface preparation was observed in this region. The spallation was thus attributed to poor substrate surface preparation. Accordingly, the weight gain data of the sample having spallation because of poor substrate surface preparation was excluded

from the weight gain data presented in Figure 3-21 for the evaluation of the Ti-BC thickness effect.
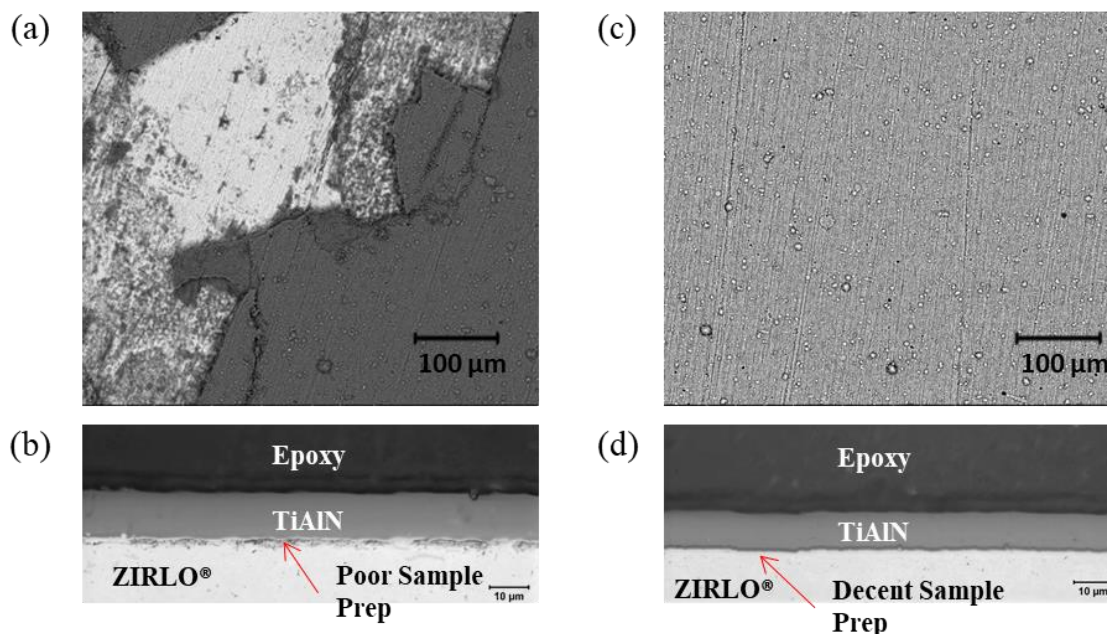
Figure 3-24. Surface (a and c) and cross-sectional (b and d) SEM-Back scattered electron images of autoclave tested 0.6 µm Ti-BC having samples with spallation (a and b) and without spallation (c and d). Cross-sectional analyses revealed that spallation at samples having 0.6 µm Ti-BC thickness was due to poor sample preparation.

High-resolution SEM imaging after autoclave testing for 3 days was performed using scanning electron microscopy (SEM)-backscattered electron (BSE) mode to understand the oxidation behavior of the coatings. Both surface and cross-sectional samples were examined. Figure 3-25a shows the surface SEM-BSE of a TiAlN coated and 3 days autoclave tested sample. The presence of the AlO(OH) (boehmite) phase that was initially detected in the XRD-BB pattern (Figure 3-23) was confirmed via the SEM analysis. The AlO(OH) phase was observed as non-uniformly distributed crystals on the sample surface with sizes ranging between 1-10 µm.

Figure 3-25b shows a cross-section SEM-BSE image of a 12 µm TiAlN coated ZIRLO® sheet. The image confirms the intact structure of the Ti-BC and uniform thickness, as the TiAlN

coating remained adherent to the surface after the autoclave testing. No substrate oxidation was observed demonstrating the contribution of the TiAlN coating in enhancing the ZIRLO® corrosion performance. Additionally, an ~4 μm thick darker (lower atomic number) region was observed close to the outer surface of the TiAlN coating after autoclave testing. This darker region indicates a compositional variation compared to the rest of the TiAlN coating. The cause of it was investigated using energy dispersive spectroscopy and the results are presented later in this section.

Figure 3-25c presents the cross-sectional SEM-BSE image of 4 μm TiAlN coated sample after the autoclave testing. No substrate oxidation was observed. The formation of AlO(OH) crystals of various sizes on the surface was confirmed with this SEM-BSE image. However, the dark region with compositional variation mentioned above was not observed.
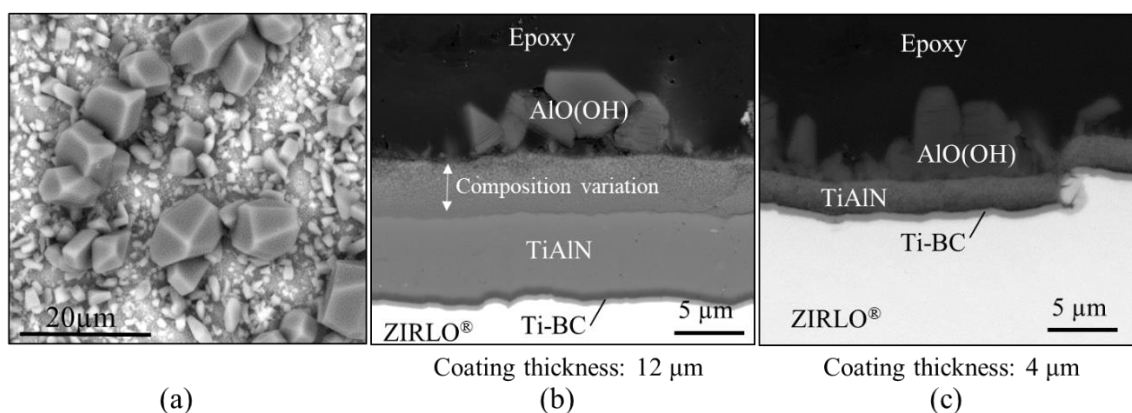
Figure 3-25. Scanning electron microscopy (SEM)- backscattered electron (BSE) images of (a) TiAlN coated and 3-day autoclave tested surface, (b) 12 μm TiAlN coated and 3-day autoclave tested sample cross-section and (c) 4 μm TiAlN coated and 3-day autoclave tested sample cross-section. SEM analyses showed a composition variation at ~4 μm region after oxidation leading to degradation of 4 μm coated samples.

Energy dispersive spectroscopy (EDS) was performed on the compositional variation region of the cross-section of the 12 μm TiAlN coating sample. Figure 3-26a shows the EDS maps obtained showing the distribution of aluminum, titanium, nitrogen, oxygen and zirconium. The ZIRLO® substrate region was observed in the zirconium map (last map) as expected. The

titanium bond coating is observed as a dense layer of ~1 μm at the interface of the ZIRLO®

substrate and the coating. The TiAlN coating was confirmed to be composed of titanium,

aluminum and nitrogen. The outer 4 μm of the coating showed aluminum depleted region,

suggesting aluminum migration to the outer surface and reacting with oxygen and hydrogen to

form the boehmite phase.

Figure 3-26b shows an EDS line scan performed starting from the AlO(OH) crystal

towards the ZIRLO® substrate. The EDS line scan confirmed the EDS map analysis observations

and showed oxygen penetration through the coating terminating before reaching the substrate.

In summary, weight gain occurred in TiAlN coated samples during high temperature and

high-pressure water corrosive environment exposure, which was attributed to the AlO(OH) and

TiO_2 formation. Since the aluminum depletion from a ~ 4 μm deep layer in the coating, studies

focused on thicker coatings, such as those having 12 μm thickness which could maintain ~2/3 of

the coating intact after oxidation.
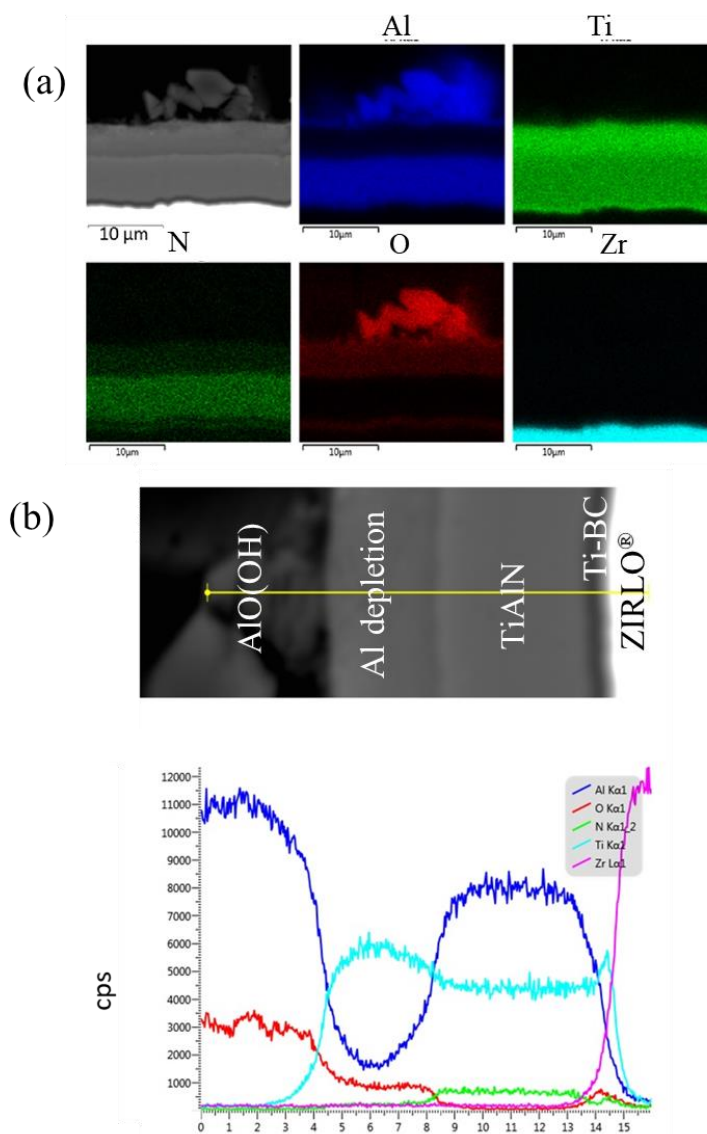
Figure 3-26. EDS analyses of TiAlN coated ZIRLO® samples with 0.875 µm surface roughness after the autoclave test at 360ºC for 3 days, (a) EDS-elemental map analysis showing Al, Ti, N, O and Zr, and (b) EDS-line scan showing Al, Ti, N, O and Zr elemental concentrations. Al is shown to have migrated from the top 4 µm TiAlN layer.

Figure 3-27 shows a scanning electron microscopy (SEM) image performed on a TiN coated and autoclave tested sample. Figure 3-27a shows the surface SEM image of the autoclave tested TiN coated sample. Some macroparticles and a texture mirroring the substrate surface were observed in the SEM surface image. Compared to the corrosion tested TiAlN coatings, the primary difference was the lack of AlO(OH) crystals observe on the surface due to the lack of Al

content in the coating. Instead, TiO_2 formation was detected on the surface which was confirmed with XRD analysis. Accordingly, the weight gain of 1.5 mg/dm^2 observed in this sample was attributed to TiO_2 formation. Cross-section analysis presented in Figure 3-27b confirmed that a uniform, intact TiN coating was maintained on the surface and no ZIRLO® substrate oxidation occurred. This suggests that TiN is a strong candidate to enhance the corrosion resistance of the ZIRLO® substrate.
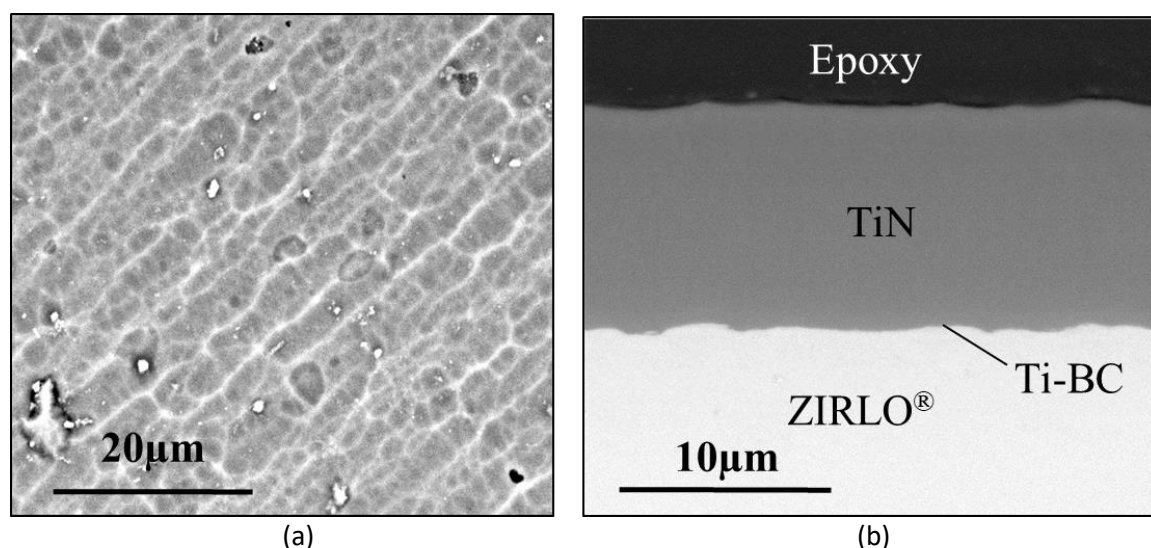
Figure 3-27. SEM- Back Scattered Electron (BSE) images of TiN/Ti/ZIRLO® (0.25 µm R_a) sample that was autoclave tested at 360 °C and 18.7 MPa for 3 days; (a) surface, and (b) polished cross-section. As shown by the polished cross-sectional images, no boehmite phase is detected on the surface of the TiN coated sample.

3.3. Multilayer TiN/TiAlN coating design architecture optimization on ZIRLO® sheets

Based on the coating corrosion performance data presented in the previous sections, a multilayer structure was considered to benefit from oxidation performance of both TiAlN and TiN layers, avoid boehmite formation at normal nuclear reactor operation temperatures, avoid crack propagation and achieve successive corrosion barrier at each layer. The optimum multilayer coating design that would provide the enhanced corrosion resistance was developed through

coating design architectures involving number of layer variation, layer thickness variation and composition grading. The corrosion performance of different coating architectures was evaluated through corrosion tests for up to 90 days in standard condition and also through supercritical water test that was performed in autoclave at University of Michigan in deaerated water at 542°C and 24.5 MPa. Corrosion tests also involved scratched samples to investigate the effect of initial scratching on the subsequent corrosion performance of the coating.

Table 3-6 lists the multilayer TiN/TiAlN coating designs investigated in this study. To compare the corrosion performance of various multilayer coating design, uncoated ZIRLO® and single layer TiN were also tested as a reference. Both sides of each sheet were coated except the sample holder part, as shown in Figure 2-4. Multilayer coated samples presented in the current section were prepared according to the following procedure: Substrate surface was prepared by SiC grinding to a substrate surface roughness of 0.25 μm R_a. Titanium bond coating was deposited using pure titanium cathode with 65 A source current and -150 V substrate bias in argon atmosphere having 1.6 Pa pressure for 8 min to achieve thickness of 0.6 μm. TiAlN layers were deposited using 33 at.% Ti- 67 at.% Al in nitrogen atmosphere having 1.6 Pa pressure with 60 A source current and -50 V substrate bias. TiN layers were deposited using pure titanium cathode in nitrogen atmosphere having 1.6 Pa partial pressure with 60 A source current and -50 V substrate bias. The total coating thickness was kept at ~10 μm. Four main multilayer TiN/TiAlN coating designs were considered: 2-layer, 4-layer, 8-layer and 16-layer structures. In the case of 2-layer TiN/TiAlN coatings two different designs were considered, one with the same layer thickness per layer corresponding to ~5.9 μm, and another having an ~1 μm TiN thickness and a ~10 μm TiAlN layer. For other multilayer TiN/TiAlN coating designs of 4-layer, 8-layer and 16-layer, each layer had the same thickness, which corresponded to ~2.2 μm, 1.2 μm and 0.7 μm, respectively.

Table 3-6. Cathodic Arc Physical Vapor Deposition Parameters for monolithic TiN and multilayer TiN/TiAlN coating fabrication.

Coating	# of layers		Deposition rate (μm /min)		Total coating Thickness, (μm)
	TiN	TiAlN	TiN	TiAlN	
TiN	1		0.018		8.1
TiN(thin)/ $Ti_{1-x}Al_xN$ (thick)	1	1	0.017	0.025	11.1
TiN/ $Ti_{1-x}Al_xN$ 2-layer	1	1	0.026	0.026	11.8
TiN/ $Ti_{1-x}Al_xN$ 4-layer	2	2	0.020	0.020	8.9
TiN/ $Ti_{1-x}Al_xN$ 8-layer	4	4	0.022	0.022	9.8
TiN/ $Ti_{1-x}Al_xN$ 16-layer	8	8	0.024	0.024	10.9

3.3.1. Autoclave testing in static pure water at 360°C and 18.7 MPa

Figure 3-28 shows the weight gain data of TiN/TiAlN multilayer coated, single layer TiN coated and uncoated ZIRLO® sheets obtained after the autoclave testing for 7 days. Four samples were tested for each coating design which is the origin of the error bars shown. The uncoated ZIRLO® sheet showed a weight gain of ~13 mg/dm^2 consistent with standard testing of ZIRLO® in Yilmazbayhan et al. [157]. Single-layer TiN coated samples and multilayer TiN/TiAlN coated samples showed much lower average weight gains at 1.5-2.2 mg/dm^2. No negative weight gain was observed, indicating no coating spallation after 7 days of autoclave testing. Note that the measured weight gain of the coated samples includes weight gain which occurred on the uncoated regions on the samples (Figure 2-4). This means that the actual weight gain of the coated sample is smaller than the values above. Regardless, the average weight gain value of coated samples is at least an order of magnitude lower than the average weight gain of uncoated ZIRLO®, a significant corrosion improvement. To confirm this corrosion improvement and better understand the performance of the coated samples, cross-section optical microscopic analysis was performed.
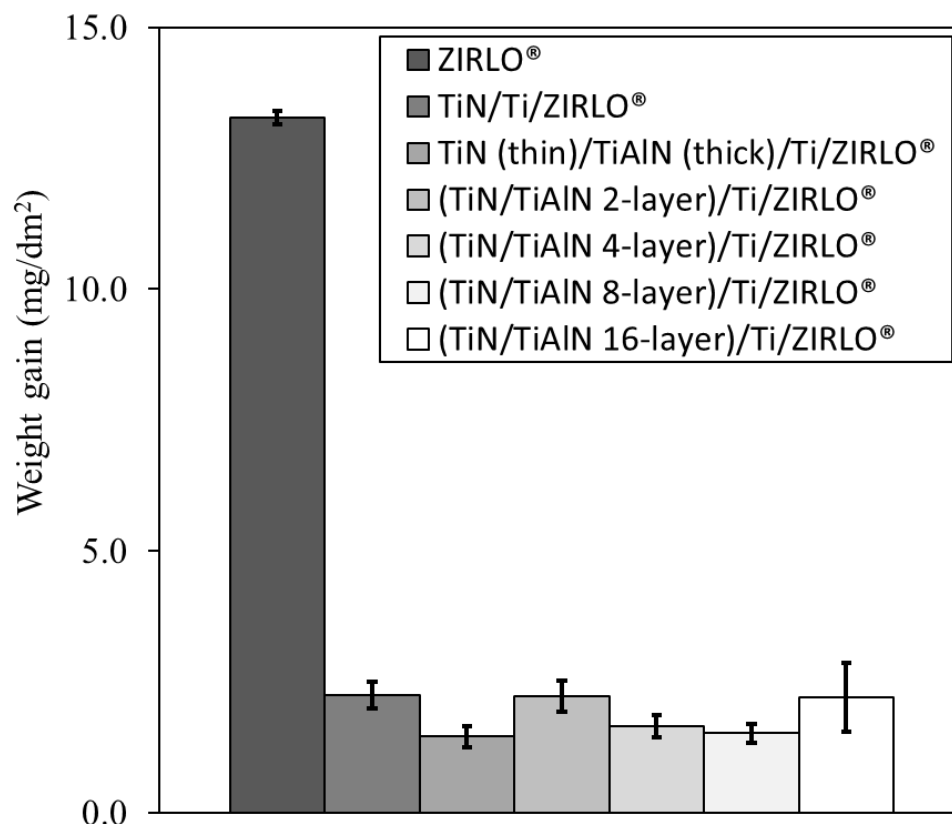
Figure 3-28. Weight gain (mg/dm^2) data of TiN/TiAlN multilayer coated, single layer TiN coated and uncoated ZIRLO® sheets tested in autoclave in static pure water at 360°C and 18.7 MPa for 7 days. Multilayer design architectures showed better corrosion resistance compared to uncoated ZIRLO® shown by the inset figure.

Figure 3-29 shows cross-section optical microscopy images of the as-deposited and 7 days autoclave tested samples of the following materials: single layer TiN coated (Figure 3-29a), TiN (thin)/TiAlN(thick) coated (Figure 3-29b), 2-layer TiN/TiAlN coated, (Figure 3-29c), 4-layer TiN/TiAlN coated (Figure 3-29d), 8-layer TiN/TiAlN coated (Figure 3-29e) and 16-layer TiN/TiAlN coated (Figure 3-29f) ZIRLO® sheets.
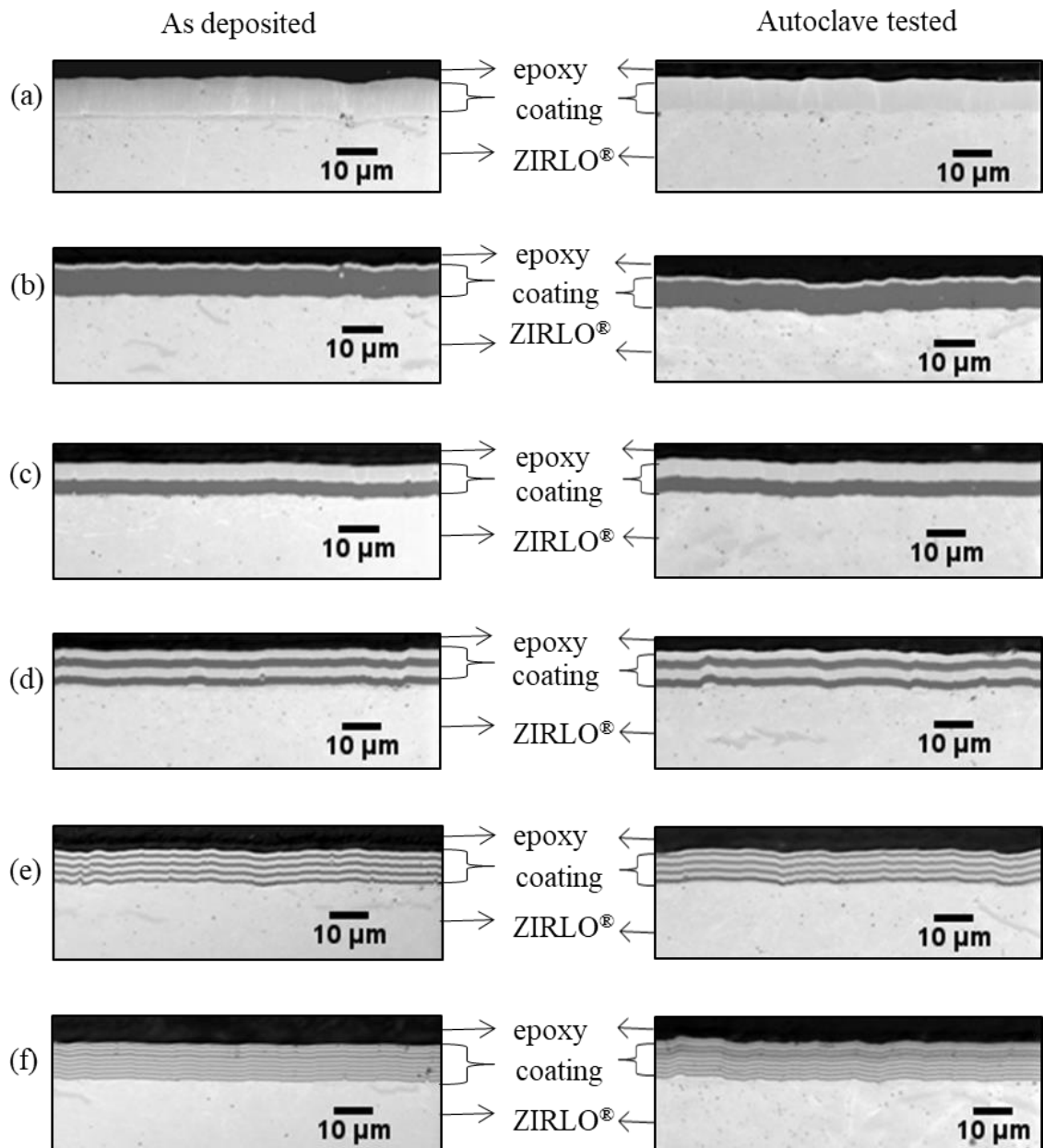
Figure 3-29. Optical images in the as-deposited condition (left) and after 7-day autoclave testing in 360ºC and 18.7 MPa water (right) for the cross-sections of samples with coatings (a) TiN, (b) TiN(thin)/TiAlN (thick), (c) TiN/TiAlN 2-layer, (d) TiN/TiAlN 4-layer, (e) TiN/TiAlN 8-layer, and (f) TiN/TiAlN 16-layer.

Cross-sectional images of as-deposited samples in Figure 3-29 show that the coating layer thicknesses were quite uniform in each case. The coatings are not much altered after the autoclave test and no delamination/spallation is observed. The ZIRLO® substrate was not oxidized and AlO(OH) crystals did not form on the surface although each sample had at least one TiAlN layer in the multilayer TiN/TiAlN coating design. This indicates that the weight gain observed can be directly related to the oxidation of the TiN top layer (if the oxidation occurred at the uncoated sample holder region is ignored). The cross-section optical microscopy analysis also confirmed that a top ~1 μm thick TiN layer is effective to prevent oxygen ingress towards the substrate and aluminum diffusion towards the surface during 7 days of autoclave testing. After confirming the corrosion performance enhancement with multilayer coatings in static pure water at 360°C and 18.7 MPa for 7 days, the corrosion tests were repeated for longer durations.

Figure 3-30 shows the weight gain data of TiN/TiAlN multilayer coated (several architectures), single layer TiN coated and uncoated ZIRLO® sheets obtained after the autoclave testing for up to 89 days. The inset weight gain diagram shows weight gain data without the uncoated ZIRLO® data to better discern the differences in the coated samples. Three samples were tested for each coating design up to 33 days and after 33 days, only two samples for each coating design were tested up to 89 days since one of the samples from each group was removed from the autoclave for characterization. After 89 days of autoclave testing ZIRLO® showed a 32 mg/dm^2 weight gain, showing parabolic or cubic kinetics as expected [157]. The single-layer TiN, 8-layer TiN/TiAlN and 16-layer TiN/TiAlN coated samples showed a positive total weight gain, increasing test duration. The maximum weight gain reached with these coatings was lower than 6 mg/dm^2, which is one fifth of the uncoated ZIRLO® weight gain. Again, this takes no account of the oxidation in the uncoated region. This suggests that multilayer coatings can provide better improved corrosion resistance relative to uncoated samples. The TiN(thin)/TiAlN(thick), 2-layer TiN/TiAlN and 4-layer TiN/TiAlN coated samples showed positive total weight gain; however, some samples (notably the 2-layer TiN (thin)/TiAlN(thick) sample) showed negative weight gain

slopes at various times indicating coating spallation. This indicates that the multilayer architecture has a strong influence on corrosion, which means that proper multilayer design is essential to achieve effective corrosion protection. Further analysis was performed on 33-day autoclave tested samples. The corresponding ZIRLO® sample showed a weight gain of ~20 mg/dm², whereas the coated samples showed weight gains around 1-3 mg/dm², again an order of magnitude lower than that of the uncoated sample. Characterizations were conducted using SEM, EDS and XRD to evaluate whether the observed weight gain was caused only by oxidation or included spallation/delamination.
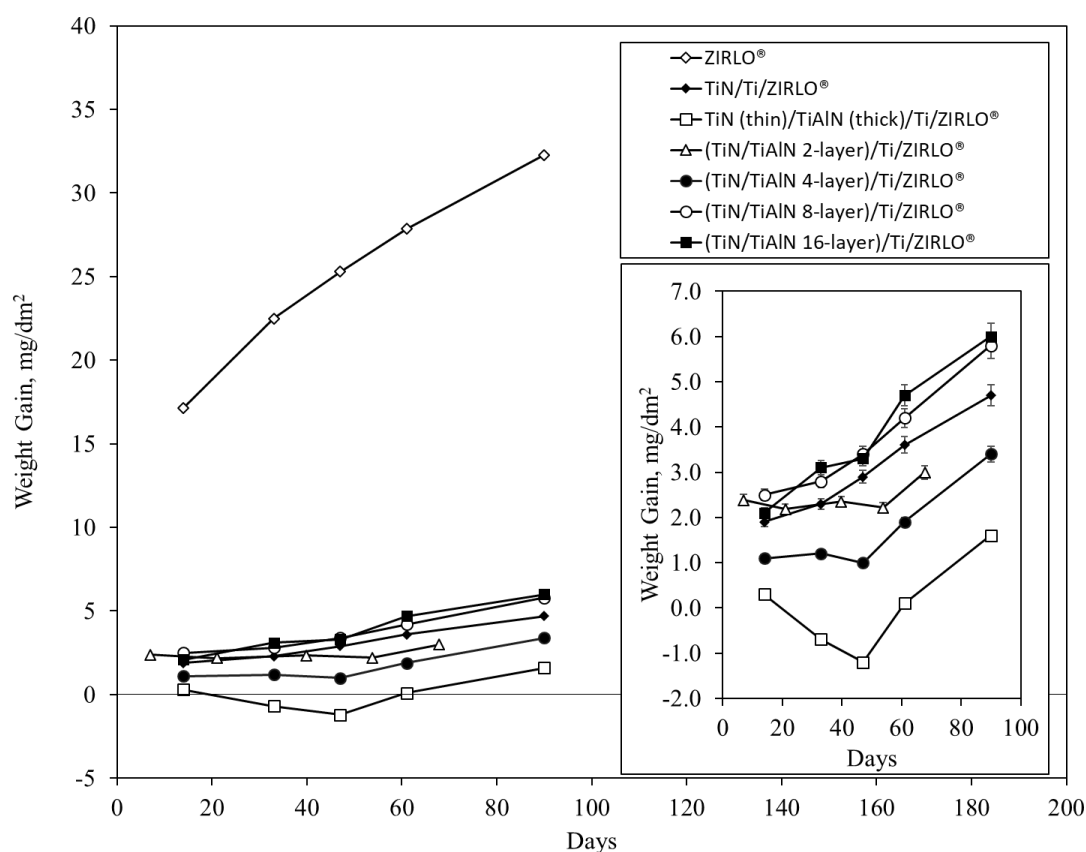
Figure 3-30. Weight gain (mg/dm^2) as a function of exposure time (days) for samples tested in autoclave at 360°C and 18.7 MPa up to 89 days. Multilayer design architectures show better corrosion resistance compared to uncoated ZIRLO® as shown in the inset figure.

Overall, the coatings were adherent to the ZIRLO® substrate during corrosion testing. Figure 3-31 shows digital and SEM images of the 2-layer TiN/TiAlN coated sample that was removed from the autoclave after 33 days of testing. This sample showed a weight gain of -3 mg/dm^2 and a considerable degree of spallation was seen on the surface, especially at the edges. At the regions, where TiN layer spalled, AlO(OH) (boehmite) formation occurred due to the interaction of the TiAlN layer with the 360°C and 18.7 MPa water. As both TiN and TiAlN layers spalled, oxidation of the ZIRLO® substrate took place leading to the formation of ZrO$_2$. Thus, it is concluded that the measured weight gain for this sample is an unreliable measure of corrosion, and the coating was not protective. The identification of the oxidation regions was performed using EDS analysis.
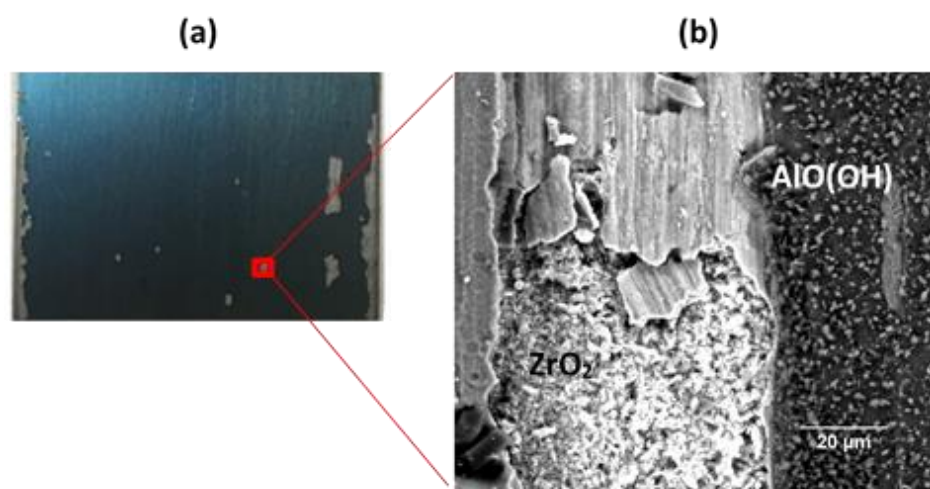
Figure 3-31. Spallation at a 2-layer coated sample after being autoclave tested in pure water at 360°C and 18.7 MPa for 33 days; (a) digital image, and (b) SEM-BSE surface image.

Phase identification of the corrosion tested samples were performed by using X-ray diffraction - Grazing Incidence (GIXRD) method. Four different incidence angles were considered to investigate formation of different oxide phases as we go from surface towards the substrate. Figure 3-32 shows GIXRD patterns of 16-layer TiN/TiAlN coated sample conducted using incident angles of 0.5°, 1°, 5° and 10°. For penetration depth calculations, the density of TiN was assumed to be 5.4 g/cm^3 and TiAlN was assumed to be 4.8 g/cm^3. Accordingly, the

corresponding penetration depths for the specified incident angles were calculated to be ~0.5, 1, 3 and 6 µm using the HighScore software, respectively. Both anatase (TiO$_2$, ICDD PDF# 00-021-1272) and rutile (TiO$_2$, ICDD PDF# 00-021-1276) phases were indexed on the pattern obtained with 0.5° incidence angle. Anatase and rutile are phases with same chemistry but different crystallographic space groups. TiN layer was indexed as cubic TiN (ICDD PDF# 04-015-0336) and TiAlN layer was indexed as cubic Ti$_{0.44}$Al$_{0.56}$N (ICDD PDF# 01-080-4072). No other oxide phase was identified as the incidence angle increased.
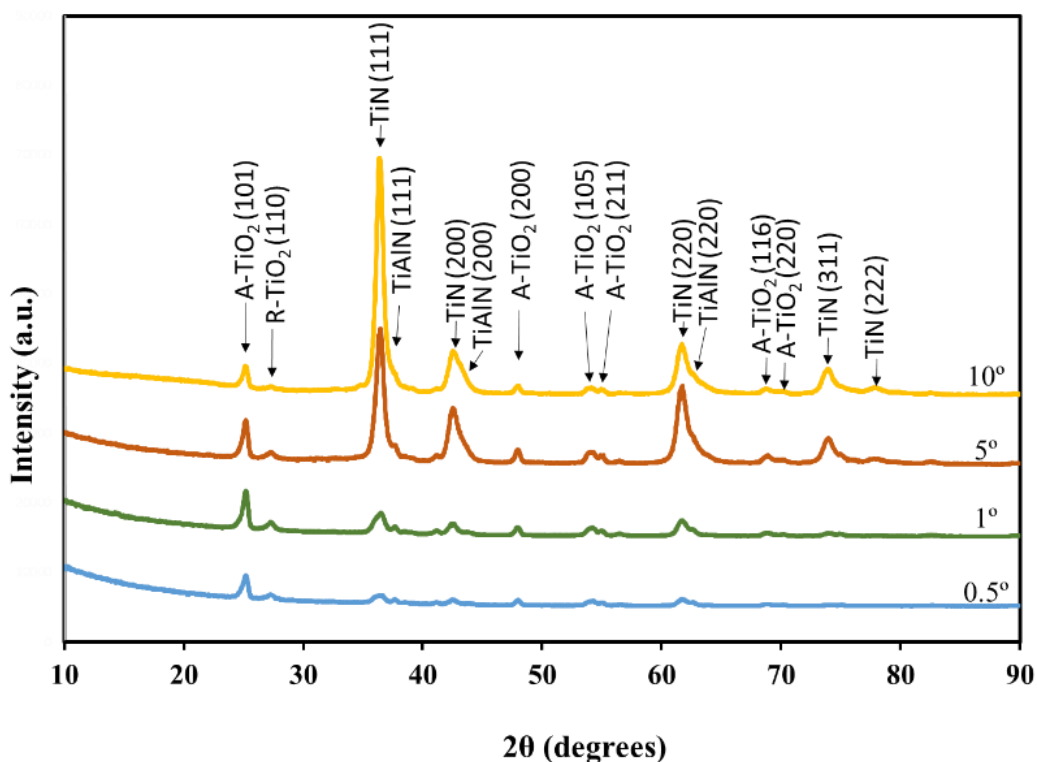
Figure 3-32. GIXRD patterns of 16-layer TiN/Ti$_{1-x}$Al$_x$N with 11.9 µm coating thickness that was exposed to the autoclave test at 360°C and saturation pressure of 18.7 MPa for 33 days. GIXRD measurement was conducted with incident angles of 0.5°, 1°, 5° and 10°. The corresponding penetration depth for specified incident angles were calculated to be ~0.5, 1, 3 and 6 µm, respectively. Oxide phases were determined to be anatase (A-TiO$_2$) and rutile (R-TiO$_2$).

Figure 3-33 shows the overlaid GIXRD patterns for all the samples in the test. For these measurements, a 1° incident angle was used for all samples. Peaks associated with oxide phases were once again confirmed to be consistent with the presence of anatase (A) (ICDD PDF# 00-021-1272), rutile (R) (ICDD PDF# 00-021-1276), and also Ti_2O_3 (ICDD PDF# 04-002-0457). No peaks from the boehmite phase were observed in these samples, although it is known that boehmite formed on the 2-layer sample (Figure 3-31).
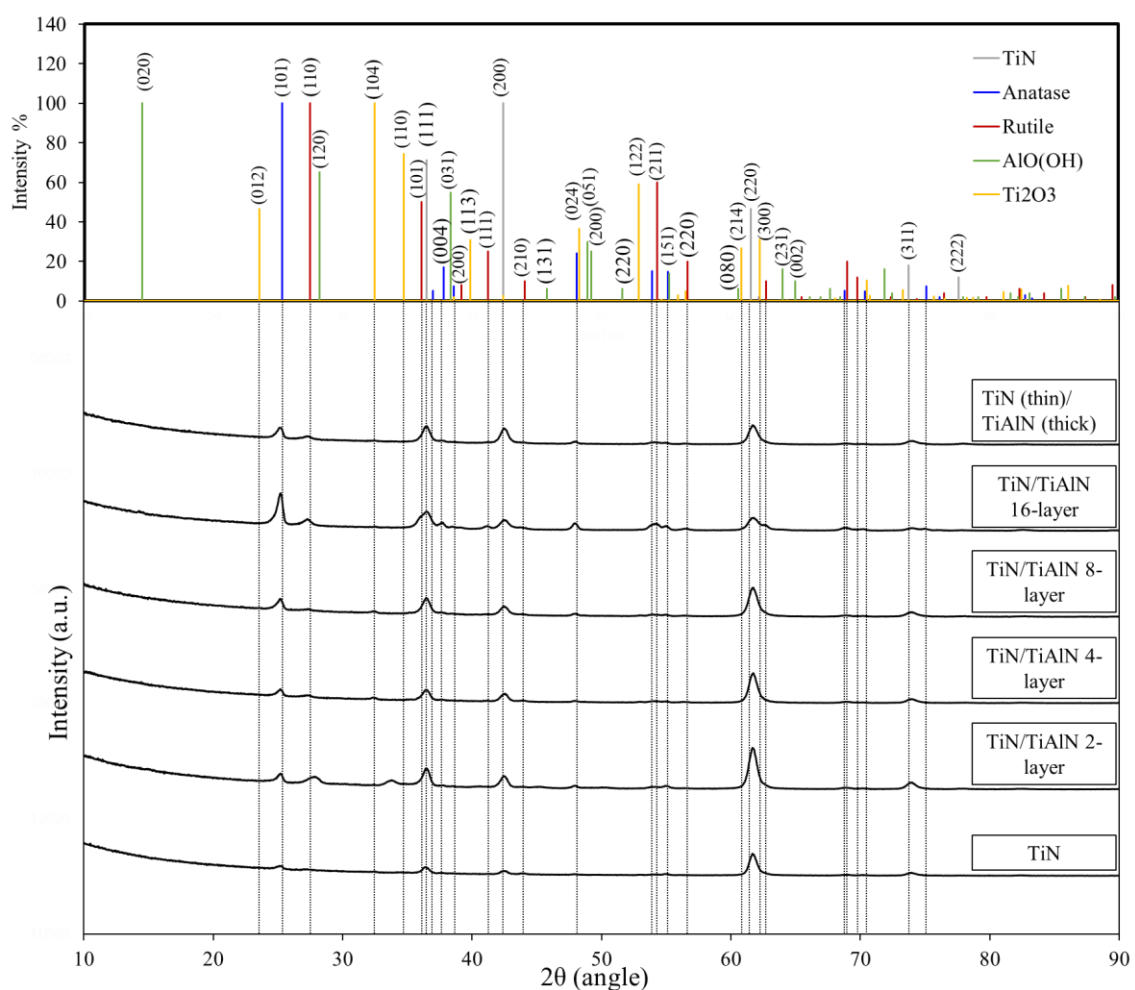
Figure 3-33. GIXRD patterns of samples that were exposed to the autoclave test at 360°C and saturation pressure of 18.7 MPa for 33 days. GIXRD measurement was conducted with an incident angle of 1°. The penetration depth was calculated to be ~1 µm, and assuming the density as 5.5 g/cm^3 for TiN.

As it was mentioned in Section 1.5.4, PWR core environment has a pH of ~7 and an electrochemical potential of -820 mV$_{SHE}$ [5,129]. Titanium Pourbaix diagrams presented in Figure 1-11 showed that for this environment, titanium forms a stable TiO$_2$ oxide and provide hydrothermal corrosion passivity [128]. After autoclave testing for 3 days, we observed anatase (metastable) phase and boehmite phase formation in the case of single-layer TiAlN coatings as shown in Figure 3-23. However, in the case of multilayer TiN/TiAlN coatings we observed rutile (stable) and Ti$_2$O$_3$ after longer durations of autoclave testing as presented in Figure 3-32 and Figure 3-33. Observation of Ti$_2$O$_3$ can indicate the presence of TiAl intermetallics in the coating since Ti$_2$O$_3$ formation is how they start oxidize [158]. The degradation observed in coatings as outermost TiN spallation or delamination, apart from macroparticle effect, can be attributed to the anatase phase formation because it has a high Pilling-Bedworth ratio of 1.95 [159], which can lead to internal compressive stresses and eventually breaking down of the layer [159,160]. As the cracks form, relaxation occurs which can render the anatase phase transform into the stable rutile phase which is more protective because of its Pilling-Bedworth ratio of 1.73 [160]. Crack formation can open the way for titanium diffusion towards surface and water diffusion towards substrate leading to the further oxide formation in anatase phase on the surface [160]. It is claimed that further oxidation lead to a two layered oxide structure with anatase phase as the outermost TiO$_2$ layer and rutile phase as the inner TiO$_2$ layer [160]. However, GIXRD analysis performed with various incidence angles providing information from various depths on the coating presented in Figure 3-32 showed that both rutile and anatase phases existed on the surface and the peak intensities did not change much as we go deeper into the coating invalidating the two-layer TiO$_2$ structure suggestion.

Figure 3-34 shows SEM-Secondary electron images of the 33-day autoclave tested single layer TiN, TiN(thin)/TiAlN(thick), 2-layer TiN/TiAlN, 4-layer TiN/TiAlN, 8-layer TiN/TiAlN and 16-layer TiN/TiAlN coated ZIRLO® sheets. The wave-like structures along the horizontal direction (with an elevated region of width ~1 µm) were attributed to polishing traces of the

substrate surface. No coating spallation, delamination or cracks on the surface were observed, but macroparticles and craters were seen on the sample surfaces. Crater formation occurred due to macroparticle expulsion because of compressive stresses in the growing film [150]. The composition of these macroparticles was determined both from surface and cross-section samples using EDS point analysis. Surface analysis showed that macroparticles were composed of ~65 at.% oxygen and ~15 at.% titanium, the rest being mostly iron, carbon, chromium and nickel, and are related to contamination from the autoclave. Cross-sectional analyses revealed that the macroparticles extended through the layers, exhibiting a composition similar to the composition of the corresponding layer.
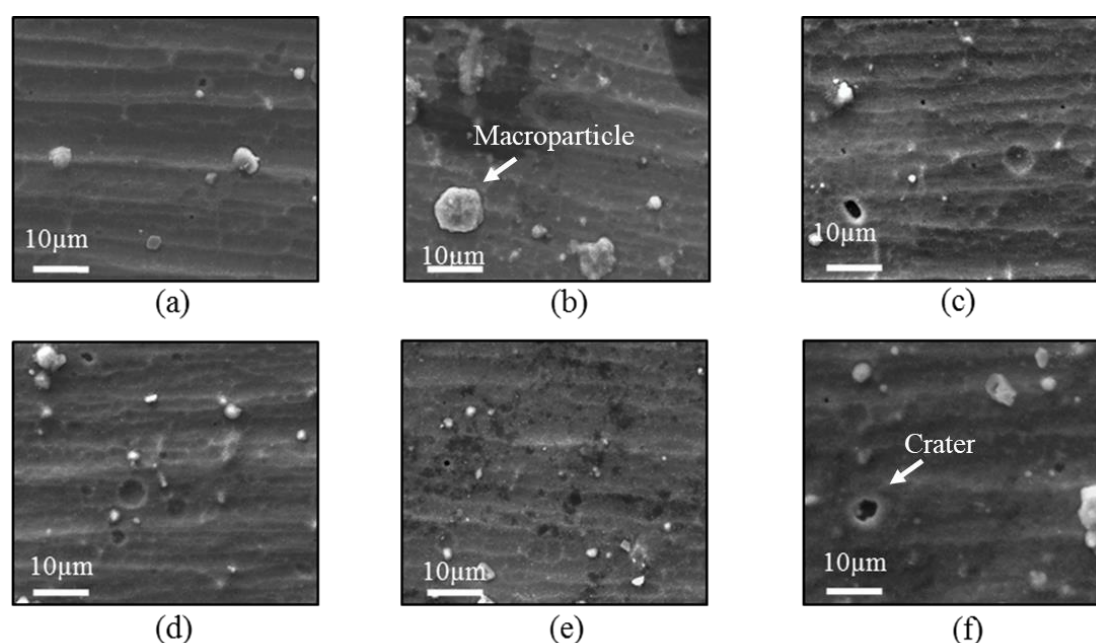
Figure 3-34. SEM-SE surface image of samples after the autoclave test at 360°C and saturation pressure of 18.7 MPa for 33 days, which were coated with: (a) TiN, (b) TiN(thin)/TiAlN(thick), (c) TiN/TiAlN 2-layer, (d) TiN/TiAlN 4-layer, (e) TiN/TiAlN 8-layer, and (f) TiN/TiAlN 16-layer.

Figure 3-35 shows the cross-section SEM-backscattered electron images of the 33-day autoclave tested samples. The layer thicknesses are quite uniform in all the samples. The coating

layers are also seeming to remain dense and well adherent to each other and to the ZIRLO®

substrate, even after 33 days of autoclave test. Coating thicknesses remained at ~10 μm similar to

the as-deposited coating thickness as initially presented in Table 3-6. The coating composition

was evaluated using EDS to assess the coating effectiveness in preventing oxygen ingress. EDS

spectra (taken from 2-layer coatings) revealed the composition of the TiAlN layers as 16 at.% Ti,

32 at.% Al and 52 at.% N. The Ti/Al ratio is in good agreement with the cathode composition of

33 at.% Ti and 67 at.% Al.
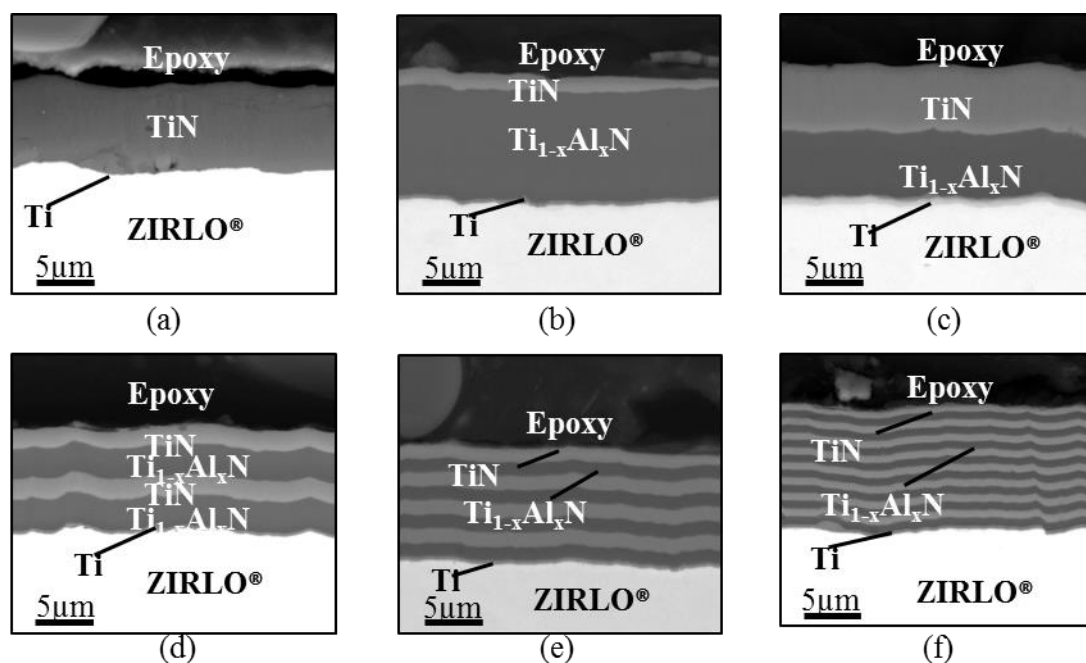
Figure 3-35. SEM-BSE cross-section image after autoclave test at 360°C and saturation pressure of 18.7 MPa for 33 days: (a) TiN, (b) TiN(thin)/TiAlN(thick), (c) TiN/TiAlN 2-layer, (d) TiN/TiAlN 4-layer, (e) TiN/TiAlN 8-layer, and (f) TiN/TiAlN 16-layer. These SEM images demonstrates that only a thin TiN layer is required as a barrier to minimize Al migration and prevent boehmite formation.

Figure 3-36a shows oxygen profile and Figure 3-36b shows a line scan of the multilayer

coating for the TiN/TiAlN 8-layer coated sample. Figure 3-36a shows that oxygen penetrated to a

depth of only ~1.5 μm into the coating multilayer, corresponding only to the outermost TiN layer.

Near the substrate/coating interface, an increase in oxygen concentration was observed which is consistent with the oxygen that was already present in the alloy when it was produced, which is acceptable up in the range of 0.09-0.16 wt.% [3]. Very little oxygen was seen within the multilayers, as shown in the line scan in Figure 3-36b. Figure 3-36b shows that the multilayer compositions are also seeming to be quite consistent throughout the layers.
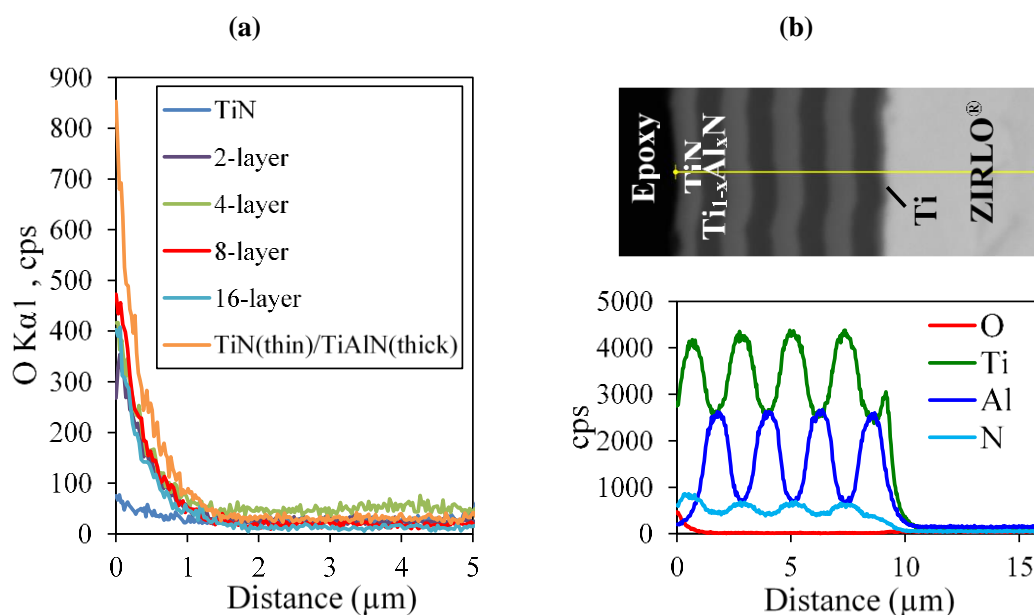
Figure 3-36. EDS cross-section line scan after autoclave testing at 360°C and saturation pressure of 18.7 MPa for 33 days, (a) oxygen profile through TiN, 2-layer, 4-layer, 8-layer, 16-layer and TiN (thin)/TiAlN(thick) coating starting from the outer layer towards the substrate and (b) oxygen, titanium, aluminum and nitrogen profile through cross-section of (8-layer TiN/TiAlN)/Ti/ZIRLO® sample.

In summary, SEM, EDS and XRD analysis confirmed that multilayer TiN/TiAlN coatings are helpful in protecting the ZIRLO® substrate against corrosion. The top TiN layer forms anatase, rutile and TiO_2 as it interacts with the 360°C and 18.7 MPa water but does not allow for boehmite formation. For that purpose, ~1 μm TiN top layer is determined to be enough to avoid oxygen ingress and aluminum egress, which contributes to the corrosion performance of the coatings. Among the investigated multilayer coating designs, the 8- and 16-layered

TiN/TiAlN coated samples showed positive weight gain through the autoclave testing up to 90 days. Specifically, the 8-layered samples showed the minimum positive weight gain among the architectures studied. Considering the ease of manufacturability when comparing 8- and 16-layered coatings, the 8-layer design architecture was chosen as the most desirable. Thus, the TiN/TiAlN 8-layer coating was determined to be the optimum architecture that makes it possible to both stop boehmite phase formation, show good adhesion, and to provide lowest weight gain, without spallation or delamination.

3.3.2. Supercritical water (SCW) testing

Supercritical water (SCW) testing was performed at the University of Michigan in autoclave in deaerated water at 542°C and 24.5 MPa for 48 hours on the same samples. Figure 3-37 shows the weight gain obtained after the SCW autoclave testing. The uncoated ZIRLO® sample showed a weight gain of 176 mg/dm^2 after the corrosion test, an expected increase from the testing at 360°C. Both the single layer TiN coated and 2-layer TiN/TiAlN coated ZIRLO® sheets showed negative weight gain, indicating coating spallation. TiN(thin)/TiAlN(thick) and 8-layer TiN/TiAlN coated samples had excessive amount of weight gain reaching to 182 mg/dm^2, i.e. even more than the uncoated ZIRLO® weight gain value. Additional characterization was performed to further study the corrosion performance of the coatings in SCW environment using scanning electron microscopy (SEM), both on surface and cross-section.
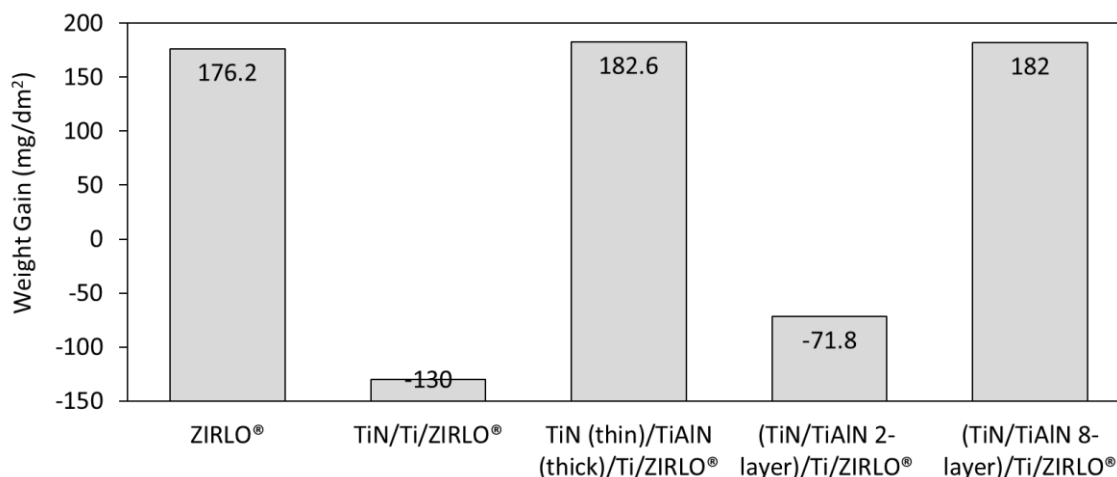
Figure 3-37. The weight gain data of uncoated ZIRLO®, TiN/Ti/ZIRLO®, TiN(thin)/TiAlN(thick)/Ti/ZIRLO®, (TiN/TiAlN 2-layer)/Ti/ZIRLO® and (TiN/TiAlN 2-layer)/Ti/ZIRLO® after supercritical water testing in deaerated water at 542°C and 24.5 MPa for 48h.

Visual examination showed significant degrees of coating spallation and delamination on all samples studied, except for the 8-layer TiN/TiAlN coated sample. Figure 3-38 shows the surface and cross-section SEM images of SCW environment tested for the following samples: uncoated ZIRLO® (Figure 3-38a), single-layer TiN coated (Figure 3-38b), TiN(thin)/TiAlN(thick) coated (Figure 3-38c), 2-layer TiN/TiAlN coated (Figure 3-38d) and 8-layer TiN/TiAlN coated (Figure 3-38e) ZIRLO® sheets. The TiN coated sample (Figure 3-38b) showed large coating delaminated regions and cracks in the oxide film. The TiN(thin)/TiAlN(thick) and 2-layer TiN/TiAlN coated samples showed a few delaminated regions and cracks in the oxide film. No AlO(OH) crystal formation occurred at the TiAlN regions that came into contact with the supercritical water environment, as expected. Two-layer coatings showed better corrosion performance than the monolithic TiN coating regardless of the coating layer thickness. For these samples approximately half of the coating surface remained adherent. In contrast, almost all the coating remained adherent on the surface of the 8-layer

TiN/TiAlN coated sample. However, even in that case high-resolution SEM images revealed microcracks on the coating surface.
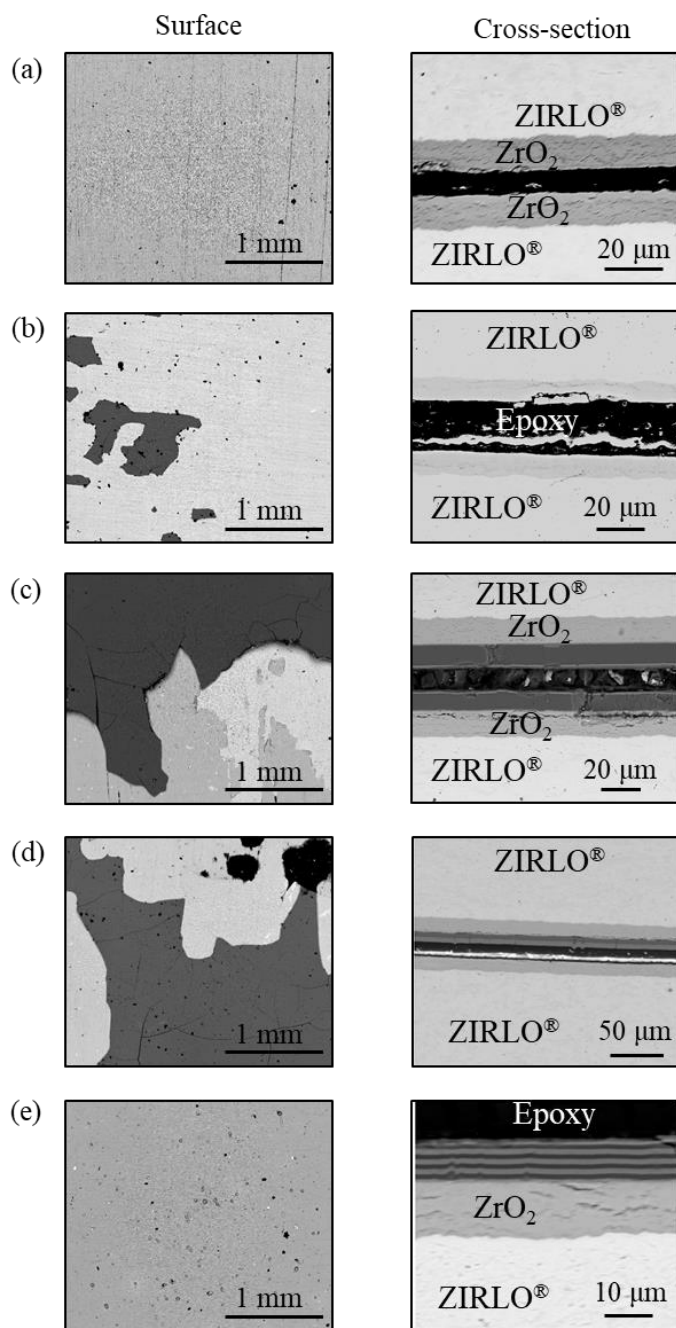
Figure 3-38. Surface and cross-section SEM-Backscattered electron images of (a) uncoated ZIRLO®, (b) TiN coated, (c) TiN (thin)/TiAlN (thick) coated, (d) TiN/TiAlN 2-layer coated, and (e) TiN/TiAlN 8-layer coated samples after exposure to supercritical water (SCW) performed at the University of Michigan autoclave at 542°C and 24.5 MPa water for 48 hours.

Cross-sectional samples for SEM examinations were prepared by cutting samples from the mid-width along the longitudinal axis to stay away from the edge effect. The results of this examination are shown in Figure 3-38. The uncoated ZIRLO® sample showed zirconium oxide formation to a thickness of ~10 µm (3-38a). In the case of monolithic TiN coating, spallation of almost all the coating led to the substrate oxidation at a thickness equal to that of the uncoated sample, as confirmed through cross-sectional SEM analysis. Among the tested coatings, the 8-layer coating design was the most promising since almost all the coating was maintained on the surface. However, cross-sectional analyses demonstrated that although the 8-layer TiN/TiAlN coating was maintained on the surface, substrate oxidation occurred to a thickness similar to that of the uncoated sample, indicating that the coatings were not protective in this environment.
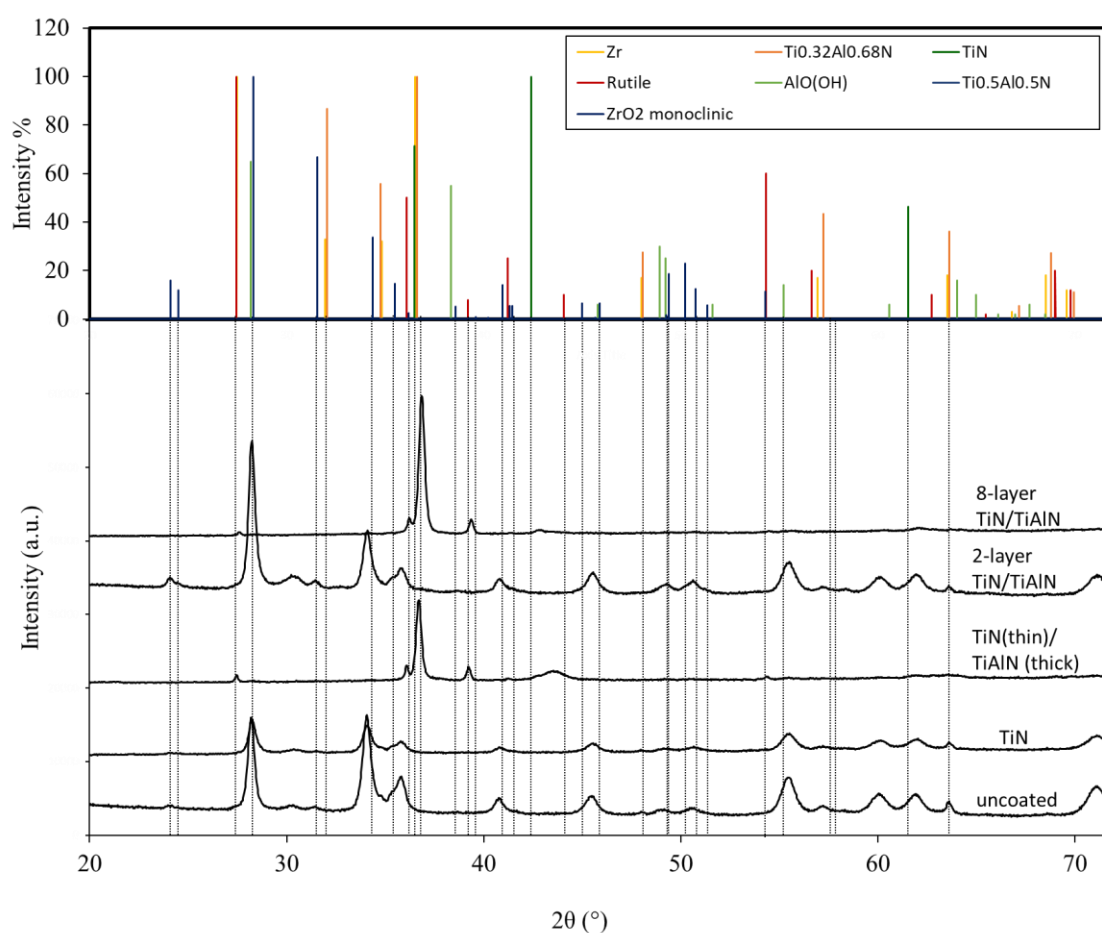
Figure 3-39. X-ray diffraction (XRD)-Bragg Brentano scans (Cu K$_\alpha$) of SCW environment tested uncoated, single layer TiN coated, TiN(thin)/TiAlN(thick) coated, 2-layer TiN/TiAlN coated and 8-layer TiN/TiAlN coated ZIRLO® sheets.

Figure 3-39 shows X-ray diffraction (XRD) – Bragg Brentano scans of the samples after SCW testing. Although the data was measured in the Bragg Brentano mode, not all the zirconium peaks were observed. The TiN layer could be identified but the TiAlN layer could not be identified. Finally peaks consistent with the presence of the anatase, rutile and monoclinic ZrO_2 were identified.

In conclusion, low coating corrosion performance might be attributed to the coating adhesion, macroparticles or coating density, indicating further optimization requirement of coating deposition parameters.

As a part of multilayer coating optimization, functionally grading was considered, and the results are presented in the Appendix B, but at the end functionally grading did not improve corrosion performance. Additionally, the corrosion performance of a scratched sample was also investigated, and the results are presented in the Appendix C. Scratching did not degrade the overall coating integrity and did not accelerate the substrate corrosion at the scratched regions.

3.4. Optimization of the 8-layer TiN/TiAlN coating architecture on ZIRLO® sheet and tube

Based on the previous analysis which confirmed that 8-layer TiN/TiAlN coating deposited on ZIRLO® substrate with a surface roughness of 0.25 μm R_a, 0.6 μm titanium bond coating, and an overall thickness of ~10 μm was the optimum design to enhance corrosion resistance, these coatings were applied on tubular samples. This is called the "standard" design. During investigation of the 8-layer coated ZIRLO® tube corrosion performance investigation, deposition parameter optimization was performed once again because of the geometry difference between sheet and tube. Additionally, substrate surface preparation method effect was also investigated. Tests involved Scratch testing on sheet samples and corrosion testing of sheet and tubular samples in autoclave in static pure water at 360°C and 18.7 MPa and high temperature

furnace testing in air. Characterizations were performed using optical profilometry, scanning electron microscopy (SEM), energy dispersive spectroscopy (EDS), X-ray diffraction (XRD) and Raman spectroscopy.

3.4.1. Scratch testing and post-scratch observations

Scratch testing was performed to investigate the effect of (i) cathode composition, (ii) deposition time and (iii) substrate surface preparation method effects on the 8-layer TiN/TiAlN coating adhesion to the ZIRLO® sheet substrate. Scratch testing was performed according to the procedure described in Section 2.4. Coating deposition parameters and substrate surface preparation methods considered for this study are summarized in Table 3-7.

Table 3-7. Substrate surface preparation method and cathodic arc physical vapor deposition (CA-PVD) parameter summary to deposit TiAlN layers in the 8-layer TiN/TiAlN coating design prepared for scratch testing. Considered parameter for each comparison group is highlighted.

Substrate surface preparation	Deposition time (min)	Negative substrate bias (V)	Arc current, TiAlN/TiN (A)	Cathode composition (at.% Ti/Al)
Green scotch brite	50	75	45/45	33/67
Green scotch brite	50	75	45/45	20/80
Grit blast	17.6	50	60/65	20/80
Grit blast	35.2	50	60/65	20/80
SiC hand grinding	35.2	50	60/65	20/80

3.4.1.1. Cathode composition variation

The cathode composition effect was once again considered for the 8-layer TiN/TiAlN coating design, as previously discussed in Section 3.2.1.3. Figure 3-40a shows the overlaid GIXRD patterns of 8-layer TiN/TiAlN layer having TiAlN layer deposited with either 20 at.% Ti – 80 at. % Al or 33 at. % Ti – 67 at. % Al. ICDD PDF patterns of TiN, $Ti_{0.5}Al_{0.5}N$ and $Ti_{0.32}Al_{0.68}N$ are provided on top of the diagram. Independent of the cathode composition, TiAlN

layer phase in both coatings was identified as $Ti_{0.32}Al_{0.68}N$. Additionally, a slight shift towards

lower angles was observed in the case of TiAlN XRD patterns as more clearly presented in Figure

3-40b.
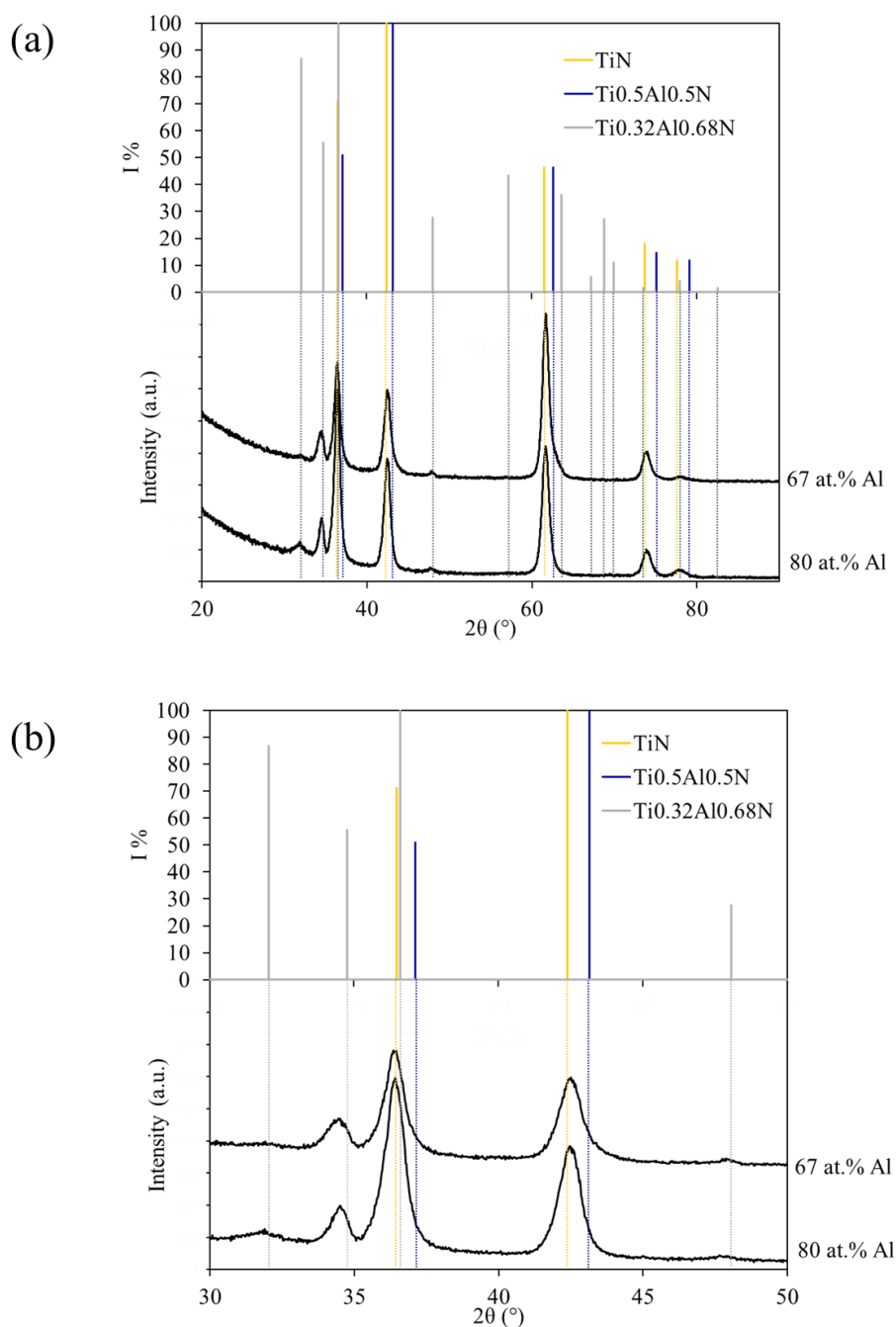
Figure 3-40. GIXRD patterns of 8-layer TiN/TiAlN layer having TiAlN layer deposited with either 20 at.% Ti – 80 at.% Al or 33 at.% Ti – 67 at.% Al; (a) 2θ range: 20-90° and (b) 2θ range: 30-50°.

Figure 3-41a shows the optical microscopy image of the scratch performed on 8-layer TiN/TiAlN coating having TiAlN layers deposited using 33 at.% Ti – 67 at.% Al cathode. Gross spallation was observed to occur after 6.15 mm scratch distance at 27 N. The gross spallation location was also confirmed with energy dispersive spectroscopy (EDS) elemental map analysis shown in Figure 3-41b. In the EDS-map analysis titanium, aluminum, nitrogen having regions and then zirconium appearance because coating spallation can be observed.
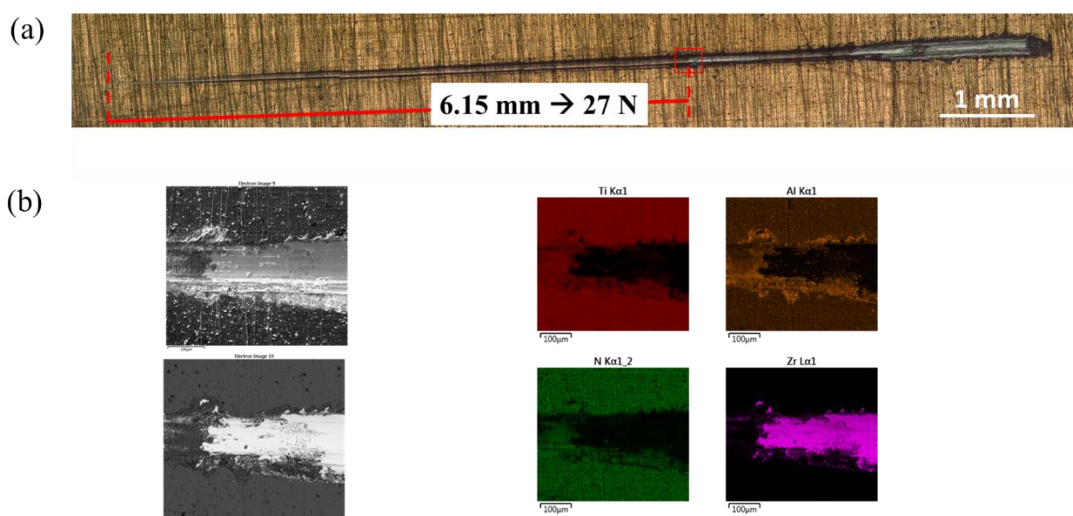
Figure 3-41. (a) Optical microscopy image and (b) EDS-elemental map analysis of the scratch on green scotch brite prepared 8-layer TiN/TiAlN/Ti/ZIRLO® sheet. (TiAlN layer deposition parameters: cathode 33 at.% Ti – 67 at. % Al, 75 V substrate bias and 45 A source current. TiN layer deposition parameters: 150 V substrate bias and 45 A source current).

Data presented in the Figure 3-42 refers to 8-layer TiN/TiAlN coated ZIRLO® sheet with TiAlN layers deposited using 20 at.% Ti – 80 at. % Al. Figure 3-42 shows scanning electron microscopy (SEM) secondary electron (SE), SEM- backscattered electron image of the scratch and corresponding load-distance data. Only one mode of failure which was identified to be gross spallation occurred. The gross spallation onset took place at ~26 N. Compared with the scratch testing data presented in Figure 3-41, it can be concluded that cathode composition variation did not affect coating adhesion significantly in the case of select deposition parameters.
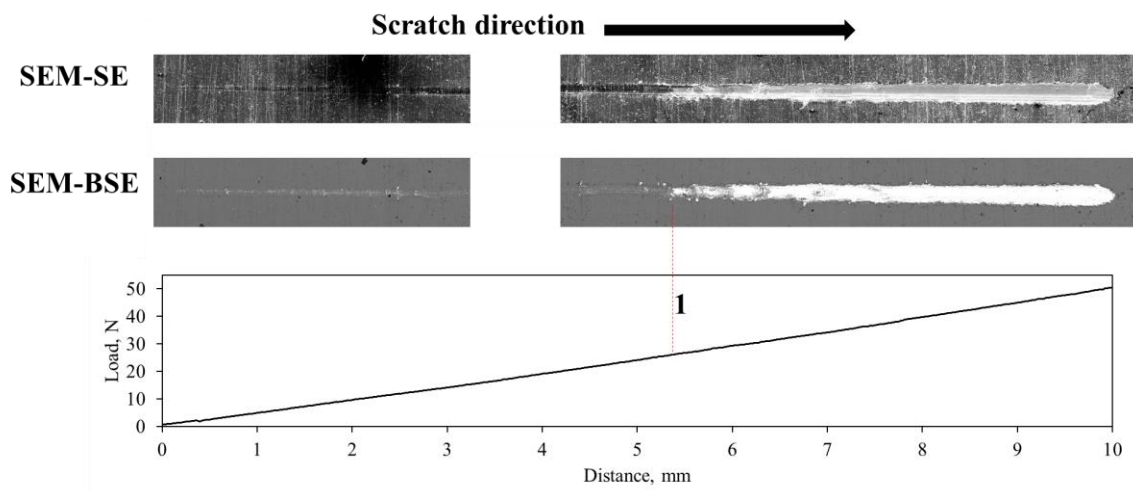
Figure 3-42. Analysis of the scratch on green scotch brite prepared 8-layer TiN/TiAlN/Ti/ZIRLO® sheet. (TiAlN layer deposition parameters: cathode 20 at.% Ti – 80 at. % Al, 75 V substrate bias and 45 A source current. TiN layer deposition parameters: 150 V substrate bias and 45 A source current).

Additionally, substrate bias variation effect was investigated by considering two different substrate biases of 50 V and 75 V during deposition of the TiAlN layer in the 8-layer TiN/TiAlN coating design while keeping other parameters constant (except TiN deposited with 65A). Figure 3-43 shows the surface scanning electron microscopy (SEM) secondary electron (SE) images of both flat and tubular samples. Surface SEM-SE images of the coatings having TiAlN layers deposited on flat and tubular samples with 50 V substrate showed a surface structure mirroring that of the substrate surface structure. As the substrate bias increased surface started to have a spatter appearance as it was previously observed in the case of single layer TiAlN coatings. The substrate bias effect on the coating appearance is more obvious in the case of tubular samples. Additionally, amount of macroparticles appeared to be decreased with increased substrate bias.
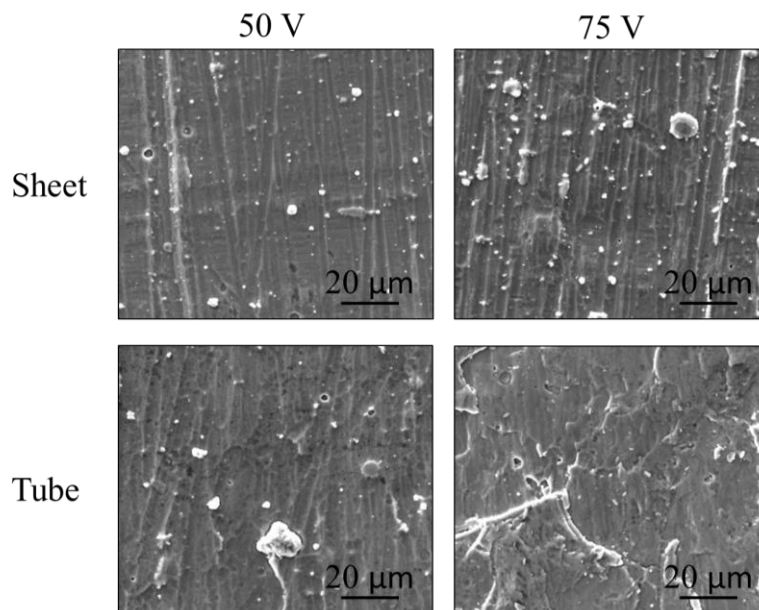
Figure 3-43. Surface scanning electron microscopy (SEM) secondary electron (SE) images of 8-layer TiN/TiAlN coated flat and tubular samples having TiAlN deposited with either 50 V or 75 V substrate bias.

Figure 3-44 shows the energy dispersive spectroscopy (EDS) elemental map analysis performed on the surface of as-deposited 8-layer TiN/TiAlN coated ZIRLO® samples. The elemental map analysis of flat sample having TiAlN layer deposited with 50 V, flat sample having TiAlN layer deposited with 75 V, tube sample having TiAlN layer deposited with 50 V and tube sample having TiAlN layer deposited with 75 V substrate are presented in Figure 3-44a, b, c and d, respectively. EDS map analysis performed on the surface confirmed that all the coatings were composed of titanium, aluminum and nitrogen. In the case of flat samples not much variation was observed between 50 V 75 V deposited coatings. However, in the case of tubular samples, the spatter appearance that was initially observed in Figure 3-44 was also confirmed to be leading to nonuniform elemental distribution which was clearly observed in the case of aluminum elemental map. The spatter appearance and nonuniform elemental distribution on the surface increased with substrate bias increase.
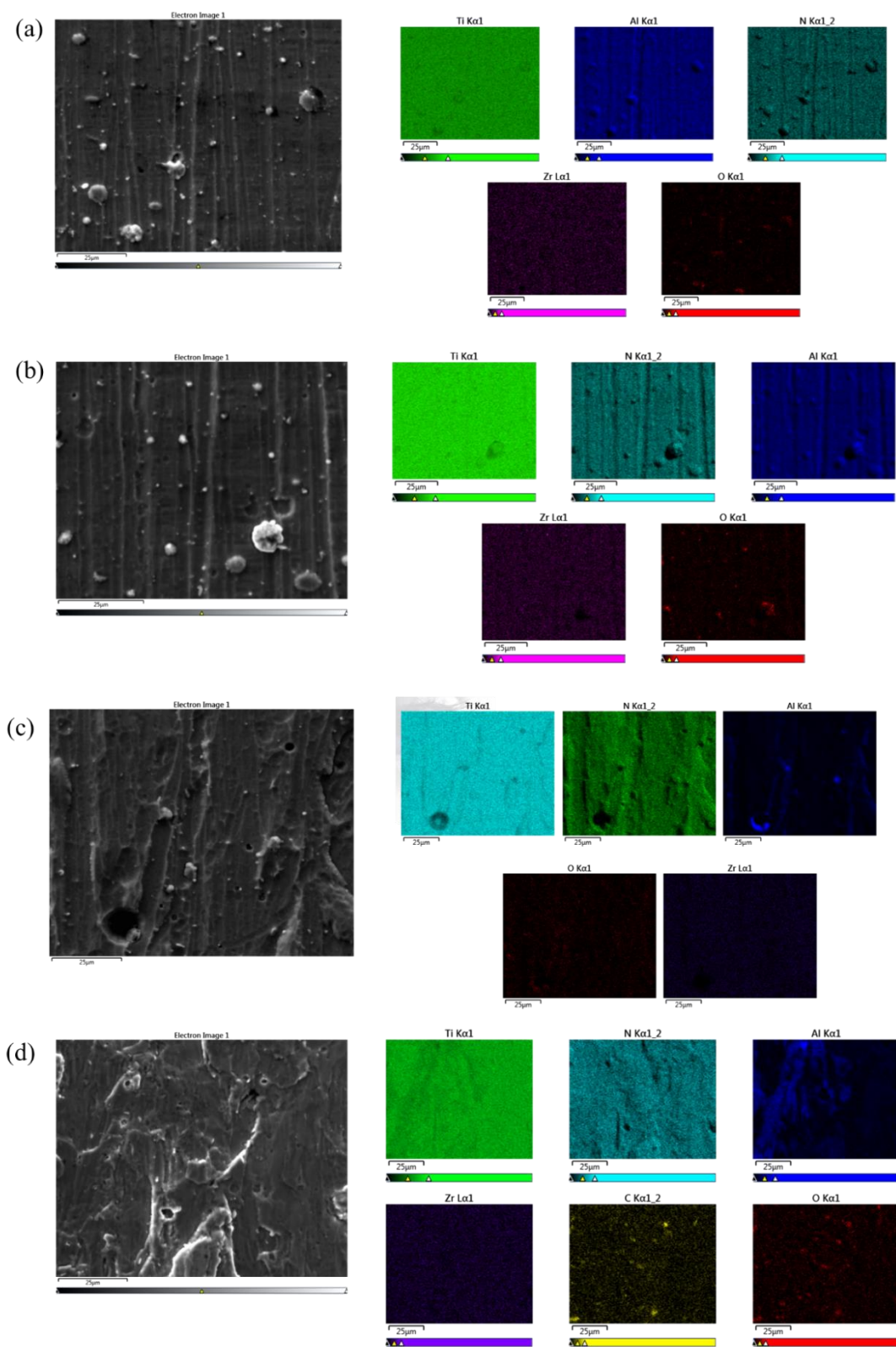
Figure 3-44. EDS elemental map analysis of 8-layer TiN/TiAlN coated flat (a, b) and tubular (c, d) samples having TiAlN deposited with either (a, c) 50 V or (b, d) 75 V substrate bias.

Figure 3-45 shows the cross-section SEM-BSE images of the flat and tube samples having TiAlN layers deposited with 50 V and 75 V substrate bias. Cross-section SEM-BSE analyses were mainly performed to determine Ti-bond coating and coating thicknesses. There was no porosity in TiAlN and TiN layers. Although there were some minor variations due to surface roughness and macroparticles, overall coatings deposited with that sample preparation showed an almost uniform layer thickness through the cross-section as shown in the cross-section SEM images. Tubular samples had thicker coatings compared to the flat sample counterparts.
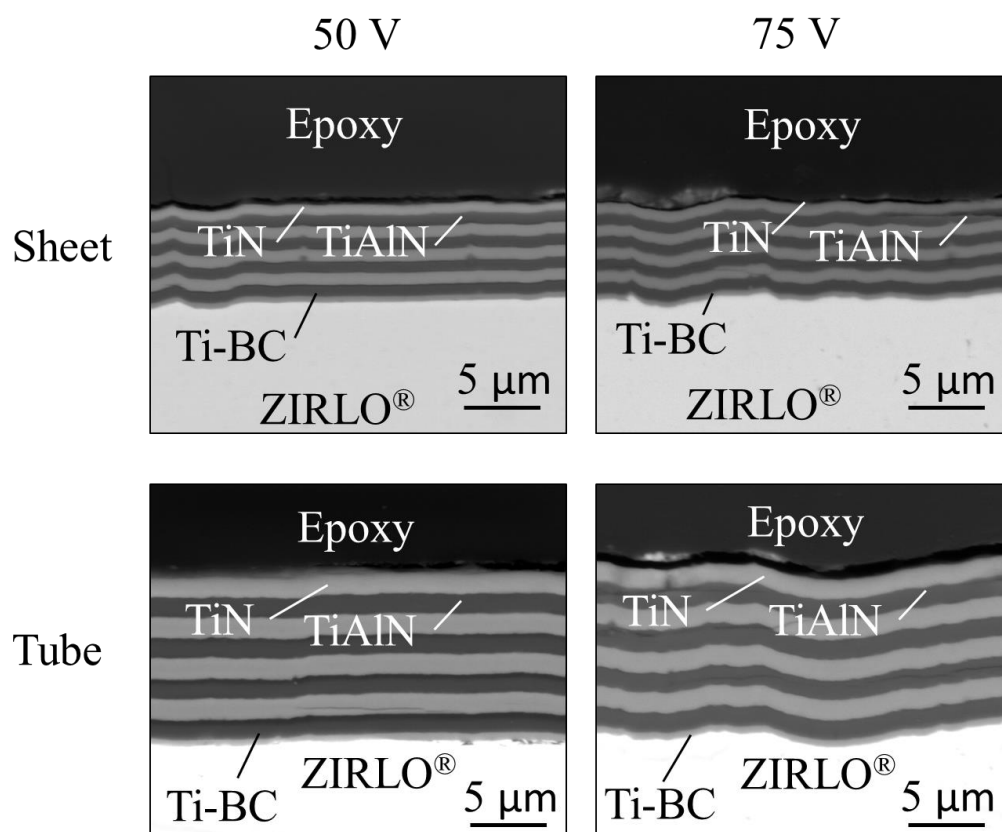
Figure 3-45. Cross-section scanning electron microscopy (SEM) secondary electron (SE) images of 8-layer TiN/TiAlN coated flat and tubular samples having TiAlN deposited with either 50 V or 75 V substrate bias.

Table 3-8 shows the Ti-BC, TiAlN and TiN layer thickness of tube and flat samples having TiAlN deposited with 50 V and 75 V substrate bias. Ti-BC, TiN and TiAlN layer

thicknesses were measured using ImageJ from cross-section SEM images with magnification 10000x by measuring thickness from 3-15 different locations at each sample. Tubular sample TiAlN and total coating thicknesses were 1.3 µm and 10.7 µm, respectively, independent of the substrate bias applied. Flat samples determined to be having thinner TiAlN coating of 0.7 µm and total coating of ~6 µm compared to the tubular samples. However, like the tubular sample thickness measurements, TiAlN and total coating thicknesses were independent of the applied substrate bias.

Table 3-8. Total coating and individual layer thickness data of 8-layer TiN/TiAlN coated flat and tubular samples having TiAlN deposited with either 50 V or 75 V substrate bias.

	Tube-50 V	Tube-75 V	Flat-50 V	Flat-75 V
Total	10.66	10.7	6.81	6.07
Ti-BC	0.45±0.12	0.46±0.10	0.36±0.03	0.40±0.14
TiAlN	1.27±0.03	1.29±0.00	0.74±0.00	0.72±0.03
TiN	1.34±0.05	1.38±0.01	0.77±0.01	0.75±0.04

Figure 3-46 shows the cross-section elemental line scan (Figure 3-46a) and cross-section elemental map analysis (Figure 3-46b) of 8-layer TiN/TiAlN coated tubular sample having TiAlN coating layers deposited using 50 V substrate bias. The EDS analysis helped to confirm the uniform coating layer deposition on the substrate surface. The EDS analysis also showed the oxygen layer at the substrate and coating interface.
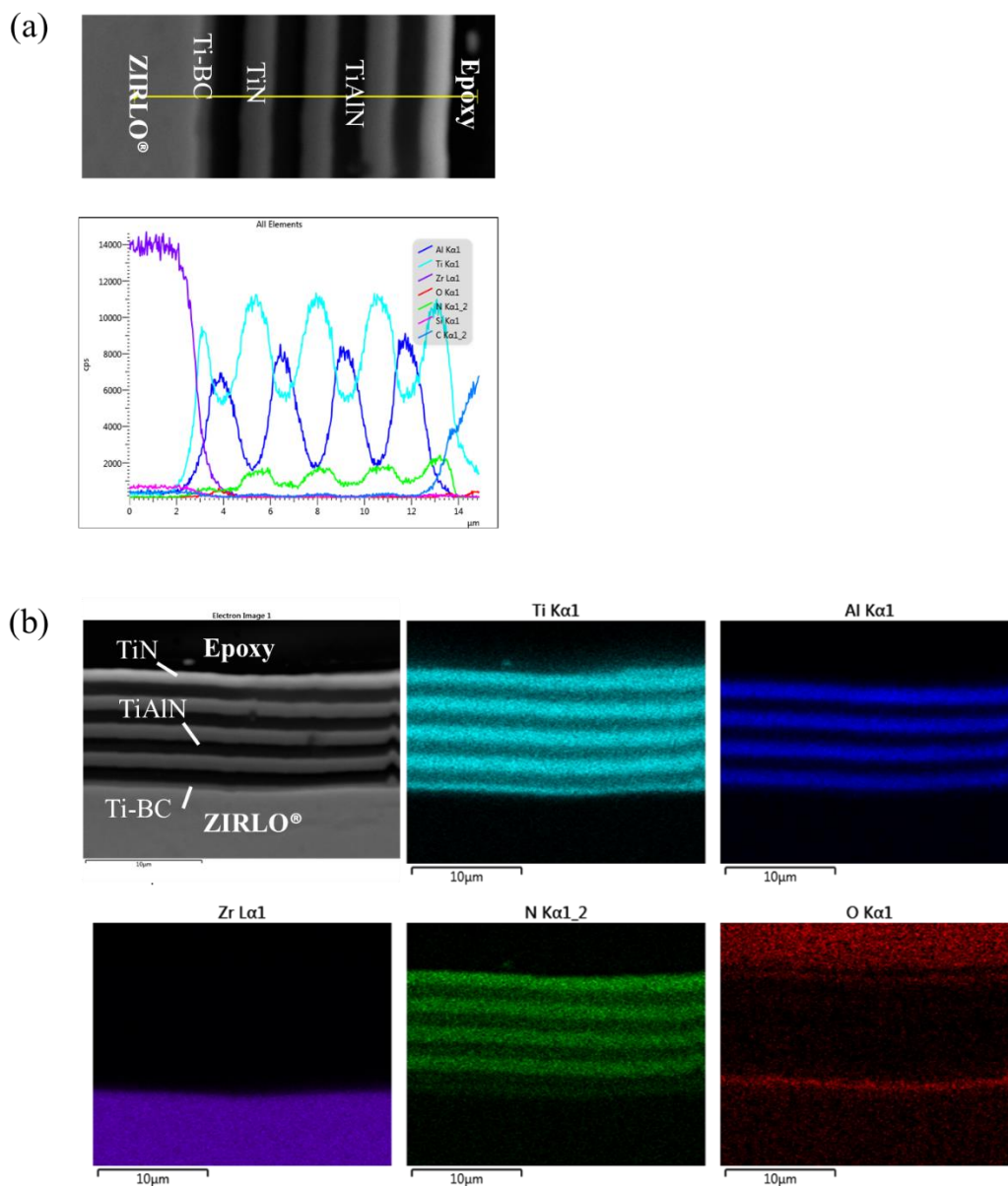
Figure 3-46. (a) EDS elemental line scan and (b) EDS- elemental map analysis of 8-layer TiN/TiAlN coated tubular sample having TiAlN deposited with either 50 V.

Figure 3-47 shows the overlaid GIXRD scans of the 8-layer TiN/TiAlN coated flat samples having TiAlN layers deposited with 50 V and 75 V substrate bias. Grazing incidence measurement was performed with 1° incidence angle. Figure 3-47a shows identification of the

coating layers as TiN and $Ti_{0.32}Al_{0.68}N$. Additionally, a 0.3° shifting towards lower angles is observed in TiAlN phase peaks, which is presented in enlarged GIXRD pattern in Figure 3-56b.
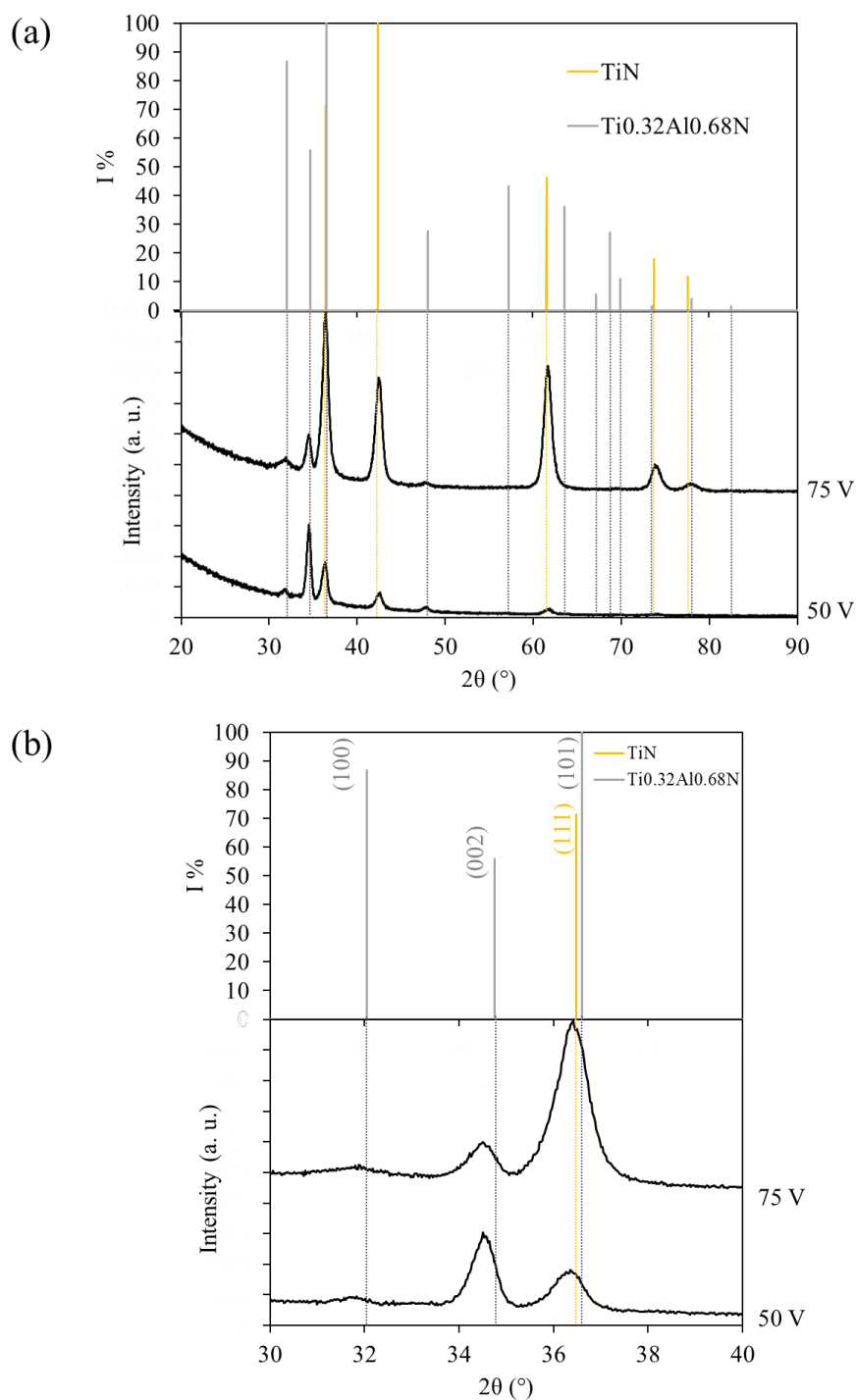
Figure 3-47. GIXRD patterns of 8-layer TiN/TiAlN coated flat and tubular samples having TiAlN deposited with either 50 V or 75 V substrate bias; (a) 2θ range: 20-90° and (b) 2θ range: 30-40°.

Finally, TEM-EDX map analysis was performed by Jing Hu at Argonne National Laboratory which showed the elemental mapping in each layer, and the columnar grain structure of the coating layers as shown in Figure 3-48.
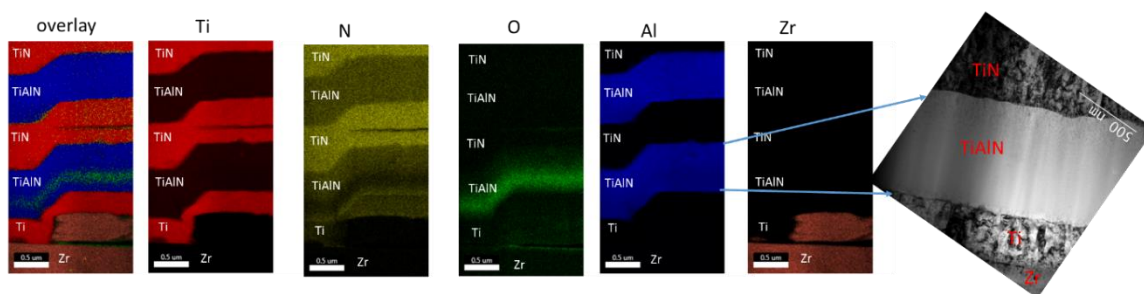
Figure 3-48. Cross-sectional sample TEM image and EDX map analysis. High magnification cross-section image revealed the columnar structure of the deposited coating and compositional variation in each layer is observed with the EDX analysis.

In summary, higher substrate bias resulted in rougher surface morphology on coated samples, leading to non-uniform coating deposition on the surface. No embedded grit was observed at the substrate and the coating interface in case of green scotch brite prepared samples, which is beneficial in terms of achieving better adhesion between the substrate and the coating. Tubular samples were shown to have thicker coatings compared to their flat counterparts, corresponding to 1.5 times more thickness. As all other parameters were kept constant but only the deposition time was varied from 35.2 to 50 min (1.4 times more duration); while depositing TiAlN layer, layer thickness also increased by ~1.4 times. There was no significant difference in coating layer thickness with substrate bias variation. Increased bias from 50 V to 75 V while depositing TiAlN layer was expected to result in an increased Al content, however no significant compositional variation was observed with EDS analysis. Increased substrate bias was also expected to increase coating density, which might have observed as a thinner coating. This thinning was observed in case of flat samples, but could not be detected in tubular samples. Decreased current from 65 A to 45 A while depositing TiN layer did not show a significant difference in EDS compositional investigation. Changing Ti/Al cathode composition from 20/80

at.% to 33/67 at.% while depositing TiAlN layer was expected to cause a decrease in the aluminum composition but no significant change could be detected with the EDS analysis. In conclusion, future coatings are decided to be deposited with 50 V substarte bias to avoid nonuniform elemental distributiona and spatter appearance that might degradade corrosion performance.

3.4.1.2. Deposition time variation

Figure 3-49 shows the cross-section SEM-BSE images of 8-layer TiN and TiAlN coatings deposited on ZIRLO® sheets with two different deposition times. Deposition of each layer was performed either with 35.2 min corresponding to 280.6 min for whole coating deposition or with 17.6 min corresponding to 140.8 min for the total coating thickness. The variation in the deposition time reflected the coating thickness as expected.
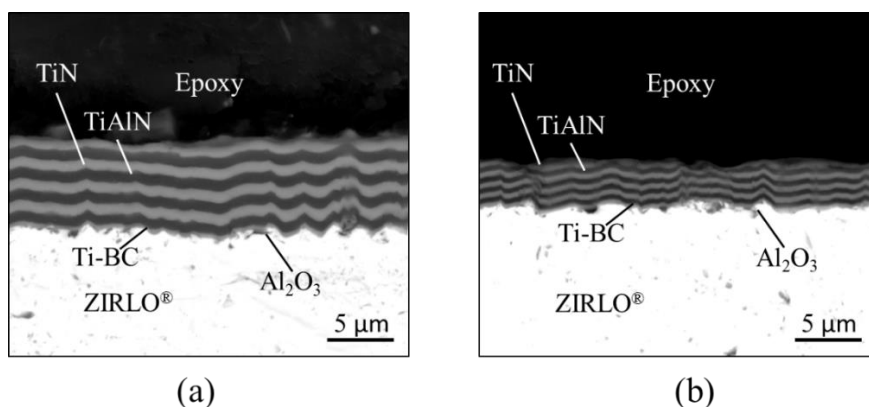
Figure 3-49. Cross-section SEM-BSE images of 8-layer TiN and TiAlN coatings deposited on ZIRLO® sheets for (a) 280.6 min and (b) 140.8 min.

Data presented in the Figure 3-50 is belong to 8-layer TiN/TiAlN coating with each layer deposited for 17.6 min. Figure 3-50 shows SEM-SE, SEM-BSE image of the scratch and corresponding load-distance data. Only one mode of failure which was identified to be gross spallation occurred. The gross spallation onset took place at ~7.9 N. Figure 3-51 shows SEM-SE, SEM-BSE image of the scratch and corresponding load-distance data performed on 8-layer

TiN/TiAlN coatings with each layer deposited for 35.2 min. Until gross spallation onset point three other damage structures were observed. First one was the buckling cracks that occurred at 2.7 N. Second one was the recovery spallation that occurred at 4.7 N. Third one, the wedging spallation, occurred at 14.7 N. Finally, gross spallation took place at 34.6 N. In conclusion, thicker coating provided better adhesion.
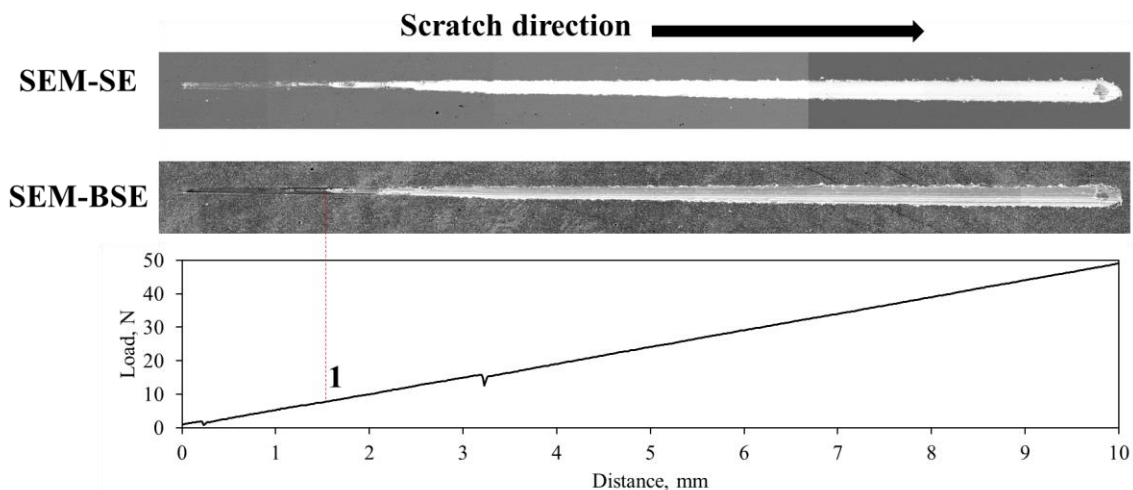
Figure 3-50. Analysis of the scratch on alumina grit blast prepared 8-layer TiN/TiAlN/Ti/ZIRLO® sheet. (TiAlN layer deposition parameters: cathode 20 at.% Ti – 80 at. % Al, 17.6 min/layer, 50 V substrate bias and 60 A source current. TiN layer deposition parameters: 150 V substrate bias and 65 A source current).
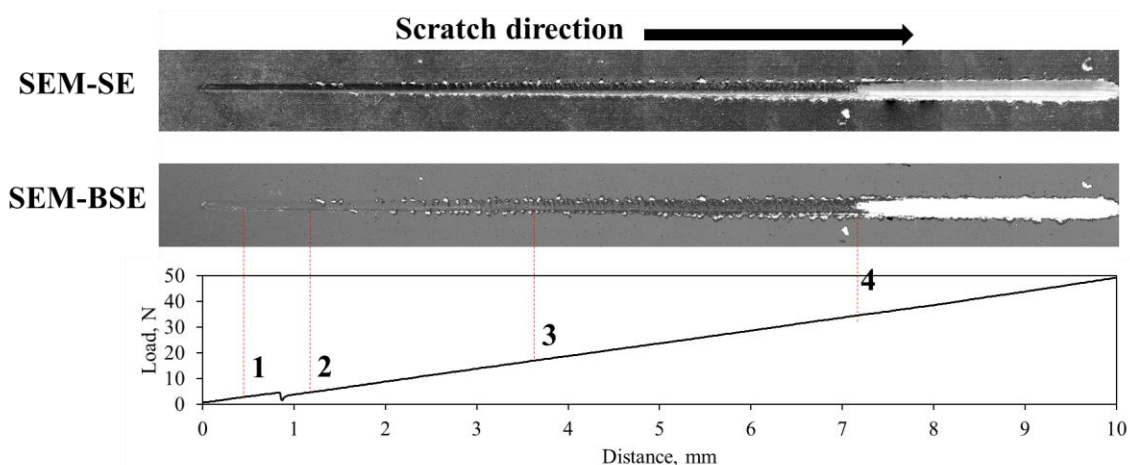
Figure 3-51. Analysis of the scratch on alumina grit blast prepared 8-layer TiN/TiAlN/Ti/ZIRLO® sheet. (TiAlN layer deposition parameters: cathode 20 at.% Ti – 80 at. % Al, 35.2 min/layer, 50 V substrate bias and 60 A source current. TiN layer deposition parameters: 150 V substrate bias and 65 A source current).

3.4.1.3. Substrate surface preparation

Scratch testing was performed on 8-layer TiN/TiAlN coatings deposited on ZIRLO®
sheet substrates prepared with either SiC hand grinding or alumina grit blasting to investigate the
effect of substrate surface preparation method on coating adhesion. Figure 3-52 shows the cross-
section SEM-BSE images of the 8-layer TiN/TiAlN coatings deposited on ZIRLO® sheets with
surfaces prepared by 400 grit alumina grit blasting (Figure 3-52a) and 800 grit SiC hand grinding
(Figure 3-52b). Cross-sectional SEM analysis showed that residual alumina grits exist on the
substrate surface, when the surface is prepared with alumina grit blasting. These grits remain at
the interface of the substrate and the titanium bond coating layer and can cause deadhesion. These
alumina residues were observed in many locations at the interface. On the other hand, samples
prepared by SiC hand grinding showed almost no residual grits at the substrate and titanium bond
coating layer interface.
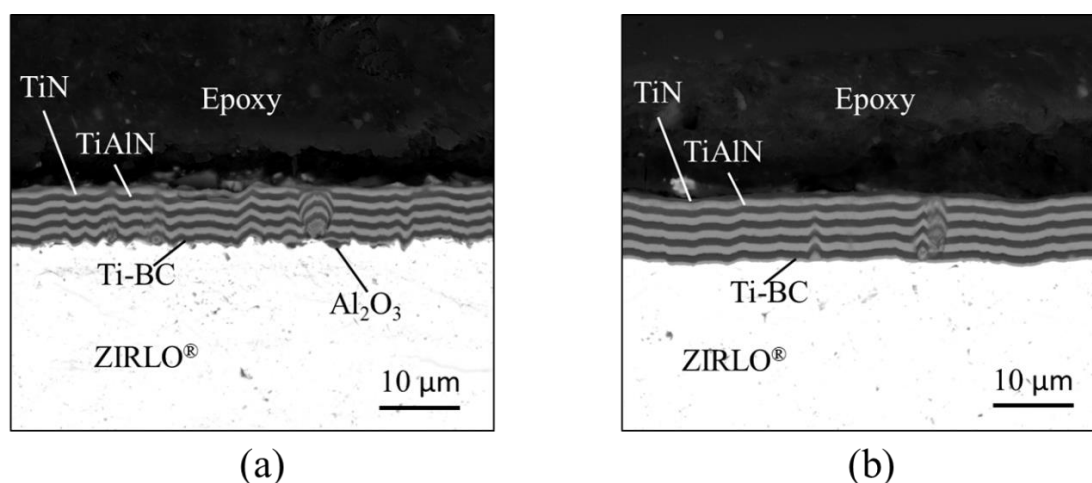
Figure 3-52. Cross-section scanning electron microscopy (SEM) – backscattered electron (BSE)
images of the 8-layer TiN/TiAlN coatings deposited on ZIRLO® sheets having surfaces prepared
by (a) 400 grit alumina grit blasting and (b) 800 grit SiC hand grinding. Alumina grit particles are
present in (a) but not in (b).

Figure 3-53 shows the EDS elemental map analysis performed on the 8-layer TiN/TiAlN
coatings deposited on ZIRLO® sheets with surfaces prepared by 400 grit alumina grit blasting
(Figure 3-53a) and 800 grit SiC hand grinding (Figure 3-53b). The EDS elemental map analysis

demonstrates uniform TiAlN and TiN layer deposition on the ZIRLO® sheet. Figure 3-53a confirmed that the residue observed at the interface was composed of aluminum and oxygen indicating it to be the alumina grit blasting procedure residue. Figure 3-53b shows an EDS map of rarely observed residue type, which showed that the residue was composed of silicon.
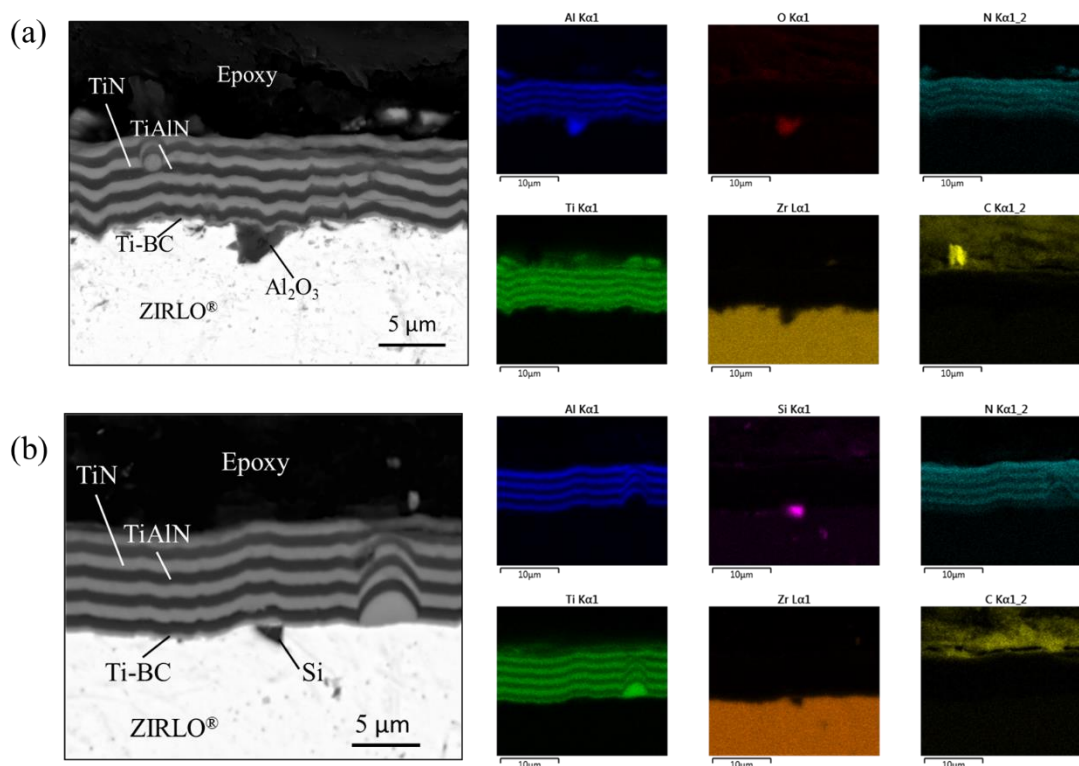
Figure 3-53. Energy dispersive spectroscopy (EDS)-elemental map analysis of the 8-layer TiN/TiAlN coatings deposited on ZIRLO® sheets having surfaces prepared by (a) 400 grit alumina grit blasting and (b) 800 grit SiC hand grinding.

The scratch testing data of alumina grit blast prepared sample was presented in Figure 3-51. Figure 3-54 refers to 8-layer TiN/TiAlN coated ZIRLO® sheet prepared with SiC hand grinding. Figure 3-54 shows SEM-SE, SEM-BSE image of the scratch and corresponding load-distance data. Until gross spallation onset point three other damage structures were observed. First one was the buckling spallation that occurred at 2 N. Second one was the lateral cracks that occurred at 8 N. Third one, the wedge spallation, occurred at 24,8 N. Finally, gross spallation

took place at 35.3 N. As expected, compared to the alumina grit blast prepared sample, SiC hand grind prepared samples showed better adhesion considering higher critical load necessary to initiate gross spallation.
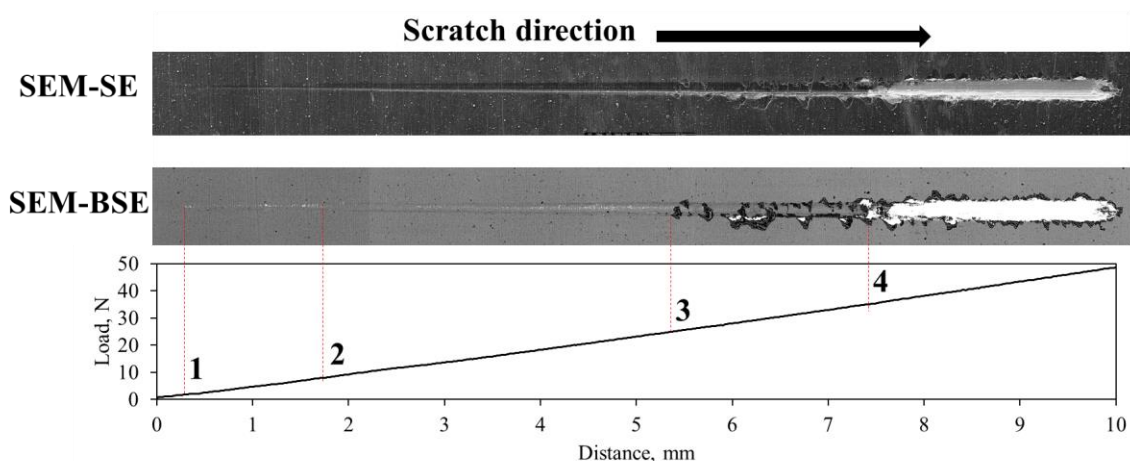
Figure 3-54. Analysis of the scratch on SiC hand grinded 8-layer TiN/TiAlN/Ti/ZIRLO® sheet. (TiAlN layer deposition parameters: cathode 20 at.% Ti – 80 at. % Al, 35.2 min/layer, 50 V substrate bias and 60 A source current. TiN layer deposition parameters: 150 V substrate bias and 65 A source current).

3.4.2. Autoclave testing and post-autoclave observations

Autoclave testing was focused on substrate surface preparation effect. Samples having substrate surfaces prepared by SiC hand grinding, SiC lathe preparation, green scotch brite grinding and alumina grit blasting were tested in static pure water at 360°C and 18.7 MPa up to 128 days. Substrate surface roughness values were adjusted to be the approximately same to be able to compare only the effect of the substrate surface preparation method. Substrate surface roughness was determined using optical profilometry. Figure 3-55 shows the substrate surface roughness values of as-received, grit blast prepared and SiC lathe prepared ZIRLO® tubes. The substrate surface roughness value was tried to be maintained around 0.25 μm R_a, which was the optimum substrate surface roughness value that was initially determined to be enhancing coating adhesion and eventually, corrosion performance. For tubular samples, the actual topography

values had substrate surface roughness values ~13 μm R_a. To be able to evaluate the substrate

surface roughness values in terms of the flat sample substrate surface roughness values that were

initially studied, cylinder form was removed from the topographical analysis.
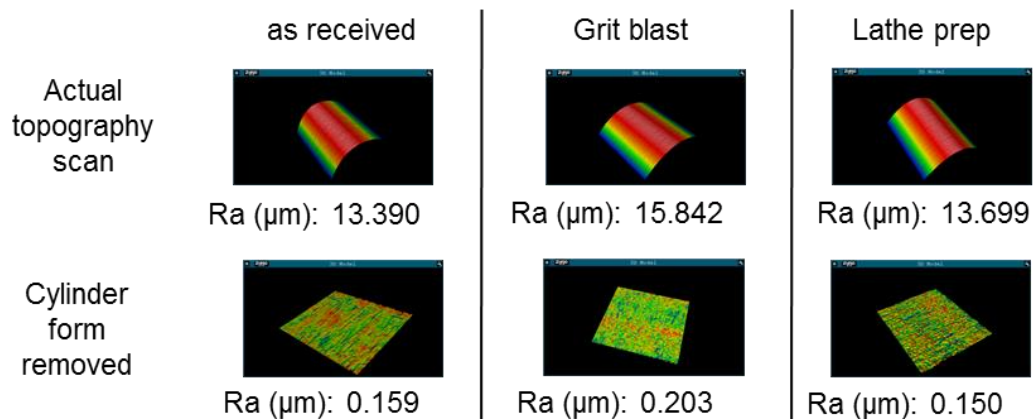
Figure 3-55. The optical profilometry results showing the surface roughness of the ZIRLO® tubes having surfaces prepared by using either alumina grit blast or SiC lathe preparation methods.

Coating deposition parameters and substrate surface preparation methods considered for

this study are summarized in Table 3-9.

Table 3-9. Substrate surface preparation method and cathodic arc physical vapor deposition (CA-PVD) parameter summary to deposit TiAlN layers in the 8-layer TiN/TiAlN coating design prepared for scratch testing. Considered parameter for each comparison group is highlighted.

Geometry	Substrate surface preparation	Deposition time (min)	Negative substrate bias (V)	Arc current, TiAlN/TiN (A)	Cathode composition (at.% Ti/Al)
Flat	SiC hand grinding	35.2	50	60/65	20/80
Tube	SiC lathe	17.6	50	60/65	20/80
Tube	Green scotch brite	35.2	50	60/65	20/80
Tube	Grit blast	35.2	50	60/65	20/80

3.4.2.1. SiC hand grinding

Autoclave tests were first performed on 8-layer TiN/TiAlN coated ZIRLO® sheets. Figure 3-56a shows the as-deposited 8-layer TiN/TiAlN coated ZIRLO® sheet. Figure 3-56b shows the image of 23 days autoclave tested sample, which had 7.1 mg/dm^2 weight gain. Color change occurred due to the oxidation as it was also observed in the case of other corrosion tested samples that were presented previously. There was no spallation or delamination of the coating. Figure 3-56c shows the average weight gain data obtained from three samples tested up to 23 days and then two samples tested up to 128 days. No negative weight gain was observed confirming no spallation of the coating.
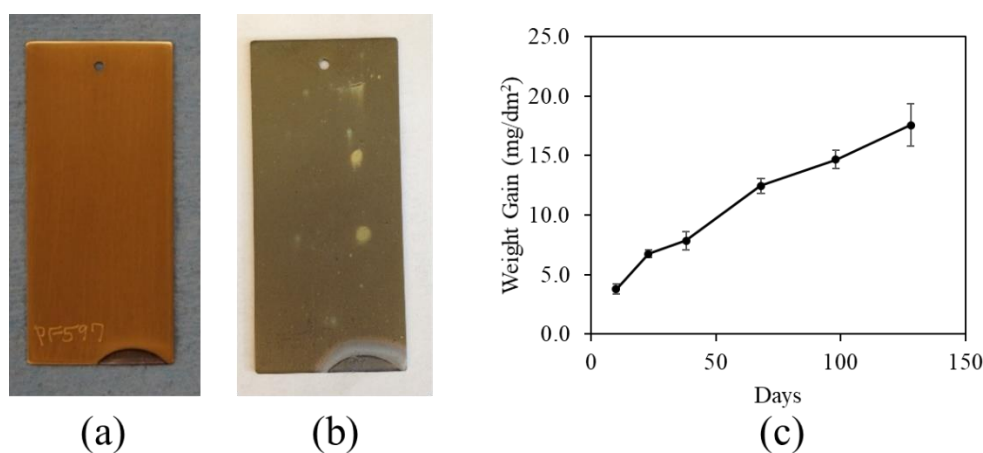
Figure 3-56. (a) Digital image of as-deposited, (b) digital image of 23 days autoclave tested and (c) weight gain data of 128 days autoclave tested 8-layer TiN/TiAlN coated ZIRLO® sheet having a surface prepared by SiC hand grinding.

Raman spectroscopy was performed to differentiate between coating and oxide phases on the surface of the as-deposited and 23 days autoclave tested 8-layer TiN/TiAlN coated ZIRLO® sheet having a surface prepared by SiC hand grinding. Figure 3-57 shows Raman spectroscopy performed on as-deposited samples and 23 days autoclave tested 8-layer TiN/TiAlN coated ZIRLO® sheet. In the as-deposited sample Raman spectra peaks were observed at 75, 216, 326,

460, 549, 620, 812 and 1121 cm^{-1}. These peaks confirmed TiN and TiAlN layers. In the case of autoclave tested samples, peaks were observed at 146, 198, 399, 446, 517, 610 and 638 cm^{-1}. These peaks are consistent with the presence of anatase and rutile phases on the surface after corrosion testing. The formation of anatase and rutile phases after corrosion test was confirmed with XRD analysis.
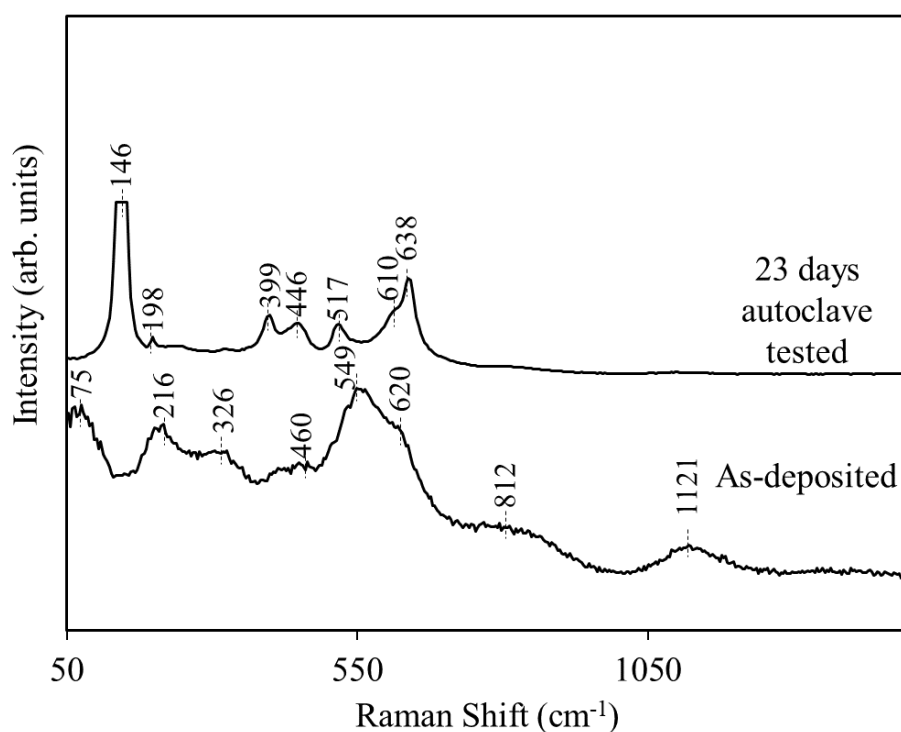
Figure 3-57. Raman spectrum of as-deposited and 23 days autoclave tested 8-layer TiN/TiAlN coated ZIRLO® sheets showing the peaks due to stokes (positive Raman shifts) scattering.

Figure 3-58 shows the X-ray diffraction (XRD) – Bragg Brentano (BB) pattern of 23 days autoclave tested 8-layer TiN/TiAlN coated ZIRLO® sheet with the surface prepared by SiC hand grinding. The ZIRLO® substrate phase was identified to be α-Zr (ICDD PDF#00-005-0665). TiN layer identified as cubic TiN (ICDD PDF# 04-015-0336) and TiAlN layer was determined to be having hexagonal Ti$_{0.32}$Al$_{0.68}$N structure (ICDD PDF# 04-017-4686). Oxide phases were identified to be anatase (A-TiO$_2$, ICDD PDF# 04-002-8296) and rutile (R-TiO$_2$, ICDD PDF# 00-

021-1276) phases confirming Raman spectroscopy results. Additionally, AlO(OH) phase was identified in the XRD-BB pattern.
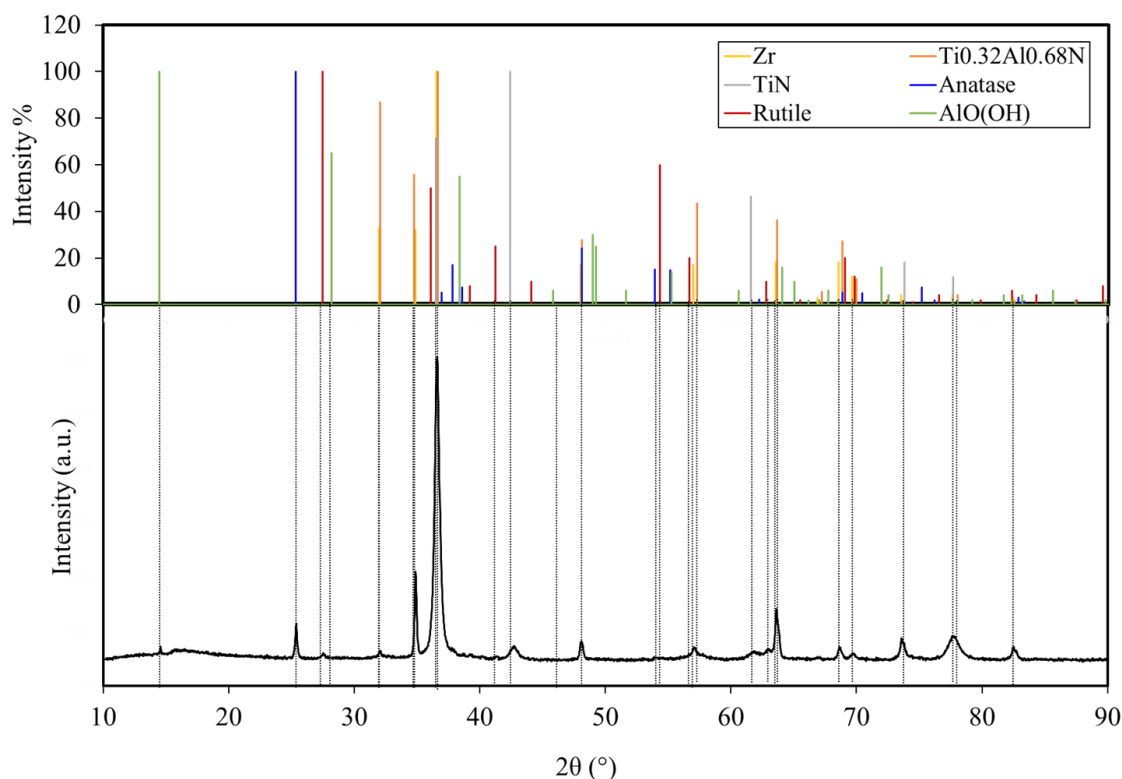
Figure 3-58. X-ray diffraction (XRD) – Bragg Brentano (BB) pattern of 23 days autoclave tested 8-layer TiN/TiAlN coated ZIRLO® sheet having a surface prepared by SiC hand grinding.

3.4.2.2. SiC lathe prepared

ZIRLO® tube surface was prepared using 800 grits SiC lathe. Figure 3-59 shows the digital images of as-deposited (Figure 3-59a), 23 days autoclave tested (Figure 3-59b), and 98 days autoclave tested (Figure 3-59c) 8-layer TiN/TiAlN coated ZIRLO® tubes having SiC lathe prepared surface. Color change was observed due to the oxidation. After 23 days of autoclave testing, some minor spallation regions on the surface was observed in a bulging appearance. These bulging regions extended after 98 days of autoclave test and lead to vast amount of spallation after 98 days of autoclave testing.

(a)　　　　　(b)　　　　　(c)
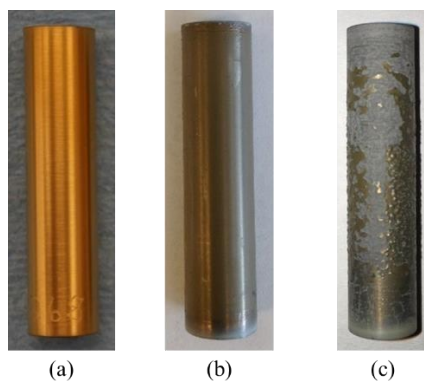
Figure 3-59. Digital images of as deposited, 23 days tested, and 98 days tested 8-layer TiN/TiAlN coatings deposited on tubular ZIRLO® substrates having surfaces prepared with SiC lathe preparation methods. Corrosion tests were performed at autoclave in static pure water at 360°C and 18.7 MPa.

Figure 3-60 shows the XRD-Grazing incidence (GIXRD) patterns collected using Cu K_α radiation. The as-deposited and 23 days autoclave tested sample grazing incidence measurements were conducted with 1° incidence angle. The 98 days autoclave tested sample grazing incidence measurement was performed with 5° incidence angle. The as-deposited, 23 days autoclave tested, and 98 days autoclave tested sample grazing incidence patterns are overlaid in Figure 3-67. The coating layers were confirmed to be composed of TiN and $Ti_{0.32}Al_{0.68}N$. After 23 days of autoclave testing, AlO(OH), anatase and rutile were determined to be formed. After 98 days autoclave testing in addition to the previously observed oxide phases, Al_2O_3 and monoclinic ZrO_2 peaks were also observed. Additionally, XRD-Bragg Brentano scan was also performed. The zirconium phase was identified to be α-Zr as before but differing from the previous XRD patterns highest intensity peak was observed to be at (101) plane of Zr, which also overlaps with the (111) peak of $Ti_{0.32}Al_{0.68}N$ and (101) peak of TiN phases. As before, anatase and rutile phases were formed at all samples. Additionally, AlO(OH) was observed at samples having vast amount of spallation.
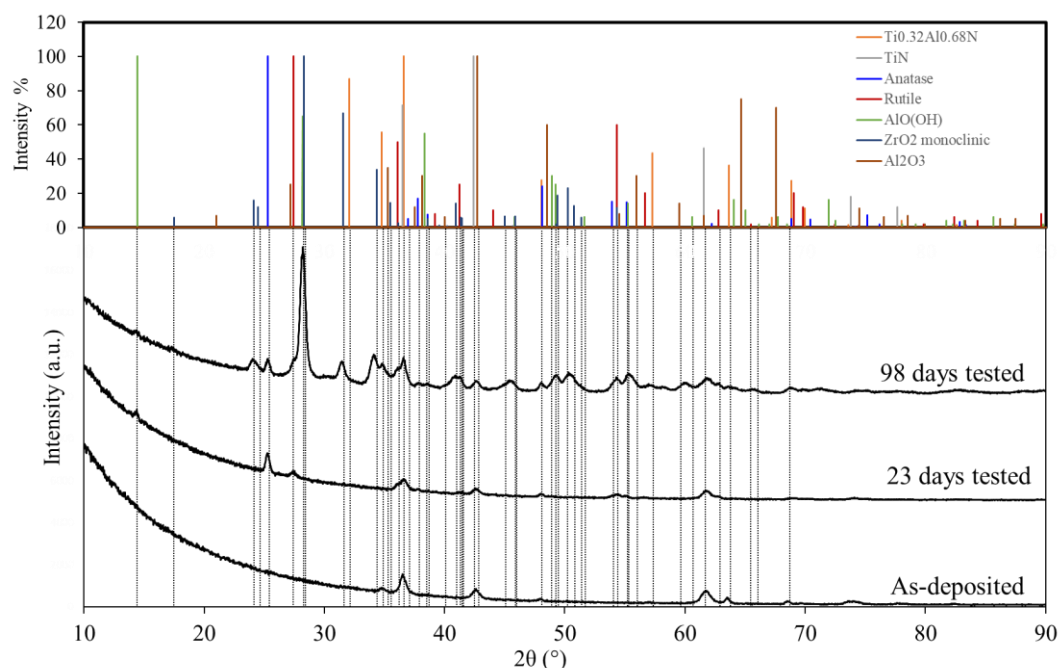
Figure 3-60. GIXRD (Cu Kα) patterns of 23 days autoclave tested 8-layer TiN/TiAlN coatings deposited on tubular ZIRLO® substrates having surfaces prepared with green scotch brite, alumina grit blast and SiC lathe prep methods.

Figure 3-61 shows the surface scanning electron microscopy images of the as-deposited (Figure 3-61a), 23 days autoclave tested (Figure 3-61b) and 98 days autoclave tested (Figure 3-61c) samples. The surface SEM images of the tested samples for two different magnifications are presented in Figure 3-61. The as-deposited sample showed a wavy structure interpreted to be mimicking the substrate surface structure. After 23 days autoclave testing, defects observed to be formed on the surface which were initially identified as bulging regions in the visual analysis. High-resolution imaging showed that these regions were small spallation regions, where the TiN top coating layer was cracked and opened the way for TiAlN layer and corrosive environment interaction, which lead to AlO(OH) crystal formation below the cracked and spalled regions. After 98 days of autoclave testing these spallation regions were extended as can be observed in Figure 3-61c, which resulted in substrate oxidation and crack formation at the edges of the spalled regions.
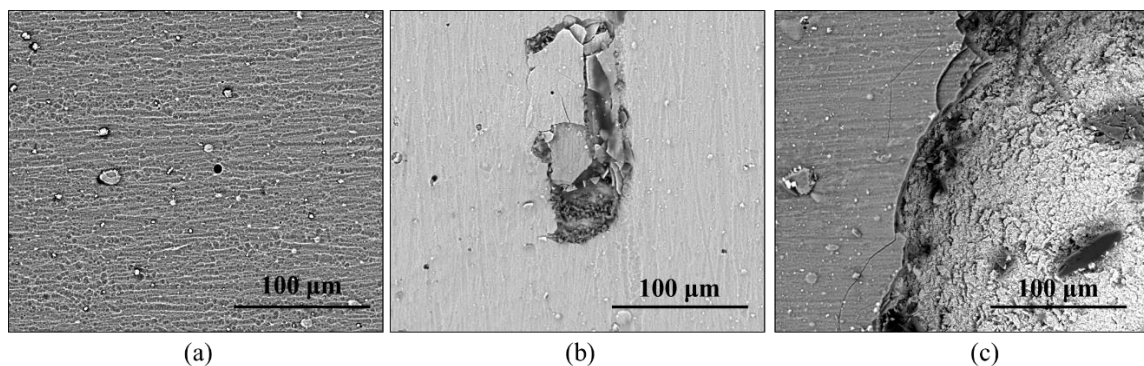
Figure 3-61. Surface SEM-Backscattered electron images of (a) as-deposited, (b) 23 days autoclave and (c) 98 days autoclave tested 8-layer TiN/TiAlN coated ZIRLO® tubes having surfaces prepared by SiC lathe method.

Figure 3-62 shows the cross-section energy dispersive spectroscopy (EDS) of the 23 days autoclave tested sample. Figure 3-62a shows the SEM and EDS analysis performed at a spallation region demonstrating the boehmite formation at the TiAlN layer, which was observed to be passing several layers of coating but still being stopped at a final successive layer showing the success of the coating. Oxidation of TiAlN layer mostly start at crater regions where the macroparticle is expelled as can be observed in cross-section SEM and EDS-elemental map images presented in Figure 3-62a. This occurs because as mentioned before, macroparticles have low adhesion to the coatings, there are gaps at the unperturbed coating and perturbed macroparticle nodule boundary which opens the way for corrosive environment to reach to lower layers of the coating. In the case of autoclave corrosion test, as water penetrates below TiN through the crater, it reacts with the following TiAlN layers leading to boehmite phase formation (Figure 3-62a) according to the reaction (1) [161]:

$$2Al + 4H_2O \rightarrow 2AlOOH + 3H_2 \qquad (1)$$
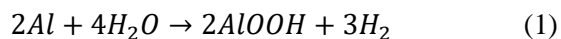
Figure 3-62b shows observation of embedded Si grits on the surface of the substrate. Figure 3-62c shows that oxidation could be stopped through the coating preventing the substrate from oxidation.
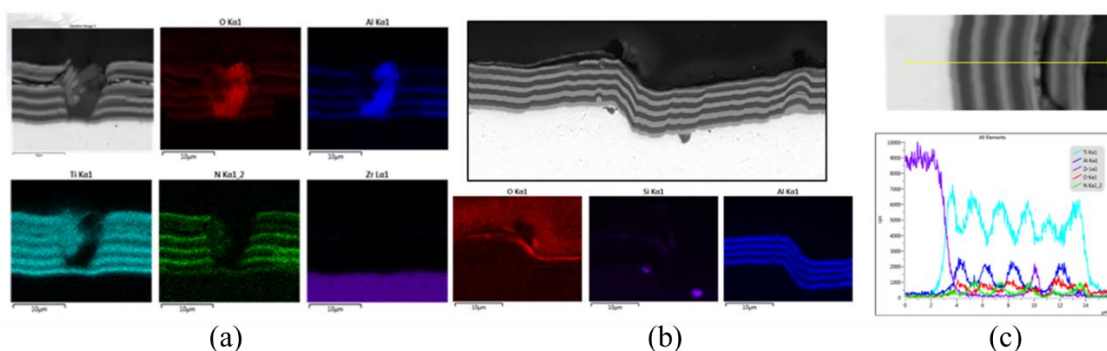
Figure 3-62. Cross-section energy dispersive spectroscopy (EDS) (a) map analysis showing the spallation region, (b) residual Si and non-uniform roughness region, and (c) EDS line scan of the 23 days autoclave tested 8-layer TiN/TiAlN coated ZIRLO® tubes having surfaces prepared by SiC lathe method.

3.4.2.3. Green scotch brite prepared

Figure 3-63 presents the digital images of green scotch brite prepared as-deposited (Figure 3-63a), 23-days (Figure 3-63b), 26-days (Figure 3-63c), and 98-days (Figure 3-63d) autoclave tested samples. Coatings had a golden color in the untested state. During the corrosion test, their color turned to blue and then, to a dull gray color due to the oxidation of the top layer. Initial coating degradation was observed as minor localized spallation points like the ones observed in the case of SiC lathe prepared samples, which later lead to larger spallation regions after 98 days autoclave testing as can be observed in Figure 3-63d.
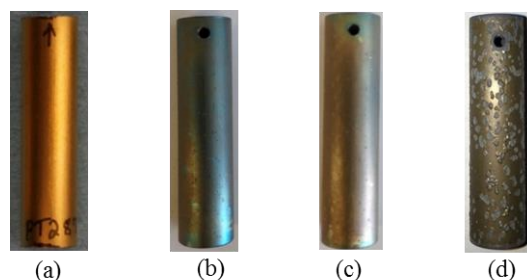
Figure 3-63. Digital images of green scotch brite prepared samples showing the coating corrosion progress on the surface through the autoclave test duration (a) untested, (b) 23 days, (c) 26 days, and (d) 98 days tested.

Figure 3-64 shows the SEM-BSE images of the 23 days, 26 days and 98 days autoclave tested samples. The coating degradation during the corrosion testing started locally by showing spallation regions having areas of ~100 x 150 μm². These spallation regions, which started to occur on the top TiN layer, were limited by successive layers that acted as an additional barrier as demonstrated in Figure 3-64a and Figure 3-64b. As the corrosive environment interacted with the TiAlN phase, boehmite phase (AlO(OH)) formed which can be observed at the edges of the spalled coatings. After 98 days of autoclave testing, spallation region enlarged, and zirconium oxidation occurred as shown in Figure 3-64c.
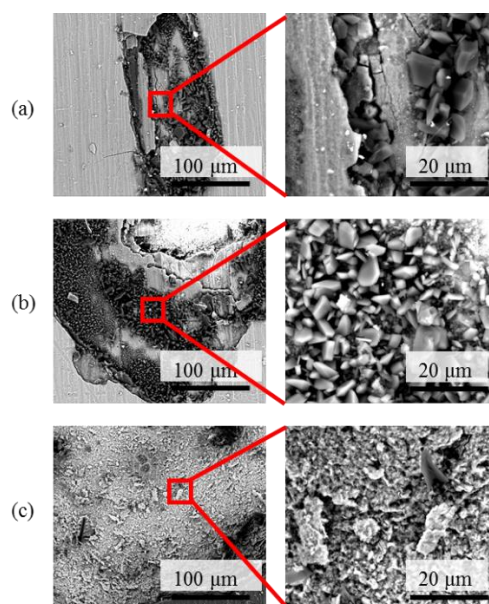
Figure 3-64. Surface SEM image of green scotch brite prepared samples showing corrosion progress on the coating after being exposed to the autoclave test in static pure at 360°C and 18.7 MPa for (a) 23 days, (b) 26 days, and (c) 98 days.

Figure 3-65a and Figure 3-65b show the EDS map analysis performed on 23 days autoclave tested 8-layer TiN/TiAlN coated ZIRLO® tube. The EDS analysis was performed at two different locations to present the corrosion behavior at spallation and no spallation regions. The spallation region EDS-elemental map analysis confirmed the surface SEM observations since with spallation at the top TiN layer, AlO(OH) formation was observed at the TiAlN layer causing cracks and delamination of the surrounding coating layer. In the case of presented EDS- map

analysis, cracks lead to the oxidation of the substrate material. Zirconium oxidation occurred with a uniform thickness at the coating spallation regions indicating that spallation did not cause a deflection in the substrate oxidation behavior. Figure 3-65b presents EDS-elemental map analysis at a region where the coating was maintained. The uniform layer thicknesses without spallation or delamination was confirmed. Figure 3-65c shows Raman spectroscopy results performed from examinations on the cross-section of 23 days autoclave tested 8-layer TiN/TiAlN coated ZIRLO® tube having a surface prepared by green scotch brite method. The optical microscopy image of the region at which the Raman spectroscopy was performed is shown in Figure 3-65c. The Raman spectrum was collected through the green line starting from the epoxy region towards the ZIRLO® substrate. Raman spectrums along the green line were collected at 1 μm increments. The overlaid Raman spectrum data at left side in Figure 3-65c presents all the data starting from epoxy. The peaks obtained at 449 and 609 cm-1 indicated rutile phase of TiO_2. Additionally, TiAlN and TiN layers were identified.

Longer oxidation durations result in excessive amount of boehmite phase formation leading to cracking of the adjacent coating and spallation of the coating layers and eventually substrate oxidation was presented for 23 days, 26 days and 98 days of autoclave testing in Figure 3-65a, b and c, respectively. This can be occurring because at high temperature as duration increases, crystallite size of the boehmite phase increases. However, d-spacing and pore size decreases. Accordingly, this may indicate a shrinkage in the phase volume as time passes at 360°C [162]. This shrinkage at the top boehmite phase could open the way for further boehmite formation at lower coating layers. Finally, the boehmite phase may be separated from the surface since there is no strong bonding in between them. Further oxidation occurs with the zirconium from the substrate at the spalled region.

Even after 98 days SEM and EDS analyses demonstrated that multilayer coating structure was maintained, and little oxygen penetration occurred. Overall, most of the coating surface remained adherent and oxygen penetration through the coating was eventually eliminated.
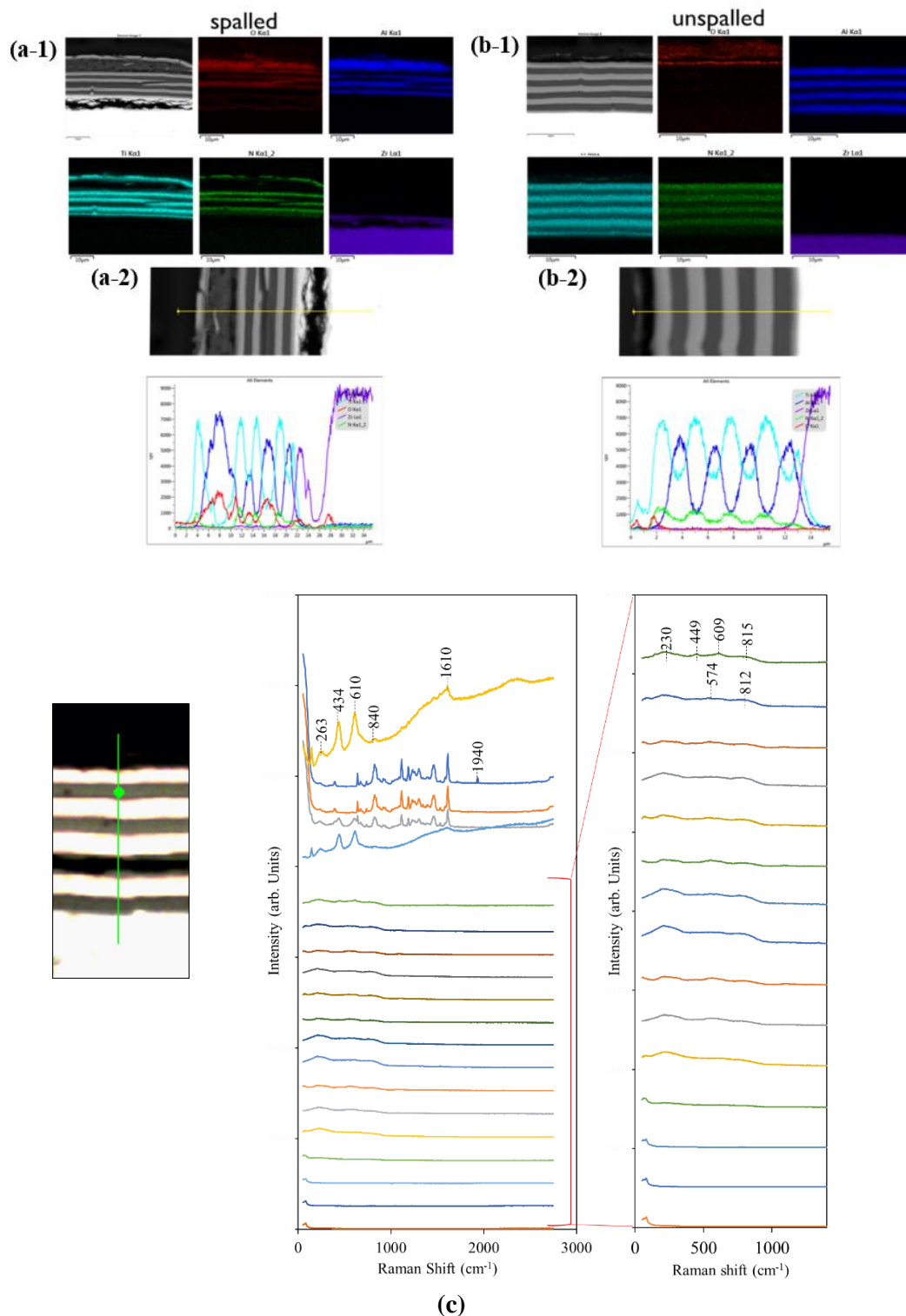
Figure 3-65. Surface analyses of the 23 days autoclave tested 8-layer TiN/TiAlN coated ZIRLO® tube having a surface prepared by green scotch brite method; (a-1) Spalled region EDS map analysis, (a-2) spalled region EDS line scan, (b-1) no spallation region EDS map analysis, (b-2) no spallation region EDS line scan, and (c) Raman spectroscopy performed on the cross-section sample along the green line indicated on the figure.

3.4.2.4. Alumina grit blast prepared

Figure 3-66 shows digital images of two sides of the as-deposited, 3-days, 10-days, 26-days 98-days and 128-days autoclave tested samples. A color change was observed after 3 days of exposure due the oxidation of the TiN layer. After 10 days, in addition to the color change, some localized spallation was observed. However, such spallation was not observed for the sample exposed to 26 days of testing. After 98-days a larger amount of spallation was observed at a localized region. This excessive spallation was not observed in the case of 128 days autoclave tested samples.
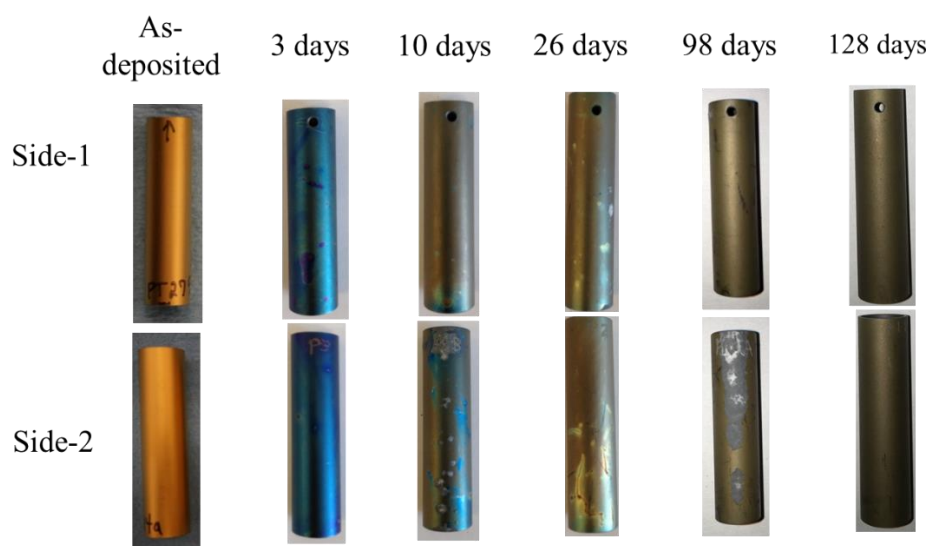
Figure 3-66. Digital images of autoclave tested (in pure water at 360°C and 18.7 MPa) 8-layer TiN/TiAlN coated grit blast prepared tubular ZIRLO® samples.

Figure 3-67 shows the X-ray diffraction (XRD) pattern obtained in Bragg Brentano scanning of as-deposited, 3 days autoclave tested,10 days autoclave tested, 26 days autoclave tested, and 98 days autoclave tested 8-layer TiN/TiAlN coated ZIRLO® tubes with surfaces prepared with alumina grit blasting. XRD-Bragg Brentano scan was performed to determine the phases formed after the corrosion testing. ZIRLO® substrate peaks were indexed as α-Zr (ICDD PDF# 00-005-0665). The outer titanium nitride phase was determined to be TiN (ICDD PDF# 04-

015-0336). The crystal structure of the TiAlN coating was difficult to confirm due to the overlap of the TiAlN peaks with the underlying peaks from the Zr substrate. After 3 days of autoclave testing, peaks corresponding to the anatase phase (A-TiO$_2$) appeared (ICDD PDF# 00-021-1272) which were attributed to oxidation of the TiN. Between 3-10 days of exposure, the boehmite phase (AlO(OH)) corresponding to ICDD PDF# 00-021-1307 formed due to localized spalled coating regions or near the metallic macroparticles. After 98 days of autoclave exposure, ZrO$_2$ (ICDD PDF# 97-002-6488) was determined to be formed in the small region where spallation of the coating occurred.
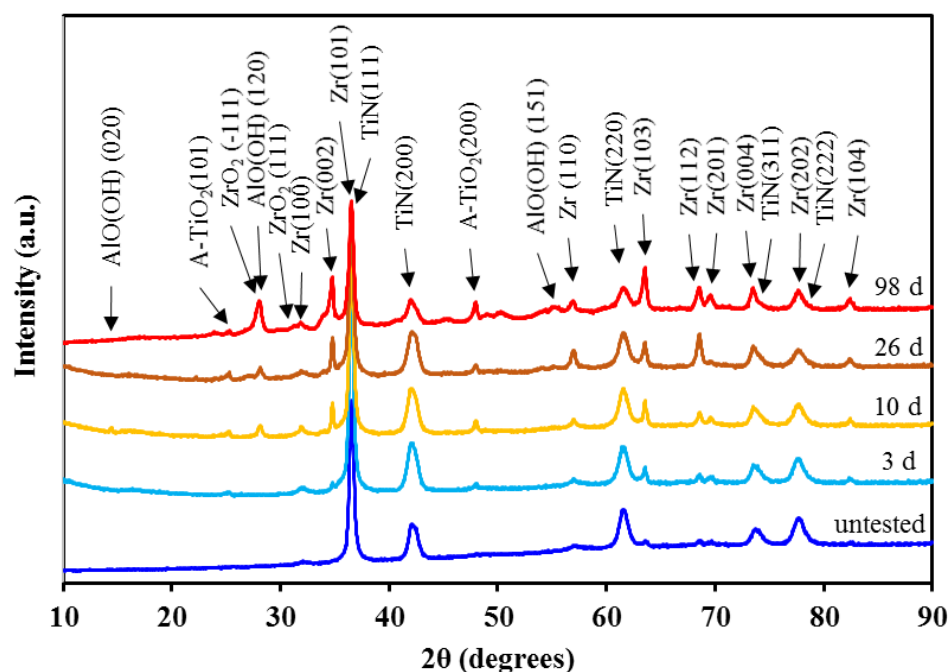
Figure 3-67. XRD-Bragg Brentano (Cu K$_\alpha$) scan patterns of 8-layer TiN/TiAlN coated grit blast prepared tubular samples that were autoclave tested in pure water at 360°C and 18.7 MPa up to 98 days.

Figure 3-68 shows the XRD-Grazing incidence patterns collected from 128 days autoclave tested 8-layer TiN/TiAlN coated ZIRLO® tube. Grazing incidence measurements were performed with incidence angles of 2° and 5°. Two different incidence angles patterns were examined to be able to evaluate phases forming on the surface at two different depths from the

sample surface. Coating layers were identified as TiN and $Ti_{0.32}Al_{0.68}N$. Oxide phases were identified to be anatase and rutile as determined with the XRD-BB analysis that was presented in Figure 3-67. Additionally, Ti_2O_3 phase was identified in the GIXRD analysis.
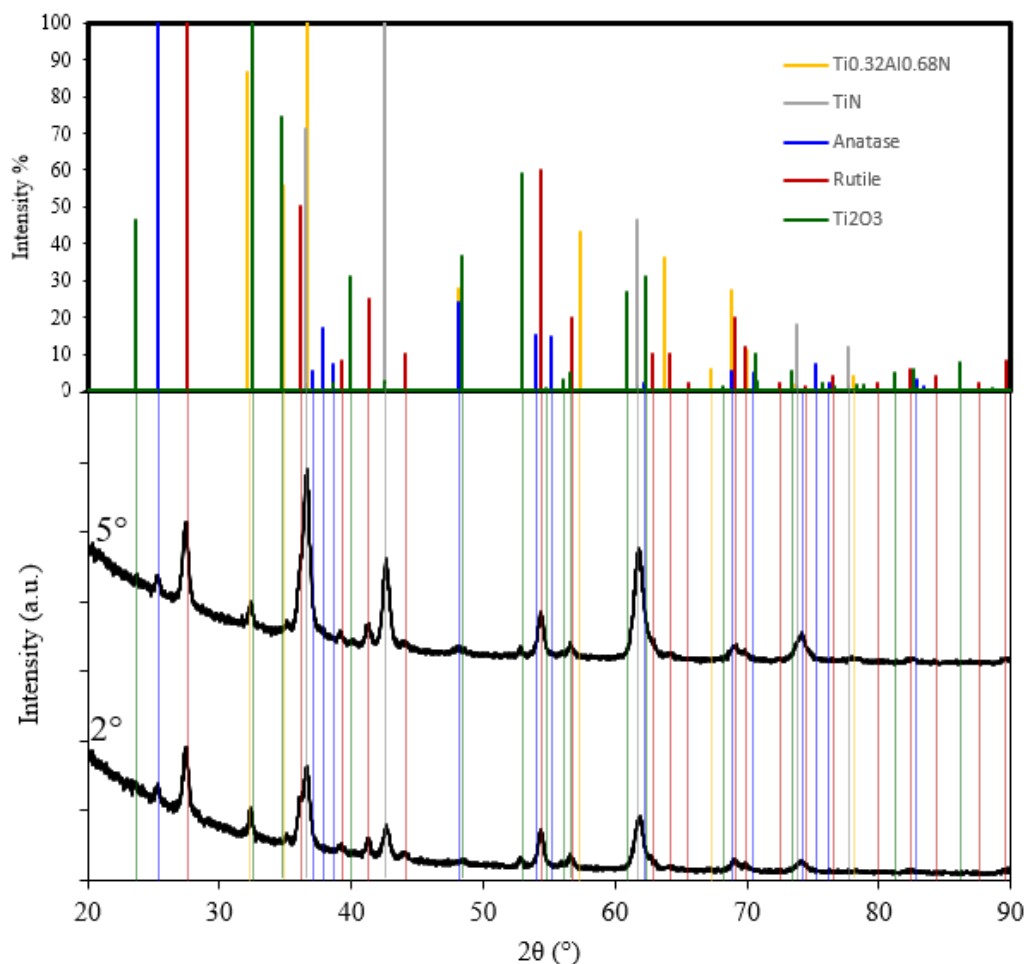
Figure 3-68. GIXRD (Cu K_α) scan patterns of 8-layer TiN/TiAlN coated grit blast prepared tubular samples that were autoclave tested in pure water at 360°C and 18.7 MPa up to 98 days. Incidences angles were 2° and 5° as indicated in the figure.

Figure 3-69 shows the surface SEM-secondary electron (SE) images of as-deposited (Figure 3-69a), 3 days autoclave tested (Figure 3-69b), 10 days autoclave tested (Figure 3-69c) and 26 days autoclave tested (Figure 3-69d) 8-layer TiN/TiAlN coated ZIRLO® tubes. SEM-SE analysis was performed to study the surface topography of the autoclave tested coatings. Considering that all the samples investigated up to now mirrored the substrate surface

topography, the grain-like topography observed on the surface of currently examined samples is attributed to the grit blasting procedures and these grain sizes were measured to be ranging from 1-5 microns.
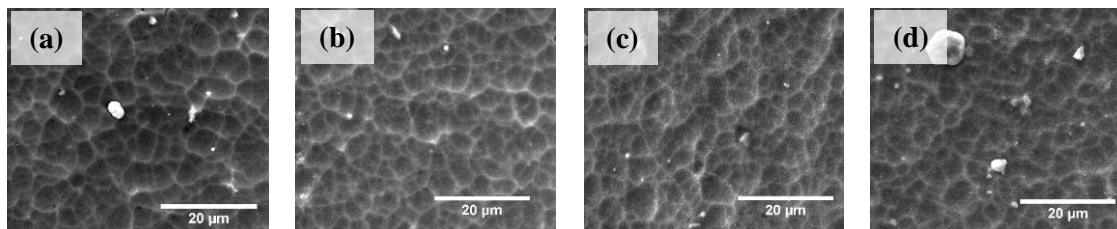
Figure 3-69. SEM Secondary electron images showing the surface morphology of the 8-layer TiN/TiAlN coated grit blast prepared tubular ZIRLO® samples in their (a) as-deposited state, and in autoclave tested state in pure water at 360°C and 18.7 MPa for (b) 3 days, (c) 10 days, and (d) 26 days.

Figure 3-70 shows the spallation surface SEM-SE images of 10-days and 26-days autoclave tested samples. In the case of 10 days autoclave tested sample (Figure 3-70a) spallation region, zirconium oxidation took place and AlO(OH) formation was observed at the edge of the spalled coating. Additionally, some fiber-like structures were observed. In the case of 26 days autoclave tested sample spallation region SEM-SE imaging, AlO(OH) phase was not observed. Zirconium substrate was oxidized as expected. Fiber-like structures were also observed in the case of 26 days autoclave tested samples. These fibers were not distributed uniformly on the spalled region. Their thicknesses varied between 0.1-1.5 µm.
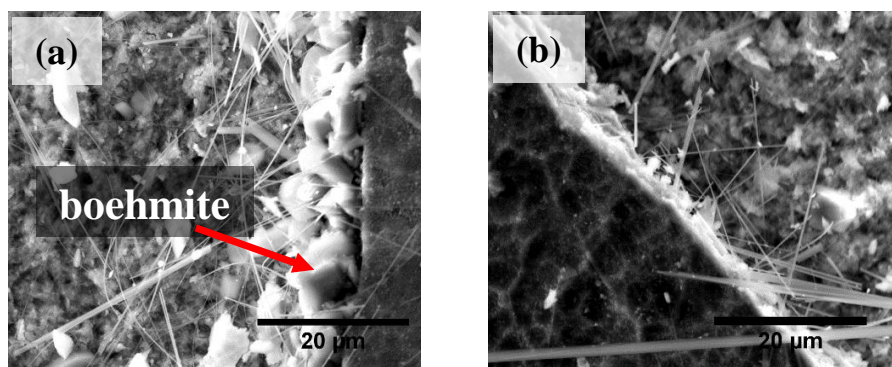
Figure 3-70. Surface SEM Secondary electron images of (a) 10 day tested and (b) 26 day tested 8-layer TiN/TiAlN coated ZIRLO® tube.

Figure 3-71 shows the EDS- elemental map analysis performed on the surface of a spallation region of the 26 days autoclave tested 8-layer TiN/TiAlN coated ZIRLO® tube. Half of the EDS image presented in Figure 3-70 shows the maintained coating on the surface and the other half shows a spallation region example. EDS analysis confirmed zirconium oxidation at the spallation region. EDS elemental analysis also demonstrated that fiber-like structures were composed of aluminum and oxygen.
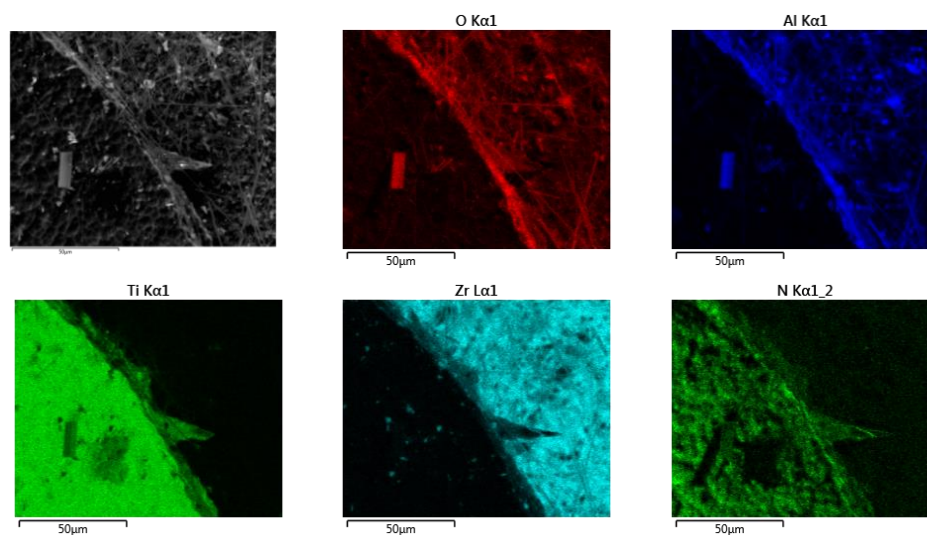
Figure 3-71. EDS Map analysis of 26-day autoclave-tested (in pure water at 360°C and 18.7 MPa) 8-layer TiN/TiAlN coated grit blast prepared tubular ZIRLO® sample.

Figure 3-72 shows the cross-section EDS- elemental map analysis (Figure 3-72a) and EDS-elemental line scan (Figure 3-72b) of the 98 days autoclave tested 8-layer TiN/TiAlN coated ZIRLO® tube. Both EDS analysis demonstrated that a uniform coating thickness was achieved. SEM and EDS map analyses presented in Figure 3-72a showed that there were embedded alumina particles from the grit blasting process at the substrate and coating interface. Nevertheless, the oxygen line scan (Figure 3-72b) demonstrated that oxygen penetration terminated near the cladding surface at the regions where the coating was maintained on the surface indicating that the coating design architecture is an excellent corrosion barrier when the

coating is adherent. 128 days tested sample results also confirmed previous results and demonstrated substrate oxidation avoidance even after 128 days.

(a)   (b)
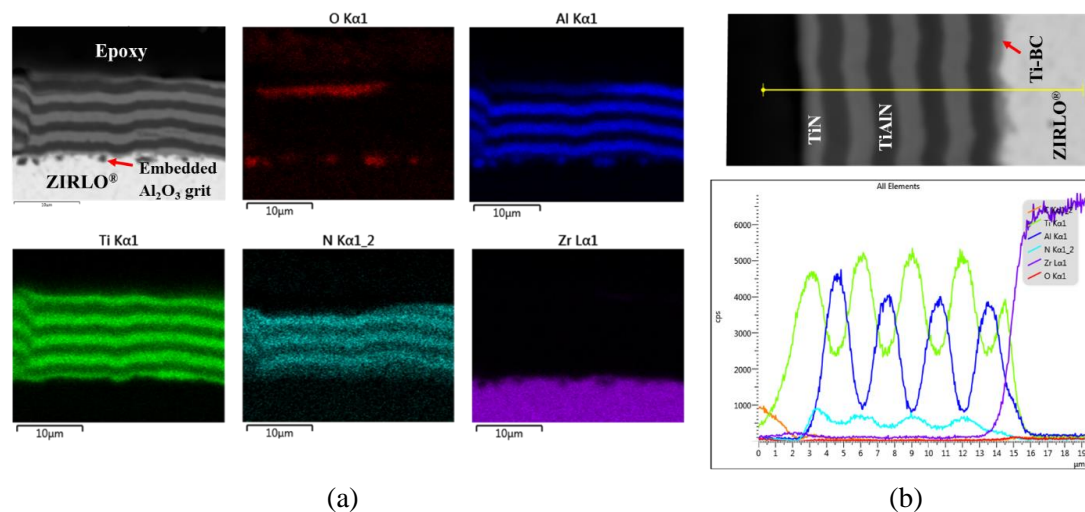
Figure 3-72. EDS analyses of 98-day autoclave-tested (in pure water at 360°C and 18.7 MPa) 8-layer TiN/TiAlN coated grit blast prepared tubular ZIRLO® sample cross-section, (a) map analysis and (b) elemental line scan.

In conclusion, although no residues were observed in the case of green scotch brite prepared samples, coatings showed widespread spallation. SiC lathe prepared showed silicon residues which can contribute to adhesion degradation. Alumina grit residues were observed in the case of alumina grit blasting prepared samples which can lead to adhesion degradation, however they seem to be performing well in the autoclave test compared to green scotch brite prepared and SiC lathe prepared. Additionally, sectioning effect was investigated, and the results are presented in Appendix D but the coating properties were observed to be uniform and there was no variation through sample sections.

3.4.3. High temperature air oxidation

Coating deposition parameters that were optimized for flat samples were applied to the outside of tubular samples and initial furnace tests were performed at 800°C air for 30 min at Westinghouse Co. Because of these corrosion tests, almost all the coatings were spalled off leading to uniform oxidation of the substrate at an amount same as the uncoated sample. Predicting the cause of spallation as stress variation between layers caused by the composition and accordingly thermal expansion coefficient variations, the coating adhesion was tried to be enhanced through functional grading of the coating layer composition. Then, the corrosion performance was tried to be evaluated through furnace tests conducted in air at 500, 600, 700, 800 and 900°C for 30 min at the Pennsylvania State University. First, functionally graded coatings were deposited as TiAlN/FG-TiN design architecture. Digital images, surface SEM and cross-section SEM images of these untested and tested samples are provided in Figure 3-73.
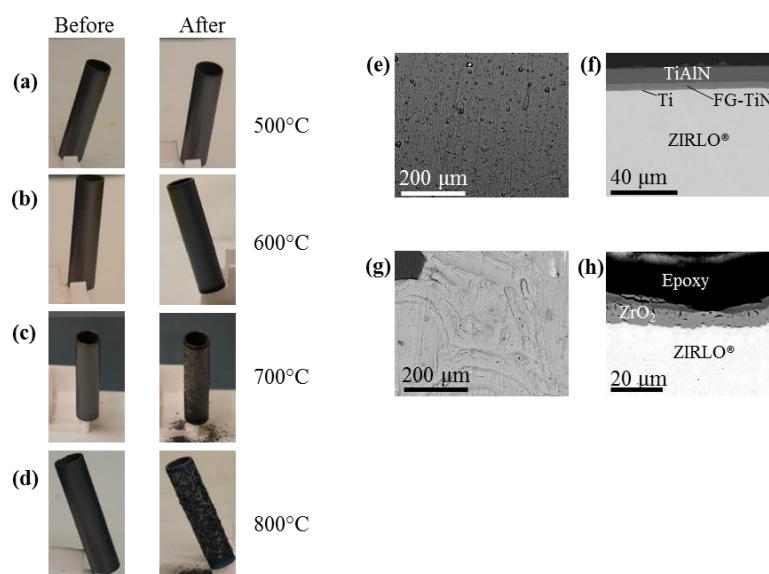
Figure 3-73. Digital images of TiAlN/FG-TiN/Ti/ZIRLO® samples that were exposed to air at elevated temperatures of (a) PT41: 500° C, (b) PT42: 600°C, (c) PT43: 700°C, and (d) PT40: 800°C at the Pennsylvania State University. SEM images of TiAlN/FG-TiN/Ti/ZIRLO® samples that were exposed to air at elevated temperatures; (e) PT41: 500° C surface, (f) PT41: 500°C cross-section, (g) PT43: 700°C surface, and (h) PT43: 700°C cross-section.

In the case of samples presented in Figure 3-73, an increase in weight was observed. After corrosion test, darkening was observed starting at 500°C, but the coatings could be maintained on surface and no substrate oxidation was observed. These observations were also valid for samples that were exposed to 600°C air for 30 min. However, they started to delaminate at 700°C. Moreover, coating cracks and spallation occurred at 700°C tested samples resulting in substrate oxidation. At 800°C, in addition to delamination, surface cracks were also observed.

Another multilayer design architecture tested in furnace at 800°C air for 30 min was TiN/TiAlN coating. The digital image of the as-deposited coating, tested coating, surface SEM image and cross-section SEM images of the tested samples are presented Figure 3-74a, b, c, and d, respectively. Initially TiN coated sample had the gold color that is significant for TiN coatings. Due to the oxidation, the tested sample changed color. In the initial visual examination performed after the autoclave test, no cracking was observed but the surface was speckled/spotted. However, SEM analyses revealed cracks on the surface, macroparticles and cross-section analysis showed uniform zirconium oxide formation underneath the cracked coating layer. The EDS-map analysis performed on the surface confirmed that the TiN coating was maintained on the surface and the macroparticles were composed of higher aluminum content. Considering that the functionally grading was less effective in enhancing the corrosion resistance, it was not applied in future generations.

(a)   (b)   (c)   (d)
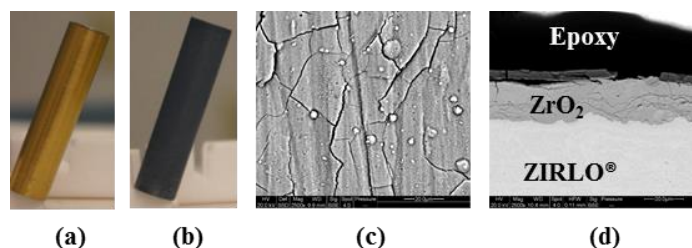
Figure 3-74. PT84- TiN /TiAlN/Ti/ZIRLO® sample; (a) digital image at as-deposited state, (b) digital image after exposure to air at 800°C for 30 min, (c) surface SEM image of tested sample, and (d) cross-section SEM-backscattered electron image of tested sample.

This chapter presented characterization results performed on as-received ZIRLO®
samples, and mechanical and corrosion test results performed on single-layer TiN, single-layer
TiAlN and multilayer TiN/TiAlN coatings deposited on sheet and tubular ZIRLO® substrates
using the cathodic arc physical vapor deposition method. Presented results exhibited the
systematic study conducted to determine the optimum deposition parameters to obtain well
adhered coatings with enhanced corrosion performance. Parameters considered for optimization
included: coating deposition time (coating thickness), substrate surface roughness, Ti-BC
thickness, nitrogen partial pressure, substrate bias, cathode composition, substrate surface
preparation method and multilayer coating design architectures. Characterization data presented
in this chapter mainly collected using optical microscopy, scanning electron microcopy, energy
dispersive spectroscopy, X-ray diffraction and Raman spectroscopy. Analysis and discussion of
the data presented in this chapter is provided in more detail in Chapter 4.

Chapter 4

Analysis and Discussion

This chapter is going to provide evaluation of the results presented in Chapter 3 regarding the mechanical and corrosion performance of the developed single-layer TiAlN, single-layer TiN and multilayer TiN/TiAlN coatings deposited on sheet and tube ZIRLO® samples using the cathodic arc physical vapor deposition method. The investigated parameters through the determination of the optimum parameters to enhance mechanical and corrosion performance involved (i) coating deposition time (coating thickness), (ii) substrate surface roughness, (iii) Ti-BC thickness, (iv) nitrogen partial pressure, (v) substrate bias, (vi) cathode composition, (vii) substrate surface preparation method and (viii) multilayer coating design architectures.

4.1. Coating deposition parameter optimization

4.1.1. Coating deposition time (coating thickness)

In section 3.2.1.2, a directly proportional relationship between the deposition time and the coating thickness was observed. The scratch test showed that an increase in coating deposition time from 150 min to 300 min led to an increase in the critical load to gross spallation from 17.84 N to 49.3 N (Figure 3-5). Further increasing the deposition time to 450 min resulted in no gross spallation during the scratch test, which were performed up to a load of 50.4 N. This result demonstrates that as the deposition time and the coating thickness increase, higher critical loads are required to cause gross spallation of the CA-PVD deposited TiAlN coatings. Some studies on TiN coatings deposited on various substrates showed that coating thickness and the critical load to cause gross spallation are inversely proportional [141]. This is because of the larger residual

stresses in the case of thicker coatings which reach their practical adhesion stress value with a lower applied stress [141]. However, this work supports that the relationship between the coating thickness and the critical load value to cause the gross spallation is directly proportional. It should be noted that ZIRLO® has a hardness of 212 HV [163] and CA-PVD TiAlN coating has a hardness of 2720 ±314 HV [164]. Thus, the evidence shown in section 3.2.1.2 suggests that higher critical load requirements in samples having thicker coatings, is due to extensive substrate deformation prior to the coating delamination [141].

Figure 3-20 presented the results obtained after autoclave corrosion testing of TiAlN coatings with four different coating thickness values. There are some examples of increased corrosion performance with increased coating thickness in literature such as tin coating on Zircaloy-4 [45], however there was no systematic study on the coating thickness effect on the corrosion performance of the CA-PVD deposited TiAlN coating on ZIRLO® substrates. Due to the residual stresses in the coating and nonuniform oxide formation on the surface, it is expected that there is an optimum coating thickness to enhance corrosion performance, as shown in Chapter 3. As discussed in Chapter 3, weight gain analysis can be used to evaluate the corrosion performance of materials. However, in the case of coatings, weight gain analysis is not sufficient due to possible coating spallation which make kinetic analysis useless.

For the coating deposition time parameter, it is evaluated that longer coating deposition time leading to the thicker coatings provides better mechanical and corrosion performance. Better mechanical performance with thicker coatings is due to a combination of high load-bearing capability of the thicker hard coating and ductile substrate deformation prior to the coating spallation. Higher corrosion performance achieved with the optimum coating thickness value of 12 µm can be attributed to the sufficient coating remaining after aluminum depletion occurring on the surface and an optimum amount of residual stress in the coating.

4.1.2. Substrate surface roughness

The optimum substrate surface roughness value was investigated based on visual observations which are partially presented in Figure 3-19 and weight gain data presented in Figure 3-20, obtained from autoclave corrosion testing. Spallation occurring at lowest substrate surface roughness value of 0.1 μm R_a, indicated low adhesion between the coating and the substrate. This can be attributed to the lack of mechanical interlocking between the substrate and the coating. The evidence shown in section 3.2.1.2 showed that rougher surfaces had higher weight gain indicating higher oxidation with less spallation. The increased oxidation can be attributed to the poor coverage of the substrate surface with coating due to deep valleys that cannot be filled during the orthogonal ion bombardment. Another reason for increased oxidation may be nonuniform coating deposition due to deposition rate variation based on surface roughness [140]. The evidence shown in Section 3.2.1.2 suggests that the reason of enhanced corrosion performance in the case of 0.25 μm R_a can be the mechanical interlocking between the substrate and the coating, and full surface coverage during coating deposition without any unfilled valley [165].

4.1.3. Titanium bond coating thickness

Another parameter considered to enhance coating adhesion and corrosion performance was the application of titanium bond coating layer in between the substrate and the coating layer. This is a technique that has been considered in literature for several applications [70,75,99,106,108,110]. Specifically, the effect of titanium usage as a bond coating layer on TiN coatings on various stainless steel substrates [108–111] was also studied and Bull et al. [108] demonstrated adhesion improvement with titanium interlayer application. Figure 3-21 showed titanium bond coating thickness affected corrosion performance. Negative weight gain occurred

at lower titanium bond coating thicknesses because of coating spallation indicating weak adhesion between substrate and the coating. However, with increasing bond coating thickness, it is possible to avoid coating spallation, indicating enhanced adhesion between the substrate and the coating. As a bond coating layer, the role of titanium is to dissolve weak native oxide (chemical gettering effect) and decrease shear stresses at the substrate-coating interface due to its ductile nature [108,110]. Bemporad et al. [166] showed that titanium interlayer thickness affects wear and hardness properties of TiN coatings and emphasized the importance of optimizing titanium thickness to benefit from its ductility to absorb intrinsic and extrinsic stresses.

However, no work has been done to investigate the effects of Ti interlayer deposited by CA-PVD between either a TiAlN coating or a TiN coating and its thickness on the corrosion resistance of ZIRLO® substrates. Compared to other PVD techniques, depositing species in CA-PVD have higher kinetic energies leading to higher compressive stresses, and these values are affected by various parameters including the type of coating and the coating thickness. Hence, the bond layer thickness should be tailored according to the type of substrate, type of coating and coating thickness in order to be able to absorb stresses associated with the coating formed during the deposition and operation. If the bond coat is too thin, it cannot absorb extrinsic (thermal) stresses associated with coating degradation exposed to extreme environmental conditions such as oxidation, moisture, or elevated temperatures. SEM examination confirms that there were delaminated regions, indicating poor coating adhesion; cracks were observed around delaminated regions which are attributed to stresses caused by oxide formation of the underlying ZIRLO® substrate.

For the titanium bond coating thickness parameter, it is evaluated that 0.6 μm bond layer/coating thickness value combinations provided good protection for increased durability against cladding corrosion under the autoclave conditions selected due to the absence of delamination and the minimal weight gain.

4.1.4. Nitrogen partial pressure

Additionally, the effect of the nitrogen partial pressure effect was investigated. Increased nitrogen partial pressure led to increased weight gain indicating lower corrosion performance. This can be attributed to the increase in aluminum content of the coating with increased nitrogen partial pressure [86] resulting in increased non-protective boehmite formation with increased nitrogen partial pressure.

For the nitrogen partial pressure parameter, it is evaluated that 1.6 Pa is the optimum value due to lower oxidation achieved.

4.1.5. Substrate bias

As it was mentioned in Section 2.3, electrons have higher mobility than ions. For that reason, first electrons move towards the substrate and we apply negative biasing to repel electrons and accelerate positive ion flux towards the substrate surface [80]. Additionally, we perform reactive deposition in nitrogen atmosphere and to achieve the compound formation, energy on the surface, which is equal to the difference between energy fed to and emitted from the surface, should be bigger than the formation energy (Enthalpy of formation of TiN, cubic TiAlN and hexagonal TiAlN are -333, +50 and +50 kJ/mol, respectively [167]) and less than the dissipation energy [140]. So, substrate bias is also effective in controlling the surface reaction intensity because energy fed to surface is calculated according to the reaction 2 [140]:

$$E = E_0 + \phi e Z \qquad (2)$$

Where E is the energy fed to the substrate surface, E_0 is the ion energy acquired at the cathode spot, Φ is the substrate bias and eZ is the ion charge.

The substrate bias effect on as-deposited single layer TiAlN coating properties were presented in Section 3.2.1.4. As shown in Figure 3-11, macroparticles with sphere-like structure

in the case of 0 V, macroparticles with perturbation in the case of 50 V and a spattered appearance on the surface was observed in the case of 100 V substrate bias. A sphere-like structure indicates solidification of macroparticle before arriving on the surface [150] or a passive deposition without a force to damage the shape of the macroparticle. Perturbation of macroparticles observed in the case 50 V can be attributed to arrival on surface in liquid state [150] or distortion in its geometry due to substrate bias. However, cross-section SEM images of coatings deposited with 100 V, showed a much thinner coating indicating that backscattering of ions were more dominant during coating deposition. So, the spatter appearance can be attributed to the backscattering of ions instead of liquid macroparticle deposition on the surface. Substrate bias effect on the amount of macroparticles were previously demonstrated in literature [168–171]. Paldey et al. [171] attributed increase in macroparticle amount to the increase in aluminum content in the coating. Kale et al. [170] attributed the high value of macroparticles at medium bias to the positive charging of macroparticles due to collisions with ions with increased velocity; whereas, macroparticle amount decrease at high bias voltage was attributed to evaporation of them before reaching to the substrate because of excess ion energy. In this study, no significant aluminum content variation was observed during the EDS analysis. Thus, the lower macroparticle amount with increased substrate bias could be the negative charging of the macroparticles in the plasma and repelling at the substrate surface [168] or evaporation due to high ion energy collusion [170].

In the XRD patterns presented in Figure 3-15, as we consider (111) peak of the $Ti_{0.5}Al_{0.5}N$ phase, we see that it is slightly shifted to lower angles and broadened as we go higher substrate bias values. One of the reasons for this is the higher titanium content in the coating at higher substrate bias values resulting in expansion of the lattice parameter compared to lower aluminum content state [172,173]. We have higher titanium content at higher bias because titanium ionization is higher compared to aluminum [140,86] and in the case of backscattering on the surface titanium is backscattered less compared to aluminum ions since titanium is heavier

[70]. Another reason is the complex residual stress state in the coating involving high compressive stresses in normal direction to the coating due to higher energy ion bombardment with increased substrate bias leading to lattice expansion parallel to the surface because of the Poisson's effect [174]. This high ion energy bombardment is also the reason of peak broadening at higher substrate biases [173]. Since the data presented in Figure 3-15 are grazing incidence patterns, it is not convenient to talk about preferred orientation, but it should be mentioned that {002} texture is observed at lower substrate bias, but {100} texture is observed at higher substrate bias values. Change of texturing with substrate bias was also observed by Ahlgren et al. [82,85]. The texturing occurrence can be attributed to the driving force to lower the overall coating energy [85].

The failure modes observed during the scratch testing of the single-layer TiAlN coatings deposited with the four different substrate bias values (0, 25, 50 and 100 V) were presented in Figure 3-16. Lowest adhesion performance with early gross spallation was expected in the case of TiAlN coating deposited with 0 V substrate bias due to its porous structure (Figure 3-12) associated with rough surface topography due to macroparticles covering the surface (Figure 3-11). However, no gross spallation was observed, which may be attributed to a resilience achieved in the coating against being depressed crushed by the scratch testing stylus due to the porous structure of the coating. The evidence shown in the 3.2.1.4 demonstrated that coatings deposited with 50 V substrate bias exhibited the best performance compared to others based on the as-deposited coating properties and mechanical performance. The higher critical load required for gross spallation in the case of 50 V substrate bias compared to 25 V can be attributed to the increased coating adhesion because of ejection of metal ions from the surface or penetration to the substrate lattice during ion bombardment leading to surface roughness and defects that can enhance coating adhesion [70]. The decreased critical load in the case of 100 V could be attributed to increased surface roughness [175].

Opposing to the mechanical performance results, increasing substrate bias from 50 to 100 V resulted in lower weight gain as shown in Figure 3-22. Lower weight gain can indicate better corrosion performance. However, it should be noted that lower weight gain can also occur because of spallation of weakly adhered top layers of the coating, which requires further characterization.

Additionally, substrate bias effect was investigated for 8-layer TiN/TiAlN coatings deposited on ZIRLO® sheet and tubes in section 3.4.1.1. There was no obvious coating property difference because of 50 V and 75 V deposited samples. Instead the main differences observed in investigated samples in this section originated from substrate geometry. Coating thicknesses varied for flat and tubular samples as shown in Figure 3-45. Total coating thickness deposited on tubular samples was ~1.6 times thicker than flat samples (Table 3-8). This thickness increased to ~1.7 times in the case of TiN layer deposition. The reason of obtaining thicker coating can be attributed to the increased number of ions captured in the case of tubular samples since the equilibrium sheath thickness is smaller for cylinder geometry according to the Child-Langmuir law [176,177]. Substrate bias increase leads to sheath thickness increase [177], which might have cause repelling of more positive metal ions leading to thinner coating in the case of flat substrates with -75 V substrate bias (Table 3-8), but this effect was not that obvious in the case of tubular geometry which can be attributed to the fact that as the radius of curvature decreases causes maximum sustainable voltage drops [177]. Additionally, CA-PVD is a line-of-sight procedure, in which the ions deposit to the surface orthogonally. In the case of tubular samples, because of the cylindrical geometry, ion arrival angle on the surface might vary from the perpendicular angle.

The evidence shown in sections 3.2.1.4 and 3.4.1.1 suggests an optimum substrate bias value for achieving dense coatings with better corrosion and mechanical performance. For the substrate bias parameter, it is evaluated that 50 V is the optimum value due to dense coating obtained with higher mechanical properties.

4.1.6. Cathode composition

In plasma deposition, TiAlN is deposited as a metastable and the amount of titanium atoms replaced by aluminum atoms can be controlled through cathode composition, evaporation rate and other deposition parameters [70,167]. Figure 3-48 shows the columnar grain structure of the deposited coatings. Dense, pore-free, columnar grains are common for arc deposited coatings because of the high ion density and resulting high ion-plating effect [178]. Since the coating microstructure is independent of the cathode microstructure [179], only the cathode composition effect was investigated in the current study. The results regarding the cathode composition effect investigation were presented in Section 3.2.1.3 for single-layer TiAlN coatings and in Section 3.4.1.1 for 8-layer TiN/TiAlN coatings. In the case of single-layer TiAlN substrate bias was 50 V and arc current was 60 A. In the case of 8-layer TiN/TiAlN deposition, substrate bias was 75 V and arc current was 45 A. The difference between the select substrate bias and arc current values used during single-layer and 8-layer coating deposition made it inconvenient to directly compare the properties of these coatings.

For cathode compositions of 20 at.% Ti – 80 at.% Al and 33 at.% Ti – 67 at.% Al, we obtained single-layer TiAlN coatings having Ti/Al ratio ~4 and ~2 as shown in Table 3-2, because cathode composition dictates [70]. Surface SEM image of single-layer TiAlN coatings presented in Figure 3-6 showed that coatings deposited with 20 at.% Ti – 80 at.% Al had more macroparticles compared to the single-layer TiAlN coatings deposited with 33 at.% Ti – 67 at.% Al. The number and size of macroparticles claimed to be decreasing with increasing cathode melting point [180–182]. Thus, since pure titanium, $Ti_{0.33}Al_{0.67}$, $Ti_{0.20}Al_{0.80}$ and aluminum have melting points of ~1670°C, ~1660°C , 1678°C and ~660°C, respectively [183], one would expect to have less macroparticles in the case of 80 at.% Al cathode. However, we observed the opposite and considering that the main difference between the two coatings deposited with two different cathodes was the increased aluminum content in coating deposited with the 80 at.% Al cathode,

the increased macroparticle amount in the case of 80 at.% Al cathode can be attributed to the increased aluminum content in the cathode [171].

The cathode composition effect on the coating was also investigated through Raman spectroscopy which is based on the lattice vibration frequency of molecules. The Raman spectra of the stokes side was presented in Figure 3-7 [184]. Scattering occurring at the acoustic range (150-300 cm^{-1}) is attributed to the titanium ion vibrations and at the optic range (400-650 cm^{-1}) is attributed to the vibration of light nitrogen atoms in TiN structure [184,185]. As aluminum is added to a TiN system, molecule becomes more complex leading to vibration-induced changes in its electronic polarizability. If the crystal structure of the coating was a perfect FCC structure, we would not be able to obtain first-order Raman spectra of TiAlN because of every ion being at a site of inversion symmetry (O$_h$ symmetry) [186]. However, because of defects existing in PVD coatings, first-order Raman spectra becomes possible for these coatings [184,187]. As we increased the aluminum content in the coating by using a 80 at.% Al cathode, we observed that the total spectral density in the gap region between the acoustic and optic modes increases. Peak shifting and broadening can be attributed to the increased amount of stoichiometric defects and increased density of first- and second- order spectra density [184,187]. Additionally, GIXRD patterns presented in Figure 3-8 showed that cubic crystal structure obtained in the case of 67 at.% Al cathode whereas hexagonal crystal structure obtained in the case of 80 at.% Al cathode. Peak broadening indicated reduced crystallinity as it was also observed in literature [107].

The effect of cathode composition effect on the coating composition was not that obvious in the case of 8-layer TiN/TiAlN coatings. However, shifting towards lower angles and texturing were observed ones again as discussed in the case of single-layer coatings.

Scratch testing results presented in sections 3.2.1.3 and 3.4.1.1 showed that higher critical load values are required to cause gross spallation in the case of coatings deposited with cathode having a 33 at.%Ti-67 at.%Al composition. This can be attributed either to the increased hardness because of more aluminum concentration in TiAlN coating leading to higher microhardness

difference between the substrate and the coating, and eventually critical load decrease [99] or to the lower surface roughness and better coating integrity due to less macroparticle that can be attributed to less aluminum content [86,171,175].

Furthermore, as we compare critical load value to cause gross spallation in single-layer and multilayer coatings, we see that multilayer coatings require lower critical load which can be attributed to less Hertzian stress distribution due to thinner layers in the case of multilayer coatings.

In summary, this work support the idea that coatings should be deposited with cathode having a 33 at.%Ti-67 at.%Al composition, because it provides lower amount of macroparticles and better mechanical performance.

4.1.7. Substrate surface preparation method

Another parameter considered to enhance coating corrosion performance was the substrate surface preparation method and the results were presented in section 3.4.1.3. The oxidation observed on the green scotch brite prepared samples were in nodular form. Green scotch brite pad involves alumina as in the case of alumina grit blasting. However, the green scotch brite had a 240-grit size which corresponds to 50 microns, while alumina grit blast grit size was 400 which corresponds to 18.3 microns. Larger grit size might have resulted in higher roughness at the interface of the substrate and the coating, which may have deteriorated coating adhesion. The blister diameter of ~0.2 mm was observed in the case of grit blast prepared tubular sample surface after 23 days of autoclave test, while green scotch brite prepared samples did not show these blisters. However, after 98 days of autoclave test, grit blast prepared samples showed a localized spallation, while green scotch brite samples showed a nodular type of corrosion uniformly distributed almost all the tubular sample surface. The localized spallation observed along a line on the grit blast prepared samples can be attributed to the cracking of the coating

because of thermal stresses, lower adhesion caused by residual stresses or non-protective iron and chromium oxides observed to be forming on the surface because of contamination during autoclave testing. The loosely adhered fiber like structures observed in the case of grit blasted samples after corrosion was identified to be involving aluminum and oxygen as shown in Figure 3-70. These fibers are in agreement with the bayerite ($Al(OH)_3$) structures observed in literature with 1 µm diameter and vertical crystal growth [188]. These bayerite fibers were observed only after corrosion testing of alumina grit blast prepared samples, and only at the complete coating spallation regions. This indicates that they are formed on the oxidized ZIRLO® surface because of corrosion of alumina residues embedded on the substrate surface (Figure 3-71).

For the substrate surface preparation method, the evidence shown in section 3.4.1.3 demonstrate that alumina grit blast prepared samples performed better in the autoclave test compared to green scotch brite prepared and SiC lathe prepared samples. The exact reason of the higher corrosion performance in the case of alumina grit blast prepared samples cannot be identified, but it may be attributed to a possible healing effect due to bayerite fibers forming with the reaction of high temperature and pressure water with the residual alumina grits at the coating and substrate interface.

4.2. Neutronic analysis

Neutronic analysis was performed by Ian Younker and Dr. Massimiliano Fratoni. A summary of this work is shown here. In principle the TiAlN coating can introduce parasitic reaction absorption into every fuel assembly. It is necessary to calculate the percentage of neutrons absorbed within each coating layer, to quantify the effect of excess neutron absorption on fuel cycle lengths, and present design solutions to maximize fuel performance without sacrificing accident tolerance. For lattice-level neutronic investigations, SERPENT Monte Carlo

code and SCALE 6.1 package TRITON, KENO-VI, CENTRM modules have been used in literature [136,189–193]. Among these, Monte Carlo codes are demonstrated to be more reliable [190]. Previously, a neutronic penalty investigation was performed for $Ti_{0.5}Al_{0.5}N$ using the SERPENT Monte Carlo Code, which concluded that a 10-30 μm coating thickness will to limit cycle length loss [136].

SERPENT Monte Carlo code [194] is utilized in the present work to understand the neutronic performance of single-layer doped and undoped TiAlN, and 8-layer TiN/TiAlN coatings. The selected reference pressurized water reactor (PWR) was the Westinghouse AP1000 with 17x17 fuel assembly [145]. Such assembly contains 264 fuel rods, 24 guide tubes, and 1 instrumentation tube. Reflective boundary conditions on four sides generate an infinite radial lattice with finite length, and assembly extremities contain axial reflectors composed of a water and steel mixture (50%-50% volume mix, 100 cm length). Core parameters are shown in Table 4-1 [145]. Cycle length and attainable burnup were projected from depletion of a single assembly averaging reactivity under the assumption of constant power throughout the lifetime of the assembly [146]. To correct for the infinite lattice model, radial leakage was assumed to be 3% [146]. Neutronic analysis for single-layer TiAlN, single-layer TiN and 8-layer TiAlN/TiN used ENDF/B-VII cross-sections. However, since ENDF/B-VII does not contain Yb cross-section data, JEFF 3.1.1 cross-section data was used for all doping results. Cross-sections (ENDF/B-VII) were applied at the following temperatures: 784°C (1057 K) for fuel, 364°C (637 K) for clad, 327°C (600 K) for coolant, and thermal scattering cross-sections were applied to the water. Depletion calculations utilized Chebyshev Rational Approximation Method (CRAM) and a high-resolution flux spectrum based on the unified energy-grid structure to calculate one-group cross-sections.

Table 4-1. The reference pressurized water reactor (PWR) design core parameters [54].

Property	Value
Total power, MW	3400
Assemblies	157
Core average coolant temperature, °C	303
Pressure, bar	155
Core average coolant density, °C	0.719
Active length, cm	426.72
Pellet diameter, cm	0.82
Clad thickness, cm	0.057
Fuel rod outer diameter, cm	0.95
Pitch-to-diameter ratio	1.326

The reference UO_2 was assumed 4.5 at.% enriched and Zircaloy-4 (0.1% Cr, 0.21% Fe, 1.45% Sn, and 98.24% Zr; 6.56 g/cm^3) was chosen as the reference cladding material. The reference cycle length was found to be 446.5 EFPD (effective full power days) with ENDF/B-VII cross-section data. The reference cycle length was recalculated to be 445.5 EFPD with JEFF 3.1.1 cross-section data. The fuel enrichment compensation was determined as described in Younker et al. [136].

To understand the neutronic impact of each coating layer, the 8-layer TiAlN/TiN was broken into its most basic parts, pure TiN, $Ti_{0.20}Al_{0.80}N$, and $Ti_{0.33}Al_{0.67}N$. Each coating was applied at thicknesses of 4, 8, and 12 μm and included the 0.6 μm Ti-BC layer. Table 4-2 shows the neutron capture percentage within coating and cycle length penalty based on this neutron capture. Two major trends occurred pertaining to neutron capture: (1) the percentage of neutrons absorbed within the coating increases linear with coating thickness; (2) overall absorption is driven by the most absorbing element, titanium. TiN captures the most neutrons because it consists of an entire atom of Ti, whereas $Ti_{0.33}Al_{0.67}N$ and $Ti_{0.20}Al_{0.80}N$ contain one-third and one-fifth of a Ti atom, respectively. The Ti-BC layer composition and thickness remained constant resulting in an unvarying percentage of captured neutrons, 0.01%. Parasitic absorption associated

with each coating leads to fewer neutrons available for fission, decreases reactivity, and ultimately shortens fuel cycles, which exhibit trends like those of neutron capture percentage. Overall the neutronic penalties stemming from $Ti_{0.20}Al_{0.80}N$, and $Ti_{0.33}Al_{0.67}N$ coatings are minor and require slight increases to fuel enrichment (< 0.05 at.%).

Table 4-2. Percentage of neutrons captured within coating/Cycle length penalty (EFPD) derived from coatings as a function of the monolithic coating composition and thickness.

Coating	Thickness, µm		
	4	8	12
TiN	0.12/-2.8	0.24/-5.1	0.37/-8.0
$Ti_{0.20}Al_{0.80}N$	0.05/-1.1	0.10/-2.5	0.15/-4.0
$Ti_{0.33}Al_{0.67}N$	0.06/-1.5	0.11/-2.7	0.17/-4.3

Neutronic penalty of 8-layer TiN/TiAlN having a coating thickness of 8 and 12 µm was investigated. To determine neutronic penalty in the case of 8-layer TiN/TiAlN coatings, layers of TiN, $Ti_{0.20}Al_{0.80}N$, and $Ti_{0.33}Al_{0.67}N$, 1 and 1.5 µm thick, combined in an alternating pattern along with a 0.6 µm Ti-BC layer. Table 4-3 shows the percentage of neutrons captured and cycle length penalty caused by the entire coating (including 0.01% from Ti bond layer) and each individual layer. As expected neutron absorption and cycle length penalty follow the trends previously described for single-layer TiN and single-layer TiAlN coating. One would envision total coating absorption and cycle length penalty values for 8-layer TiN/TiAlN to lie between those of pure TiN and TiAlN, which they do. As in the case of single-layer coatings, neutronic penalties are low and less than 0.08 at.% excess fuel enrichment is necessary to match reference cycle length.

Table 4-3. Percentage of neutrons captured within each coating layer/ Cycle length penalty (EFPD) derived from multilayer coatings as a function of the 8-layer coating composition and thickness.

Coating	Thickness, µm	Capture, %			EFPD
		TiAlN	TiN	Total	
$Ti_{0.20}Al_{0.80}N$/TiN	8	0.05	0.12	0.18	-4.1
$Ti_{0.33}Al_{0.67}N$/TiN		0.06	0.12	0.19	-4.2
$Ti_{0.20}Al_{0.80}N$/TiN	12	0.07	0.18	0.27	-5.7
$Ti_{0.33}Al_{0.67}N$/TiN		0.08	0.18	0.28	-6.0

The neutronic penalty effect of Y and Yb doping on TiAlN coating was investigated through consideration of four dopant concentrations: 1, 2, 5, and 10 wt.%. TiAlN layers were doped with either Y, Yb, or a 50%-50% mixture of both. Investigated doping concentrations and corresponding cycle length penalty values are summarized in Table 4-4. To provide the most conservative analysis, the 8-layer TiAlN/TiN with the highest neutronic penalty was doped, in this case 12 μm thick $Ti_{0.33}Al_{0.67}N$/TiN. TiN layer composition remained constant. $Ti_{0.33}Al_{0.67}N$ compositions incorporated the dopant concentrations, while scaling the previous $Ti_{0.33}Al_{0.67}N$ composition accordingly. $Ti_{0.33}Al_{0.67}N$ densities were also adjusted to account for denser doping agents. Microscopic radiative capture cross-sections at 327°C (600 K) for titanium, yttrium, and ytterbium, and percentage of neutrons captured within doped 12 μm 8-layer $TiN/Ti_{0.33}Al_{0.67}N$ coating as a function of dopant and concentration are presented in Figure 4-1. Yttrium contains a neutron absorption cross-section lower than titanium. Thus, cycle length penalty (Table 5) and coating absorption (Figure 1a) trend inversely with yttrium concentration. Conversely, ytterbium possesses an absorption cross-section much larger than titanium, causing increased neutronic penalty. Linear progression of neutron capture for the entire 12 μm 8-layer $Ti_{0.33}Al_{0.67}N$/TiN coating was observed when doped with Y, Yb, and a Y/Yb mixture (Figure 1b). As one would expect, the Y/Yb mixture produces results in between those of Y and Yb. Dopant limits shall not exist when using yttrium, however strong consideration should be given to minimize ytterbium concentration. Although, worst-case scenario (10 wt.% Yb) only requires less than 0.1 at.% fuel enrichment compensation.

Table 4-4. Cycle length penalty (EFPD) derived from doped 12 μm 8-layer TiN/Ti$_{0.33}$Al$_{0.67}$N coating as a function of dopant and concentration. Coating absorption and cycle length penalty trend inversely with yttrium concentration.

Dopant	Density (g/cm³)	Composition, wt.%					Composition, at.%					EFPD
		N	Al	Ti	Y	Yb	N	Al	Ti	Y	Yb	
None	3.56	29.2	37.5	33.3	0	0	50.00	33.32	16.68	0	0	445.5
Y1	3.56	28.9	37.1	33	1	0	49.86	33.22	16.65	0.27	0.00	-6.2
Y2	3.57	28.6	36.8	32.6	2	0	49.70	33.18	16.57	0.55	0.00	-6.2
Y5	3.61	27.8	35.6	31.6	5	0	49.38	32.81	16.41	1.40	0.00	-5.9
Y10	3.67	26.2	33.8	30	10	0	48.44	32.43	16.22	2.91	0.00	-5.4
Yb1	3.6	28.9	37.1	33	0	1	49.93	33.26	16.67	0.00	0.14	-6.5
Yb2	3.64	28.6	36.8	32.6	0	2	49.83	33.27	16.61	0.00	0.28	-6.6
Yb5	3.78	27.8	35.6	31.6	0	5	49.72	33.04	16.53	0.00	0.72	-6.9
Yb10	4	26.2	33.8	30	0	10	49.14	32.89	16.45	0.00	1.52	-7.6
Y0.5/Yb0.5	3.58	28.9	37.1	33	0.5	0.5	49.90	33.24	16.66	0.14	0.07	-6.5
Y1/Yb1	3.61	28.6	36.8	32.6	1	1	49.77	33.23	16.59	0.27	0.14	-6.4
Y2.5/Yb2.5	3.7	27.8	35.6	31.6	2.5	2.5	49.55	32.92	16.47	0.70	0.36	-6.6
Y5/Yb5	3.84	26.2	33.8	30	5	5	48.79	32.66	16.34	1.47	0.75	-6.9

(a)
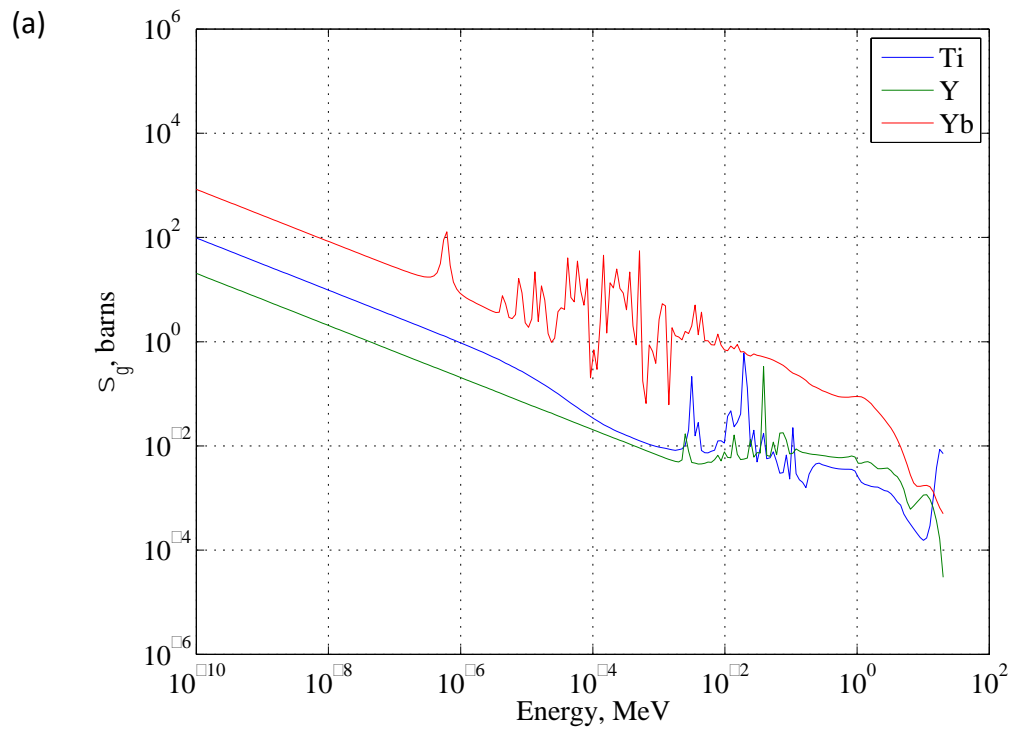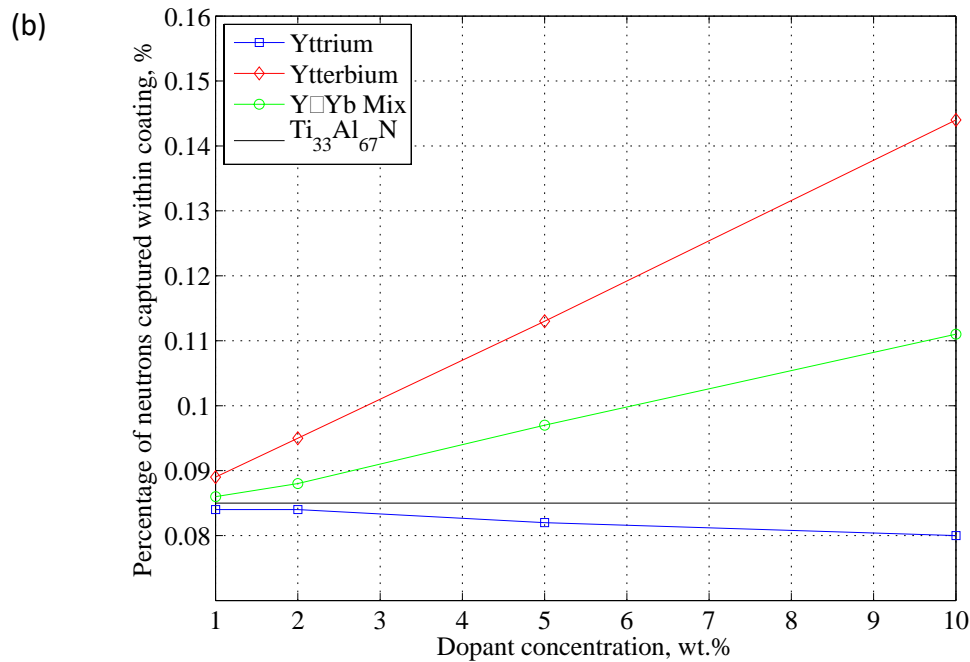
Figure 4-1. (a) JEFF 3.1 microscopic radiative capture cross-sections at 327°C (600 K) for titanium, yttrium, and ytterbium. (b) Percentage of neutrons captured within doped 12 μm 8-layer TiN/Ti$_{0.33}$Al$_{0.67}$N coating as a function of dopant and concentration.

The evidence shown in this section suggests that to minimize the penalty derived from such coatings it is necessary to:

o   reduce coating thickness,

o   decrease the titanium concentration,

o   increase the yttrium concentration, and

o   lower the ytterbium concentration.

In summary, if 12 μm 8-layer TiAlN/TiN coatings with high titanium and ytterbium concentrations become required to ensure safety, the overall neutronic impact is minor and fuel enrichment compensation will not exceed 0.1 at.%. Thin TiAlN/TiN based ceramic coatings remain viable ATF options as they do not significantly limit fuel performance compared to conventional fuel.

4.3. Conclusions on coating deposition parameter optimization

There are optimum coating thickness, substrate roughness, titanium bond coating thickness, nitrogen partial pressure, substrate bias, cathode composition and substrate surface preparation methods to satisfy corrosion, mechanical and neutronic penalty requirements. While many conclusions can be drawn from the discussed results, main conclusions regarding deposition parameter optimization can be summarized as below:

1) Based on the performed analysis, this optimum coating thickness value is determined to be ~10 μm.

2) Optimum substrate surface roughness is determined to be 0.25 μm R_a to satisfy mechanical interlocking between the coating and the substrate and full coverage of the substrate surface.

3) Optimum titanium bond coating thickness is determined to be 0.6 μm, which enabled lowest positive weight gain indicating better corrosion performance.

4) Optimum nitrogen partial pressure is 1.6 Pa.

5) A negative substrate bias value of 50 V is observed to be a convenient value to obtain well adhered, dense and corrosion resistant coatings. However, it should be stated that 25-75 V substrate bias is observed to be an acceptable range and there is a 100 V limit at which coating integrity becomes severely damaged.

6) A cathode composition of 33 at.% Ti- 67 at.% Al determined to be providing desired coating composition and lower macroparticle amount resulting in better mechanical performance.

7) Different substrate preparation methods determined to be effective on the corrosion behavior of the coating. Among the investigated methods, SiC hand grinding and the alumina grit blasting determined to be the more convenient ones.

Chapter 5

Conclusions and Future Work

5.1. Conclusions

Research on accident-tolerant fuels (ATFs) that can delay the deleterious consequences of a loss-of-coolant-accident (LOCA) is a topic of recent interest. In the reactor, because the cladding outer surface is in contact with the coolant water, corrosion performance is one of the main cladding performance evaluation criteria. Accordingly, the cladding materials developed are expected to improve or at least maintain their properties during normal operation (water at 280-330°C and 15.5 MPa [4,5]) and during accident conditions (LOCA or RIA). Full replacement of the cladding tube, a hybrid design combining the currently used zirconium-based alloys with a composite design or application of a protective coating on already existing zirconium-based alloy claddings are all possible routes under consideration to create an accident tolerant fuel [11]. Among these, protective coating development is the least cumbersome approach due to no major change requirement in cladding material. Historically, TiAlN and TiN coatings deposited on various substrates are observed to be enhancing corrosion performance in air, oxygen and water environments at high temperatures due to passivating oxide layer formation. However, while developing coating for nuclear fuel claddings, low neutronic penalty, mechanical properties, ease of fabrication, adhesion of the developed coating to the zirconium-based alloy cladding and coating deposition method scalability to the production size are the major challenges.

Cathodic arc physical vapor deposition is a flexible method that can be modified through adjustment of deposition parameters. The optimum deposition parameters to deposit well adhered, dense nitride-based coatings on ZIRLO® substrates is systematically studied in this

thesis using a carefully designed stepwise approach. Developed coatings are subjected to scratch tests and long-term corrosion tests. First, the single-layer TiAlN and single-layer TiN coating deposition on ZIRLO® sheets were studied (Section 3-2) with a detailed characterization of as-deposited coating properties (topography, uniformity, crystal structure, residual stresses), failure modes during scratch testing and oxide formation after corrosion testing. Mechanical and oxidation performance of TiN/TiAlN coatings deposited on ZIRLO® sheets were studied (Section 3-3). Finally, the corrosion performance of developed 8-layer TiN/TiAlN coating deposited on ZIRLO® tubes was studied (Section 3-4). Throughout these stages the parameters considered for coating optimization included: (i) substrate surface roughness, (ii) substrate surface preparation method, (iii) titanium bond coating layer thickness, (iv) total coating thickness, (v) cathode composition, (vi) substrate bias, (vii) nitrogen partial pressure and (viii) multilayer design architecture.

The mechanical and corrosion test results clearly showed how vital the deposition parameter optimization is to achieve the desired coating performance while depositing TiN and TiAlN coatings on ZIRLO® substrates using the cathodic arc physical vapor deposition. Conclusions on determined optimum deposition parameters were summarized in section 4.3. Thicker coatings hypothesized to be providing more corrosion performance because of unreacted coating remaining ratio after oxidation test, providing more adhesion because of more load-bearing capacity but also should be limited to avoid neutronic penalty. Additionally, thicker coatings can lead to more residual stress in the coating that could cause degradation, which should be considered when developing coatings with enhanced performance requirement. Coating composition mirrors the cathode composition. In the case of higher aluminum content having cathode (20 at.%Ti-80 at.%Al), due to the increase in the aluminum content in the coating, hexagonal crystal structure is observed which led to lower mechanical performance and higher amount of macroparticles degrading the coating integrity. Another factor that is effective on the

amount and on the geometry of the macroparticles is the substrate bias. Lower substrate bias results in increased amount of macroparticles with spherical geometry and a porous coating with low density. Increasing substrate bias decreases macroparticles with enhanced coating density. However, after a critical value of 100 V determined in this study, backscatter of ions occurs during deposition degrading coating density and uniformity, which decreases coating adhesion. And in multilayer design architecture investigation, it was concluded that 8-layer TiN/TiAlN multilayer coating is the best architecture, as it showed the best corrosion performance considering lowest positive weight gain without spallation and oxygen penetration stop at ~1μm distance from the surface.

It was hypothesized that adherent TiN and TiAlN coatings could be deposited on ZIRLO substrates using cathodic arc physical vapor deposition with some anticipated outcomes such as good adhesion on substrate, full coverage of surface, passivating layer formation and resistance to crack propagation. These were hypothesized to be based on the characteristics of the cathodic arc physical vapor deposition process and on the properties of the TiN and TiAlN coatings. Through the study, it is shown that there is an optimum recipe of substrate surface roughness (0.25 μm R_a), titanium bond coating thickness (0.6 μm), substrate bias (-50 V), nitrogen partial pressure (1.6 Pa) and multilayer design (8-layer) to achieve enhanced coating adhesion and corrosion performance. The evidence in this thesis showed that this hypothesis is correct. In conclusion, optimized TiN/TiAlN coatings deposited by CA-PVD method are promising for nuclear fuel cladding applications to develop ATFs but further study should be performed as described in Section 5.2.

5.2. Future Work

Macroparticles were determined to be the most detrimental defect in the deposited coatings. Future study should consider strategies for eliminating or for further minimization of

these defects. Elimination of macroparticles in the coatings through filter usage is possible, but this would cause a decrease in deposition efficiency. So, its value of modifying the deposition procedure to eliminate macroparticles considering the advantages and disadvantages should be evaluated in future studies. Additionally, to evaluate the effect of residual stresses on the coating properties, an X-ray diffractometer with a high resolution ψ goniometer can be employed to make more precise residual stress measurements.

This thesis work is mainly focused corrosion performance during normal operation but a limited study was performed to evaluate accident condition behavior of the coatings. In an accident, temperatures can reach above 1200°C, involving water corrosion at much higher temperatures than the normal operation condition and steam corrosion. Thus, more extensive (systematic) higher temperature and pressure water corrosion tests should be conducted, and steam corrosion tests should be performed systematically to investigate oxidation behavior, determine oxidation kinetics and evaluate the accident condition performance of the developed coatings. Furthermore, a quenching test investigation can also be performed to evaluate the performance of the coatings in the case of an emergency core cooling system incorporation that can take place during the development of an accident.

Because when coating flat samples, the clamping region remained uncoated, the sample holder can be modified to hang flat samples during coating deposition instead of clamping to render the full surface coverage during the deposition process. A similar case is also valid for tubular samples which can only be coated on the outside surface. These uncoated regions create regions for corrosive environment interaction with the substrate material during testing and may be misleading in the corrosion performance evaluation of the developed coatings.

Coating compositions were measured with EDS which is a method known for its low energy resolution. Furthermore, the EDS quantitative analysis were performed without using standard samples. Future EDS studies should be performed using standard samples. Additionally,

an alternative method that can provide better resolution might be considered to obtain make more precise measurements.

The assessment of hydrogen generation and diffusion through the developed coating during corrosion during normal operation and accident conditions are vital to evaluate the corrosion performance in nuclear reactor environment. The hydriding performance of the developed coatings can be investigated using a Gas Reaction Controller LPB technique and measuring hydrogen concentration with an hydrogen analyzer as described in [135].

Additionally, claddings are expected to be wear resistant to maintain their performance during in reactor operation against damages such as fretting. Thus, future studies should involve hardness tests to evaluate wear performance that can be experienced due to fretting during in-reactor operation. Ring-compression test (RCT), three-point-bend test (3-PBT), four-point-bend test (4-PBT), axial tensile test, ring-stretch test or axial restraint test to assess ductility and strength of the coated cladding to interpret the oxidation and temperature limit that the cladding would maintain its geometry during transient condition.

Finally, materials experience microstructural changes under neutron irradiation which can affect their mechanical and corrosion resistance properties. This requires in-reactor tests to evaluate the irradiation growth, creep, pellet-cladding mechanical interaction which are effective in deteriorating cladding performance, especially in the case of accident conditions.

References

[1]   Top Fuel 2015, in: Conf. Proc. Part 1, European Nuclear Society, Zurich, Switzerland, 2015: p. 98.

[2]   C.R.F. Azevedo, Selection of fuel cladding material for nuclear fission reactors, Eng. Fail. Anal. 18 (2011) 1943–1962. doi:10.1016/j.engfailanal.2011.06.010.

[3]   J.R. Lamarsh, A.J. Baratta, Power Reactors and Nuclear Steam Supply Systems, in: Introd. to Nucl. Eng., 3rd ed., Prentice Hall, 2001: pp. 136–185.

[4]   J.K. Shultis, R.E. Faw, Fundamentals of nuclear science and engineering, 1st Editio, CRC Press, Boca Raton, FL, 2002.

[5]   T.R. Allen, R.J.M. Konings, A.T. Motta, Corrosion of Zirconium Alloys, in: Compr. Nucl. Mater., 1st ed., Elsevier Inc., 2012: pp. 49–68. doi:10.1016/B978-0-08-056033-5.00063-X.

[6]   T. Alam, M.K. Khan, M. Pathak, K. Ravi, R. Singh, S.K. Gupta, A review on the clad failure studies, Nucl. Eng. Des. 241 (2011) 3658–3677. doi:10.1016/j.nucengdes.2011.08.009.

[7]   Z. Duan, H. Yang, Y. Satoh, K. Murakami, S. Kano, Z. Zhao, et al., Current status of materials development of nuclear fuel cladding tubes for light water reactors, Nucl. Eng. Des. 316 (2017) 131–150. doi:10.1016/j.nucengdes.2017.02.031.

[8]   R. Krishnan, M.K. Asundi, Zirconium alloys in nuclear technology, Proc. Indian Aead. Sci. (Engg. Sei.). 4 (1981) 41–56.

[9]   M. Steinbrück, M. Böttcher, Air oxidation of Zircaloy-4, M5® and ZIRLO™ cladding alloys at high temperatures, J. Nucl. Mater. 414 (2011) 276–285. doi:10.1016/j.jnucmat.2011.04.012.

[10] A.S. Zaimovskii, Zirconium alloys in nuclear power, Sov. At. Energy. 45 (1978) 1165–1168. doi:10.1007/BF01118114.

[11] K. Barrett, S. Bragg-Sitton, D. Galicki, Advanced LWR Nuclear Fuel Cladding System Development Trade-off Study, Idaho National Laboratory, Report number: Inl/Ext-12-27090, 2012.

[12] S. Bragg-Sitton, Development of advanced accident- tolerant fuels for commercial LWRs, Nucl. News. (n.d.) 83–91.

[13] G. Sabol, ZIRLO^{TM} — An Alloy Development Success, J. ASTM Int. 2 (2005) 12942. doi:10.1520/JAI12942.

[14] S.J. Zinkle, K.A. Terrani, J.C. Gehin, L.J. Ott, L.L. Snead, Accident tolerant fuels for LWRs: A perspective, J. Nucl. Mater. 448 (2014) 374–379. doi:10.1016/j.jnucmat.2013.12.005.

[15] Fukushima Nuclear Accident Analysis Report, Tokyo Electric Power Company, Inc., n.d.

[16] K.A. Terrani, S.J. Zinkle, L.L. Snead, Advanced oxidation-resistant iron-based alloys for LWR fuel cladding, J. Nucl. Mater. 448 (2014) 420–435. doi:10.1016/j.jnucmat.2013.06.041.

[17] N.P. Neureiter, B.J. Garrick, R.A. Bari, J. Beard, Percy M., M.Q. Brewster, M.L. Corradini, et al., Lessons learned from the Fukushima nuclear accident for improving safety of U.S. Nuclear Plants, The National Academy of Sciences, July, Washington, D.C., 2014.

[18] L. Hallstadius, S. Johnson, E. Lahoda, Cladding for high performance fuel, Prog. Nucl. Energy. 57 (2012) 71–76. doi:10.1016/j.pnucene.2011.10.008.

[19] C.P. Deck, H.E. Khalifa, B. Sammuli, T. Hilsabeck, C.A. Back, Fabrication of SiC–SiC composites for fuel cladding in advanced reactor designs, Prog. Nucl. Energy. 57 (2012) 38–45. doi:10.1016/j.pnucene.2011.10.002.

[20]   J.D. Stempien, D.M. Carpenter, G. Kohse, M.S. Kazimi, Characteristics of Composite Silicon Carbide Fuel Cladding After Irradiation Under Simulated PWR Conditions Nuclear Systems, Nucl. Technol. 183 (2013) 13–29. doi:10.13182/NT12-86.

[21]   Y. Lee, M.S. Kazimi, A structural model for multi-layered ceramic cylinders and its application to silicon carbide cladding of light water reactor fuel, J. Nucl. Mater. 458 (2015) 87–105. doi:10.1016/j.jnucmat.2014.12.013.

[22]   C.H. Henager, E.A. Le, R.H. Jones, A model stress analysis of swelling in SiC/SiC composites as a function of fiber type and carbon interphase structure, J. Nucl. Mater. 329–333 (2004) 502–506. doi:10.1016/j.jnucmat.2004.04.110.

[23]   T. Nozawa, Y. Katoh, L.L. Snead, The effect of neutron irradiation on the fiber/matrix interphase of silicon carbide composites, J. Nucl. Mater. 384 (2009) 195–211. doi:10.1016/j.jnucmat.2008.11.015.

[24]   D. Kim, H.-G. Lee, J.Y. Park, W.-J. Kim, Fabrication and measurement of hoop strength of SiC triplex tube for nuclear fuel cladding applications, J. Nucl. Mater. 458 (2015) 29–36. doi:10.1016/j.jnucmat.2014.11.117.

[25]   J.G. Stone, R. Schleicher, C.P. Deck, G.M. Jacobsen, H.E. Khalifa, C.A. Back, Stress analysis and probabilistic assessment of multi-layer SiC-based accident tolerant nuclear fuel cladding, J. Nucl. Mater. 466 (2015) 682–697. doi:10.1016/j.jnucmat.2015.08.001.

[26]   M. Ben-Belgacem, V. Richet, K.A. Terrani, Y. Katoh, L.L. Snead, Thermo-mechanical analysis of LWR SiC/SiC composite cladding, J. Nucl. Mater. 447 (2014) 125–142. doi:10.1016/j.jnucmat.2014.01.006.

[27]   W.-J. Kim, D. Kim, J.Y. Park, Fabrication and material issues for the application of SiC composites to LWR fuel cladding, Nucl. Eng. Technol. 45 (2013) 565–572. doi:10.5516/NET.07.2012.084.

[28]   Y. Katoh, L.L. Snead, T. Nozawa, T. Hinoki, A. Kohyama, N. Igawa, et al., Mechanical

properties of chemically vapor-infiltrated silicon carbide structural composites with thin carbon interphases for fusion and advanced fission applications, Mater. Trans. 46 (2005) 527–535. doi:10.2320/matertrans.46.527.

[29]   Y. Katoh, L.L. Snead, C.H. Henager, T. Nozawa, T. Hinoki, A. Iveković, et al., Current status and recent research achievements in SiC/SiC composites, J. Nucl. Mater. 455 (2014) 387–397. doi:10.1016/j.jnucmat.2014.06.003.

[30]   Y. Katoh, K. Ozawa, C. Shih, T. Nozawa, R.J. Shinavski, A. Hasegawa, et al., Continuous SiC fiber, CVI SiC matrix composites for nuclear applications: Properties and irradiation effects, J. Nucl. Mater. 448 (2014) 448–476. doi:10.1016/j.jnucmat.2013.06.040.

[31]   K. Yueh, K.A. Terrani, Silicon carbide composite for light water reactor fuel assembly applications, J. Nucl. Mater. 448 (2014) 380–388. doi:10.1016/j.jnucmat.2013.12.004.

[32]   C. Lorrette, C. Sauder, P. Billaud, C. Hossepied, G. Loupias, J. Braun, et al., SiC/SiC composite behavior in LWR conditions and under high temperature steam environment, in: Top Fuel 2015, Zurich, Switzerland, 2015: pp. 126–134.

[33]   B. Cheng, Y.J. Kim, P. Chou, Improving Accident Tolerance of Nuclear Fuel with Coated Mo-alloy Cladding, Nucl. Eng. Technol. 48 (2016) 16–25. doi:10.1016/j.net.2015.12.003.

[34]   B.A. Pint, K.A. Terrani, Y. Yamamoto, L.L. Snead, Material Selection for Accident Tolerant Fuel Cladding, Metall. Mater. Trans. E. 2 (2014) 190–196. doi:10.1007/s40553-015-0056-7.

[35]   R.B. Rebak, K.A. Terrani, W.P. Gassmann, J.B. Williams, K.L. Ledford, S. Nuclear, Improving Nuclear Power Plant Safety with FeCrAl Alloy Fuel Cladding, MRS Adv. 2 (2017) 1–8. doi:10.1557/adv.201.

[36]   M. Kurata, Research and Development Methodology for Practical Use of Accident Tolerant Fuel in Light Water Reactors, Nucl. Eng. Technol. 48 (2016) 26–32. doi:10.1016/j.net.2015.12.004.

[37] C. Tang, M. Stueber, H.J. Seifert, M. Steinbrueck, Protective coatings on zirconium-based alloys as accident-tolerant fuel (ATF) claddings, Corros. Rev. 35 (2017) 141–165. doi:10.1515/corrrev-2017-0010.

[38] K. Sridharan, S.P. Harrington, A.K. Johnson, J.R. Licht, M.H. Anderson, T.R. Allen, Oxidation of plasma surface modified zirconium alloy in pressurized high temperature water, Mater. Des. 28 (2007) 1177–1185. doi:10.1016/j.matdes.2006.01.019.

[39] D.Q. Peng, X.D. Bai, F. Pan, H. Sun, B.S. Chen, Influence of aluminum ions implanted on oxidation behavior of ZIRLO alloy at 500°C, Vacuum. 80 (2006) 530–536. doi:10.1016/j.vacuum.2005.08.026.

[40] U.D. Abdelrazek, S.W. Sharkawy, H. a. El-Sayed, Pyrolytic carbon coating of Zircaloy-4 tubes at relatively low temperatures, J. Nucl. Mater. 249 (1997) 159–164. doi:10.1016/S0022-3115(97)00214-6.

[41] P. Ashcheulov, R. Škoda, J. Škarohlíd, A. Taylor, L. Fekete, F. Fendrych, et al., Thin polycrystalline diamond films protecting zirconium alloys surfaces: From technology to layer analysis and application in nuclear facilities, Appl. Surf. Sci. 359 (2015) 621–628. doi:10.1016/j.apsusc.2015.10.117.

[42] H.-G. Kim, I.-H. Kim, J.-Y. Park, Y.-H. Koo, Application of Coating Technology on Zirconium-Based Alloy to Decrease High-Temperature Oxidation, in: Zircon. Nucl. Ind. 17th Int. Symp. ASTM STP 1543, 2014: pp. 30–31. doi:10.1520/STP154320120161.

[43] J.R. Baczynski, Master of Science Thesis "High temperature steam oxidation of titanium-coated Zircaloy-2 and Titanium-Zirconium Alloys," University of Illinois at Urbana-Champaign, 2014. http://hdl.handle.net/2142/50540.

[44] H. Yeom, B. Maier, R. Mariani, D. Bai, P. Xu, K. Sridharan, et al., Development of zirconium-silicide coatings for accident tolerant zirconium-alloy fuel cladding, in: Int. Congr. Adv. Nucl. Power Plants (ICAPP 2016), 2016: pp. 2126–2131.

[45] K. Hauffe, V. Martinez, Oxidation and Corrosion of Tin-Coated Zircaloy-4, J. Electrochem. Soc. 123 (1976) 595–602. doi:10.1149/1.2132892.

[46] S. V. Ivanova, E.M. Glagovsky, K.Y. Nikonorov, I.I. Belugin, I.A. Khazov, Methods to Increase Corrosion Stability and Wear Resistance of LWR Active Core Zirconium Components during Operation and in Conditions of Loss-of-Coolant Accident, in: Proc. Top Fuel 2013, n.d.: pp. 334–350.

[47] H.-G. Kim, I.-H. Kim, Y.-I. Jung, D.-J. Park, J.-Y. Park, Y.-H. Koo, High-Temperature Oxidation Behavior of Cr-Coated Zirconium Alloy, in: Proc. Top Fuel 2013, 2013: pp. 842–846.

[48] J.-H. Park, H.-G. Kim, J. Park, Y.-I. Jung, D.-J. Park, Y.-H. Koo, High temperature steam-oxidation behavior of arc ion plated Cr coatings for accident tolerant fuel claddings, Surf. Coatings Technol. 280 (2015) 256–259. doi:10.1016/j.surfcoat.2015.09.022.

[49] H.-G. Kim, I.-H. Kim, Y.-I. Jung, D.-J. Park, J.-Y. Park, Y.-H. Koo, Adhesion property and high-temperature oxidation behavior of Cr-coated Zircaloy-4 cladding tube prepared by 3D laser coating, J. Nucl. Mater. 465 (2015) 531–539. doi:10.1016/j.jnucmat.2015.06.030.

[50] H.G. Kim, J.H. Yang, W.J. Kim, Y.H. Koo, Development Status of Accident-tolerant Fuel for Light Water Reactors in Korea, Nucl. Eng. Technol. 48 (2016) 1–15. doi:10.1016/j.net.2015.11.011.

[51] D.-J. Park, H.-G. Kim, Y.-I. Jung, J.-H. Park, J.-H. Yang, Y.-H. Koo, Behavior of an improved Zr fuel cladding with oxidation resistant coating under loss-of-coolant accident conditions, J. Nucl. Mater. 482 (2016) 75–82. doi:10.1016/j.jnucmat.2016.10.021.

[52] J. Carr, G. Vasudevamurthy, L. Snead, B. Hinderliter, C. Massey, Investigations of Aluminum-Doped Self-Healing Zircaloy Surfaces in Context of Accident-Tolerant Fuel Cladding Research, J. Mater. Eng. Perform. 25 (2016) 2347–2355. doi:10.1007/s11665-

016-2094-4.

[53] W.G. Luscher, E.R. Gilbert, S.G. Pitman, E.F. Love, Surface modification of Zircaloy-4 substrates with nickel zirconium intermetallics, J. Nucl. Mater. 433 (2013) 514–522. doi:10.1016/j.jnucmat.2012.05.039.

[54] K.A. Terrani, C.M. Parish, D. Shin, B.A. Pint, Protection of zirconium by alumina- and chromia-forming iron alloys under high-temperature steam exposure, J. Nucl. Mater. 438 (2013) 64–71. doi:10.1016/j.jnucmat.2013.03.006.

[55] W. Zhong, P.A. Mouche, X. Han, B.J. Heuser, K.K. Mandapaka, G.S. Was, Performance of iron-chromium-aluminum alloy surface coatings on Zircaloy 2 under high-temperature steam and normal BWR operating conditions, J. Nucl. Mater. 470 (2016) 327–338. doi:10.1016/j.jnucmat.2015.11.037.

[56] R. H.Baney, J.S. Tulenko, An Innovative Ceramic Corrosion Protection System for Zircaloy Cladding, Revised Project Summary and 4th Quarter Report, NERI Research Project No. 4508230 - 12, FG03-99SF21882, Gainesville, FL, 2000.

[57] Y. Al-Olayyan, G.E. Fuchs, R. Baney, J. Tulenko, The effect of Zircaloy-4 substrate surface condition on the adhesion strength and corrosion of SiC coatings, J. Nucl. Mater. 346 (2005) 109–119. doi:10.1016/j.jnucmat.2005.05.016.

[58] B.R. Maier, B.L. Garcia-Diaz, B. Hauch, L.C. Olson, R.L. Sindelar, K. Sridharan, Cold spray deposition of Ti_2AlC coatings for improved nuclear fuel cladding, J. Nucl. Mater. 466 (2015) 1–6. doi:10.1016/j.jnucmat.2015.06.028.

[59] H. Yeom, B. Hauch, G. Cao, B. Garcia-Diaz, M. Martinez-Rodriguez, H. Colon-Mercado, et al., Laser surface annealing and characterization of Ti_2AlC plasma vapor deposition coating on zirconium-alloy substrate, Thin Solid Films. 615 (2016) 202–209. doi:10.1016/j.tsf.2016.07.024.

[60] D.A. Roberts, Master of Science Thesis "Magnetron Sputtering and Corrosion of Ti-Al-C

and Cr-Al-C coatings for Zr-alloy Nuclear Fuel Cladding," The University of Tennessee, 2016.

[61]   J.H. Sung, T.H. Kim, S.S. Kim, Fretting damage of TiN coated zircaloy-4 tube, Wear. 250–251 (2001) 658–664. doi:10.1016/S0043-1648(01)00674-3.

[62]   F. Khatkhatay, L. Jiao, J. Jian, W. Zhang, Z. Jiao, J. Gan, et al., Superior corrosion resistance properties of TiN-based coatings on Zircaloy tubes in supercritical water, J. Nucl. Mater. 451 (2014) 346–351. doi:10.1016/j.jnucmat.2014.04.010.

[63]   K.T. Kim, K. Park, J.Y. Park, S. Noh, The Effect of a Ceramic Coating on Zr Alloys in Terms of Corrosion, Trans. Korean Nucl. Soc. Spring Meet. (2013) 30–31.

[64]   K. Daub, R. Van Nieuwenhove, H. Nordin, Investigation of the impact of coatings on corrosion and hydrogen uptake of Zircaloy-4, J. Nucl. Mater. 467 (2015) 260–270. doi:10.1016/j.jnucmat.2015.09.041.

[65]   D. Jin, F. Yang, Z. Zou, L. Gu, X. Zhao, F. Guo, et al., A study of the zirconium alloy protection by Cr_3C_2-NiCr coating for nuclear reactor application, Surf. Coatings Technol. 287 (2016) 55–60. doi:10.1016/j.surfcoat.2015.12.088.

[66]   S.T. Park, Doctor of Philosophy Thesis "Amorphous alumina oxidation protective coatings for zircaloy based on a compositional gradient layer system," University of Florida, 2004.

[67]   A.S. Kuprin, V.A. Belous, V.N. Voyevodin, V.V. Bryk, R.L. Vasilenko, V.D. Ovcharenko, et al., Vacuum-arc chromium-based coatings for protection of zirconium alloys from the high-temperature oxidation in air, J. Nucl. Mater. 465 (2015) 400–406. doi:10.1016/j.jnucmat.2015.06.016.

[68]   A.S. Kuprin, V.A. Belous, V.N. Voyevodin, V. V. Bryk, R.L. Vasilenko, V.D. Ovcharenko, et al., High-temperature air oxidation of E110 and Zr-1Nb alloys claddings with coatings, UDC 669.296:621.793, Probl. At. Sci. Technol. 89 (2014) 126–132.

[69] U. Wiklund, P. Hedenqvist, S. Hogmark, B. Stridh, M. Arbell, Multilayer coatings as corrosion protection of Zircaloy, Surf. Coatings Technol. 86–87 (1996) 530–534. doi:10.1016/S0257-8972(96)03001-0.

[70] S. PalDey, S. Deevi, Single layer and multilayer wear resistant coatings of (Ti, Al) N: a review, Mater. Sci. Eng. A. 342 (2003) 58–79. doi:10.1016/S0921-5093(03)00473-8.

[71] S.K. Han, Jeon G., Yoon, Joo S., Kim, Hyung J., High temperature wear resistance of (TiAl)N films synthesized by cathodic arc plasma deposition, Surf. Coatings Technol. 86–87 (1996) 82–87.

[72] K.L. Lin, M.Y. Hwang, C.D. Wu, The deposition and wear properties of cathodic arc plasma deposition TiAlN deposits, Mater. Chem. Phys. 46 (1996) 77–83. doi:10.1016/0254-0584(96)80134-9.

[73] J.G. Han, K.H. Nam, I.S. Choi, The shear impact wear behavior of Ti compound coatings, Wear. 214 (1998) 91–97. doi:10.1016/S0043-1648(97)00205-6.

[74] Y. Wang, A study of PVD coatings and die materials for extended die-casting die life, Surf. Coatings Technol. 94–95 (1997) 60–63. doi:10.1016/S0257-8972(97)00476-3.

[75] T. Suzuki, D. Huang, Y. Ikuhara, Microstructures and grain boundaries of (Ti,Al)N films, Surf. Coatings Technol. 107 (1998) 41–47. doi:10.1016/S0257-8972(98)00550-7.

[76] R.D. James, D.L. Paisley, K.A. Gruss, S. Parthasarthi, B.R. Tittmann, Y. Horie, et al., Adhesion evaluation of TiN and (Ti, Al)N coatings on titanium 6Al-4V, Mater. Res. Soc. Symp. Proc. 410 (1996) 377–382.

[77] A. Anders, A review comparing cathodic arcs and high power impulse magnetron sputtering (HiPIMS), Surf. Coat. Technol. 257 (2014) 308–325. doi:10.1016/j.surfcoat.2014.08.043.

[78] E. Lugscheider, C. Barimani, C. Wolff, S. Guerreiro, G. Doepper, Comparison of the structure of PVD-thin films deposited with different deposition energies, Surf. Coatings

Technol. 86–87 (1996) 177–183.

[79] R.L. Boxman, D.M. Sanders, P.J. Martin, eds., Handbook of Vacuum Arc Science and Technology: Fundamentals and Applications, Noyes Publications, Park Ridge, New Jersey, 1995.

[80] A. Anders, Cathodic arc plasma deposition, Vac. Technol. Coat. 3 (2002) 1–26. doi:10.1016/0040-6090(88)90494-4.

[81] W.D. Sproul, Physical vapor deposition tool coatings, Surf. Coatings Technol. 81 (1996) 1–7. doi:10.1016/0257-8972(95)02616-9.

[82] M. Ahlgren, H. Blomqvist, Influence of bias variation on residual stress and texture in TiAlN PVD coatings, Surf. Coatings Technol. 200 (2005) 157–160. doi:10.1016/j.surfcoat.2005.02.078.

[83] S.J. Bull, Failure modes in scratch adhesion testing, Surf. Coatings Technol. 50 (1991) 25–32. doi:10.1016/0257-8972(91)90188-3.

[84] J.A. Sue, A.J. Perry, J. Vetter, Young's modulus and stress of CrN deposited by cathodic vacuum arc evaporation, Surf. Coatings Technol. 68–69 (1994) 126–130. doi:10.1016/0257-8972(94)90149-X.

[85] C. Gautier, J. Machet, Study of the growth mechanisms of chromium nitride films deposited by vacuum ARC evaporation, Thin Solid Films. 295 (1997) 43–52. doi:10.1016/S0040-6090(96)09164-X.

[86] B.F. Coll, R. Fontana, A. Gates, P. Sathrum, (Ti-Al)N advanced films prepared by arc process, Mater. Sci. Eng. A. 140 (1991) 816–824. doi:10.1016/0921-5093(91)90519-S.

[87] M.K. Kazmanli, M. Ürgen, A.F. Cakir, Effect of nitrogen pressure, bias voltage and substrate temperature on the phase structure of Mo-N coatings produced by cathodic arc PVD, Surf. Coatings Technol. 167 (2003) 77–82. doi:10.1016/S0257-8972(02)00866-6.

[88] J.-P. Bars, D. David, E. Etchessahar, J. Debuigne, Titanium α-Nitrogen Solid Solution

Formed by High Temperature Nitriding: Diffusion of Nitrogen, Hardness, and Crystallographic Parameters, Metall. Trans. A. 14A (1983) 1537–1543.

[89]   C. Vahlas, B.D. Ladouce, P.Y. Chevalier, C. Bernard, L. Vandenbulcke, A Thermodynamic Evaluation of the Ti-N System, Thermochim. Acta. 180 (1991) 23–37. doi:10.1007/BF02666327.

[90]   L. Toth, Transition Metal Carbides and Nitrides, Volume 7, Elsevier, 1971.

[91]   O. Knotek, M. Bhomer, T. Leyendecker, On structure and properties of sputtered Ti and Al based hard compound films, J. Vac. Sci. Technol. A Vacuum, Surfaces, Film. 4 (1986) 2695. doi:10.1116/1.573708.

[92]   W.-D. Münz, Titanium aluminum nitride films: A new alternative to TiN coatings, J. Vac. Sci. Technol. A. 4 (1986) 2717. doi:10.1116/1.573713.

[93]   R. Cremer, M. Witthaut, D. Neuschütz Value-Addition Metallurgy The Minerals, Met. Mater. Soc. (1998) 249.

[94]   P.J. Spencer, Computational thermochemistry: From its early Calphad days to a cost-effective role in materials development and processing, Calphad Comput. Coupling Phase Diagrams Thermochem. 25 (2001) 163–174. doi:10.1016/S0364-5916(01)00040-2.

[95]   M. Zhou, Y. Makino, M. Nose, K. Nogi, Phase transition and properties of Ti–Al–N thin films prepared by R.F.-plasma assisted magnetron sputtering, Thin Solid Films. 339 (1999) 203–208. doi:10.1016/S0040-6090(98)01364-9.

[96]   S. Inamura, K. Nobugai, F. Kanamaru, The Preparation of NaCI-Type TiAlN Solid Solution, J. Solid State Chem. 68 (1987) 124–127.

[97]   M. Tuilier, M. Pac, M. Gîrleanu, G. Covarel, G. Arnold, P. Louis, Electronic and atomic structures of behavior thin films related to their damage Electronic and atomic structures of $Ti_{1-x}Al_xN$ thin films related to their damage behavior, J. Appl. Phys. 83524 (2008). doi:10.1063/1.2907415.

[98] V. Tomashik, P. Perrot, Aluminium – Nitrogen – Titanium, in: G. Effenberg, S. Ilyenko (Eds.), Ternary Alloy Syst. - Phase Diagrams, Crystallogr. Thermodyn. Data Light Met. Syst. Part 3 Sel. Syst. from Al-Fe-V to Al-Ni-Zr, New Series, MSIT (Materials Science International Team, Landolt-Börnstein, New Series), 2005: pp. 322–333.

[99] D. Wang, C. Chang, K. Wong, Y. Li, W. Ho, Improvement of the interfacial integrity of (Ti, Al)N hard coatings deposited on high speed steel cutting tools, Surf. Coatings Technol. 121 (1999) 388–394.

[100] M. Canay, C.A. Danon, D. Arias, Phase transition temperature in the Zr-rich corner of Zr-Nb-Sn-Fe alloys, J. Nucl. Mater. 280 (2000) 365–371.

[101] P. Salim, J.H.C. da Silva, Enclosure 2 to TXX-01171 ERX-2001-005-NP ZIRLO Cladding and Boron Coating Models for TXU Electric's Loss of Coolant Accident Analysis Methodologies, 2001.

[102] D.B. Scott, Physical and Mechanical Properties of Zircaloy 2 and 4, WCAP-3269-41, 1965.

[103] P. Hidnert, Thermal expansion of titanium, J. Res. Natl. Bur. Stand. (1934). 30 (1943) 101. doi:10.6028/jres.030.008.

[104] M.K. Samani, X.Z. Ding, S. Amini, N. Khosravian, J.Y. Cheong, G. Chen, et al., Thermal conductivity of titanium aluminum silicon nitride coatings deposited by lateral rotating cathode arc, Thin Solid Films. 537 (2013) 108–112. doi:10.1016/j.tsf.2013.04.029.

[105] A. Kimura, H. Hasegawa, K. Yamada, T. Suzuki, Metastable $Ti_{1-x}Al_xN$ films with different Al content, J. Mater. Sci. Lett. 9 (2000) 601–602. http://www.springerlink.com/index/VULM2233T21848V2.pdf.

[106] T. Ikeda, S. Satoh, Phase formation and characterization of hard coatings in the Ti-Al-N system prepared by the cathodic arc ion plating method, Thin Solid Films. 195 (1991) 99–110. doi:10.1016/0040-6090(91)90262-V.

[107] S.P. Pemmasani, K. Valleti, R.C. Gundakaram, K. V. Rajulapati, R. Mantripragada, S. Koppoju, et al., Effect of microstructure and phase constitution on mechanical properties of $Ti_{1-x}Al_xN$ coatings, Appl. Surf. Sci. 313 (2014) 936–946. doi:10.1016/j.apsusc.2014.06.112.

[108] S.J. Bull, P.R. Chalker, C.F. Ayres, D.S. Rickerby, The influence of titanium interlayers on the adhesion of titanium nitride coatings obtained by plasma-assisted chemical vapour deposition, Mater. Sci. Eng. A. 139 (1991) 71–78. doi:10.1016/0921-5093(91)90599-I.

[109] K.A. Pischow, L. Eriksson, E. Harju, A.S. Korhonen, E.O. Ristolainen, The influence of titanium interlayers on the adhesion of PVD TiN coatings on oxidized stainless steel substrates, Surf. Coatings Technol. 58 (1993) 163–172. doi:10.1016/0257-8972(93)90003-7.

[110] D.S. Rickerby, S.J. Bull, T. Robertson, A. Hendry, The role of titanium in the abrasive wear resistance of physically vapour-deposited TiN, Surf. Coatings Technol. 41 (1990) 63–74.

[111] G.S. Kim, S.Y. Lee, J.H. Hahn, B.Y. Lee, J.G. Han, J.H. Lee, et al., Effects of the thickness of Ti buffer layer on the mechanical properties of TiN coatings, Surf. Coatings Technol. 171 (2003) 83–90. doi:10.1016/S0257-8972(03)00243-3.

[112] M. Wittmer, J. Noser, H. Melchior, Oxidation kinetics of TiN thin films, J. Appl. Phys. 52 (1981) 6659–6664. doi:10.1063/1.328659.

[113] D. McIntyre, J.E. Greene, G. Håkansson, J.E. Sundgren, W.D. Münz, Oxidation of metastable single-phase polycrystalline $Ti_{0.5}Al_{0.5}N$ films: Kinetics and mechanisms, J. Appl. Phys. 67 (1990) 1542–1553. doi:10.1063/1.345664.

[114] H.G. Tompkins, Oxidation of titanium nitride in room air and in dry O_2, J. Appl. Phys. 70 (1991) 3876–3880. doi:10.1063/1.349194.

[115] F. Vaz, L. Rebouta, M. Andritschky, M.F. da Silva, J.C. Soares, Thermal oxidation of

Ti$_{1-x}$Al$_x$N coatings in air, J. Eur. Ceram. Soc. 17 (1997) 1971–1977. doi:10.1016/S0955-2219(97)00050-2.

[116]   A. Vennemann, H.-R. Stock, J. Kohlscheen, S. Rambadt, G. Erkens, Oxidation resistance of titanium-aluminium-silicon nitride coatings, Surf. Coatings Technol. 174–175 (2003) 408–415. doi:10.1016/S0257-8972(03).00407-9.

[117]   S. Korablov, M. Yoshimura, Hydrothermal corrosion of TiN PVD films on SUS-304, Corros. Sci. 45 (2003) 531–543. doi:10.1016/S0010-938X(02)00143-9.

[118]   S. Korablov, M.A.M. Ibrahim, M. Yoshimura, Hydrothermal corrosion of TiAlN and CrN PVD films on stainless steel, Corros. Sci. 47 (2005) 1839–1854. doi:10.1016/j.corsci.2004.08.009.

[119]   J.H. Hsieh, A.L.K. Tan, X.T. Zeng, Oxidation and wear behaviors of Ti-based thin films, Surf. Coat. Technol. 201 (2006) 4094–4098. doi:10.1016/j.surfcoat.2006.08.026.

[120]   Y.C. Chim, X.Z. Ding, X.T. Zeng, S. Zhang, Oxidation resistance of TiN, CrN, TiAlN and CrAlN coatings deposited by lateral rotating cathode arc, Thin Solid Films. 517 (2009) 4845–4849. doi:10.1016/j.tsf.2009.03.038.

[121]   S.-M. Yang, Y.-Y. Chang, D.-Y. Lin, D.-Y. Wang, W. Wu, Thermal stability of TiAlN and nanocomposite TiAlSiN thin films., J. Nanosci. Nanotechnol. 9 (2009) 1108–1112. doi:10.1166/jnn.2009.C098.

[122]   R. Qiang, H. Shejun, Effects of Ti$_{0.5}$Al$_{0.5}$N coatings on the protecting against oxidation for titanium alloys, Rare Met. 29 (2010) 154–161. doi:10.1007/s12598-010-0027-1.

[123]   L. Zhu, M. Hu, W. Ni, Y. Liu, High temperature oxidation behavior of Ti$_{0.5}$Al$_{0.5}$N coating and Ti$_{0.5}$Al$_{0.4}$Si$_{0.1}$N coating, Vacuum. 86 (2012) 1795–1799. doi:10.1016/j.vacuum.2012.04.013.

[124]   J. Desmaison, P. Lefort, M. Billy, Oxidation of titanium nitride in oxygen: Behavior of TiN$_{0.83}$ and TiN$_{0.79}$ plates, Oxid. Met. 13 (1979) 203–222.

http://www.springerlink.com/index/R03K7556M84H5281.pdf.

[125] J. Desmaison, P. Lefort, M. Billy, Oxidation mechanism of titanium nitride in oxygen, Oxid. Met. 13 (1979) 505–517. doi:10.1007/BF00812775.

[126] J. Piippo, B. Elsener, H. Böhni, Electrochemical characterization of TiN coatings, Surf. Coatings Technol. 61 (1993) 43–46. doi:10.1016/0257-8972(93)90200-8.

[127] S. Rudenja, P. Kulu, E. Talimets, V. Mikli, O. Forsen, Corrosion performance of titanium-based composite coatings deposited by physical vapour deposition, in: Proc. Est. Acad. Sci. Eng., 1996: pp. 14–25.

[128] W.G. Cook, R.P. Olive, Pourbaix diagrams for chromium, aluminum and titanium extended to high-subcritical and low-supercritical conditions, Corros. Sci. 58 (2012) 291–298. doi:10.1016/j.corsci.2012.02.002.

[129] K.A. Terrani, Y. Yang, Y.-J. Kim, R. Rebak, H.M. Meyer, T.J. Gerczak, Hydrothermal corrosion of SiC in LWR coolant environments in the absence of irradiation, J. Nucl. Mater. 465 (2015) 488–498. doi:10.1016/j.jnucmat.2015.06.019.

[130] E.P. Meagher, G.A. Lager, Polyhedral thermal expansion in the TiO_2 polymorphs: refinement of the crystal structures of rutile and brookite at high temperature, Can. Mineral. 17 (1979) 77–85. doi:10.1103/PhysRevB.76.235307.

[131] J.A. Van Orman, K.L. Crispin, Diffusion in Oxides, Rev. Mineral. Geochemistry. 72 (2010) 757–825. doi:10.2138/rmg.2010.72.17.

[132] A.F. Beck, M.A. Heine, E.J. Caule, M.J. Pryor, The kinetics of the oxidation of Al in oxygen at high temperature, Corros. Sci. 7 (1967) 1–22. doi:10.1016/S0010-938X(67)80066-0.

[133] P. Eklund, M. Sridharan, G. Singh, J. Bøttiger, Thermal Stability and Phase Transformations of γ-/Amorphous-Al_2O_3 Thin Films, Plasma Process. Polym. 6 (2009) S907–S911. doi:10.1002/ppap.200932301.

[134] T. Nabatame, T. Yasuda, M. Nishizawa, M. Ikeda, T. Horikawa, A. Toriumi, Comparative Studies on Oxygen Diffusion Coefficients for Amorphous and γ- Al_2O_3 Films using 18 O Isotope, Jpn. J. Appl. Phys. 42 (2003) 7205–7208. doi:10.1143/JJAP.42.7205.

[135] E.B. Kashkarov, N.N. Nikitenkov, A.N. Sutygina, A.O. Bezmaternykh, V.N. Kudiiarov, M.S. Syrtanov, et al., Hydrogenation behavior of Ti-implanted Zr-1Nb alloy with TiN films deposited using filtered vacuum arc and magnetron sputtering, Appl. Surf. Sci. (2017) 1–7. doi:10.1016/j.apsusc.2017.04.035.

[136] I. Younker, M. Fratoni, Neutronic evaluation of coating and cladding materials for accident tolerant fuels, Prog. Nucl. Energy. 88 (2016) 10–18. doi:10.1016/j.pnucene.2015.11.006.

[137] D. Mattox, Handbook of Physical Vapour Deposition (PVD) Processing: Film Formation, Adhesion, Surface Preparation and Contamination Control, Noyes Publications, Westwood, New Jersey, 1998. doi:10.1080/10426919908907566.

[138] V.F. Puchkarev, S.M. Chesnokov, Erosion rate and voltage distribution in contracted (with cathode spot) and diffuse (spotless) low-current vacuum arcs, J. Phys. D. Appl. Phys. 25 (1992) 1760–1766. doi:10.1088/0022-3727/25/12/011.

[139] P.A. Lindfors, W.M. Mularie, G.K. Wehner, Cathodic arc deposition technology, Surf. Coatings Technol. 29 (1986) 275–290. doi:DOI: 10.1016/0257-8972(86)90001-0.

[140] B.A. Eizner, G.V. Markov, A.A. Minevich, Deposition stages and applications of CAE multicomponent coatings, Surf. Coatings Technol. 79 (1996) 178–191. doi:10.1016/0257-8972(95)02427-1.

[141] ASTM C1624-05 Standard Test Method for Adhesion Strength and Mechanical Failure Modes of Ceramic Coatings by Quantitative Single Point Scratch Testing, 5 (2009) 1–29. doi:10.1520/C1624-05R15.Scope.

[142] ASTM G2: Standard Test Method for Corrosion Testing of Products of Zirconium ,

Hafnium , and Their Alloys in Water at 680°F (360°C) or in Steam at 750°F (400°C), 6 (n.d.) 1–8. doi:10.1520/G0002.

[143] ASTM E2009-08: Standard Test Methods for Oxidation Onset Temperature of Hydrocarbons by Differential Scanning Calorimetry, (2014). doi:10.1520/E2009-08R14E01.2.

[144] J. Leppänen, Serpent – a Continuous-energy Monte Carlo Reactor Physics Burnup Calculation Code, VTT Technical Research Centre of Finland, March 6, 2013.

[145] Westinghouse Electric Company LLC, CHAPTER 4 AP1000 Design Control Document 4 . Reactor AP1000 Design Control Document, (2011) 1–12.

[146] M. Fratoni, E. Greenspan, Neutronic design of hydride fueled BWRs, Nucl. Eng. Des. 239 (2009) 1531–1543. doi:10.1016/j.nucengdes.2009.01.016.

[147] J.P. Foster, R.J. Comstock, S.A. Worcester, G.P. Sabol, ZIRLO Material for Light Water Reactor Applications, 5,112,573, 1992.

[148] D.O. Northwood, X. Meng-Burany, B.D. Warr, Microstructure of Zr-2.5Nb Alloy Pressure Tubing, Zircon. Nucl. Ind. Ninth Int. Symp. ASTM STP1132. (1991) 156–176. doi:10.1520/STP1132-EB.

[149] C.R. Brundle, C.A. Evans, Jr., S. Wilson, eds., Encyclopedia of Materials Characterization, Butterworth-Heinemann, 1992.

[150] W.D. Münz, D.B. Lewis, S. Creasey, T. Hurkmans, T. Trinh, W. Ijzendorn, Defects in TiN and TiAIN coatings grown by combined cathodic arc/unbalanced magnetron technology, Vacuum. 46 (1995) 323–330. doi:10.1016/0042-207X(94)E0029-X.

[151] M.I. Lembke, D.B. Lewis, W.-D. Münz, Localised oxidation defects in TiAlN/CrN superlattice structured hard coatings grown by cathodic arc/ unbalanced magnetron deposition on various substrate materials, Surf. Coatings Technol. 125 (2000) 263–268. doi:10.1016/S0257-8972(99)00571-X.

[152] I. Petrov, P. Losbichler, D. Bergstrom, J.E. Greene, W.-D. Münz, T. Hurkmans, et al., Ion-assisted growth of TiAlN/TiNbN multilayers by combined cathodic-arc/magnetron-sputter deposition, Thin Solid Films. 302 (1997) 179–192.

[153] J.M. Andersson, J. Vetter, J. Müller, J. Sjölén, Structural effects of energy input during growth of Ti1-xAlxN (0.55≤x≤0.66) coatings by cathodic arc evaporation, Surf. Coatings Technol. 240 (2014) 211–220. doi:10.1016/j.surfcoat.2013.12.018.

[154] D.M. Mattox, 2-Substrate (Real) Surfaces and Surface Modification, 1998. doi:10.1016/B978-0-8155-2037-5.00002-2.

[155] L. Szparaga, J. Ratajski, A. Zarychta, Multi objective optimization of wear resistant TiAlN and TiN coatings deposite by PVD techniques, Arch. Mater. Sci. Eng. 48 (2011) 33–39.

[156] Y. Liu, I. Bhamji, P.J. Withers, D.E. Wolfe, A.T. Motta, M. Preuss, Evaluation of the interfacial shear strength and residual stress of TiAlN coating on ZIRLO^{TM} fuel cladding using a modified shear-lag model approach, J. Nucl. Mater. 466 (2015) 718–727. doi:10.1016/j.jnucmat.2015.06.003.

[157] A. Yilmazbayhan, A.T. Motta, R.J. Comstock, G.P. Sabol, B. Lai, Z. Cai, Structure of zirconium alloy oxides formed in pure water studied with synchrotron radiation and optical microscopy: Relation to corrosion rate, J. Nucl. Mater. 324 (2004) 6–22. doi:10.1016/j.jnucmat.2003.08.038.

[158] P.K. Datta, H.L. Du, R. Ricker, J.S. Burnell-Gray, Corrosion of Intermetallics, ASM Handb. Vol. 13B Corros. Mater. 13 (2005) 490–512. doi:10.1361/asmhba0003837.

[159] F. Di Quarto, K. Doblhofer, H. Gerischer, Instability of anodically formed TiO_2 layers, Electrochim. Acta. 23 (1978) 195–201.

[160] T.K. Kim, J.H. Baek, B.K. Choi, Y.H. Jeong, Influence of ammonia on the corrosion behavior of Ti-Al-Zr alloy in 360°C water, Met. Mater. Int. 13 (2007) 47–52.

doi:10.1007/BF03027822.

[161] T.S. Kannan, P.K. Panda, V.A. Jaleel, Preparation of pure boehmite, α–Al$_2$O$_3$ and their mixtures by hydrothermal oxidation of aluminium metal, J. Mater. Sci. Lett. 16 (1997) 830–834.

[162] K. Okada, T. Nagashima, Y. Kameshima, A. Yasumori, T. Tsukada, Relationship between formation conditions, properties, and crystallite size of boehmite., J. Colloid Interface Sci. 253 (2002) 308–314. doi:10.1006/jcis.2002.8535.

[163] F. Rickhey, M. Kim, H. Lee, N. Kim, Evaluation of combined hardening coefficients of Zircaloy-4 sheets by simple shear test, Mater. Des. 65 (2015) 995–1000. doi:10.1016/j.matdes.2014.10.027.

[164] M. Brova, Ytterbium-doped Titanium Aluminum Nitride Coatings for the Oxidation Resistance of ZIRLO® Nuclear Fuel Cladding, 2016.

[165] D.M. Mattox, Film Characterization and Some Basic Film Properties, 1998. doi:10.1016/B978-0-8155-2037-5.00011-3.

[166] E. Bemporad, M. Sebastiani, C. Pecchio, S. De Rossi, High thickness Ti / TiN multilayer thin coatings for wear resistant applications, Surf. Coatings Technol. 201 (2006) 2155–2165. doi:10.1016/j.surfcoat.2006.03.042.

[167] H. Holleck, Metastable coatings - Prediction of composition and structure, Surf. Coatings Technol. 36 (1988) 151–159. doi:10.1016/0257-8972(88)90145-4.

[168] H. Freller, H. Haessler, Ti$_x$Al$_{1-x}$N films deposited by ion plating with an arc evaporator, Thin Solid Films. 153 (1987) 67–74. doi:10.1016/0040-6090(87)90170-2.

[169] E. Erturk, H.-J. Heuvel, Adhesion and structure of TiN arc coatings, Thin Solid Films. 153 (1987) 135–147.

[170] A.N. Kale, K. Ravindranath, D.C. Kothari, P.M. Raole, Tribological properties of (Ti,Al)N coatings deposited at different bias voltages using the cathodic arc technique,

Surf. Coatings Technol. 145 (2001) 60–70. doi:10.1016/S0257-8972(01)01296-8.

[171] S. PalDey, S.C. Deevi, Properties of single layer and gradient (Ti,Al)N coatings, Mater. Sci. Eng. A. 361 (2003) 1–8. doi:10.1016/S0921-5093(03)00473-8.

[172] H.C. Barshilia, M.S. Prakash, A. Jain, K.S. Rajam, Structure, hardness and thermal stability of TiAlN and nanolayered TiAlN/CrN multilayer films, Vacuum. 77 (2005) 169–179. doi:10.1016/j.vacuum.2004.08.020.

[173] K. Sato, N. Ichimiya, A. Kondo, Y. Tanaka, Microstructure and mechanical properties of cathodic arc ion-plated (Al,Ti)N coatings, Surf. Coatings Technol. 163–164 (2003) 135–143. doi:10.1016/S0257-8972(02)00610-2.

[174] L. Karlsson, L. Hultman, M.P. Johansson, J.-E. Sundgren, H. Ljungcrantz, Growth, microstructure, and mechanical properties of arc evaporated TiCxN1−x (0≤x≤1) films, Surf. Coatings Technol. 126 (2000) 1–14. doi:10.1016/S0257-8972(00)00518-1.

[175] P.J. Blau, Chapter 7, Scratch Adhesion Testing, in: Lab Handb. Scratch Testing, , Blue Rock Technical Publ., Oak Ridge, TN, 2002: p. 7.1-7.15.

[176] V.M. Khoroshikh, S.A. Leonov, V.A. Belous, Influence of substrate geometry on ion-plasma coating deposition process, Probl. At. Sci. Technol. (2008) 72–76. doi:10.1109/DEIV.2008.4676863.

[177] M.M.M. Bilek, Effect of sheath evolution on metal ion implantation in a vacuum arc plasma source, J. Appl. Phys. 89 (2001) 923. doi:10.1063/1.1331072.

[178] H.G. Prengel, A.T. Santhanam, R.M. Penich, P.C. Jindal, K.H. Wendt, Advanced PVD-TiAlN coatings on carbide and cermet cutting tools, Surf. Coatings Technol. 94 (1997) 597–602. doi:10.1016/S0257-8972(97)00503-3.

[179] A. Kimura, T. Murakami, K. Yamada, T. Suzuki, Hot-pressed Ti-Al targets for synthesizing Ti 1yx Al x N films by the arc ion plating method, Thin Solid Films. 382 (2001) 101–105.

[180] J.E. Daalder, Cathode spots and vacuum arcs, Phys. 104C. 104 (1981) 91–106. doi:10.1016/0378-4363(81)90040-1.

[181] W.-D. Münz, I.J. Smith, D.B. Lewis, S. Creasey, Droplet formation on steel substrates during cathodic steered arc metal ion etching, Vacuum. 48 (1997) 473–481. doi:10.1016/S0042-207X(96)00307-7.

[182] S.G. Harris, E.D. Doyle, A.C. Vlasveld, P.J. Dolder, Dry cutting performance of partially filtered arc deposition titanium aluminium nitride coatings with various metal nitride base coatings, Surf. Coatings Technol. 146–147 (2001) 305–311. doi:10.1016/S0257-8972(01)01421-9.

[183] H. Wang, R.C. Reed, J.C. Gebelin, N. Warnken, On the modelling of the point defects in the ordered B2 phase of the Ti-Al system: Combining CALPHAD with first-principles calculations, CALPHAD Comput. Coupling Phase Diagrams Thermochem. 39 (2012) 21–26.

[184] C.P. Constable, J. Yarwood, W.-D. Münz, Raman microscopic studies of PVD hard coatings, Surf. Coatings Technol. 116–119 (1999) 155–159. doi:10.1016/S0257-8972(99)00072-9.

[185] W. Spengler, R. Kaiser, First and second order Raman scattering in transition metal compounds, Solid State Commun. 18 (1976) 881–884. doi:10.1016/0038-1098(76)90228-3.

[186] W. Spengler, R. Kaiser, A.N. Christensen, G. Mueller-Vogt, Raman scattering, superconductivity, and phonon density of states of stoichiometric and nonstoichiometric TiN, Phys. Rev., B. 17 (1978) 1095–1101.

[187] H.C. Barshilia, K.S. Rajam, Raman spectroscopy studies on the thermal stability of TiN, CrN, TiAlN coatings and nanolayered TiN/CrN, TiAlN/CrN multilayer coatings, J. Mater. Res. 19 (2004) 3196–3205. doi:10.1557/JMR.2004.0444.

[188] R.K. Hart, The formation of films on aluminium immersed in water, Trans. Faraday Soc. 53 (1956) 1020–1027.

[189] N.R. Brown, H. Ludewig, A. Aronson, G. Raitses, M. Todosow, Neutronic evaluation of a PWR with fully ceramic microencapsulated fuel. Part I: Lattice benchmarking, cycle length, and reactivity coefficients, Ann. Nucl. Energy. 62 (2013) 538–547. doi:10.1016/j.anucene.2013.05.025.

[190] S. Chen, C. Yuan, Neutronic Analysis on Potential Accident Tolerant Fuel-Cladding Combination U_3Si_2-FeCrAl, Sci. Technol. Nucl. Install. 2017 (2017). doi:10.1155/2017/3146985.

[191] X. Wu, T. Kozlowski, J.D. Hales, Neutronics and fuel performance evaluation of accident tolerant FeCrAl cladding under normal operation conditions, Ann. Nucl. Energy. 85 (2015) 763–775. doi:10.1016/j.anucene.2015.06.032.

[192] O. Novák, M. Ševeček, Neutronic analysis of the candidate multi-layer cladding materials with enhanced accident tolerance for VVER reactor, in: 2017 Water React. Fuel Perform. Meet., 2017.

[193] N.M. George, K. Terrani, J. Powers, A. Worrall, I. Maldonado, Neutronic analysis of candidate accident-tolerant cladding concepts in pressurized water reactors, Ann. Nucl. Energy. 75 (2015) 703–712. doi:10.1016/j.anucene.2014.09.005.

[194] J. Leppanen, PSG2/Serpent-A continuous-energy Monte Carlo reactor physics burnup calculation code, VTT Technical Research Centre of Finland, March 5 (2012).

Appendix A: Residual Stress Calculation

The following calculation is done to determine the extrinsic residual stresses occurred upon cooling to room temperature from the deposition temperature:

$$\sigma_{CTE} = \frac{E_C}{1 - v_C} \int_{T_d}^{T_f} (\alpha_S - \alpha_C) dT$$

Assuming constant thermal expansion

$$\sigma_{CTE} = \frac{E_C}{1 - v_C} (\alpha_S - \alpha_C)(T_f - T_d)$$

$\alpha_S = 6.3 \; x \; 10^{-6} \; \text{K}^{-1}$

$\alpha_C = 7.5 \; x \; 10^{-6} \; \text{K}^{-1}$

$v_C = 0.23$

$E_C = 406.5 \; \text{GPa}$

$T_f = 25 \; °\text{C}$

$T_d = 325 \; °\text{C}$

$$\sigma_{CTE} = 0.190 \; GPa$$

The following calculation is done to determine the extrinsic residual stresses occurred upon cooling to room temperature after the autoclave test:

$$\sigma_{CTE} = \frac{E_C}{1 - v_C} \int_{T_d}^{T_f} (\alpha_S - \alpha_C) dT$$

Assuming constant thermal expansion

$$\sigma_{CTE} = \frac{E_C}{1 - v_C} (\alpha_S - \alpha_C)(T_f - T_a)$$

$\alpha_S = 6.3 \; x \; 10^{-6} \; \text{K}^{-1}$

$\alpha_C = 7.5 \; x \; 10^{-6} \; \text{K}^{-1}$

$$v_C = 0.23$$

$$E_C = 406.5 \text{ GPa}$$

$$T_f = 25 \text{ °C}$$

$$T_a = 360 \text{ °C}$$

$$\sigma_{CTE} = 0.210 \ GPa$$

Appendix B: Scratched Sample Corrosion Performance

As a part of the coating corrosion performance investigation, scratched samples were tested in autoclave with their unscratched counterparts to evaluate whether there were accelerated corrosion or healing effect in the case of scratched samples. Figure B-1 shows digital images of scratched (Figure B-1a) and unscratched (Figure B-1b) 2-layer TiN/TiAlN coated ZIRLO® sheets, and weight gain data (Figure B-1c) obtained after autoclave testing in static pure water at 360°C and 18.7 MPa for 47 days. The spallation on the surface of both samples was visually obvious. Spallation was concentrated around scratches in the case of the scratched sample surface. This spallation was also reflected to the weight gain data as negative weight gain reaching to -24 mg/dm^2 in the case of scratched and -21 mg/dm^2 in the case of unscratched sample. Weight gain data obtained for both samples were like each other indicating similar corrosion rate, but the scratched one showed a slightly more negative weight gain value. Further investigation was performed using SEM and EDS analysis.
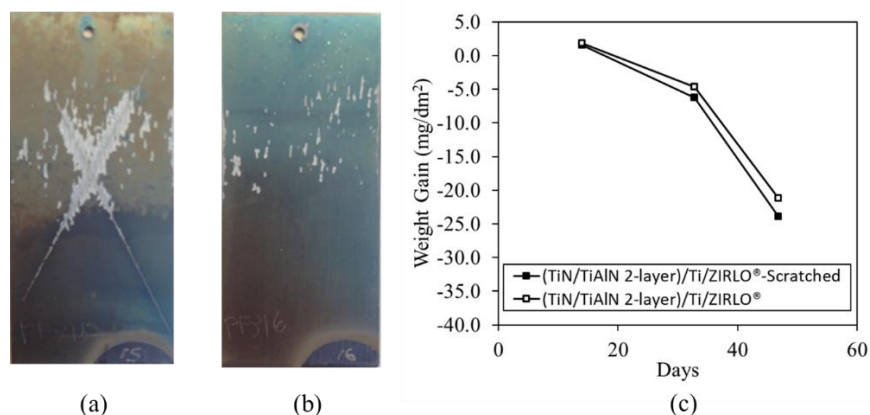

(a) (b) (c)

Figure B-1. (a) Digital image of scratched (2-layer TiN/TiAlN)/Ti/ZIRLO®, (b) digital image of unscratched 2-layer TiN/TiAlN/Ti/ZIRLO® and (c) weight gain data after autoclave testing in static pure water at 360°C and 18.7 MPa for 47 days.

Figure B-2 shows the surface SEM image of the scratched and autoclave tested sample. Figure B-2a shows the general appearance of the scratch, showing buckling of the coating occurred because of scratching, spallation and delamination regions. Additionally, crack formation occurred around scratches which are presented with higher resolution in Figure B-2b.
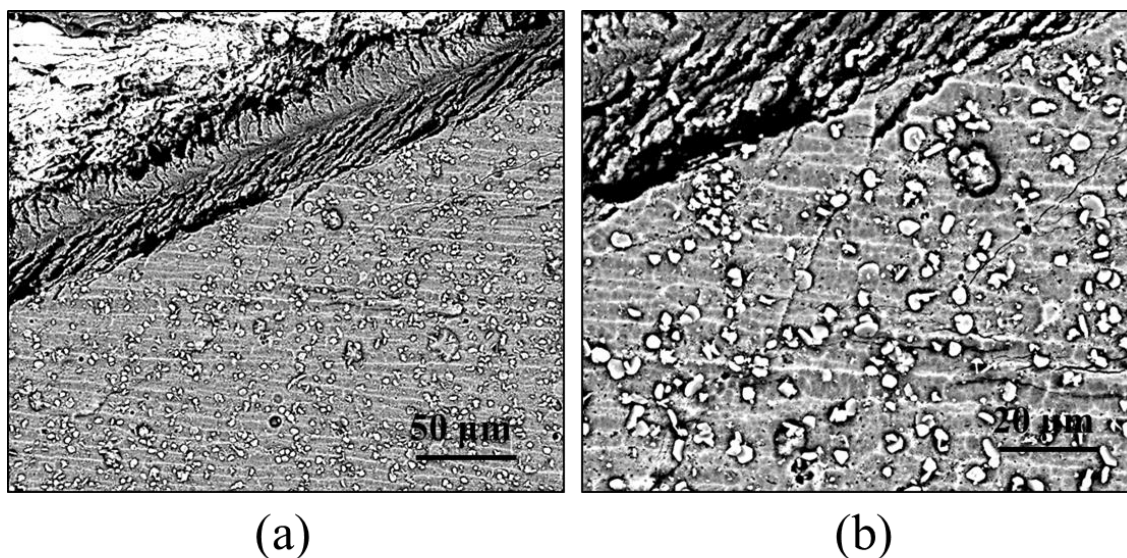

(a) (b)

Figure B-2. Scanning electron microscopy (SEM) backscattered electron (BSE) image showing (a) general scratch appearance and (b) cracks formed around the scratched region on the surface of the 2-layer TiN/TiAlN coated, scratched and autoclave tested sample in static pure water at 360°C and 18.7 MPa for 47 days.

Figure B-3 presents the EDS point analysis data obtained from the surface of scratched 2-layer TiN/TiAlN coated ZIRLO® sheet autoclave tested for 47 days. The EDS point analyses were performed at two sites, one corresponding to a spallation region and the other site corresponding to a region where the coating was maintained on the surface. Figure B-3a shows the electron microscopy image and the two sites that the point analyses were conducted. The chemical compositions obtained from these two sites are presented in Figure B-3b. The spallation region (Site 1) was confirmed to be having ZrO_2 and the maintained coating confirmed to be having TiO_2 on the surface according to the EDS point analyses. At the coating region, nitrogen

was also observed origin from the TiN layer. Additionally, minor amount of carbon was observed at the EDS analysis of both sites which was because of the contamination in the autoclave.

Site 1

Element	Wt%	Atomic %
C	1.05	3.52
O	25.40	63.81
Zr	72.33	31.87

Site 2

Element	Wt%	Atomic %
C	1.28	2.72
N	2.88	5.23
O	38.80	61.78
Ti	55.22	29.37

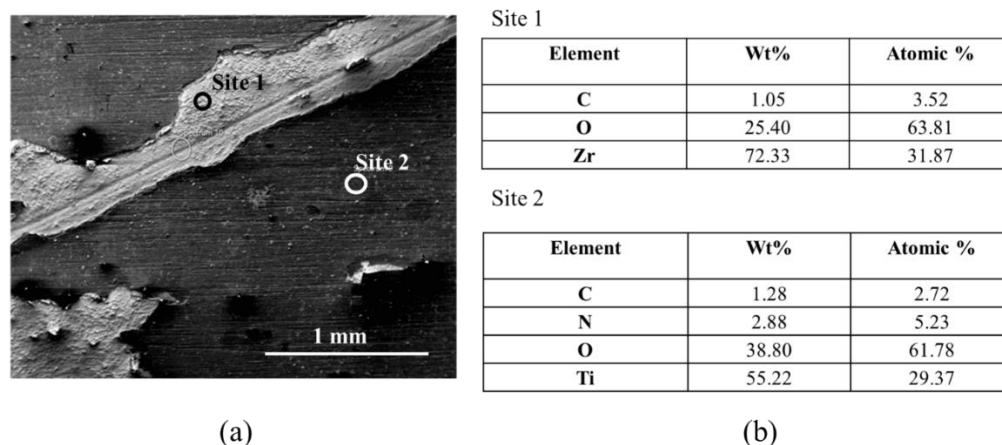(a)   (b)

Figure B-3. Energy dispersive spectroscopy (a) electron microscopy image showing the point analysis sites and (b) chemical analysis data of spallation site (site 1) and coating site (site 2) performed on the scratched (2-layer TiN/TiAlN)/Ti/ZIRLO® autoclave tested in static pure water at 360°C and 18.7 MPa for 47 days.

Figure B-4 shows the cross-section SEM-BSE images of the scratched regions. Cross-section sample was prepared by cutting the sample into half perpendicular to the longitudinal axis and then, molding the cut halves after placing them adjacent to each other. In these images two side of the scratched sample are shown. The sample that is shown at the upper part of the image has coating on the surface. The bottom part of the SEM-BSE images (Figure B-4a and Figure B-4b) represent the scratched regions. These cross-section SEM images showed that the scratch depth was ~10 µm. As it was previously observed on the surface digital images in Figure 3-38, scratched regions were assisted with coating spallation regions. These coating spallation regions were confirmed once again with the cross-section analysis. At the spallation regions, zirconium dioxide determined to be forming at a uniform thickness of 2.7±0.26 µm at the region where the substrate surface was exposed to the corrosive environment. Whereas at the regions where the coating was maintained, ZIRLO® substrate was not oxidized.
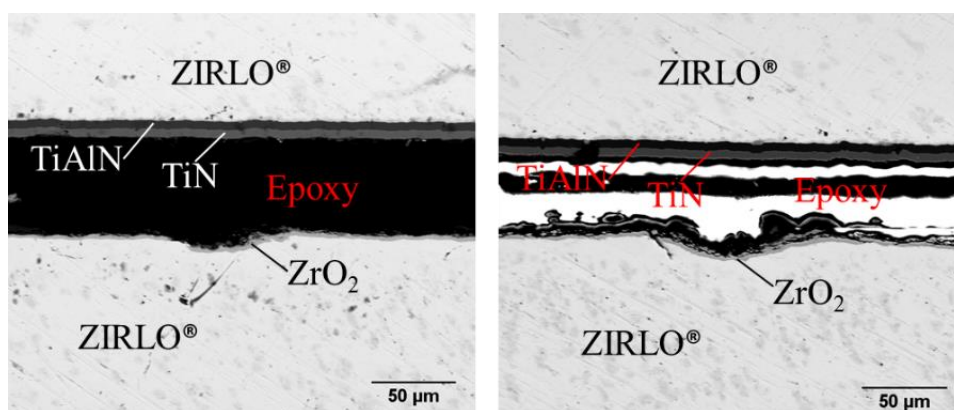
Figure B-4. (a) Digital images of scratched and unscratched 2-layer TiN/TiAlN coated samples autoclave tested in static pure water at 360°C and 18.7 MPa for 47 days. Figures in (b) and (c) are the cross-section SEM- BSE images of the two scratched regions along the cross-sectioned side of the sample.

Appendix C: Functionally Grading

Functionally grading was performed to achieve a smooth transition from the pure titanium layer to the TiAlN layer which will provide compensation of the thermal expansion coefficient differences between different layers leading to the coating adhesion enhancement. Based on the 2-layer TiN/TiAlN coating design three different functional grading approaches of 10%, 20% and 30% were investigated. Functionally grading was performed by increasing the nitrogen pressure during deposition of the TiAlN layer. Both sides of the ZIRLO® sheets were coated after deposition of the titanium bond coating layer with a thickness of ~0.6 μm. Before autoclave testing, one side of the samples were scratched to simultaneously evaluate the effect of scratching on the corrosion performance of these coatings. Autoclave testing was performed in autoclave in static pure water at 360°C and 18.7 MPa for 89 days.

Figure C-1 shows the front and back images of the autoclave tested samples. Samples showed color variations on the surface in a color ranging between a bright purple and a matte green color. These color changes were attributed to the oxidation of the coatings. Scratched regions showed minor spallation, which were much less compared to the 2-layer TiN/TiAlN coated sample that was presented in the previous section. This indicated an enhanced corrosion performance of the 2-layer TiN/TiAlN coated sample achieved with functionally grading of the TiAlN layer. Cross-section analysis was performed to determine whether there was any oxidation of the substrate ZIRLO® both at the scratched and unscratched regions. Red dash line on the images indicate the regions at which the cross-section analysis was performed.
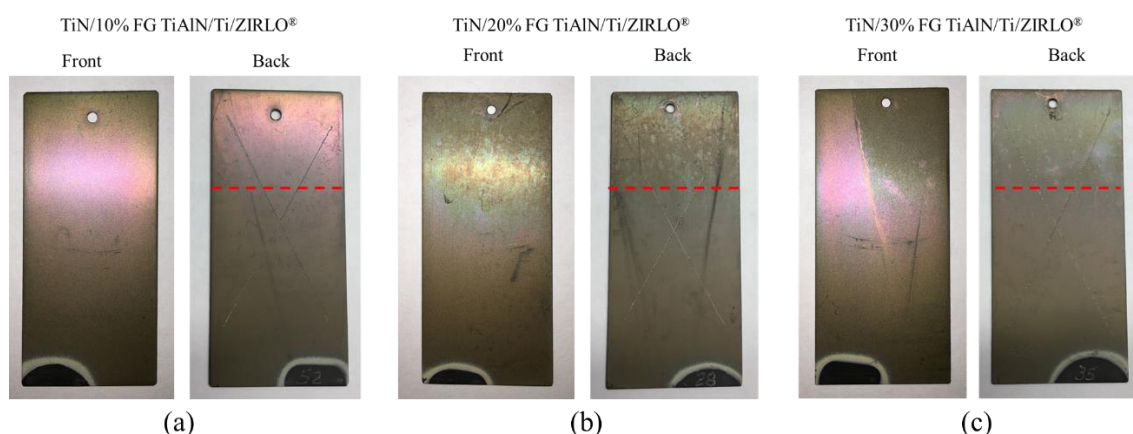
Figure C-1. Digital images of the 89 days autoclave tested TiN/10% FG TiAlN/Ti/ZIRLO®, TiN/20% FG TiAlN/Ti/ZIRLO® and TiN/30% FG TiAlN/Ti/ZIRLO® samples.

Figure C-2 shows the weight gain data obtained during the autoclave testing. Weight gain data of both the scratched and unscratched samples having coatings deposited with the same parameters were provided. All the coatings showed negative weight gain indicating coating spallation and poor adhesion. However, compared to the not functionally graded sample data that was presented in Figure 3-38, much less negative weight gain was observed, which is promising in terms of functionally grading contribution to enhancing adhesion of the coating to the substrate.
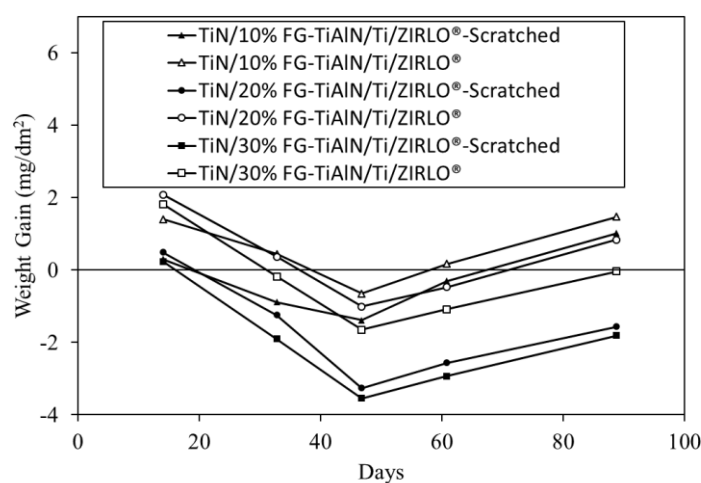

Figure C-2. Weight gain data of the 89 days autoclave tested scratched and unscratched TiN/10% FG TiAlN/Ti/ZIRLO®, TiN/20% FG TiAlN/Ti/ZIRLO® and TiN/30% FG TiAlN/Ti/ZIRLO® samples.

Figure C-3 shows the cross-section SEM-BSE images of the 89 days autoclave tested TiN/10% FG TiAlN/Ti/ZIRLO®, TiN/20% FG TiAlN/Ti/ZIRLO® and TiN/30% FG TiAlN/Ti/ZIRLO® samples. Uniform Ti-BC, TiAlN and top TiN layers were observed on the substrate surface. Functionally grading regions were also noticed in the SEM-BSE cross-section images because of image contrast caused by the atomic number variation. Macroparticles were observed as usual. 20%FG TiAlN and 30%FG TiAlN having coatings had some porosities in the coating. 10%FG TiAlN having coating observed to be having a thinner coating compared to other two coating designs.
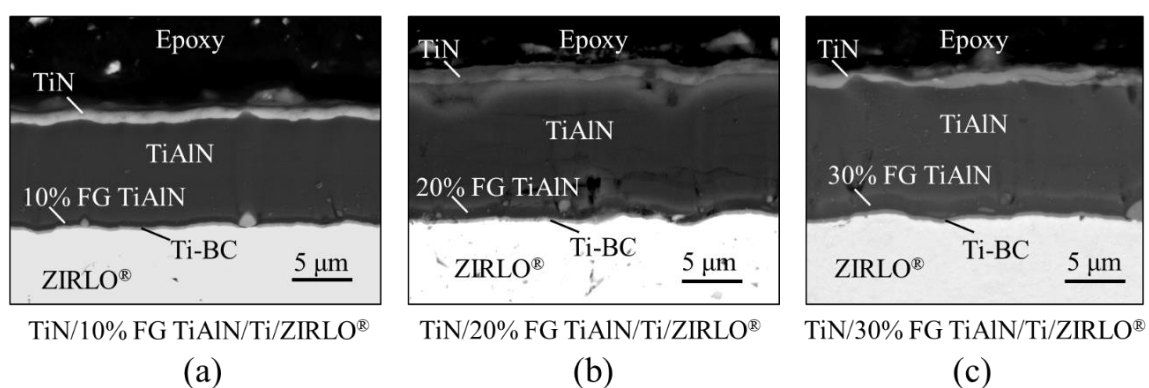

Figure C-3. Cross-section SEM-BSE images of the 89 days autoclave tested TiN/10% FG TiAlN/Ti/ZIRLO®, TiN/20% FG TiAlN/Ti/ZIRLO® and TiN/30% FG TiAlN/Ti/ZIRLO® samples.

Figure C-4 shows the EDS-line scans performed on the cross-section of the 89 days autoclave tested TiN/10% FG TiAlN/Ti/ZIRLO®, TiN/20% FG TiAlN/Ti/ZIRLO® and TiN/30% FG TiAlN/Ti/ZIRLO® samples to evaluate oxygen penetration, and functionally grading regions. EDS-elemental line scans confirmed achievement of the functionally grading during the deposition process. Titanium oxide formation on the surface was also confirmed. No substrate oxidation was observed at the line scan performed region where the coating was maintained on the surface.
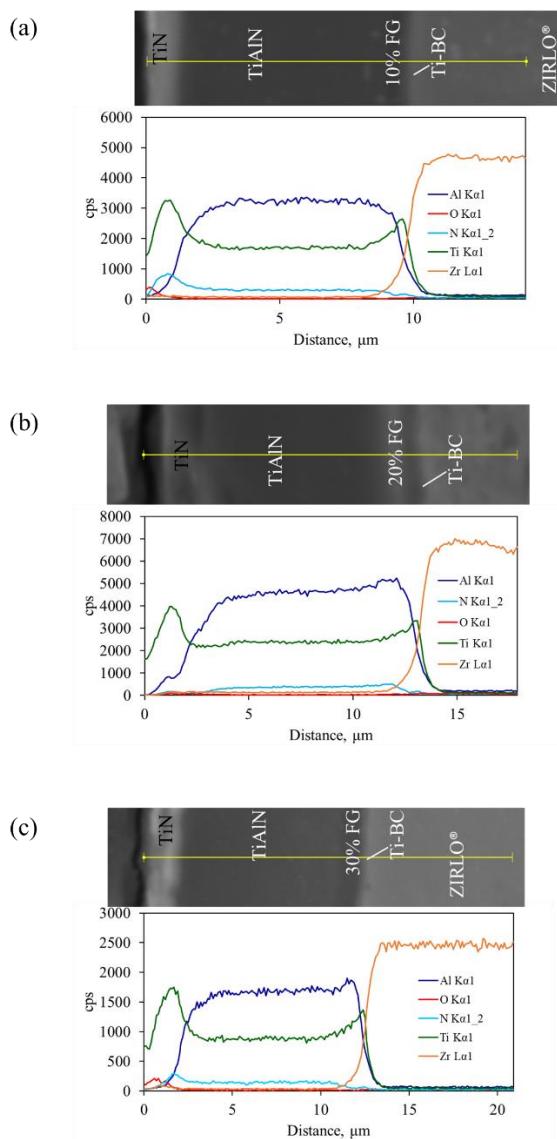
Figure C-4. EDS-elemental line scans of the 89 days autoclave tested TiN/10% FG TiAlN/Ti/ZIRLO®, TiN/20% FG TiAlN/Ti/ZIRLO® and TiN/30% FG TiAlN/Ti/ZIRLO® samples.

Figure C-5 shows the EDS-elemental map analysis performed on the scratched regions of the 89 days autoclave tested TiN/10% FG TiAlN/Ti/ZIRLO®, TiN/20% FG TiAlN/Ti/ZIRLO® and TiN/30% FG TiAlN/Ti/ZIRLO® samples. EDS map analysis confirmed substrate oxidation at the scratched regions and titanium oxide formation on the surface of the coatings where the TiN layer was able to be maintained on the surface. The electron images taken during the EDS

analysis also confirmed the cracked and almost crumbled structure of the coatings after scratching. However, although the integrity of the coatings was diminished because of the scratching that was performed before the autoclave testing, substrate oxidation was able to be prevented through remaining coatings that were well adhered to the substrate surface.

In summary, functionally grading provided promising results in terms of enhancing the coating adhesion to the substrate surface, which could be beneficial when it was performed to another multilayer TiN/TiAlN coating design such as 8-layer coating which was already determined to be the optimum multilayer TiN/TiAlN coating design to further improve its adhesion and corrosion resistance performance.
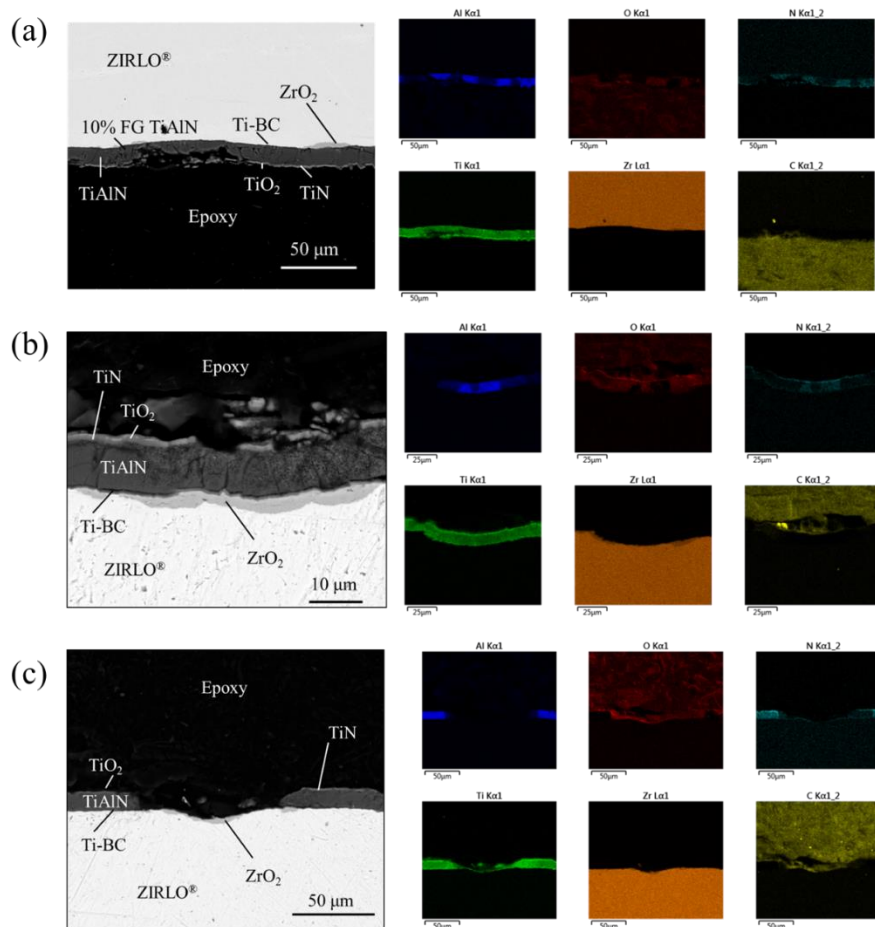

Figure C-5. EDS- Elemental map analysis of the 89 days autoclave tested TiN/10% FG TiAlN/Ti/ZIRLO®, TiN/20% FG TiAlN/Ti/ZIRLO® and TiN/30% FG TiAlN/Ti/ZIRLO® samples.

Appendix D: Sectioning Effect

During the characterization of the tested samples, coating degradation was suspected to be initiated from the edges. Although, coating uniformity on the surface of the tubular sample was tried to be investigated along the axis of previous samples, since the sample length was small (~4 cm) for this macroscale deposition process, no nonuniformity was observed. To confirm this finding, sectioning approach was decided to be conducted, in which an ~15 cm (6") tube sample was coated and then, cut into three 4 cm sections as shown in Figure D-1. Several samples that were prepared by either green scotch brite or grit blasting method were investigated for this effort. The sectioning effect slightly observed only in case of green scotch brite prepared samples. The substrate surface of the examined sample was prepared by lengthwise green scotch brite hand grinding method. Then, 8-layer TiN/TiAlN coating was deposited on the surface with a cathode composition of Ti/Al: 20/80 at.%. Coatings were exposed to static pure water at 360°C and 18.7 MPa for 98 days in an autoclave. To evaluate the coating uniformity and the corrosion performance XRD, SEM and EDS analyses were performed. During visual analysis, it was observed that although there was not a significant difference at the corrosion behavior of the section a and b, section c always showed less corrosion at the top region.
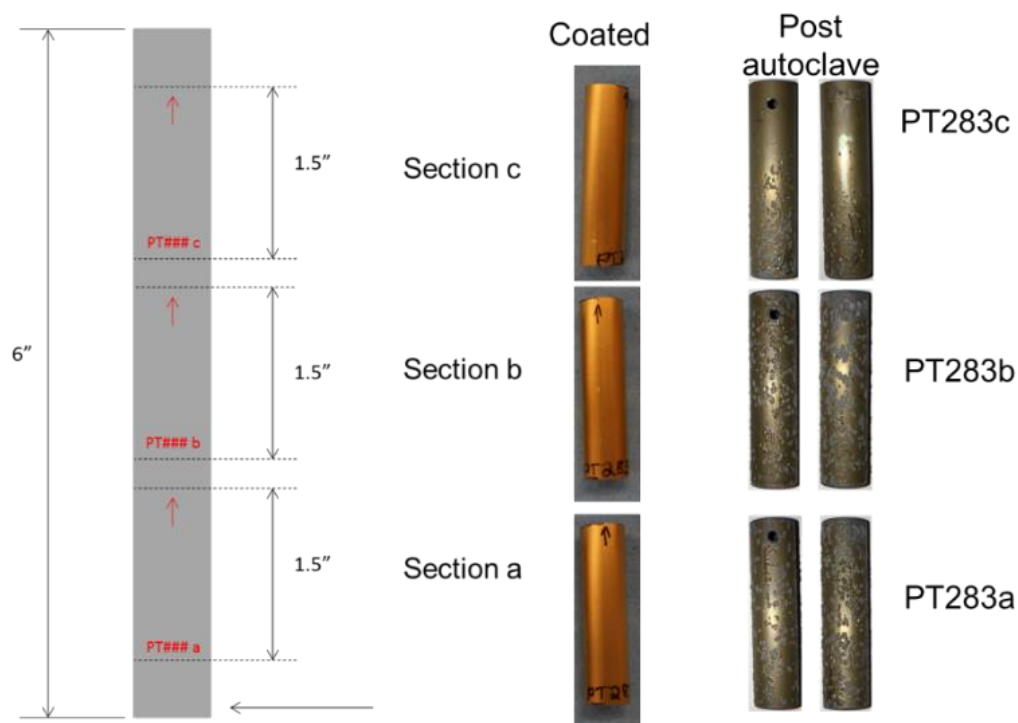
Figure D-1. Digital images of as-deposited and autoclave tested sample sections that were corrosion tested in static pure water at 360°C and 18.7 MPa for 98 days.

Figure D-2 shows the SEM-BSE surface images of the autoclave tested sample. It was observed that there was oxidation all over the surface. There were localized spallation and boehmite formation on the sample surface. The vast amount of spallation was observed at the cutting regions corresponding to the edges of the tube, which lead to zirconium oxide formation that was confirmed with EDS analysis. Similar results observed during characterization of other sections. Thus, it can be concluded that there was no sectioning effect, the spallation observed at the edges was due to the cutting process during sectioning.
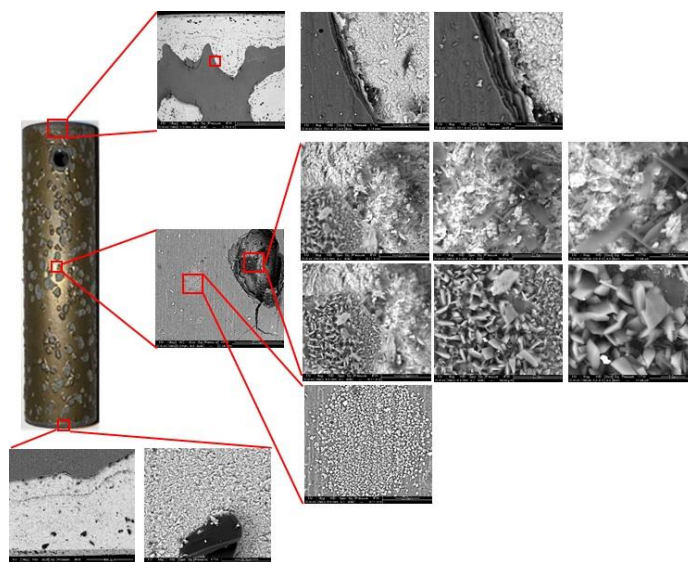
Figure D-2. Digital image and surface SEM-BSE images of sample sections that were corrosion tested in static pure water at 360°C and 18.7 MPa for 98 days

ECE ALAT

EDUCATION

The Pennsylvania State University, University Park, PA   August 2013 – May 2018
Ph.D., GPA: 3.77 / 4.0
Department of Materials Science and Engineering (MatSE)
Thesis: Ceramic Coatings for Nuclear Fuel Cladding to Enhance Accident Tolerance.

The Middle East Technical University, Ankara, Turkey
M.Sc.,GPA: 3.71 / 4.0   September 2009 - September 2012
Department of Metallurgical and Materials Engineering
Thesis: Analysis of Magnesium Addition, Hydrogen Porosity and T6 Heat Treatment Effects on Mechanical and Microstructural Properties of Pressure Die Cast 7075 Aluminum Alloy.

B.Sc., GPA: 3.04 / 4.00 – Honors Student   September 2003 - June 2007
Department of Metallurgical and Materials Engineering

WORK EXPERIENCE

Graduate Assistant, The Pennsylvania State University, August 2013 – present

R&D Engineer, The Mechanical and Chemical Industry (MKE) Corporation, April 2009 – August 2013

Quality Engineer, The Mechanical and Chemical Industry (MKE) Corporation**,** March 2009 – April 2009

Scientific Programs Assistant Expert, The Scientific and Technological Research Council of Turkey (TUBITAK), September 2007 – February 2009

Intern, The Turkish Atomic Energy Authority (TAEK), July – August 2006

Intern, The Turk Tractor and Agricultural Machinery Corporation, August – September 2005

PUBLICATIONS

- J. Hu, M. Li, M. Kirk, **E. Alat**, D. Wolfe and A. Motta, In situ ion irradiation and annealing experiments of multilayer (TiN, TiAlN) accident tolerant fuel (ATF) coatings on Zr cladding alloys (in preparation).

- **E. Alat**, M. Brova, I. Younker, A. T. Motta, M. Fratoni, and D. E. Wolfe, High Temperature Performance and Neutronic Analysis of TiN/ Doped TiAlN Coatings on ZIRLO® (in preparation).

- M. Brova, **E. Alat**, R. Sherbondy, M. A. Pauley, A.T. Motta, and D. E. Wolfe, Ytterbium-Doped Titanium Aluminum Nitride coatings for nuclear fuel cladding (submitted to Surf. Coat. Technol., 2017).

- S. A. Ebrahim, **E. Alat**, V. Fudurich, F. A. Sohag, F.-B. Cheung, S. M. Bajorek, K. Tien, and C. L. Hoxie, An experimental investigation of the effects of surface conditions on pool-boiling heat transfer for various materials, conference paper, The 17th International Topical Meeting on Nuclear Reactor Thermal Hydraulics (NURETH-17), China.

- E. Alat, A.T. Motta, R. J. Comstock, J. M. Partezana, and D. E. Wolfe, Multilayer ceramic coating for corrosion (C3) resistance of nuclear fuel cladding, Materials Science and Technology (MS&T16), conference paper, October 2016, Salt Lake City, Utah, USA.

- **E. Alat**, A.T. Motta, R. J. Comstock, J. M. Partezana, and D. E. Wolfe, Multilayer (TiN, TiAlN) ceramic coatings for nuclear fuel cladding, J. Nucl. Materials 478 (2016) 236-244.

- **E. Alat**, A.T. Motta, R. J. Comstock, J. M. Partezana, and D. E. Wolfe, Ceramic coating for corrosion (C3) resistance of nuclear fuel cladding, Surf. Coat. Technol. 281 (2015) 133-143.

LEADERSHIP ACTIVITIES, AWARDS AND HONORS

- **MatSE Representative at the Earth and Minerals Science (EMS) Graduate Council**, December 2016-2017.
- **Paper reviews for journals:** Fusion Engineering and Design, Scientific Reports, Journal of Nuclear Materials.
- **PPG Elevator Pitch Competition, 3rd Place**, June 2017.
- **Graduate Exhibition Video Competition, 2nd Place**, April 2017.
- **iMATSE Graduate Students Travel Award,** May 2016.
- **14th Annual Graduate Student Poster Competition, Group Poster Award, 1st Place**, April 2016.
- **The EMS Centennial Research Travel Award,** March 2016